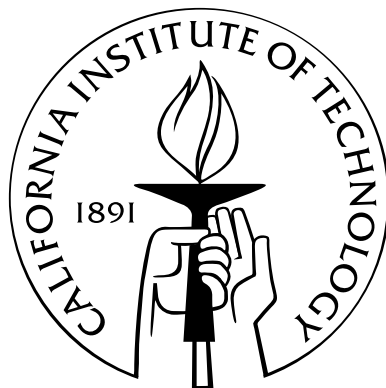


I. Nickel-Exchanged Zincosilicate Catalysts
for the Oligomerization of Propylene
and
II. Organic SDA-Free Catalysts for the
Methanol-to-Olefins Reaction

Thesis by

Mark A. Deimund

In Partial Fulfillment of the Requirements
for the Degree of
Doctor of Philosophy



California Institute of Technology
Pasadena, California

2015

(Defended 28 April 2015)

To my family for their encouragement, love, and support.

To my labmates for their insight, mentorship, and camaraderie.

Acknowledgments

I'd like to thank my advisor, Mark E. Davis, for his support and guidance throughout my PhD. You have taught me to think and act as a PhD should, both in dealing with my research challenges in the lab and with my collaborative work with other researchers. More importantly, aside from research, you have taught me how to deal with people, both in good situations and bad, always with a smile and a plan. With your enthusiasm and input, I've come to truly love the synthesis and characterization of molecular sieves.

Additionally, I would like to thank Jay Labinger, John Bercaw, and Rick Flagan of my PhD committee for their insightful discussions, suggestions, and feedback on my research work throughout the past several years.

Jay, your input at the numerous Davis group meetings throughout the past few years, as well as your insight into the fundamentals of chemistry, has been invaluable in advancing my understanding of not only light olefin oligomerization, but how to approach and tackle complicated research problems. I think it is safe to say that without your input, I would have missed out on a large portion of both the chemistry and the problem-solving skills I have learned at Caltech.

John, both in your inorganic chemistry course and in my collaborations with you and your research group, I've gained a new understanding of and appreciation for organometallic chemistry. I've truly enjoyed being able to collaborate with your postdocs to advance our work with combined catalytic systems. I hope that my enthusiasm for new chemistry and love of lab work will always shine through as yours does.

Rick, your suggestions and input on the hardware of my reaction testing systems

during my candidacy presentation has served me greatly in helping to construct and calibrate numerous systems in the Davis lab. You probably don't remember, but our conversations during my visit weekend all those years ago were a large reason for my choice of Caltech for graduate school, and I know beyond a shadow of a doubt that I made the right decision as a result of our interactions.

My collaborative work with Dr. Matt Winston, Dr. Dave Leitch, and Dr. Keith Steelman (all of the Bercaw group) has also widely broadened my practical knowledge of and respect for homogeneous catalysis. In working with these three postdocs, I have learned more than I ever thought possible about homogeneous catalysis and the synthetic challenges encountered in making new ligands for exciting hydrocarbon chemistry. I may never personally synthesize such organometallic compounds in the lab, but the bar has been set very high for any future collaborators in this field.

Work with my other labmates has taught me even more about engineering, chemistry, and how to serve as an effective team member.

First, I'd like to thank Yashodhan Bhawe for passing on the techniques of zeolite synthesis and characterization, as well as catalyst reaction testing. His training greatly advanced my understanding of heterogeneous catalysis, and I'm truly appreciative of the chance to learn the tools of the molecular sieve synthesis world. In the brief time we were able to work together, his knowledge effectively kept the Davis lab running at the high level for which it is known, without any interruptions or slowdowns.

Bingjun, Raj, and Ricardo: your mentorship has meant the world to me. Your insight and input into my lab work really advanced me from having an undergraduate mentality to becoming a knowledgeable, critically thinking graduate student. All the commentary and support during my candidacy examination process was immeasurably helpful. I know the friendships we built will continue to live on and support us throughout our entire careers. I can't wait to see you all at the next conferences and catch up.

To Luke and Lucy, your collaboration on the methanol-to-olefins work has been much appreciated and truly enriching. I hope that you have been able to learn as

much from me about zeolite synthesis, characterization, and reaction testing as I have from you about teamwork and project management.

Joel, Kramer, Josh, and Marat: you four have been a solid friend group with whom I can always go to for a fresh perspective and sound advice, or, just as easily, forgetting about lab work and relaxing. I'm thankful for the countless Friday night happy hours, long days at work, and trips across LA getting to know this city and one another. We have forged a solid bond in such a short period of time, and despite where we may end up in our careers across the globe, we will never be too far apart. I look forward to discovering where life may take us all.

Ben and Michiel, I've enjoyed getting to know both of you, both inside and outside of the lab. Your insight into the chemistry and catalysis of structure directing agents and molecular sieves has been so valuable to me and to the entire lab. In my collaborations with each of you, I hope you've been able to learn as much from me as I've been able to learn from you.

Devin, our conversations about life outside of work at countless happy hours and Caltech events have been so insightful and refreshing. I hold you in the highest regard, and I know that you will do even greater things than you have already accomplished.

To John, Steven, and Kevin: I hope that I've been able to pass on enough knowledge to you over these past three months. I know our time together in lab has been short, but I leave you in the capable hands of your fellow graduate students, and I know that you will succeed if you continue your hard work. Always remember that graduate school should cause you to grow and develop – not just in scientific knowledge, but as a person and a teammate as well.

From all of these collaborations, I've learned so many new critical thinking and technical skills in graduate school, many of which are contained and described in this thesis. But, more importantly, I've learned several things that I haven't recorded in the subsequent chapters. In one of life's strange juxtapositions, graduate school has contained both the best and worst times of my life.

My time and experience in graduate school at Caltech has shown me that I am capable of far more than I ever expected.

My friends have shown me that there is life beyond work. Work will consume as much time as one allows it, but choosing to give that time to other pursuits and to other people is always worth it.

My family, above all else, has shown me that I truly can count on them, even in the hardest of times. My mother and father have always made it known that I can come to them for anything, with unwavering support and understanding. I have relied on them more in the past few years for emotional support and guidance than perhaps I ever have in my life. As a result, I now feel closer to my family than ever before, and I give thanks daily that they've walked beside me on the rough road I've traveled. My brothers likewise have given their unconditional love and support, challenging me to become a better person – to grow my spirit and my character in addition to my mind and my body. Through all of life's challenges, having someone to rely on means far more than anything else we may have or hope to have.

Abstract

Nickel-containing catalysts are developed to oligomerize light olefins. Two nickel-containing zirconosilicates (Ni-CIT-6 and Ni-Zn-MCM-41) and two nickel-containing aluminosilicates (Ni-HiAl-BEA and Ni-USY) are synthesized as catalysts to oligomerize propylene into C_{3n} (C_6 and C_9) products. All catalysts oligomerize propylene, with the zirconosilicates demonstrating higher average selectivities to C_{3n} products, likely due to the reduced acidity of the Zn heteroatom.

To test whether light alkanes can be incorporated into this oligomerization reaction, a supported homogeneous catalyst is combined with Ni-containing zirconosilicates. The homogeneous catalyst is included to provide dehydrogenation/hydrogenation functions. When this tandem catalyst system is evaluated using a propylene/*n*-butane feed, no significant integration of alkanes are observed.

Ni-containing zirconosilicates are reacted with 1-butene and an equimolar propylene/1-butene mixture to study other olefinic feeds. Further, other divalent metal cations such as Mn^{2+} , Co^{2+} , Cu^{2+} , and Zn^{2+} are exchanged onto CIT-6 samples to investigate stability and potential use for other reactions. Co-CIT-6 oligomerizes propylene, albeit less effectively than Ni-CIT-6. The other M-CIT-6 samples, while not able to oligomerize light olefins, may be useful for other reactions, such as $deNO_x$.

Molecular sieves are synthesized, characterized, and used to catalyze the methanol-to-olefins (MTO) reaction. The Al concentration in SSZ-13 samples is varied to investigate the effect of Al number on MTO reactivity when compared to a SAPO-34 sample with only isolated Si Brønsted acid sites. These SSZ-13 samples display reduced transient selectivity behavior and extended reaction lifetimes as Si/Al increases; attributable to fewer paired Al sites. MTO reactivity for the higher Si/Al SSZ-13s re-

sembles the SAPO-34 sample, suggesting that both catalysts owe their stable reaction behavior to isolated Brønsted acid sites.

Zeolites CHA and RHO are prepared without the use of organic structure-directing agents (OSDAs), dealuminated by steam treatments (500°C-800°C), and evaluated as catalysts for the MTO reaction. The effects of temperature and steam partial pressure during steaming are investigated. X-ray diffraction (XRD) and Ar physisorption show that steaming causes partial structural collapse of the zeolite, with degradation increasing with steaming temperature. ^{27}Al MAS NMR spectra of steamed materials reveal the presence of tetrahedral, pentacoordinate, and hexacoordinate aluminum.

Proton forms of as-synthesized CHA (Si/Al=2.4) and RHO (Si/Al=2.8) rapidly deactivate under MTO testing conditions (400°C, atmospheric pressure). CHA samples steamed at 600°C performed best among samples tested, showing increased olefin selectivities and catalyst lifetime. Acid washing these steamed samples further improved activity. Reaction results for RHO were similar to CHA, with the RHO sample steamed at 800°C producing the highest light olefin selectivities. Catalyst lifetime and C₂-C₃ olefin selectivities increase with increasing reaction temperature for both CHA-type and RHO-type steamed samples.

Contents

Acknowledgments iv

Abstract viii

I Nickel-Exchanged Zincosilicate Catalysts for the Oligomerization of Propylene 1

1 Introduction to Part I: Light Olefin Oligomerization & Molecular Sieve CIT-6 2

1.1 Background 2

1.2 Motivation and Strategy 4

1.3 Proposed Catalysts and Objectives 9

2 Synthesis of Ni-CIT-6, Ni-Zn-MCM-41, Ni-HiAl-BEA, and Ni-USY for the Oligomerization of Propylene 12

2.1 Introduction 12

2.2 Experimental Section 14

2.2.1 Synthesis of Porous Materials 14

2.2.2 Ni²⁺ Exchange and Zn Heteroatom Protection 15

2.2.3 Characterization 16

2.2.4 Reaction Testing 17

2.3 Results and Discussion 18

2.3.1 Characterization of Materials Used as Catalysts 18

2.3.2 Reaction Testing 19

2.4	Summary	25
3	Combined Oligomerization and Transfer Hydrogenation Catalysts to Operate on a Mixed Alkane/Alkene Feed	27
3.1	Introduction	27
3.2	Experimental Section	30
3.2.1	Synthesis of Porous Heterogeneous Catalysts	30
3.2.2	Synthesis of Ir-based Homogeneous Catalysts and Deposition on Supports	31
3.2.3	Characterization	31
3.2.4	Reaction Testing	32
3.3	Results and Discussion	32
3.3.1	Characterization of Porous Materials	32
3.3.2	Characterization of Supported Homogeneous Catalysts	33
3.3.3	Reaction Testing	34
3.4	Summary	37
4	Additional Oligomerization Work	39
4.1	Introduction	39
4.2	Experimental Section	40
4.2.1	Synthesis of Porous Materials	40
4.2.2	Divalent Metal Ion Exchanges	40
4.2.3	Characterization	41
4.2.4	Calcination and Reaction Testing	41
4.3	Results and Discussion	42
4.3.1	Characterization of Metal-Exchanged Materials Used as Catalysts	42
4.3.2	Reaction Testing	44
4.4	Summary	49
5	Conclusions and Suggested Future Work for Part I	51
5.1	Conclusions	51

5.2	Recommended Future Work	53
II	Organic SDA-Free Materials for the Methanol-to-Olefins Reaction	55
6	Introduction to Part II: The Methanol-to-Olefins (MTO) Reaction	56
6.1	Background	56
6.2	Motivation and Strategy	59
6.3	Proposed Catalysts and Objectives	63
7	Effect of Heteroatom Concentration in SSZ-13 on the Methanol-to- Olefins Reaction	67
7.1	Introduction	67
7.2	Experimental Section	72
7.2.1	Synthesis of Microporous Materials	72
7.2.1.1	Isolated Si SAPO-34 Material	72
7.2.1.2	SSZ-13 Materials	72
7.2.1.3	Product Recovery	73
7.2.2	Calcination and Ammonium Exchange	73
7.2.3	Characterization	73
7.2.4	MTO Reaction Testing	75
7.3	Results and Discussion	76
7.3.1	Characterization	76
7.3.2	MTO Reaction Testing	80
7.4	Summary	83
8	Post-Synthetic Treatments on CHA and RHO to Enhance Methanol- to-Olefins Activity	85
8.1	Introduction	85
8.2	Experimental Section	88
8.2.1	CHA Synthesis	88

8.2.2	RHO Synthesis	89
8.2.3	Steaming and Acid Washing Treatments	89
8.2.4	Characterization	92
8.3	Results and Discussion	94
8.3.1	Characterization	94
8.3.2	Effect of Steaming Temperature and Acid Washing for CHA .	94
8.3.3	Effect of Steaming Temperature for RHO	101
8.3.4	Effect of Steam Partial Pressure for CHA	104
8.3.5	Effect of Steam Partial Pressure for RHO	108
8.4	Summary	112
9	Effect of Post-Synthetic Treatments on MTO Reactivity for CHA-Type and RHO-Type Materials	114
9.1	Introduction	114
9.2	Experimental Section	115
9.2.1	MTO Reaction Testing	115
9.3	Results and Discussion	115
9.3.1	Effect of Steaming Temperature and Acid Washing for CHA .	115
9.3.2	Effect of Reaction Temperature for CHA	119
9.3.3	Effect of Steaming Temperature for RHO	120
9.3.4	Effect of Reaction Temperature for RHO	123
9.4	Summary	124
10	Conclusions and Suggested Future Work for Part II	126
10.1	Conclusions	126
10.2	Recommended Future Work	128
11	Summary and Future Direction	131
11.1	Overall Conclusions	131
11.2	Future Directions	133
	Bibliography	134

A	Oligomerization Catalyst Characterization and Reaction Data	146
A.1	Characterization of Materials Used as Catalysts	146
A.2	Reaction Data at Two Reaction Temperatures	153
A.3	Complete Selectivity Graphs for All Reaction Runs	154
A.4	Comparisons of Reaction Data at 180°C and 250°C For Ni-CIT-6 and Samples Exchanged with Mg ²⁺ or Ca ²⁺ , Calcined, and Ni ²⁺ -Exchanged	162
A.5	Post-Reaction Powder XRDs	163
A.6	Post-Reaction TGAs of Spent Catalysts	163
B	Mixed Catalysts Characterization	167
B.1	Characterization of Materials Used as Catalysts	167
C	Post-Synthetic Treatment Characterization and Reaction Data	169
C.1	Study on the Effect of Steam Treatment on SSZ-13 for MTO	169
C.2	Further Catalyst Characterization	172
C.3	Steaming Experiments with Zeolite Y and CHA	172
C.4	MTO Reaction Data for Fresh and Regenerated Steamed CHA	181
D	Additional Publications	184
D.1	Highly Active Mixed-Metal Nanosheet Water Oxidation Catalysts Made by Pulsed-Laser Ablation in Liquids	184
D.2	The Facile Preparation of Aluminosilicate RTH Across a Wide Com- position Range Using a New Organic Structure Directing Agent	184
D.3	Synthesis of RTH-type Zeolites Using a Diverse Library of Imidazolium Cations	184
D.4	Effect of Pore and Cage Size on the Formation of Aromatic Intermedi- ates During the Methanol-to-Olefins Reaction	185
D.5	Upgrading Light Hydrocarbons: A Tandem Catalytic System for Alkane/Alkene Coupling	185

List of Figures

1.1	Framework structure of zeolite beta.	3
1.2	FCC process flow sheet. ¹	4
1.3	Oligomerization reactions of propylene and butylene.	5
1.4	Acid-catalyzed oligomerization reaction mechanism.	6
1.5	Nickel-catalyzed oligomerization process.	7
1.6	Comparison of Ni ²⁺ -exchanged zeolites and zirconosilicate molecular sieves.	8
1.7	Example reaction scheme for transfer hydrogenation and oligomerization.	11
2.1	Powder XRD patterns of nickel-exchanged, calcined materials: Ni-CIT-6, Ni-Zn-MCM-41, Ni-HiAl-BEA, and Ni-USY.	18
2.2	Representative time-on-stream profiles of conversion, C ₆ and C ₉ selectivity for Ni-CIT-6 (A), Ni-Zn-MCM-41 (B), Ni-HiAl BEA (C), and Ni-USY (D) at 180°C.	20
2.3	Representative time-on-stream profiles of conversion and C ₆ and C ₉ selectivity for Ni-CIT-6 (A), Ni-Zn-MCM-41 (B), Ni-HiAl-BEA (C), and Ni-USY (D) at 250°C.	22
2.4	Hexene isomer linear-to-branched ratios for Ni-CIT-6, Ni-Zn-MCM-41, Ni-HiAl-BEA, and Ni-USY at 180°C (A) and 250°C (B).	24
3.1	Tandem catalysis cycle.	29
3.2	Ir-based pincer ligand catalysts for transfer hydrogenation: Ir-POCOP (A), Ir-PCP (B), Ir-tBu ₄ -anthrphos (C), Ir-iPr ₄ -tris(phosphinoaryl) benzene (D), Ir-PNP (E), Ir-ferrocene (F), and Ir-POCSP (G).	31

3.3	Powder XRD patterns of nickel-exchanged, calcined materials Ni-CIT-6 and Ni-Zn-MCM-41.	33
3.4	Reaction data for Ni-CIT-6 and Ir-PNP supported on mesoporous carbon with propylene/ <i>n</i> -butane at 180°C.	35
3.5	Reaction data for Ni-CIT-6 and mesoporous carbon support with propylene/ <i>n</i> -butane at 180°C.	36
3.6	Reaction data for pure mesoporous carbon support with propylene/ <i>n</i> -butane at 180°C.	37
4.1	Powder XRD patterns of M-CIT-6 materials.	43
4.2	Powder XRD patterns of Pt-containing zincosilicates.	43
4.3	Reaction data for Ni-CIT-6 with 1-butene at 180°C.	45
4.4	Reaction data for Ni-Zn-MCM-41 with 1-butene at 180°C.	45
4.5	Reaction data for Ni-CIT-6 with equimolar propylene and 1-butene at 180°C.	46
4.6	Reaction data for Ni-Zn-MCM-41 with equimolar propylene and 1-butene at 180°C.	48
4.7	Reaction data for Co-CIT-6 with propylene at 250°C.	49
6.1	MTO hydrocarbon pool mechanism. ²	57
6.2	CHA cage structure. ³	58
6.3	Typical reaction data for SSZ-13 (A) and SAPO-34 (B) at 400°C, 1.3 h ⁻¹ WHSV (10% MeOH in inert), and atmospheric pressure.	59
6.4	N,N,N-trimethyl-1-adamantylammonium hydroxide.	60
6.5	Unsteamed H-SSZ-13 sample (Si/Al = 5).	61
6.6	Steamed H-SSZ-13 sample (Si/Al = 5).	62
7.1	Isolated vs. islanded Si sites in SAPO-34 (A) and isolated vs. paired sites in SSZ-13 (B).	71
7.2	Powder XRD pattern of the proton form of the SAPO-34 sample with isolated Si sites.	76

7.3	Powder XRD patterns of the proton forms of (A) SSZ-13A, (B) SSZ-13B, (C) SSZ-13C, (D) SSZ-13D, and (E) SSZ-13E.	77
7.4	²⁹ Si NMR spectra for the calcined SAPO-34 sample.	79
7.5	Representative MTO reaction data obtained at 400°C for the calcined SAPO-34.	80
7.6	Representative MTO reaction data obtained at 400°C for the ammonium-exchanged and calcined: (A) SSZ-13A, (B) SSZ-13B, (C) SSZ-13C, (D) SSZ-13D, and (E) SSZ-13E.	81
7.7	Cu/Al ratio, initial propane selectivity, and theoretical paired framework Al site content, as a function of framework Si/Al ratio for the SSZ-13 samples.	83
8.1	Powder XRD patterns of the as-synthesized CHA, CHA samples steamed at 500°C, 600°C, and 700°C at a steam partial pressure of 47.3 kPa, and the CHA sample steamed at 600°C and acid washed (bottom to top).	95
8.2	²⁷ Al MAS NMR spectra of the as-synthesized CHA, the CHA samples steamed at 500°C, 600°C, and 700°C at a steam partial pressure of 47.3 kPa, and the CHA sample steamed at 600°C and acid washed (bottom to top).	96
8.3	²⁹ Si MAS NMR spectra of the as-synthesized CHA, the CHA samples steamed at 500°C, 600°C, and 700°C at a steam partial pressure of 47.3 kPa, and the CHA sample steamed at 600°C and acid washed (bottom to top).	97
8.4	Ar physisorption isotherms of the as-synthesized and 500°C -700°C steamed CHA samples, and 600°C steamed and acid-washed CHA: (A) full isotherms, (B) normalized adsorption isotherms plotted on a semi-logarithmic scale, and (C) NLDFT cumulative pore volume vs. pore diameter.	99
8.5	Powder XRD patterns of the as-synthesized RHO, RHO samples steamed at 600°C, 700°C, and 800°C at a steam partial pressure of 47.3 kPa (bottom to top).	101

8.6	^{27}Al MAS NMR spectra of the as-synthesized RHO and the RHO samples steamed at 600°C, 700°C, and 800°C at a steam partial pressure of 47.3 kPa (bottom to top).	102
8.7	^{29}Si MAS NMR spectra of the as-synthesized RHO and the RHO samples steamed at 600°C, 700°C, and 800°C at a steam partial pressure of 47.3 kPa (bottom to top).	103
8.8	Powder XRD patterns of CHA samples steamed at 600°C with varying partial pressures of steam.	105
8.9	^{27}Al MAS NMR spectra of CHA samples steamed at 600°C with varying partial pressures of steam.	106
8.10	^{29}Si MAS NMR spectra of CHA samples steamed at 600°C with varying partial pressures of steam.	106
8.11	Ar physisorption isotherms of the as-synthesized and 600°C steamed CHA samples under varying steam partial pressures: (A) full isotherms, (B) normalized adsorption isotherms plotted on a semi-logarithmic scale and (C) NLDFIT cumulative pore volume vs. pore diameter.	107
8.12	Powder XRD patterns of RHO samples steamed at 800°C with varying partial pressures of steam.	109
8.13	^{27}Al MAS NMR spectra of RHO samples steamed at 800°C with varying partial pressures of steam.	110
8.14	^{29}Si MAS NMR spectra of RHO samples steamed at 800°C with varying partial pressures of steam.	110
9.1	Representative MTO reaction data obtained at 400°C for: as-synthesized H-CHA (A), 500°C steamed CHA (B), 600°C steamed CHA (C), 700°C steamed CHA (D), and 600°C steamed and acid washed CHA (E). . .	116
9.2	MTO reaction data for CHA-S600B80 obtained at reaction temperatures of 350°C (A), 400°C (B), 450°C (C), and CHA-S600B80A at 450°C (D). . .	120

9.3	Representative MTO reaction data obtained at 400°C for as-synthesized H-RHO (A), 600°C steamed RHO (B), 700°C steamed RHO (C), and 800°C steamed RHO (D).	121
9.4	MTO reaction data for RHO-S800B80 obtained at reaction temperatures of 350°C (A), 400°C (B), and 450°C (C).	124
A.1	Patterns of a.) as-received USY, b.) Ni-USY, and c.) calcined Ni-USY.	146
A.2	XRD patterns of a.) as-made CIT-6, b.) Ni-CIT-6, and c.) calcined Ni-CIT-6.	147
A.3	XRD patterns of a.) as-made Zn-MCM-41, b.) Ni-Zn-MCM-41, and c.) calcined Ni-Zn-MCM-41.	147
A.4	XRD pattern of Tosoh zeolite beta used as seeds.	148
A.5	XRD patterns of a.) as-made HiAl-BEA, b.) Ni-HiAl-BEA, and c.) calcined Ni-HiAl-BEA.	148
A.6	²⁷ Al NMR of HiAl BEA.	149
A.7	Argon adsorption isotherm for Ni-CIT-6.	150
A.8	Argon adsorption isotherm for Ni-HiAl-BEA.	150
A.9	Argon adsorption isotherm for Ni-USY.	151
A.10	Argon adsorption isotherm for Ni-Zn-MCM-41.	151
A.11	Ammonia TPD for nickel-exchanged, calcined samples.	152
A.12	Propylene conversion vs. TOS for all catalysts at 180°C.	153
A.13	Propylene conversion vs. TOS for all catalysts at 250°C.	153
A.14	All selectivities vs. TOS for Run #1 Ni-CIT-6 at 180°C.	154
A.15	All selectivities vs. TOS for Run #2 Ni-CIT-6 at 180°C.	154
A.16	All selectivities vs. TOS for Run #1 Ni-CIT-6 at 250°C.	155
A.17	All selectivities vs. TOS for Run #2 Ni-CIT-6 at 250°C.	155
A.18	All selectivities vs. TOS for Run #1 Ni-Zn-MCM-41 at 180°C.	156
A.19	All selectivities vs. TOS for Run #2 Ni-Zn-MCM-41 at 180°C.	156
A.20	All selectivities vs. TOS for Run #1 Ni-Zn-MCM-41 at 250°C.	157
A.21	All selectivities vs. TOS for Run #2 Ni-Zn-MCM-41 at 250°C.	157

A.22	All selectivities vs. TOS for Run #1 Ni-HiAl-BEA at 180°C.	158
A.23	All selectivities vs. TOS for Run #2 Ni-HiAl-BEA at 180°C.	158
A.24	All selectivities vs. TOS for Run #1 Ni-HiAl-BEA at 250°C.	159
A.25	All selectivities vs. TOS for Run #2 Ni-HiAl-BEA at 250°C.	159
A.26	All selectivities vs. TOS for Run #1 Ni-USY at 180°C.	160
A.27	All selectivities vs. TOS for Run #2 Ni-USY at 180°C.	160
A.28	All selectivities vs. TOS for Run #1 Ni-USY at 250°C.	161
A.29	All selectivities vs. TOS for Run #2 Ni-USY at 250°C.	161
A.30	Reaction comparisons for Ni-CIT-6 at 180°C (A), Ni-CIT-6 at 250°C (B), Ni-Mg-CIT-6 at 180°C (C), Ni-Mg-CIT-6 at 250°C (D), Ni-Ca-CIT-6 at 180°C (E), and Ni-Ca-CIT-6 at 250°C (F).	162
A.31	XRD patterns for all catalysts post-reaction.	163
A.32	TGA for Ni-CIT-6 at 180°C post-reactions.	163
A.33	TGA for Ni-Zn-MCM-41 at 180°C post-reactions.	164
A.34	TGA for Ni-Zn-MCM-41 at 250°C post-reactions.	164
A.35	TGA for Ni-HiAl-BEA at 180°C post-reactions.	165
A.36	TGA for Ni-HiAl-BEA at 250°C post-reactions.	165
A.37	TGA for Ni-USY at 250°C post-reactions.	166
B.1	XRD patterns of a.) as-made CIT-6, b.) Ni-CIT-6, and c.) calcined Ni-CIT-6 for use in the tandem catalyst system.	167
B.2	XRD patterns of a.) as-made Zn-MCM-41, b.) Ni-Zn-MCM-41, and c.) calcined Ni-Zn-MCM-41 for use in the tandem catalyst system.	168
C.1	MTO reaction data for fresh (unsteamed) H-SSZ-13 Si/Al = 5.	170
C.2	MTO reaction data for steamed H-SSZ-13 Si/Al=5.	171
C.3	MTO reaction data for H-SAPO-34.	171
C.4	²⁷ Al NMR of as-synthesized K-CHA.	172
C.5	Powder XRD patterns of unsteamed NH ₄ NaY and NH ₄ NaY samples steamed for 3 h at 550°C in order of increasing steam partial pressure (bottom to top).	175

C.6	Powder XRD patterns of NH_4NaY samples steamed for 3 h at 650°C in order of increasing steam partial pressure (bottom to top).	176
C.7	^{27}Al NMR spectra of unsteamed NH_4NaY and NH_4NaY samples steamed for 3 h at 550°C in order of increasing steam partial pressure (bottom to top).	177
C.8	^{27}Al NMR spectra of NH_4NaY samples steamed for 3 h at 650°C in order of increasing steam partial pressure (bottom to top).	177
C.9	Powder XRD patterns of $\text{NH}_4\text{Na-Y}$ samples steamed for 8 h at 800°C in order of increasing steam partial pressure (bottom to top).	178
C.10	^{27}Al MAS NMR of $\text{NH}_4\text{Na-Y}$ samples steamed for 8 h at 800°C in order of increasing steam partial pressure (bottom to top).	179
C.11	Powder XRD patterns of CHA samples steamed for 3 h at 500°C in order of increasing steam partial pressure (bottom to top).	180
C.12	^{27}Al MAS NMR of CHA samples steamed for 3 h at 500°C in order of increasing steam partial pressure (bottom to top).	180
C.13	MTO reaction data obtained at 400°C for 600°C steamed CHA during the initial reaction run.	181
C.14	MTO reaction data obtained at 400°C for 600°C steamed CHA after regeneration of spent catalyst.	182
C.15	MTO reaction data obtained at 450°C for 600°C steamed and acid washed CHA during the initial reaction test.	182
C.16	MTO reaction data obtained at 450°C for 600°C steamed and acid washed CHA after regeneration of spent catalyst.	183

List of Tables

2.1	Elemental compositions for oligomerization catalysts.	19
3.1	Elemental compositions of Ni-CIT-6 and Ni-Zn-MCM-41.	33
3.2	Ir-based transfer hydrogenation catalysts tested for the tandem catalysis system.	34
4.1	Elemental compositions of M-CIT-6, Ni-Zn-MCM-41, and Pt-containing samples.	44
7.1	SAPO-34 characterization data.	78
7.2	SSZ-13 characterization data.	78
8.1	Summary of steaming conditions, Si/Al ratios, and acid site concentrations for dealuminated CHA samples.	90
8.2	Summary of steaming conditions, Si/Al ratios, and acid site concentrations for dealuminated RHO samples.	91
8.3	Micropore volumes of the as-synthesized and steamed CHA samples.	100
9.1	Maximum combined C ₂ -C ₃ olefin selectivities for CHA near complete conversion and deactivation times of catalysts tested.	117
9.2	Maximum combined C ₂ -C ₃ olefin selectivities for RHO near complete conversion and deactivation times of catalysts tested.	122
A.1	Pore volumes for porous materials.	149
A.2	Brønsted acid site concentrations for the nickel-containing materials.	152
C.1	Summary of zeolite Y and CHA steaming conditions.	174

Part I

Nickel-Exchanged Zincosilicate Catalysts for the Oligomerization of Propylene

Chapter 1

Introduction to Part I: Light Olefin Oligomerization & Molecular Sieve CIT-6

This chapter serves as an introduction to Part I of my thesis, with a literature review on light olefin oligomerization, including both the nickel- and acid-catalyzed reaction pathways. The conversion of light olefins into longer chain hydrocarbons is discussed as a potential pathway to additional gasoline and distillate transportation fuels. Previously studied catalysts for both mechanisms of oligomerization are reviewed, and the desire to use heterogeneous zincosilicates (such as CIT-6) rather than aluminosilicates for nickel-catalyzed oligomerization is explained. Project objectives and proposed strategies for the oligomerization work are then outlined.

1.1 Background

Molecular sieves, while not currently used industrially for oligomerization, exhibit many desirable properties for use as industrial catalysts in other reactions. Molecular sieves are microporous, crystalline solids consisting of a three-dimensional network of tetrahedrally coordinated atoms (T-atoms), such as silicon, aluminum, or zinc. These T-atoms are connected to one another at their corners by oxygen atoms; thus, tetrahedra such as SiO_4^{4-} and AlO_4^{5-} are the elementary building units. Secondary building units may then arise from these tetrahedra to form complex crystal structures.

Non-tetravalent atoms (such as Al^{3+}) create charges in the molecular sieve framework that must be balanced by counterions such as protons, alkali/alkaline earth metal cations, or organic molecules like ammonium salts. If protons are the charge-balancing elements, the molecular sieve materials can exhibit strong Brønsted acidity and may participate in acid-catalyzed reactions. If the heteroatom is Al^{3+} , these materials are aluminosilicates called zeolites. Figure 1.1 shows the structure of a typical zeolite:⁴

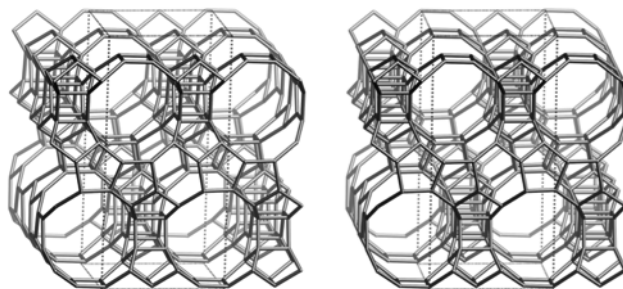


Figure 1.1: Framework structure of zeolite beta.

The pore diameters in microporous materials are less than 20 \AA , enabling them to exhibit shape and size selectivity by restricting the entry of certain molecules into these pores.⁵ Furthermore, the inner channel sizes may also restrict the formation of reaction intermediates and/or products due to their size and/or shape. As such, molecular sieves are frequently used for tasks such as water purification or gas separation.⁶ These materials also tend to be thermally stable, and some can withstand intense temperatures (in some cases $T > 800^\circ\text{C}$) without structural collapse. The charged framework sites, in combination with the shape and size selectivity of these materials, make them excellent catalysts for numerous reactions. For this reason, microporous materials are frequently used in oil refineries as catalysts for operations such as cracking, hydrocracking, isomerization, or alkylation.

1.2 Motivation and Strategy

Fluid catalytic cracking (FCC) is one of the most important refining processes to convert heavy oils into more valuable products, such as gasoline and distillate fuels. In the United States, FCC units typically process nearly 5 million barrels of oil per day, and FCC naphtha provides 35%-45% of the blending stocks in refinery gasoline blending pools.^{1,7} A typical FCC flow sheet is shown in Figure 1.2:

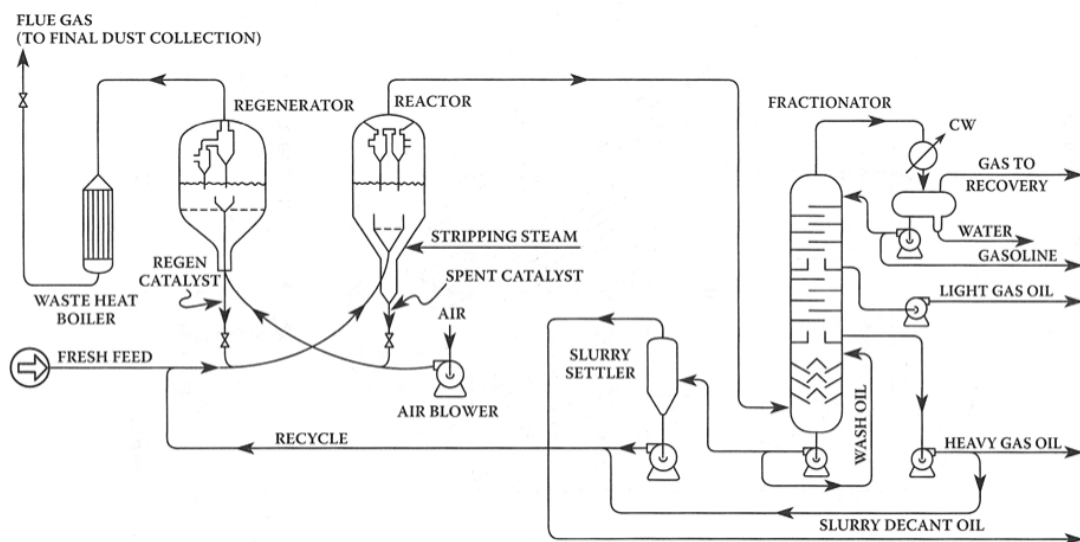


Figure 1.2: FCC process flow sheet.¹

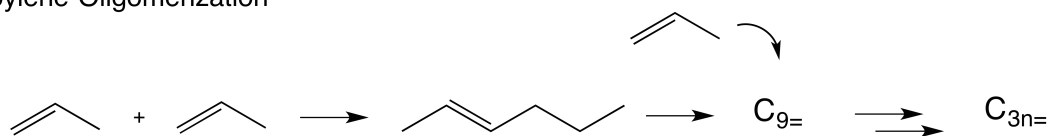
From the heavy fractions of crude oil processed by these FCC units, typically 65wt% gasoline (C_{5+}) and light cycle oils are produced; however, approximately 15-20wt% olefinic gases (ethylene, propylene, and butylene) are also produced.¹ Other light gases (methane, ethane, propane, etc.), as well as coke (5wt%), make up the balance of FCC products.

These olefinic gases (the stream labeled “Gas to Recovery” in Figure 1.2) can be valuable raw materials for other chemical processes, such as the manufacture of polymers; however, expensive separations (depropanizers, debutanizers, etc. in a gas recovery unit) are required to purify them for further use. Typically, the methane and ethane are separated and used for fuel gas in the refinery, but the higher hydrocarbons have limited refinery uses. For example, only minimal amounts of butane and

butylene can be blended into gasoline before the Reid vapor pressure (RVP) of the gasoline blend becomes too high, making it unusable in vehicle engines. Therefore, it is sometimes desirable to convert these gases (particularly propylene, butylene, and isobutylene) into liquids for subsequent hydrogenation and blending into high-octane gasoline or diesel feedstocks.

Oligomerization is one such method to convert these olefinic gases into liquids, and example reactions for the conversion of propylene and butylene into higher hydrocarbons are shown below in Figure 1.3:

Propylene Oligomerization



Butylene Oligomerization

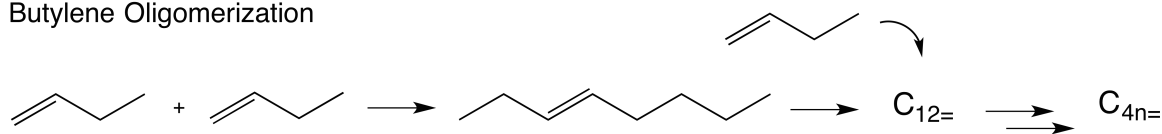


Figure 1.3: Oligomerization reactions of propylene and butylene.

This oligomerization reaction can occur primarily by two mechanisms: via acid catalysis or by a nickel-catalyzed mechanism. In the acid-catalyzed mechanism (Figure 1.4), the acidic proton, typically a Brønsted site within a zeolite, attaches to the double bond of the olefin, forming a carbocation. This carbocation may then interact with another olefin, attaching to the double bond in a similar manner to that of the initial acidic proton. The dimerization product may then eliminate a proton and desorb, forming a simple dimer, or it may continue to react with more olefins, forming an oligomer. Stereochemistry of the resulting oligomer product depends on how the subsequent olefin attaches to the carbocation. Double-bond or skeletal isomerization of the resulting oligomers may also occur at these Brønsted acid sites.

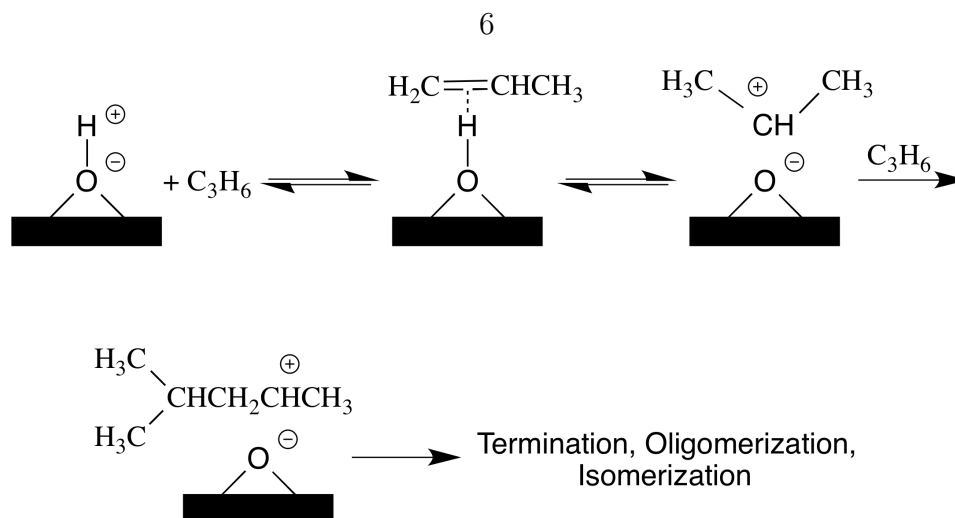


Figure 1.4: Acid-catalyzed oligomerization reaction mechanism.

Microporous solid acid catalysts, such as zeolites H-ZSM-5 or H-Y, and nonporous solid acid catalysts, like phosphoric acid or alumina-silica gels, perform oligomerization of light olefins by this mechanism.⁸

The nickel-based oligomerization process (Figure 1.5), in contrast, involves coordination of an olefin to the Ni metal center. Further addition of another olefin will then result in the oligomerization product. Depending on the orientation (1'-1', 1'-2', 2'-1', or 2'-2'), different hexene isomers can be formed. These newly formed olefins may then desorb from the metal center, or they may further react with another bound olefin to form a longer-chain oligomer.

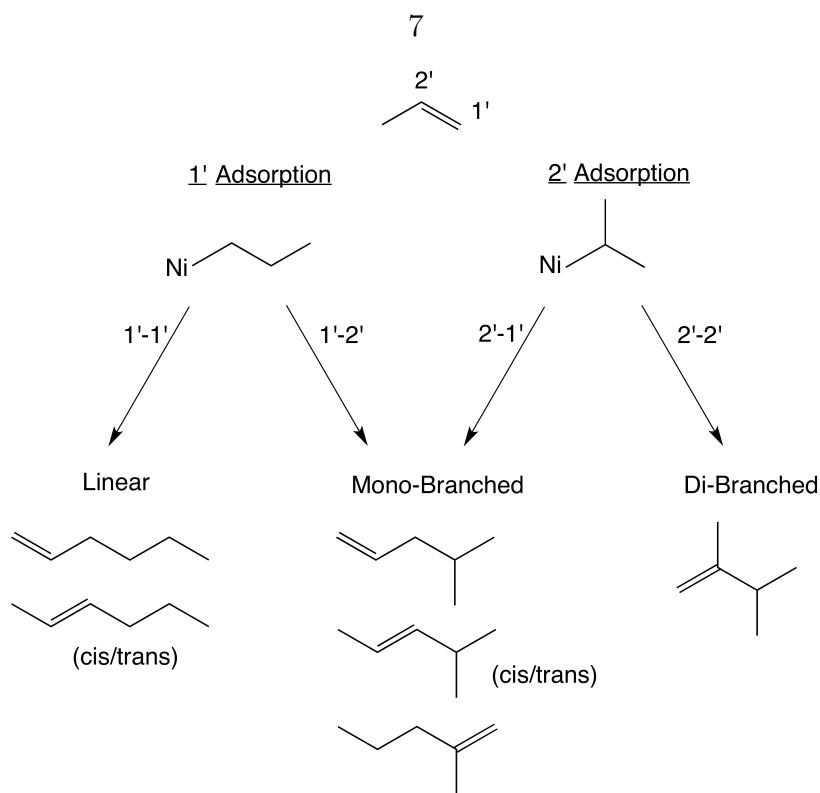


Figure 1.5: Nickel-catalyzed oligomerization process.

While the acid-catalyzed mechanism is effective at oligomerizing light olefins, the product distribution is not always particularly selective due to the acidic proton catalyzing other reactions (such as cracking and isomerization) in addition to simple oligomerization. With the nickel-catalyzed mechanism, light olefins can more selectively form oligomerization products without excessive undesired side products due to reactions only occurring via the transition metal. This increased oligomer selectivity is obviously preferable for industrial applications, where product separations through processes such as distillation can be very expensive.

Previously, the Ni^{2+} ion exchanged onto molecular sieves such as faujasite (zeolite X or zeolite Y) or ZSM-5 have been shown to oligomerize these $\text{C}_2\text{-C}_4$ olefins to liquid olefins (C_{6+}).^{9, 10, 11, 12, 13} These catalysts have been reported to exhibit oligomerization activity at reaction temperatures from 25°C to 350°C , and from pressures slightly above atmospheric to over 35 bar. Other aluminosilicates, such as silica-alumina combined with nickel oxide, have also been shown to perform this oligomerization reaction.^{14, 15} Mobil's Olefins to Gasoline/Distillate (MOGD) process is one attempt

at a commercial-scale process with a nickel-containing molecular sieve catalyst capable of producing gasoline and/or distillate fuels from olefinic gases; however, the process does not produce exclusively C_{6+} products (liquids), thus requiring a separator and second reactor.¹⁶ A large-scale MOGD test run was executed in a Mobil refinery in 1981, but no industrial process is currently employed.¹⁷

While these molecular sieves are generally practical and useful catalysts, they do exhibit some drawbacks if used as oligomerization catalysts. Primarily, since Ni^{2+} is a divalent ion, two aluminum tetrahedra in a zeolite (each with a 1- charge) are required to counterbalance this charge. These aluminum tetrahedra must be adjacent to one another (separated only by a single SiO_4 tetrahedron due to Loewenstein's rule),¹⁸ or the orientation of the zeolite framework must be such that two 1- charges from aluminum tetrahedra are capable of counterbalancing the Ni^{2+} charge.¹⁹ Adjacent aluminum tetrahedra are referred to as paired sites, and the high aluminum content in materials such as zeolite Y (Si/Al molar ratio ≈ 3) provides an increased probability of paired aluminum sites occurring in the zeolite framework. While many paired sites in zeolites can be occupied by these divalent Ni^{2+} ions, lone aluminum tetrahedra (with 1- charges) still remain throughout the zeolite framework. These lone aluminum sites may possess strong acid activity or host other species, which can catalyze undesired side reactions (such as cracking), thereby producing a wide variety of products in addition to the desired oligomerization products.

Zincosilicates, however, only possess a single type of framework charge site: the Zn^{2+} atom in the framework creates a 2- charge on the zinc tetrahedron. Figure 1.6 below demonstrates this difference between zeolites and zincosilicate molecular sieves:

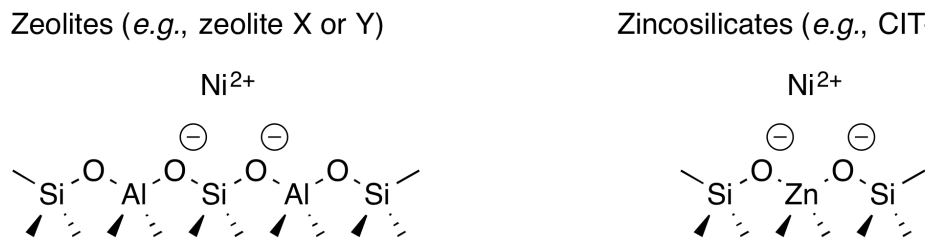


Figure 1.6: Comparison of Ni^{2+} -exchanged zeolites and zincosilicate molecular sieves.

This charge site can accommodate the Ni^{2+} ion in a 1:1 exchange ratio, with no lone 1- sites. Thus, with zincosilicates, no lone charges are present to exhibit strong acid activity and catalyze undesired cracking reactions. While lone 2- zinc sites are present, they exhibit reduced acidity relative to the aluminum sites.²⁰ This decreased acidity allows greater selectivity to the desired oligomerization products without the production of additional cracking products.

Other desired properties for an industrial oligomerization catalyst include high olefinic gas conversions, high selectivities to liquid products, and stable catalyst performance for extended periods of time, with or without regeneration. Nickel-containing molecular sieves exhibiting high oligomerization activity and selectivity to desired products may then yield an industrially viable oligomerization catalyst.

1.3 Proposed Catalysts and Objectives

To this end, CIT-6, a zincosilicate molecular sieve with *BEA topology, has been subjected to Ni^{2+} exchange and is investigated as an oligomerization catalyst capable of converting propylene into higher olefins (C_6 and C_9 products). The synthesis of CIT-6 was first reported by Takewaki et al. in 1999, and it has been studied as a useful precursor to a wide range of molecular sieve materials of the *BEA topology.^{21, 22, 23}

In addition to CIT-6, this project compares the oligomerization activity of three other catalysts that have undergone Ni^{2+} exchange: Zn-MCM-41, high-aluminum zeolite beta (HiAl-BEA), and ultra-stable zeolite Y (USY). These nickel-containing zincosilicate and zeolite catalysts have been synthesized and reaction tested in an attempt to develop a viable catalyst for the oligomerization of light olefins into liquids for blending into high-octane gasoline and diesel fuels.

Zn-MCM-41 is a zincosilicate like CIT-6; however, it is mesoporous with the hexagonal MCM-41 pore structure. Takewaki et al. reported synthesizing this material for use as an intermediate material in the formation of molecular sieves with *BEA framework type, while Hartmann et al. synthesized this material and the related mesoporous zincosilicate MCM-48 prior to this synthesis for use in redox

reactions.^{24, 25, 26} This mesoporous material was chosen to compare the effect of pore size on the oligomerization activity and product distribution for a mesoporous zincosilicate relative to a large-pore zincosilicate molecular sieve (CIT-6). A Zn-MCM-41 was produced to compare the activity of the two materials.

Typical zeolite beta is available commercially in a Si/Al molar ratio of approximately 12.5-250; however, HiAl-BEA has a Si/Al molar ratio of approximately 5-7.^{27, 28} This material has the same *BEA topology as CIT-6, but with aluminum heteroatoms present in the framework, as opposed to framework zinc, to investigate the oligomerization activity differences between the two heteroatoms. The higher aluminum content in HiAl-BEA increases the probability of paired aluminum tetrahedra occurring, in turn producing more net 2- charge sites and thus allowing Ni²⁺ cations to be exchanged at a comparable level to that of CIT-6 (which has Si/Zn = 10-15). Unfortunately, the lone aluminum sites present may also exhibit strong acid activity, catalyzing unwanted cracking or isomerization reactions.

HiAl-BEA has also been industrially synthesized under the trade name ZEOSTAR BEA (Nippon Chemical Industrial Co., Ltd.), and for this reason the material was selected as a commercially viable option for the nickel oligomerization catalyst.

Ultra-stable zeolite Y (USY) was used as a comparison to the previous studies of oligomerization with faujasites (zeolite Y); however, USY has a lower Al content than these materials (Si/Al = 6.0 in this case, as compared to NaY with a typical Si/Al molar ratio of 3) to again allow for comparable nickel loadings among each material tested. The zeolite USY used in this study was obtained from Zeolyst (Zeolyst CBV-712). USY is typically used as a cracking catalyst in FCC units, due to its strong acid activity and good thermal stability.

Progress on this project has demonstrated the successful conversion of propylene into oligomerization products with each of these catalysts; however, improvements to catalytic activity and stability are still required before any of these catalysts can be industrially relevant. Other desirable catalyst properties include high propylene conversion with limited selectivity to cracking products under moderate processing conditions (e.g., T<300°C) and the ability to be regenerated with negligible loss of

activity.

While this project initially focuses on development of a catalyst capable of performing light olefin oligomerization, this oligomerization catalyst may also be incorporated into a tandem catalysis system for the oligomerization of both light olefins and light paraffins into liquid hydrocarbons. In such a system, one catalyst (e.g., an organometallic complex or transition metal deposited onto a molecular sieve) will perform a dehydrogenation reaction, producing hydrogen and converting the paraffin to a more reactive olefin. The second catalyst will then oligomerize the olefin molecules (both those initially present in the FCC off-gas and those produced by dehydrogenation). Finally, hydrogen produced in the dehydrogenation reaction will be returned to the oligomerization product. Figure 1.7 demonstrates this desired reaction scheme for propane:

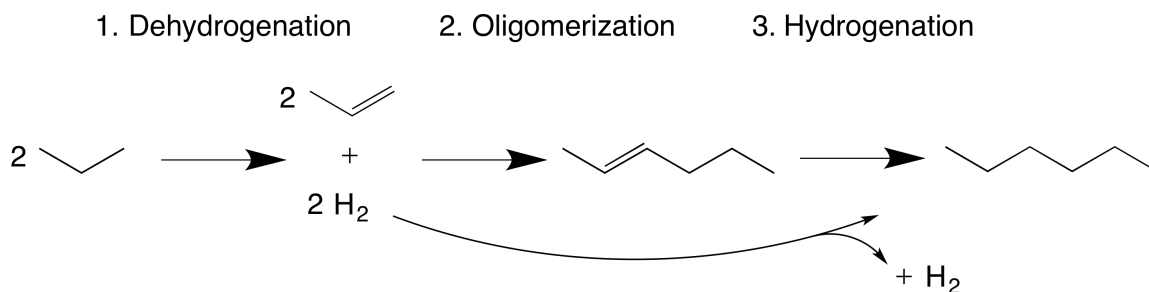


Figure 1.7: Example reaction scheme for transfer hydrogenation and oligomerization.

Currently, homogeneous organometallic catalysts supported on silica have been reported to perform the transfer hydrogenation reaction, and these materials may be combined with the oligomerization catalyst into a single material.²⁹ Platinum has also been shown to perform propane dehydrogenation when deposited on CIT-6 and transfer hydrogenation when supported on zeolites, providing additional possibilities for a tandem catalyst (e.g., Ni-CIT-6 impregnated with platinum or another transition metal).^{30, 31} Thus, paraffinic gases, as well as olefinic gases, could be converted to liquid products with the combination of an oligomerization catalyst and an organometallic complex or transition metal.

Chapter 2

Synthesis of Ni-CIT-6, Ni-Zn-MCM-41, Ni-HiAl-BEA, and Ni-USY for the Oligomerization of Propylene¹

2.1 Introduction

Nickel-containing aluminosilicate catalysts are capable of oligomerizing light olefins (C_2 - C_4) to higher molecular weight liquid hydrocarbons for blending into gasoline and distillate transportation fuel streams.^{8, 12} The exchange of Ni^{2+} cations into zeolites that have framework topologies such as FAU and MFI have been shown to give catalysts that can oligomerize these light olefins to liquid olefins (C_{6+}) at reaction temperatures of 25-350°C, and at pressures from slightly above atmospheric to over 35 bar.^{9, 10, 11, 13, 32, 33} Other aluminosilicates, such as amorphous silica-alumina combined with nickel oxide^{14, 15, 34} and nickel-exchanged mesoporous materials,^{35, 36, 37} are also able to perform these types of oligomerization reactions. While aluminosilicate materials are generally effective as oligomerization catalysts, they do exhibit some drawbacks.

As discussed previously, Ni^{2+} is a divalent cation, requiring two nearby framework aluminum atoms to counterbalance the positive charge.¹⁹ High aluminum content in

¹Information contained in this chapter was originally published in *ACS Catalysis* (Deimund, M.A.; Labinger, J.A.; Davis, M.E. *ACS Catal.* 2014, 4, 4189-4195. DOI: 10.1021/cs501313z).

materials such as zeolites X or Y (Si/Al molar ratio \approx 1-3) provide an increased probability of paired aluminum sites to occur in the zeolite frameworks, and thus allow for higher Ni^{2+} exchanges, but unexchanged aluminum can yield additional Brønsted acid sites. The strong Brønsted acidity can catalyze oligomerization, but may also give undesired side reactions (such as cracking), thereby producing a wide variety of products in addition to the desired oligomers.⁸ It has been shown that the Ni^{2+} ion sites alone are sufficient to perform light olefin oligomerization;³⁸ thus, Brønsted sites are unnecessary in the presence of the Ni^{2+} cations.

As previously shown, the framework Zn^{2+} atoms in zincosilicates create two anionic charges per zinc heteroatom that can accommodate the Ni^{2+} ion in a 1:1 exchange ratio, leaving no unpaired charge centers (Figure 1.6). Furthermore, unexchanged zinc-based charge centers exhibit significantly reduced acidity relative to the aluminum sites.²⁰ The absence of strong Brønsted acidity may provide greater selectivity to the desired oligomerization products. Here, we explore the use of zincosilicate-based catalysts for the oligomerization of light olefins. CIT-6, a zincosilicate molecular sieve with *BEA topology,^{21, 22, 23} is exchanged with Ni^{2+} and tested as a catalyst for converting propylene into higher olefins (C_6 and C_9 products). Additionally, we investigate high-aluminum zeolite beta (HiAl-BEA),^{39, 40, 41} Zn -MCM-41,^{24, 25, 26} and ultra-stable zeolite Y (USY) to study the effects of (i) Al versus Zn heteroatom in the *BEA topology, and (ii) the nature of the zincosilicate solid (microporous vs mesoporous), as well as comparison to a previously studied catalyst (USY), respectively. We attempted to keep the number of Ni^{2+} exchange sites and Ni^{2+} loadings comparable between all solids (hence, the use of HiAl-BEA and USY). Similar Si/Zn and Si/(2Al) ratios are maintained, as well as Ni/Zn and Ni/(2Al) ratios, to allow for meaningful comparisons.

2.2 Experimental Section

2.2.1 Synthesis of Porous Materials

All materials (with the exception of USY) were synthesized following known recipes.^{22, 24, 39} The zeolite USY was obtained from Zeolyst (Zeolyst CBV-712, $\text{SiO}_2/\text{Al}_2\text{O}_3 = 12$, NH_4^+ -form).

CIT-6 was synthesized according to the method of Takewaki et al.²² A synthesis gel of composition 1 SiO_2 / 0.03 $\text{Zn}(\text{OAc})_2$ / 0.65 TEAOH / 0.05 LiOH / 30 H_2O was prepared with Ludox AS-40 as the silica source, zinc acetate dihydrate (Aldrich), tetraethylammonium hydroxide (Aldrich, 35wt% in water), and lithium hydroxide monohydrate powder (Aldrich). The gel was charged into a Teflon-lined, stainless steel autoclave and heated statically at 140°C for 7.5 days under autogenous pressure. The crystalline white solid in the bottom of the Teflon liner was recovered by centrifugation, extensively washed with water and acetone, and dried at 100°C overnight.

The mesoporous zincosilicate Zn-MCM-41 was synthesized in a manner similar to that described by Takewaki et al.²⁴ A synthesis gel of composition 1 SiO_2 / 0.024 $\text{Zn}(\text{OAc})_2$ / 0.5 NaOH / 0.61 CTAB / 60 H_2O was prepared with Ludox AS-40 as the silica source, zinc acetate dihydrate (Aldrich), NaOH pellets (Aldrich), and cetyltrimethylammonium bromide powder (Aldrich). The gel was charged into a Teflon-lined, stainless steel autoclave and heated statically at 110°C for 5 days under autogenous pressure. The white solid in the bottom of the Teflon liner was recovered by centrifugation, extensively washed with water and acetone, and dried at room temperature overnight.

High-aluminum zeolite beta (HiAl-BEA) was synthesized according to a seeded procedure similar to that described by Majano et al.³⁹ A synthesis gel of composition 1 SiO_2 / 0.025 Al_2O_3 / 0.325 Na_2O / 25 H_2O was prepared with Ludox AS-40 as the silica source, sodium aluminate (Alfa Aesar) as the alumina source, and a 50wt% NaOH solution. The gel was seeded with commercial zeolite beta from Tosoh (Tosoh HSZ-930NHA, $\text{SiO}_2/\text{Al}_2\text{O}_3 = 27$, NH_4^+ -form). The gel was homogenized and charged

into a Teflon-lined stainless steel autoclave. The autoclave was heated statically at 110°C for 6 days. The procedure for collection of the zeolite material was similar to that described for CIT-6.

2.2.2 Ni²⁺ Exchange and Zn Heteroatom Protection

Ni²⁺ ion exchange was performed at 75°C (25°C for Zn-MCM-41) for 5 h using a 0.01 M solution of Ni(NO₃)₂ (Sigma Aldrich, hexahydrate) that had been pH-adjusted to 7.0 using 0.01 M NaOH solution. For each exchange, 250 mg of material was added to 25 mL of solution. The materials were then separated from the Ni(NO₃)₂ solution via centrifugation, washed with distilled water, and dried. After the Ni²⁺ exchange, each material exhibited a pale green color.

Calcination or acid extraction is required to remove the tetraethylammonium (TEA⁺) cation from CIT-6. Some of the zinc heteroatoms may also be undesirably removed from the CIT-6 framework via this process, destroying the 2- exchange site and forming ZnO particles. Thus, a means of protecting the zinc heteroatom while still allowing for removal of the organic template used in synthesis (consequently activating the catalyst) is necessary. It was determined that direct exchange of a divalent cation (Ni²⁺ used here for catalysis purposes, although Mg²⁺ or Ca²⁺ work as well) onto the as-made material (still containing the TEA⁺ cation) in a pH-neutral exchange solution, followed by calcination, could protect the framework zinc while allowing for removal of the TEA⁺ cation. This is presumed to be due to the presence of the divalent M²⁺ cation, which prevents hydrolysis of framework oxygen bonds to the zinc heteroatom by blocking the water from interacting with the bonds, as well as by charge stabilization, wherein a hard cation helps stabilize and preserve the exchange site under the extreme steaming conditions. In cases where Mg²⁺ or Ca²⁺ ions were initially exchanged (using a 1 M MgCl₂ or 1 M CaCl₂ solution, pH-adjusted to 7.0 with dilute NaOH, for 5 h at 75°C), calcination and subsequent exchange with the Ni²⁺ cation using the procedure described above was possible. CIT-6 samples that underwent calcination without the initial exchange of Mg²⁺ or Ca²⁺ did not give

good exchange of Ni^{2+} into the CIT-6 material, presumably due to removal of the zinc heteroatom from the framework during calcination (as shown by greatly reduced zinc content from elemental analysis) or hydrolysis of Zn-O bonds to destroy the divalent framework charge site.

While the as-made material can have the Ni^{2+} cation directly exchanged onto it as described previously (provided the pH of the exchange solution is adjusted to 7.0) and activated via calcination, the protection via divalent cations does provide another means to protect the divalent zinc exchange site in situations where organic removal is desired but Ni^{2+} exchange is not needed.

2.2.3 Characterization

The as-made materials were characterized by powder X-ray diffraction (XRD) on a Rigaku Miniflex II diffractometer with Cu $K\alpha$ radiation ($\lambda=1.54184 \text{ \AA}$), to determine structure type and give an estimate of purity. In each diffraction pattern for CIT-6, HiAl-BEA, or USY, 2θ angles from 4° to 40° were acquired with a sampling window of 0.010° and a scan speed of $0.100^\circ/\text{min}$, while the X-ray source was at 30 kV and 15 mA. For Zn-MCM-41, 2θ angles from 1.5° to 40° were acquired, again with a sampling window of 0.010° and a scan speed of $0.100^\circ/\text{min}$, while the X-ray source was at 30 kV and 15 mA.

Scanning electron microscopy/energy dispersive spectroscopy (SEM/EDS) analyses were conducted on a JEOL JSM-6700F instrument equipped with an Oxford INCA Energy 300 X-ray energy dispersive spectrometer. The SEM/EDS was used to determine the morphology, as well as the Si/Zn and Ni/Zn (or Si/Al and Ni/Al) of the materials.

Solid-state NMR spectroscopy was performed on a Bruker AM 300 spectrometer equipped with high power amplifiers for solids. Samples were spun at the magic-angle (MAS) in 4 mm ZrO_2 rotors. ^{27}Al MAS NMR (78.2 MHz) spectra were obtained at a spinning rate of 12 kHz and referenced to a 1 M aqueous aluminum nitrate solution (0 ppm).

To quantify the number and strength of the Brønsted acid sites present in each catalyst, NH_3 temperature-programmed desorption (TPD) was performed on each nickel-exchanged, calcined material. The materials were pelletized, crushed, and sieved. Particles between 0.6 mm and 0.18 mm were supported between quartz wool beds in a continuous flow quartz-tube reactor (part of an Altamira AMI-200 reactor system). Bed temperature was monitored via a thermocouple inserted directly into the catalyst bed, and desorbing products were monitored via a Dymaxion mass spectrometer with m/z scanning capability.

Once loaded, samples were heated to 150°C for 1 h at $10^\circ\text{C}/\text{min}$, followed by heating to 600°C for 1 h at $10^\circ\text{C}/\text{min}$ in flowing helium (50 sccm) to remove any adsorbed species. Samples were then cooled to 160°C , and NH_3 was dosed onto each sample at a flow rate of 5 sccm in 50 sccm helium until no further NH_3 uptake was observed via the mass spectrometer (typically <5 min). After a 8 h purge in flowing helium (50 sccm) to remove any physisorbed NH_3 , the sample was heated to 600°C at rate of $2^\circ\text{C}/\text{min}$ in 20 sccm helium while the mass spectrometer monitored desorbing products, namely $m/z = 17$ fragments corresponding to NH_3 . The sample was held at 600°C for 2 h to ensure all species had fully desorbed.

2.2.4 Reaction Testing

Prior to reaction testing, all materials were calcined in breathing-grade air. The materials were heated to 150°C at $1^\circ\text{C}/\text{min}$, held for 3 h at 150°C , then heated further to 580°C at $1^\circ\text{C}/\text{min}$ and held for 12 h, all under flowing air.

The calcined materials were pelletized, crushed, and sieved. Particles between 0.6 mm and 0.18 mm were supported between glass wool beds in an Autoclave Engineers BTRS, Jr. 316 SS continuous flow, tubular reactor.

For reaction testing, a mixture of propylene and an inert gas (composition 85mol% propylene, balance He/Ar) was supplied to the 3/8" ID 316 SS tubular reactor, with total flow such that a weight-hourly space velocity (WHSV) of 1.0 h^{-1} was attained.

Each catalyst was tested at 180°C and 250°C after the initial calcination, as well

as after a second calcination in flowing air to determine regeneration potential. In a typical run, 200 mg of dry catalyst was loaded. Reactor effluent gases were analyzed using an on-stream GC/FID/TCD Agilent GC 7890A with Plot-Q capillary columns installed. Conversions and selectivities were computed on a carbon mole basis.

2.3 Results and Discussion

2.3.1 Characterization of Materials Used as Catalysts

The powder XRD patterns of the porous solids used here, after nickel exchange and calcination, are shown in Figure 2.1. Additional powder XRD data (for each material as synthesized, after nickel exchange, and after calcination) are shown in Figures A.1, A.2, A.3, A.4, and A.5 in the Appendix.

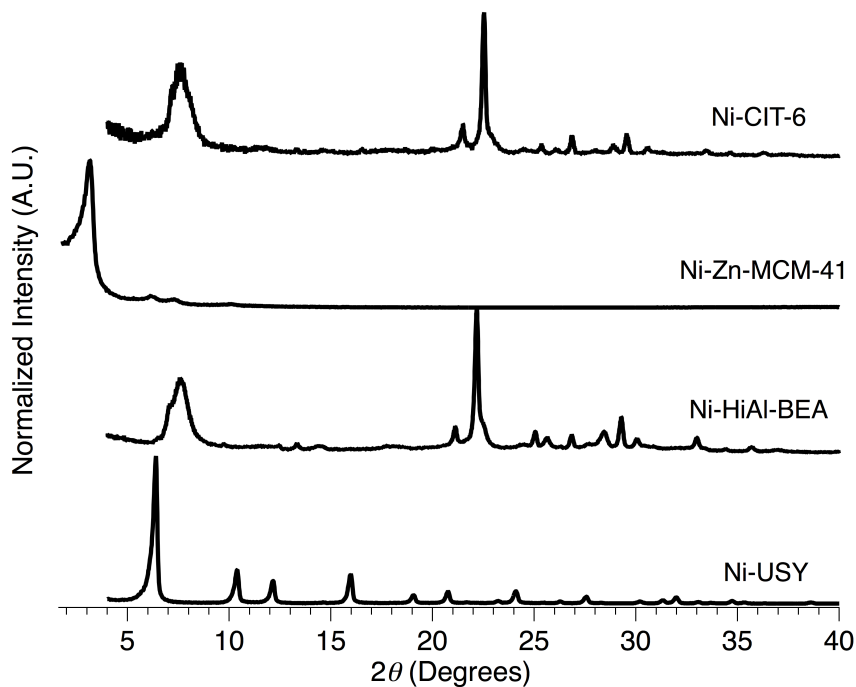


Figure 2.1: Powder XRD patterns of nickel-exchanged, calcined materials: Ni-CIT-6, Ni-Zn-MCM-41, Ni-HiAl-BEA, and Ni-USY.

A summary of the elemental compositions (by EDS) of the solids used for reaction testing is shown in Table 2.1. The Si/Zn for CIT-6 (and thus the number of sites

available for Ni^{2+} exchange) is similar to the $\text{Si}/(2\text{Al})$ ratios in HiAl-BEA and USY, since these zeolites required paired aluminum sites for the Ni^{2+} exchange. However, the Zn-MCM-41 could only be reliably synthesized at a Si/Zn ratio approximately twice that of these materials. Nonetheless, we were able to maintain a comparable number of Ni^{2+} exchange sites.

Material	Si/Zn	Ni/Zn
Ni-CIT-6	10.8	0.55
Ni-Zn-MCM-41	22.7	0.59
	Si/Al	Ni/Al
Ni-HiAl-BEA	4.2	0.39
Ni-USY	5.8	0.33

Table 2.1: Elemental compositions for oligomerization catalysts.

Micropore volumes for the microporous materials were determined by Ar adsorption, and volumes are consistent with previously reported syntheses (Table A.1 and Figures A.7, A.8, A.9, and A.10 of the Appendix). ^{27}Al MAS NMR spectra were obtained for each aluminosilicate solid, and the results show only tetrahedral aluminum (Figure A.6 of the Appendix). Ammonia TPD also shows consistently fewer Brønsted acid sites in the zincosilicates as compared to the aluminosilicates (Figure A.11 and Table A.2 of the Appendix).

2.3.2 Reaction Testing

Figure 2.2 illustrates typical reaction data for each of the four different catalysts tested at 180°C . Each material, with the exception of Ni-Zn-MCM-41, exhibits decreased propylene conversion with increasing time-on-stream (TOS) as the catalyst deactivates. The main C_6 products observed in all cases are 2-hexene, 2-methyl-2-pentene, and 4-methyl-2-pentene. One of those, 2-methyl-2-pentene, is likely formed via double-bond migration of the expected primary products (2-methyl-1-pentene and 4-methyl-2-pentene) at Brønsted acid sites resulting from unexchanged zinc or

aluminum heteroatoms. The zincosilicates exhibited only this double-bond isomerization, while the aluminosilicates also catalyzed cracking reactions to form non- C_{3n} products, likely due to the relative acidic strength of the framework zinc and aluminum heteroatoms.²⁰ As TOS increases, these isomerization sites in each material deactivate, and more primary products are observed in the hexene product mixture. Selectivity to C_9 products (primarily olefins) increases with increasing TOS, and typically stabilizes by approximately 100 mins on stream. Full conversion and selectivity data for each of these materials at both 180°C and 250°C are shown in Figures A.12-A.29 of the Appendix. Reaction data for the materials exchanged with Mg^{2+} or Ca^{2+} before calcination and subsequent exchange with Ni^{2+} are shown in Figure A.30 of the Appendix.

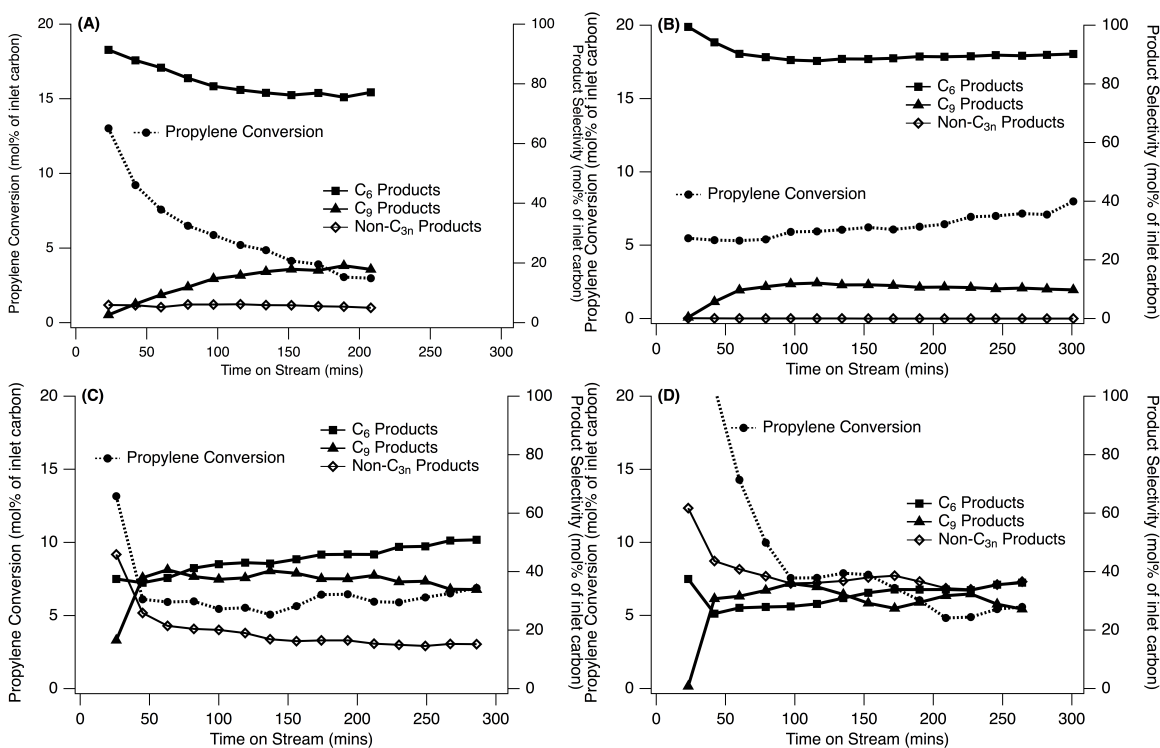


Figure 2.2: Representative time-on-stream profiles of conversion, C_6 and C_9 selectivity for Ni-CIT-6 (A), Ni-Zn-MCM-41 (B), Ni-HiAl BEA (C), and Ni-USY (D) at 180°C.

For each material, post-reaction powder XRD patterns show no loss of structure (Figure A.31 of the Appendix). Additionally, carbon balances are typically over 95%

for the duration of each reaction run, with the exception of the initial sample for the run, where propylene is likely initially being held up on the sample to begin forming the first olefins. Post-reaction thermogravimetric analysis (TGA) experiments on each spent catalyst reveal mass losses above 150°C of approximately 4%-15%, with less mass loss observed for the zincosilicates relative to the aluminosilicates (see Figures A.32-A.37 of the Appendix). Regeneration by calcination in flowing breathing-grade air recovered nearly all of catalytic activity observed initially for each material.

Both materials with the *BEA framework (Ni-CIT-6 and Ni-HiAl-BEA) exhibit similar TOS behavior with respect to propylene conversion, but the product distribution for Ni-HiAl-BEA is not as selective to C_{3n} products as Ni-CIT-6; C₇-C₉ saturated and unsaturated products are observed in amounts comparable to that of the C₆ products. Selectivity to C₄ and C₅ saturated and unsaturated products is low (<10% total); oligomerization and subsequent cracking products are primarily observed.

The strong Brønsted acid sites in Ni-HiAl-BEA appear to catalyze cracking and isomerization, resulting in the observed C₇ and C₈ products. This suggests that the nickel ions present in the *BEA structure are similarly active for the production of simple oligomerization products with either heteroatom present (zinc or aluminum), while residual Brønsted acid sites in the framework are likely responsible for the observed differences in product selectivity resulting from double-bond isomerization and/or cracking of primary C_{3n} products.

The two zincosilicates (Ni-CIT-6 and Ni-Zn-MCM-41) exhibit by far the highest selectivities to C_{3n} oligomerization products, and Ni-Zn-MCM-41 has the most stable propylene conversion with increasing TOS. This stability observed for the Ni-Zn-MCM-41 is likely due to the larger mesopores that are not as susceptible to blockage from carbon deposits as the micropores in Ni-CIT-6. Selectivities to non-C_{3n} products (Figure 2.2) for Ni-CIT-6 are no more than 6% at any time at 180°C. For Ni-Zn-MCM-41, propylene conversion remained stable at 6-8% throughout the reaction test; however, the selectivity to C₉ products is approximately half that observed for Ni-CIT-6. Total selectivities to non-C_{3n} products are <1% for all time-on-stream points.

The observed increase in propylene conversion and on-stream stability with the increase in pore size for the zincosilicates (from microporous Ni-CIT-6 to mesoporous Ni-Zn-MCM-41) is also consistent with that reported by Mlinar et al. in the comparison of microporous aluminosilicate Ni-Na-X to mesoporous aluminosilicate Ni-Al-MCM-41.³⁶ Further, hexene product isomer distributions reported for Ni-Na-X are similar to those of Ni-CIT-6, although the zincosilicate tends to produce more linear products.³³ The Ni²⁺-exchanged USY material initially gives the highest propylene conversion and has the lowest C_{3n} product selectivities (less than 65% at 180°C) of any material tested. This is likely due to the presence of residual Brønsted acid sites within the FAU framework that catalyze oligomerization and cracking reactions, in addition to oligomerization at the nickel cation sites. In agreement with previous studies, high cracking activity is initially present at these strong acid sites until they deactivate, after which oligomerization proceeds more selectively.^{37, 42}

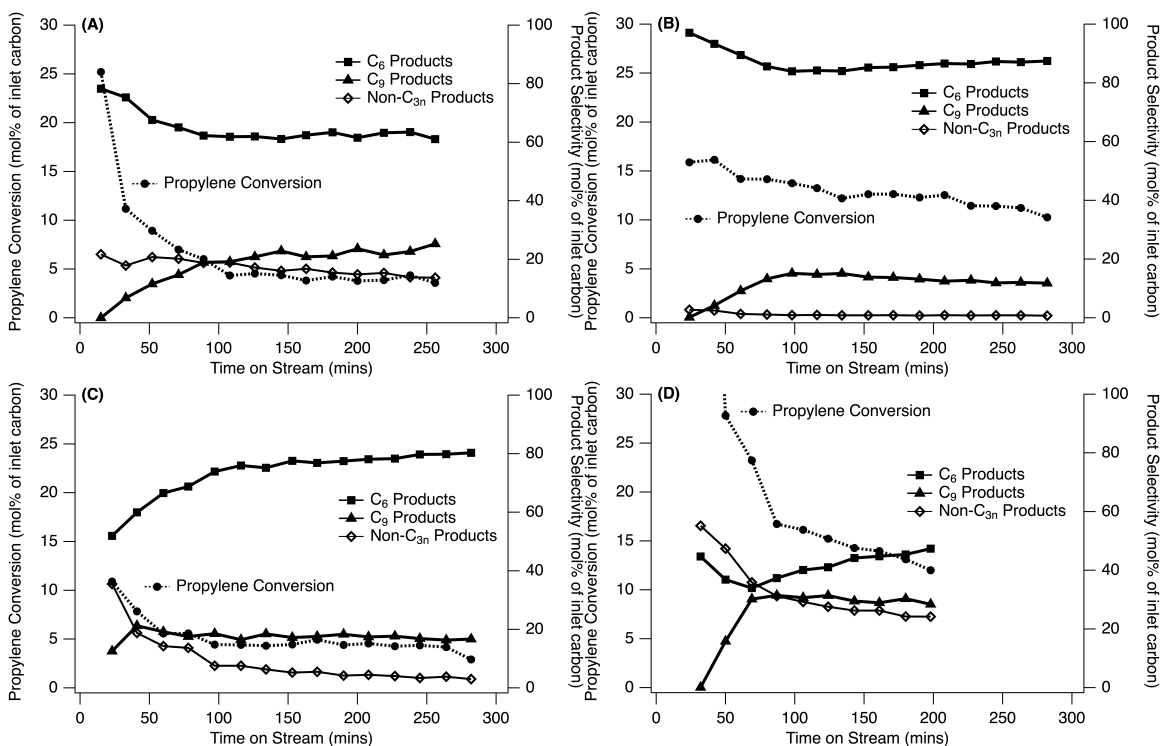


Figure 2.3: Representative time-on-stream profiles of conversion and C₆ and C₉ selectivity for Ni-CIT-6 (A), Ni-Zn-MCM-41 (B), Ni-HiAl-BEA (C), and Ni-USY (D) at 250°C.

Figure 2.3 shows similar behavior for each of the four materials at 250°C. TOS behavior for each material at 250°C is similar to that observed at 180°C, with a few exceptions. Propylene conversion increases with the increase in temperature for each material, with the exception of Ni-HiAl-BEA. Ni-CIT-6 gives higher selectivity to C₉ products at 250°C than at 180°C (~22% versus ~18%), with the corresponding selectivities to C₆ products decreasing (non-C_{3n} selectivities are typically less than 20%). However, more hexene products resulting from double-bond isomerization (such as 2-methyl-2-pentene) are observed at 250°C than at 180°C. A similar increase in formation of double-bond isomerization products at 250°C relative to 180°C is also observed for Ni-Zn-MCM-41. A slight decline in propylene conversion is observed over the reaction time profile, but the material still exhibits very stable conversion with increasing time on stream. Total selectivities to non-C_{3n} products are again quite low (<1%) for all data points.

For Ni-HiAl-BEA, propylene conversion decreases with the increase in reaction temperature from 180°C to 250°C. This suggests that catalyst deactivation may be more rapid at the higher reaction temperature. Additionally, while carbon balances remain near 100% for both reaction tests, regeneration does not fully recover the initial catalyst activity.

At 250°C, Ni-USY exhibits slightly reduced selectivities to C₉ products (~30%) relative to those at 180°C (~30-35%), while total selectivities to C₆ products increase from approximately 30-35% at 180°C to 40-45% at 250°C for most data points. Additionally, selectivities to C₄ and C₅ products have slightly decreased, while selectivities to C₇ and C₈ products have increased, suggesting increased cracking of C₉ products and reduced cracking of C₆ products at 250°C. This could be attributed to faster deactivation of strong Brønsted acid sites at 250°C. While C_{3n} products were still the predominant products observed, the wide variety of cracking products and relatively low selectivity to the desired products make Ni-USY unsuitable as a selective oligomerization catalyst under these conditions.

Interestingly, selectivity for the major product, 2-methyl-2-pentene, decreases slightly with increasing TOS for the zincosilicates, while it increases with TOS for

the aluminosilicates. This observation suggests that the residual acid sites in zincosilicates are not strong enough to catalyze cracking reactions but are still capable of isomerizing the primary oligomerization products. It is possible that the residual acid sites in the aluminosilicates are strong enough to catalyze cracking reactions, producing chiefly cracking products initially and leading to a relative lack of isomerization products. As these strong acid sites in the aluminosilicates deactivate with increasing TOS, the isomerization products could then begin to accumulate. These observations suggest that zincosilicates should be used if selectivity to simple oligomerization products is desired.

Further analysis of the hexene isomers formed from the oligomerization reaction also reveals that the zincosilicates typically exhibit much higher linear-to-branched ratios than the aluminosilicates. These higher linear-to-branched ratios observed for the zincosilicates are believed to be the result of a difference in the fine structural details around the nickel cation relative to that of the aluminosilicates. Figure 2.4 shows the linear-to-branched ratios for each material at 180°C and 250°C.

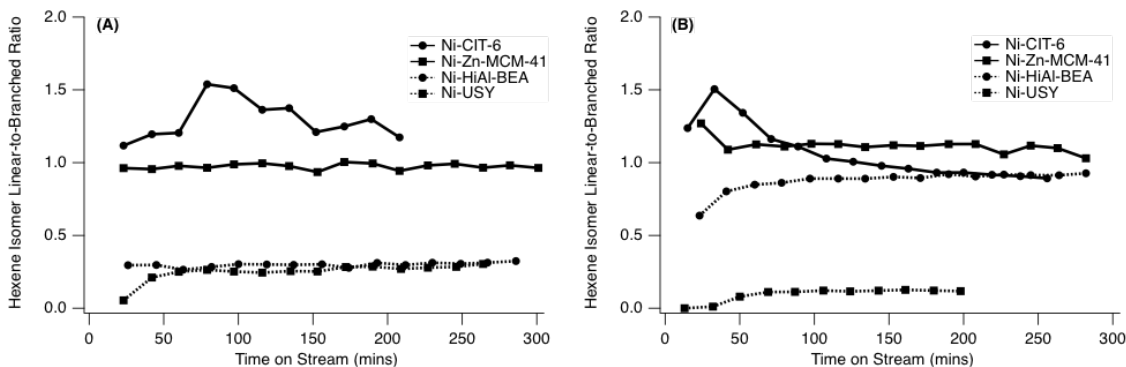


Figure 2.4: Hexene isomer linear-to-branched ratios for Ni-CIT-6, Ni-Zn-MCM-41, Ni-HiAl-BEA, and Ni-USY at 180°C (A) and 250°C (B).

The ratios are fairly constant with TOS, with the exception of Ni-CIT-6, which exhibits a maximum before declining to a stable ratio at increasing TOS for both reaction temperatures. Ni-Zn-MCM-41 has stable linear-to-branched ratios very near 1.0 for both reaction temperatures. At 180°C, both aluminosilicate catalysts have constant ratios of approximately 0.3, with the exception of the initial Ni-USY ratio.

However, at 250°C, Ni-HiAl-BEA has a significantly higher linear-to-branched ratio, again showing behavior similar to that of the zincosilicates at this elevated reaction temperature. The linear-to-branched ratio observed for Ni-USY at 250°C decreases to values just above 0.1 for the duration of the reaction test. Linear hexene isomers may be useful or desirable in the synthesis of specialty chemicals, although in the synthesis of gasoline, this linearity is undesirable.

2.4 Summary

Ni²⁺ ion was exchanged onto four molecular sieves and their ability to catalyze propylene oligomerization compared. Each material tested was capable of oligomerizing propylene, albeit with varying conversions and C_{3n} product selectivities, under the reaction conditions tested. For all catalysts except Ni-HiAl-BEA, the propylene conversion increased with increasing temperature. The opposite trend for Ni-HiAl-BEA could be due to a faster oligomerization site deactivation as temperature increases.

Double-bond isomerization from the hexenes formed directly by propylene dimerization was observed for all catalysts. Further, cracking reactions of these C_{3n} products were observed in the aluminosilicates, particularly Ni-USY (this catalyst was the least selective to C_{3n} products tested). Detailed characterization of the hexene isomers formed by each catalyst revealed that the zincosilicates also typically had much higher linear-to-branched hexene isomer ratios than the aluminosilicates.

The two *BEA framework materials with zinc and aluminum heteroatoms (Ni-CIT-6 and Ni-HiAl-BEA, respectively) exhibit similar time-on-stream behavior with respect to propylene conversion; however, the product distribution for Ni-HiAl-BEA is not as selective to oligomers as Ni-CIT-6, as evidenced by the relative selectivities to C_{3n} products for the two materials. Cracking products (non-C_{3n}) were also observed with Ni-HiAl-BEA. These additional cracking reactions to produce C₇ and C₈ products were likely catalyzed by the strong Brønsted acidity of the solid. Hexene selectivity and overall propylene conversion were higher at both reaction temperatures for the mesoporous Ni-Zn-MCM-41 relative to the microporous Ni-CIT-6. This was

likely due to the larger pores within Ni-Zn-MCM-41, which remained unblocked by hydrocarbons for longer periods on stream. Ni-Zn-MCM-41 had the highest, most stable conversions and highest selectivities to hexene products. Ni-USY, while it had the highest propylene conversions at each temperature, also exhibited the poorest selectivities to C_{3n} products. The wide variety of these products makes this material unsuitable as an oligomerization catalyst under the reaction conditions tested.

These observations validate the hypothesis that matching the charge of the framework heteroatom with that of the exchanged ion can reduce undesirable side reactions catalyzed by unexchanged, strong Brønsted acid sites, and suggest that zirconosilicates may well be interesting materials for light olefin oligomerization.

Chapter 3

Combined Oligomerization and Transfer Hydrogenation Catalysts to Operate on a Mixed Alkane/Alkene Feed

This work was partially completed in collaboration with Dr. David Leitch and Dr. Keith Steelman (Bercaw Group at Caltech), both of whom synthesized and characterized the supported homogeneous catalysts.

3.1 Introduction

Currently, light hydrocarbons ($C_{<6}$), while abundant from myriad sources such as fluid catalytic cracking (FCC) units in refineries, natural gas, and Fischer-Tropsch synthesis, are not particularly useful as fuels due to their low energy density.^{1, 43, 44} Upgrading of light alkenes into higher molecular weight compounds through oligomerization has been discussed in the previous chapter, but light alkanes have been more difficult to incorporate into heavier hydrocarbon products. To combine these smaller molecules for upgrading, mild reaction conditions with lower temperatures are thermodynamically preferable, as the entropic cost of combining smaller hydrocarbons into longer chains excludes higher temperatures ($T > 250^\circ\text{C}$ for propylene). One possible means to achieve this coupling of alkanes and alkenes is alkane metathesis, which has been investigated by several research groups.^{45, 46, 47} In alkane metathesis, the

two primary steps are alkane dehydrogenation and alkene metathesis, forming a C_{2n-2} alkane and an ethane from two C_n alkanes; however, only a few of these reactions avoid statistical distributions of hydrocarbon products, instead having selectivity to a single desired C_{2n-2} product.^{48, 49, 50} These studies also involve heavier liquid hydrocarbon molecules, but work is still needed to sufficiently incorporate light hydrocarbons.

While homogeneous transition metal-based transfer hydrogenation catalysts and oligomerization catalysts have been independently well-studied by several research groups on pure alkane feeds as cited previously, none have investigated a combined transfer hydrogenation/oligomerization catalytic system to operate on mixed light alkane/alkene feeds in either batch or flow reaction systems. Use of such a mixed feed then takes advantage of many realistic byproduct streams, such as the light gas stream from FCC units.

In this chapter, a tandem catalyst system^{51, 52} is proposed as a means to create longer-chain, gasoline- or diesel-range hydrocarbons from light alkane/alkene mixtures which better replicate real refinery feed streams. The catalytic system is comprised of a transfer hydrogenation catalyst that activates the feed alkanes to alkenes, and an oligomerization catalyst that performs the alkene oligomerization, while the first catalyst then replaces the abstracted hydrogen atoms onto the resulting alkene to produce a net alkylation product, as outlined in Section 1.3 of Chapter 1 and shown in Figure 3.1.⁵³ Such a catalytic system would be able to perform a net alkylation reaction on hydrocarbons in a mixed alkane/alkene feed without the use of dangerous sulfuric or hydrofluoric acid, as is currently employed in refineries.¹

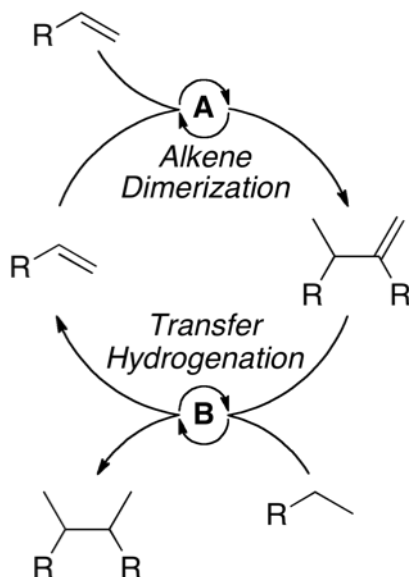


Figure 3.1: Tandem catalysis cycle.

Recent work from the Bercaw group at Caltech has demonstrated the potential for such a catalytic system to occur in both liquid phase batch and semi-batch reactions.^{53, 54} In the first reported study,⁵³ an Ir-based pincer ligand transfer hydrogenation catalyst^{55, 56, 57, 58, 59, 60, 61, 62} and a Ta-based oligomerization catalyst^{63, 64} work to dehydrogenate heptane and oligomerize the resulting heptenes and added 1-hexene to form C_{12} , C_{13} , and C_{14} alkene products, but the catalysts are unable to perform the final step of the catalytic cycle shown in Figure 3.1 (Part B - hydrogenation of the newly formed alkene dimers). An approach involving an alkene substrate as a sacrificial hydrogen acceptor to close the cycle has also been shown to work,⁵⁴ but clearly it is preferable to close the cycle with alkenes formed solely by the transfer hydrogenation catalyst.

Additionally, while this combined system shows promise in liquid phase hydrocarbon reactions, industrial alkane/alkene feedstocks are typically gaseous. For this reason, heterogeneous catalysts are generally preferred. The heterogeneous Ni-based catalysts described in the previous chapter (specifically Ni-CIT-6 and Ni-Zn-MCM-41) can be used to perform the oligomerization reaction; however, a heterogeneous transfer hydrogenation catalyst must be developed. Supporting the previously de-

scribed homogeneous transfer hydrogenation catalysts on heterogeneous supports (such as mesoporous carbon, aluminosilicates, or zincosilicates) is one potential solution. These Ir-based catalysts also tend to perform the hydrogenation step more effectively on linear molecules,⁵⁴ so the Ni-containing zincosilicates are selected for use as oligomerization catalysts, due to their higher selectivity to linear hexene products.

Here, the synthesis, preparation, and reactivity of heterogeneous oligomerization and transfer hydrogenation catalysts in an equimolar gaseous alkane/alkene feed (propylene/*n*-butane) are investigated. Ni-CIT-6 and Ni-Zn-MCM-41 are utilized as oligomerization catalysts, while several Ir-based pincer ligand transfer hydrogenation catalysts are synthesized and tested. Each homogeneous transfer hydrogenation catalyst is deposited on several different supports, such as alumina, Al-MCM-41, Zn-MCM-41, and mesoporous carbon in loadings from 10wt% to 50wt%, depending upon the catalyst and support. Physical mixtures of these catalyst pairs then are loaded into a continuous-flow reactor with equimolar alkane/alkene reactant flows, and oligomerization and transfer hydrogenation activity are monitored via GC/FID/TCD.

3.2 Experimental Section

3.2.1 Synthesis of Porous Heterogeneous Catalysts

CIT-6 was synthesized according to the method of Takewaki et al. as discussed in Chapter 2.²² The mesoporous zincosilicate Zn-MCM-41 was also synthesized in the same manner as that described by Takewaki et al., again discussed in Chapter 2.²⁴

Ni²⁺ ion exchange onto the samples was performed for 5 h at 75°C for Ni-CIT-6 and 25°C for Zn-MCM-41 using a 0.01 M solution of Ni(NO₃)₂ (Sigma Aldrich, hexahydrate) that had been pH-adjusted to 7.0 using 0.01 M NaOH solution. For each exchange, 250 mg of material was added to 25 mL of solution. The materials were then separated from the Ni(NO₃)₂ solution via centrifugation, washed with distilled water, and dried. After the Ni²⁺ exchange, Ni-CIT-6 and Ni-Zn-MCM-41 both exhibited a

pale green color.

3.2.2 Synthesis of Ir-based Homogeneous Catalysts and Deposition on Supports

Each ligand and Ir-based transfer hydrogenation catalyst shown in Figure 3.2 was prepared according to reported literature procedures from Göttker-Schnetmann et al. (A),⁵⁹ Huang et al. (B),⁶⁰ Haenel et al. (C),⁶⁵ Chao et al. (D),⁶⁶ Tanaka et al. (E),⁶⁷ Avent et al. (F),⁶⁸ and McInturff et al. (G).⁶⁹ The Ir-based catalysts were then deposited on the supports (silica, alumina, Al-MCM-41, Zn-MCM-41, and mesoporous carbon samples) by incipient wetness impregnation to form the heterogeneous transfer hydrogenation catalysts.

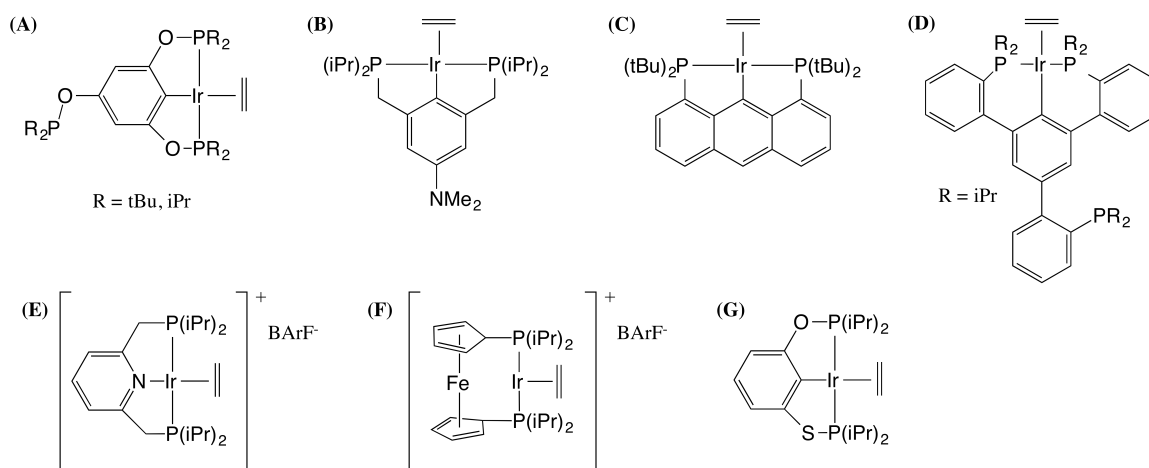


Figure 3.2: Ir-based pincer ligand catalysts for transfer hydrogenation: Ir-POCOP (A), Ir-PCP (B), Ir-tBu₄-anthrathos (C), Ir-iPr₄-tris(phosphinoaryl) benzene (D), Ir-PNP (E), Ir-ferrocene (F), and Ir-POCSP (G).

3.2.3 Characterization

Powder XRD patterns for the Ni-CIT-6 and Ni-Zn-MCM-41 samples were obtained with a Rigaku MiniFlex II instrument using Cu K α radiation ($\lambda=1.54184 \text{ \AA}$) to determine structure type and purity. Morphology and elemental composition were determined via scanning electron microscopy/energy dispersive spectroscopy (SEM/EDS)

on a ZEISS 1550VP instrument equipped with an Oxford X-Max SDD energy dispersive X-ray spectrometer.

To confirm the correct synthesis and purification for the Ir-based ligands, liquid-phase ^1H , ^{13}C , and ^{31}P NMRs were obtained for the homogeneous catalysts tested.

3.2.4 Reaction Testing

Prior to reaction testing, Ni-CIT-6 and Ni-Zn-MCM-41 were calcined in breathing-grade air by heating to 150°C at $1^\circ\text{C}/\text{min}$, held for 3 h at 150°C , then heated further to 580°C at $1^\circ\text{C}/\text{min}$ and held for 6 h, all under flowing air. Ni-CIT-6, Ni-Zn-MCM-41, and the supported Ir-based materials were then individually pelletized, crushed, and sieved. Particles between 0.6 mm and 0.18 mm of each catalyst type (a Ni-containing zincosilicate for oligomerization and a supported Ir-based catalyst for transfer hydrogenation) were physically mixed and supported between glass wool beds in an Autoclave Engineers BTRS, Jr. 316 SS continuous flow, tubular reactor. Due to the air-sensitive nature of the Ir-based ligands, loading of the reactor tube was performed in an argon glovebox.

For reaction testing, an equimolar mixture of propylene and *n*-butane was supplied to the 3/8" ID 316 SS tubular reactor, with total flow such that a weight-hourly space velocity (WHSV) of 0.5 h^{-1} was attained. Each catalyst mixture was tested at 180°C . In a typical run, 200 mg of each dry solid catalyst was loaded (400 mg total). Reactor effluent gases were analyzed using an on-stream GC/FID/TCD Agilent GC 7890A with Plot-Q capillary columns installed. Conversions and selectivities were computed on a carbon mole basis.

3.3 Results and Discussion

3.3.1 Characterization of Porous Materials

The powder XRD patterns of the Ni-CIT-6 and Ni-Zn-MCM-41 used here, after nickel exchange and calcination, are shown in Figure 3.3. Additional powder XRD data (for

both Ni-CIT-6 and Ni-Zn-MCM-41 as synthesized, after nickel exchange, and after calcination) are shown in Figures B.1 and B.2 of the Appendix.

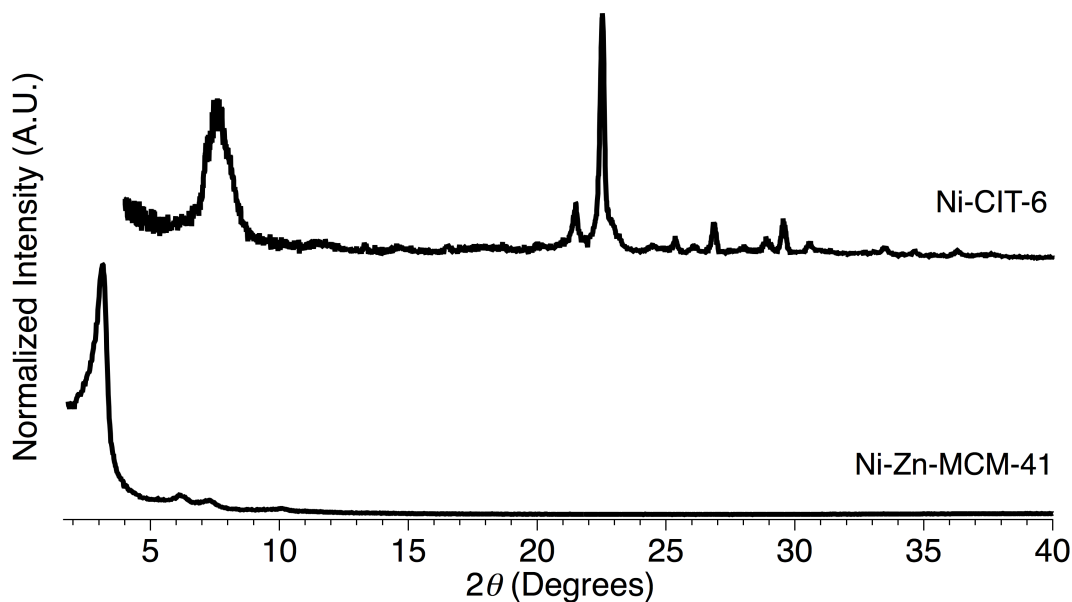


Figure 3.3: Powder XRD patterns of nickel-exchanged, calcined materials Ni-CIT-6 and Ni-Zn-MCM-41.

The elemental compositions of the two heterogeneous materials are shown in Table 3.1.

Material	Si/Zn	Ni/Zn
Ni-CIT-6	12.9	0.42
Ni-Zn-MCM-41	21.0	0.86

Table 3.1: Elemental compositions of Ni-CIT-6 and Ni-Zn-MCM-41.

3.3.2 Characterization of Supported Homogeneous Catalysts

Liquid NMRs of each Ir-based catalyst revealed that the correct ligands had been synthesized and that the catalysts were intact. Weight loadings between 10wt% and 50wt% were achieved, depending upon the ligand and support used. Table 3.2 outlines the combinations of ligands and supports that underwent reaction testing:

Ir-based Catalyst	Heterogeneous Support				Mesoporous Carbon
	Silica	Alumina	Al-MCM-41	Zn-MCM-41	
(A) Ir-POCOP	10wt%	10wt%	10wt%	10wt%	10wt%
(B) Ir-PCP	10wt%	10wt%	10wt%	10wt%	10wt%
(C) Ir-tBu ₄ -anthraphos	–	10wt%	10wt%	10wt%	10wt%
(D) Ir-iPr ₄ -tris(phosphinoaryl) benzene	–	10wt%	–	10wt%	10, 30, & 50wt%
(E) Ir-PNP	–	–	–	10wt%	10, 30, & 50wt%
(F) Ir-ferrocene	–	–	10wt%	10wt%	10, 30, & 50wt%
(G) Ir-POCSP	–	–	10wt%	–	–

Table 3.2: Ir-based transfer hydrogenation catalysts tested for the tandem catalysis system.

3.3.3 Reaction Testing

In reaction testing of the combined catalysts, only significant oligomerization of propylene to C₆ and C₉ products was observed. Trace C₇ products were also observed for some catalyst combinations (those supported on silica, alumina, or the MCM-41s), but no appreciable *n*-butane conversion was observed in these systems (reported conversions in the following figures are approaching the analytical limits of the reaction testing apparatus for butane). The initial “conversions” observed for each reaction test are likely due to material holdup on the catalyst, as the carbon balances are quite poor for each initial sample point. Further control experiments with only the oligomerization catalyst present in the propylene/*n*-butane feed revealed nearly identical selectivities to these C₇ products. This similarity in C₇ selectivities for most supports in the absence of the transfer hydrogenation catalysts suggests the supported homogeneous catalysts are inactive for the conversion of *n*-butane to butenes,

and consequently to the formation of C_7 products. Thus, the observed C_7 products likely result from interaction with the mesoporous carbon or from cracking reactions in the zincosilicates, not from the transfer hydrogenation catalysts.

Interestingly, however, when the Ir-based catalysts are supported on mesoporous carbon, some C_7 products (primarily toluene), as well as benzene, are formed in more substantial quantities. Control experiments further revealed that these additional benzene and toluene products observed were in fact forming as a result of the reactivity of the mesoporous carbon, rather than activity of the Ir-based homogeneous catalysts themselves. Figures 3.4 and 3.5 show the reaction data for Ni-CIT-6 when combined with the mesoporous carbon in two cases: one with a transfer hydrogenation catalyst (Ir-PNP) deposited onto the carbon, and one with only the mesoporous carbon support.

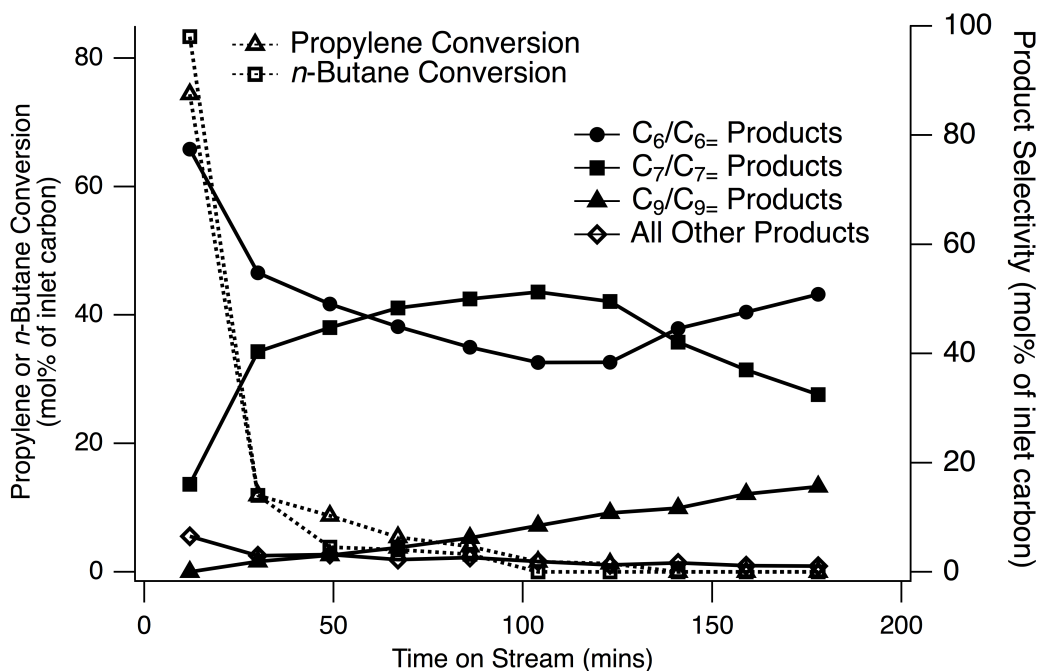


Figure 3.4: Reaction data for Ni-CIT-6 and Ir-PNP supported on mesoporous carbon with propylene/*n*-butane at 180°C.

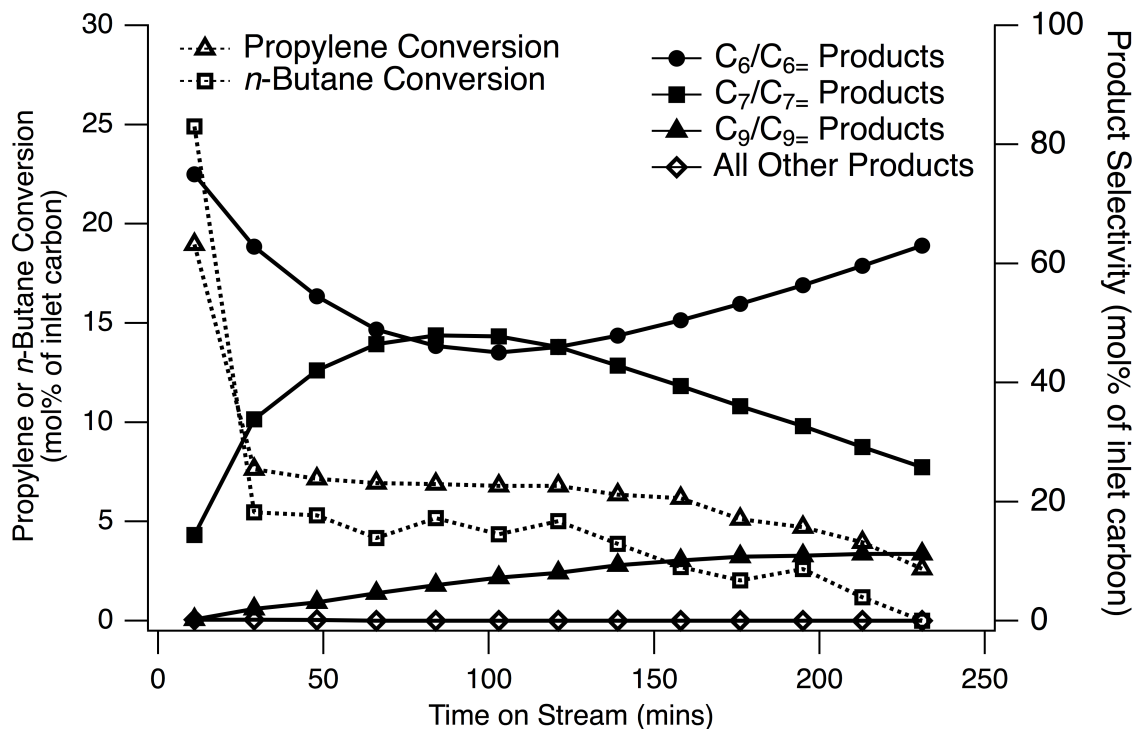


Figure 3.5: Reaction data for Ni-CIT-6 and mesoporous carbon support with propylene/*n*-butane at 180°C.

Both reactions were conducted at 180°C in an equimolar propylene/*n*-butane feed. Very little difference in activity is observed between the two test cases, again demonstrating that the Ir-based catalysts are inactive under these conditions. It is also worth noting that in both cases, the initially high selectivity to C₆ products is due entirely to benzene formation, presumably by the mesoporous carbon. As TOS then increases, this initial benzene selectivity decreases while toluene (nearly all of the C₇ products observed) production increases to a maximum value before declining. As this decline in C₇ selectivity occurs, the selectivity to C₆ and C₉ oligomerization products begins to increase and eventually dominate the reaction, as is observed for reaction tests with only Ni-CIT-6.

The reaction data for a final control experiment is also shown in Figure 3.6 in which the pure mesoporous carbon support is the only material present in the reactor under an equimolar feed of propylene and *n*-butane. Again, initial formation of

benzene followed by toluene is observed in the absence of a transfer hydrogenation catalyst. The high initial conversion observed is likely due to absorption of propylene and *n*-butane to the mesoporous carbon surface.

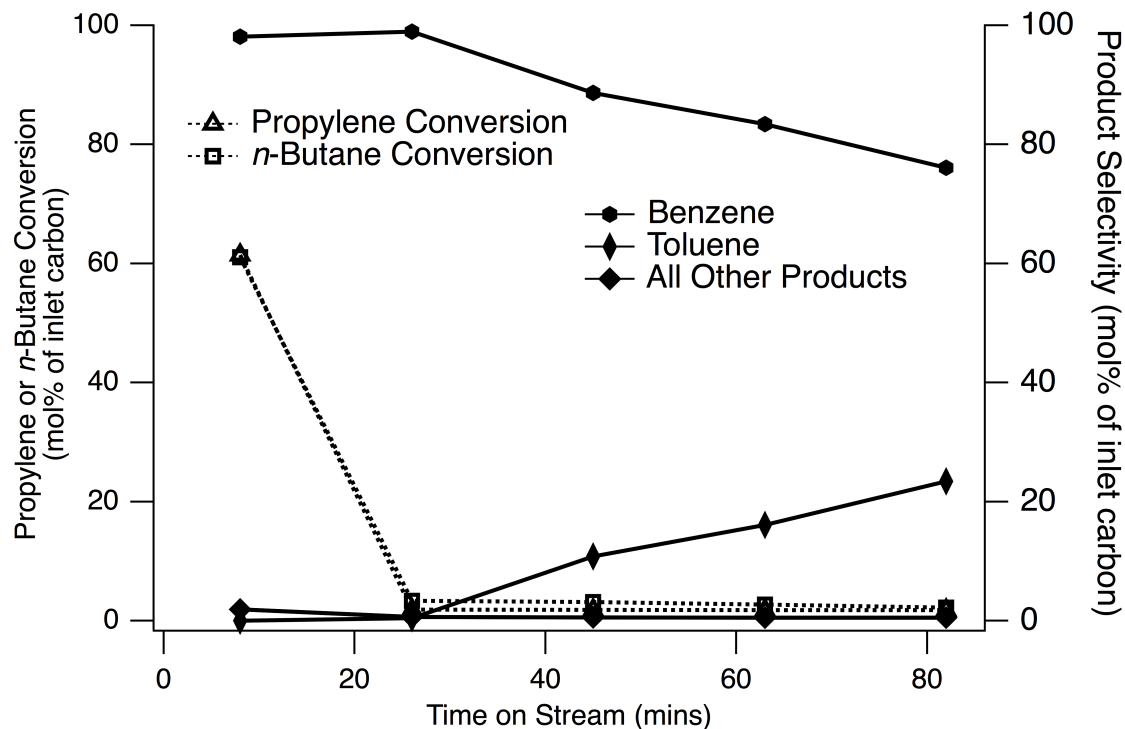


Figure 3.6: Reaction data for pure mesoporous carbon support with propylene/*n*-butane at 180°C.

Interestingly, the presence of both propylene and *n*-butane was required to form these aromatic products: a pure feed of either reactant over mesoporous carbon would not produce any benzene or toluene.

3.4 Summary

The two zincosilicate-based oligomerization catalysts studied in the previous chapter (Ni-CIT-6 and Ni-Zn-MCM-41) were combined with supported homogeneous Ir-based transfer hydrogenation catalysts in an attempt to form a heterogenous tandem catalysis system for converting a mixed light alkane/alkene feed into longer-chain hydrocarbon products. While the nickel-containing zincosilicate oligomerization catalysts

react with propylene as expected, the transfer hydrogenation catalysts appear inactive in converting the *n*-butane to butenes. As a result, only simple C_{3n} oligomerization products were primarily observed in the reactor effluent. C₇ products, suggestive of some incorporation of *n*-butane into the alkene dimerization, were also present for homogeneous catalysts supported on mesoporous carbon; however, control experiments revealed that the mesoporous carbon support appears to be the source of these products (primarily benzene and toluene). The remainder of any C₇ products observed may simply be attributed to cracking reactions over the oligomerization catalysts.

Thus, at the time of this study, the tandem system cannot yet convert alkanes from a mixed alkane/alkene gaseous feed into oligomerizable alkenes. Accordingly, further work is needed to improve the activity of the Ir-based transfer hydrogenation catalysts, specifically in the gas phase, to realize this tandem catalysis cycle. New homogeneous catalysts may be developed, and new heterogeneous supports may be utilized. Additionally, the reaction apparatus may be modified to operate at higher pressures for the reactant gases, since the higher reaction pressure may increase the activity of the supported homogeneous catalysts.

Chapter 4

Additional Oligomerization Work

4.1 Introduction

In addition to the oligomerization work outlined in the previous two chapters, new reaction stream blends were studied to explore the reactivity of other light olefins with these new zirconosilicate supports (CIT-6 and Zn-MCM-41). Ni-CIT-6 and Ni-Zn-MCM-41 were studied under flows of 1-butene and an equimolar mixture of propylene/1-butene to investigate how the different olefins and feed concentrations could affect conversion and product selectivities.

Pt-Ni-Zn-MCM-41 was also reaction-tested with an equimolar mixture of propylene and *n*-butane to determine if Pt could act as a heterogeneous transfer hydrogenation catalyst at elevated temperatures ($>400^{\circ}\text{C}$), fulfilling the role of the Ir-based catalysts studied in Chapter 3. As discussed in Chapter 3, such a combined transfer hydrogenation/oligomerization catalyst could be effective in converting gaseous mixed alkane/alkene feeds into fuel-range hydrocarbons within a single reactor. To this end, the mesoporous zirconosilicate oligomerization catalyst was chosen for Pt impregnation, since it is capable of oligomerizing propylene at temperatures much higher than the aluminosilicates without forming cracking products (up to 450°C for Ni-Zn-MCM-41 vs. approximately 180°C for Ni-Na-Y). Reaction products were again characterized by GC/FID/TCD.

The discovery of the neutral-pH method to successfully exchange divalent ions onto CIT-6 without destroying the Zn heteroatom exchange site (presented in Chapter 2)

opens up a new family of catalysts based on CIT-6. Such a series of zincosilicate-supported materials could be very interesting in transition-metal catalyzed reactions, where high product selectivity is possible and strong Brønsted acidity is not required. For example, several transition metals (such as Mn^{2+} , Co^{2+} , Cu^{2+} , and Zn^{2+}) on microporous materials have been shown to be active for a wide range of reactions, such as oxidation of alkanes, removal of NO and NO_2 from exhaust gas streams (de NO_x), acetic acid synthesis, and aromatization of light alkanes.^{70, 71, 72, 73, 74, 75, 76, 77, 78, 79, 80, 81, 82, 83} Accordingly, several divalent transition metals were exchanged onto CIT-6 to investigate catalyst stability, and the resulting catalysts subsequently underwent oligomerization reaction testing as a screening reaction. However, only Co-CIT-6 exhibited propylene oligomerization activity.

4.2 Experimental Section

4.2.1 Synthesis of Porous Materials

A large batch of CIT-6 was synthesized according to the method of Takewaki et al. as discussed in Chapter 2.²² The mesoporous zincosilicate Zn-MCM-41 was synthesized again as described by Takewaki et al. in Chapter 2.²⁴

4.2.2 Divalent Metal Ion Exchanges

All divalent ion exchange were performed for 5 h at 75°C for CIT-6 samples and 25°C for Zn-MCM-41 samples using a 0.01 M solution of each divalent cation. $\text{Ni}(\text{NO}_3)_2$ was again used to prepare the Ni^{2+} exchange solution. For Cu^{2+} , $\text{Cu}(\text{OAc})_2 \cdot \text{H}_2\text{O}$ was used to prepare the exchange solution. Similarly, MnSO_4 was used for Mn^{2+} , $\text{CoCl}_2 \cdot 6 \text{H}_2\text{O}$ was used for Co^{2+} , and $\text{Zn}(\text{OAc})_2$ was used as a Zn^{2+} source. All solutions were pH-adjusted to 7.0 using 0.01 M NaOH solution. For each exchange, 250 mg of material was added to 25 mL of solution. The materials were then separated from the exchange solutions via centrifugation, washed with distilled water three times, and dried. After the M^{2+} exchanges, Ni-CIT-6 exhibited a pale green color, Cu-

CIT-6 exhibited a pale blue color, Mn-CIT-6 exhibited a faint pink color, Co-CIT-6 exhibited a deep blue color, and Zn-CIT-6 remained white.

Pt impregnation was performed on Ni-Zn-MCM-41 samples after Ni²⁺ exchange by mixing a solution of Pt(NH₃)₄Cl₂·H₂O and water with the Ni-exchanged material (in a mass ratio of 1.00 g Ni-containing catalyst : 0.0091 g Pt(NH₃)₄Cl₂·H₂O : 3.90 g H₂O), stirring vigorously, and drying the sample by rotary evaporation. Platinated samples were then allowed to further dry overnight at 100°C.

4.2.3 Characterization

Powder XRD patterns for CIT-6 and Zn-MCM-41 materials were obtained with a Rigaku MiniFlex II instrument using Cu K α radiation ($\lambda=1.54184$ Å) to determine structure type and purity. Morphology and elemental composition were determined via scanning electron microscopy/energy dispersive spectroscopy (SEM/EDS) on a ZEISS 1550VP instrument equipped with an Oxford X-Max SDD energy dispersive X-ray spectrometer.

4.2.4 Calcination and Reaction Testing

Prior to reaction testing, all metal-exchanged CIT-6 materials (M-CIT-6s), Ni-Zn-MCM-41s, and all platinated Ni-containing materials were calcined in breathing-grade air. Samples were heated to 150°C at 1°C/min, held for 3 h at 150°C, then heated further to 580°C at 1°C/min and held for 12 h, all under flowing breathing-grade air in a muffle furnace.

These calcined materials were then pelletized, crushed, and sieved. Particles between 0.6 mm and 0.18 mm were supported between glass wool beds in an Autoclave Engineers BTRS, Jr. 316 SS continuous flow, tubular reactor.

Ni-CIT-6 and Ni-Zn-MCM-41 were tested in alternative feed gases to further investigate the effect of reactant on oligomerization activity: pure 1-butene and an equimolar mixture of propylene and 1-butene were used. WHSV values of 1.0 h⁻¹ were used in all cases.

For reaction testing of Pt-Ni-CIT-6 and Pt-Ni-Zn-MCM-41, an equimolar mixture of propylene and *n*-butane was supplied to the reactor with total flow such that a WHSV of 1.0 h⁻¹ was again achieved. These Pt-containing samples were reaction tested at 400°C after the initial calcination, in an attempt to make use of platinum's ability to dehydrogenate alkanes at higher temperatures. If platinum formed any olefins from the *n*-butane, these olefins could then be potentially oligomerized by the Ni cation to form heavier products, essentially performing the tandem catalysis cycle with a single catalyst. This reaction, while unlikely due to the thermodynamic unfavorability of oligomerization at elevated temperatures, could be an interesting method to form heavier products from light olefins.

For reaction testing of the M-CIT-6 samples, a mixture of propylene and an inert gas (composition 85mol% propylene, balance He/Ar) was supplied to the 3/8" ID 316 SS tubular reactor, with total flow such that a WHSV of 1.0 h⁻¹ was attained. Each M-CIT-6 catalyst was tested at 180°C and 250°C after the initial calcination.

In a typical reaction testing run for any of the materials, 200 mg of dry catalyst was loaded. Reactor effluent gases were analyzed using an on-stream GC/FID/TCD Agilent GC 7890A with Plot-Q capillary columns installed. Conversions and selectivities were computed on a carbon mole basis.

4.3 Results and Discussion

4.3.1 Characterization of Metal-Exchanged Materials Used as Catalysts

The powder XRD patterns of the M-CIT-6 samples used here, after metal exchange and calcination, are shown in Figure 4.1.

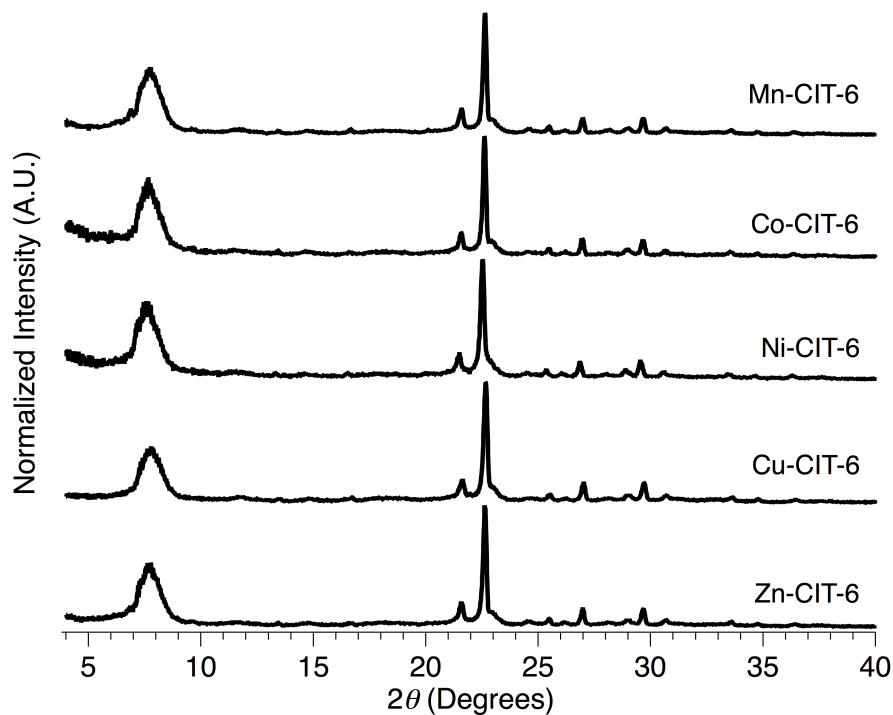


Figure 4.1: Powder XRD patterns of M-CIT-6 materials.

Powder XRD patterns for Pt-containing zincosilicate samples are shown in Figure 4.2. The relative intensity of the lower-angle peak is consistent with some framework damage caused by the platinum impregnation and subsequent calcination of the CIT-6 sample.

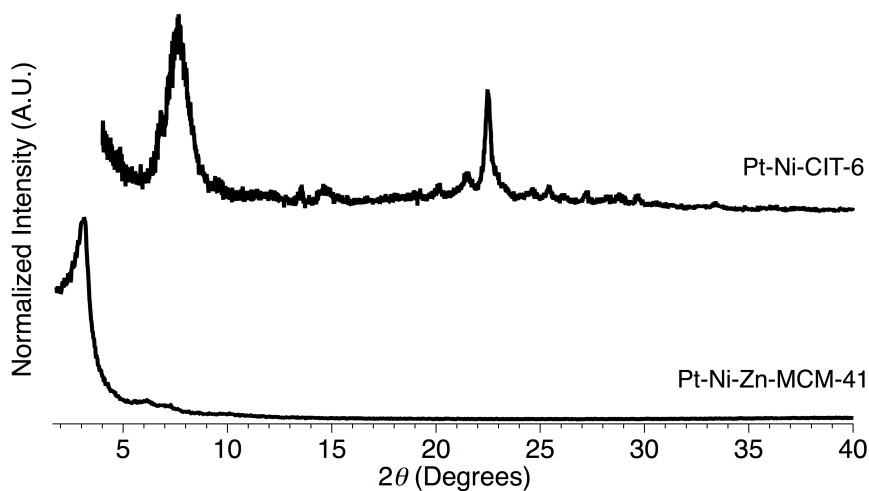


Figure 4.2: Powder XRD patterns of Pt-containing zincosilicates.

Table 4.1 shows the elemental compositions of each metal-exchanged zincosilicate sample.

Material	Si/Zn	M ²⁺ /Zn
Mn-CIT-6	10.6	0.13
Co-CIT-6	12.3	0.12
Ni-CIT-6	12.9	0.21
Cu-CIT-6	12.2	0.12
Zn-CIT-6	9.0	-
Ni-Zn-MCM-41	21.0	0.86
	Si/Zn	Pt wt%
Pt-Ni-CIT-6	12.9	1.1
Pt-Ni-Zn-MCM-41	23.4	2.4

Table 4.1: Elemental compositions of M-CIT-6, Ni-Zn-MCM-41, and Pt-containing samples.

4.3.2 Reaction Testing

Both Ni-CIT-6 and Ni-Zn-MCM-41 are active for oligomerization under all feed compositions. Reaction of Ni-CIT-6 with solely 1-butene produce some C₈ products, as expected; however, the main products are C₄ species that underwent double-bond isomerization to form a mixture of butenes. Figure 4.3 shows this reaction behavior. Thus, Ni-CIT-6 primarily acts as an isomerization catalyst, with some oligomerization activity under these feed conditions.

Ni-Zn-MCM-41 exhibits similar behavior, with an initial formation of some lighter species (namely propane and propylene) from 1-butene before forming C₄ and C₈ products, as with Ni-CIT-6. Ni-Zn-MCM-41 also produced trace C₁₂ products, unlike Ni-CIT-6. Figure 4.4 shows this behavior.

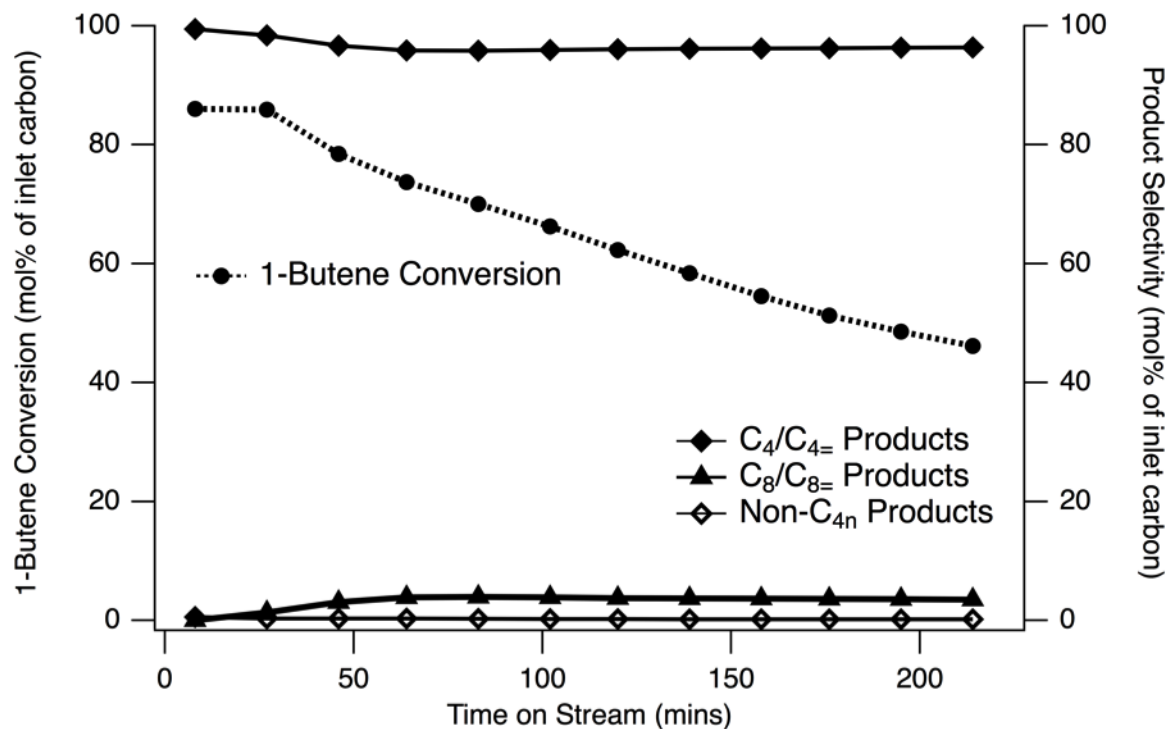


Figure 4.3: Reaction data for Ni-CIT-6 with 1-butene at 180°C.

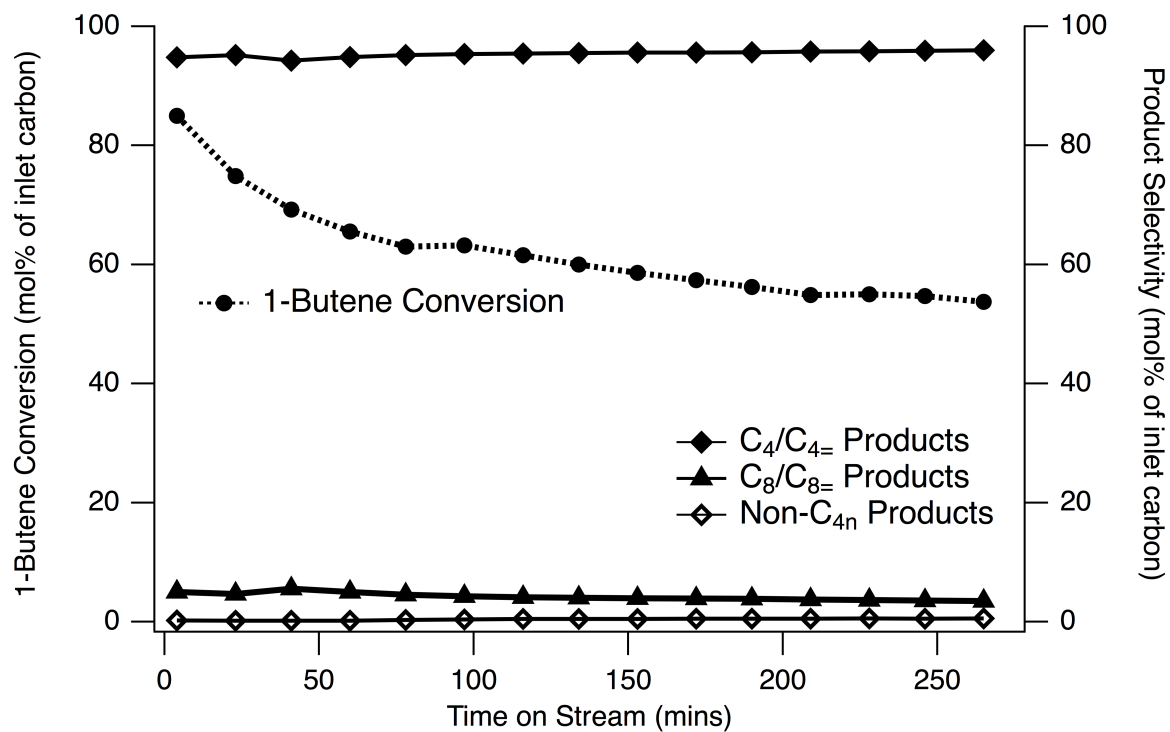


Figure 4.4: Reaction data for Ni-Zn-MCM-41 with 1-butene at 180°C.

Thus, both nickel-containing oligomerization catalysts were active for butene oligomerization, but they primarily performed double-bond isomerization of the 1-butene reactant.

Reaction with an equimolar feed of propylene and 1-butene for the two nickel-containing zincosilicates formed a mixture of C_6 , C_7 , and C_8 products as dimers, in addition to heavier products from trimerization of each olefin and butene isomers. Again, C_{12} products were observed in trace levels for Ni-Zn-MCM-41. Figure 4.5 shows this reaction behavior for Ni-CIT-6 at 180°C.

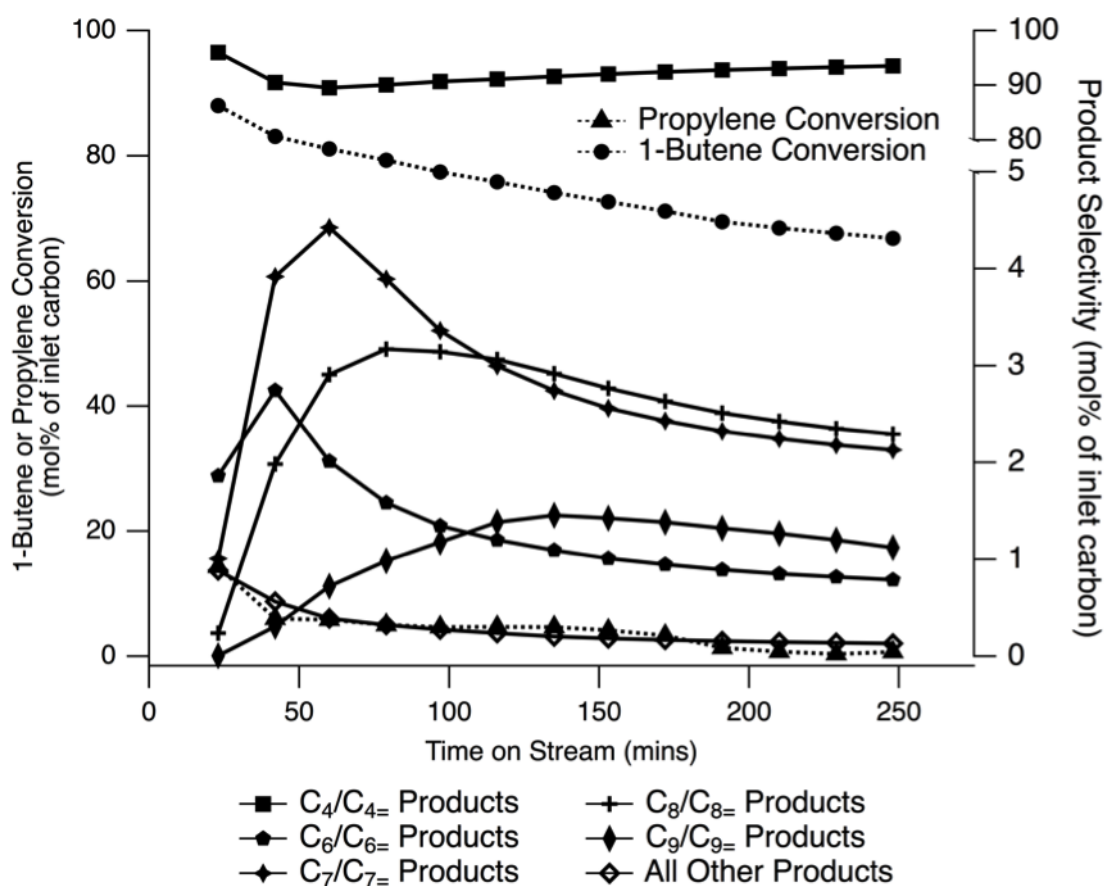


Figure 4.5: Reaction data for Ni-CIT-6 with equimolar propylene and 1-butene at 180°C.

Isomerization of 1-butene was the primary reaction observed, with the majority of 1-butene converted to other butenes (*cis*- and *trans*-2-butene). By comparing the ratios of isomerization products to dimerization or co-dimerization products, we see

that isomerization is approximately 15 times more active for 1-butene than reaction with another 1-butene or propylene molecule.

As TOS increases for Ni-CIT-6, selectivities to the simple C₆, C₇, and C₈ oligomerization products increase briefly before decreasing after approximately 50 mins TOS. C₉ products build up until approximately 140 mins TOS before declining, and the other dimers begin to stabilize by approximately 200 mins on stream. Interestingly, selectivity to C₇ products is highest initially, suggesting that co-dimerization of propylene and butene can occur, as this selectivity is much higher than observed for Ni-CIT-6 on either pure olefin reactant feed. Additionally, C₈ products are formed at a higher selectivity than C₆ products. This is an unexpected result, as typically the shorter-chain olefins should have higher oligomerization reactivity, *i.e.*, propylene > 1-butene; however, the increased coverage of 1-butene on the Ni atoms and/or the higher isomerization activity of 1-butene could contribute to this shift in observed selectivities. Selectivity to other products is low, as has been observed previously with Ni-CIT-6 in these oligomerization reactions.

Ni-Zn-MCM-41 (Figure 4.6 below) exhibits similar behavior, albeit with a faster drop in 1-butene conversion and higher selectivities to the desired C₇ and C₈ oligomerization products relative to Ni-CIT-6. However, unlike Ni-CIT-6, the selectivities for the other oligomerization products remain steadier with increasing TOS. Again, butene double-bond isomerization forms the products with the highest selectivity, while C₇ and C₈ products are formed at unexpectedly high selectivities relative to C₆ products, as with Ni-CIT-6.

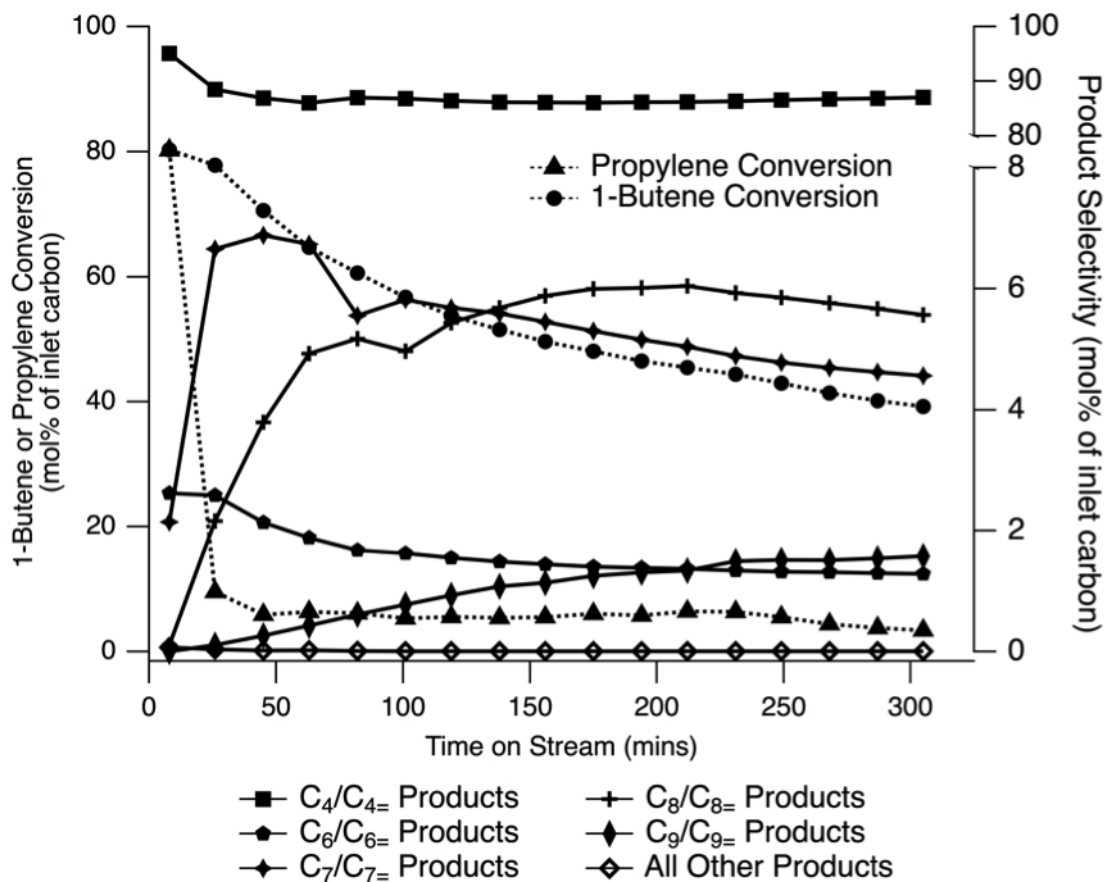


Figure 4.6: Reaction data for Ni-Zn-MCM-41 with equimolar propylene and 1-butene at 180°C.

The Pt-containing materials were then tested at a higher temperature (400°C) in an attempt to allow the Pt to act as a metal transfer hydrogenation catalyst. However, any elevated temperatures were not sufficient to incorporate the *n*-butane into the product mixture or form observable butenes. This inactivity could be due to the fact that the temperature was likely insufficiently high for the Pt to perform any dehydrogenation (previous reports suggest that temperatures >500°C are required).³⁰ These higher reaction temperatures also resulted in substantial oligomer cracking (forming non-C_{3n} products), negating the effects of any combined transfer hydrogenation-oligomerization that may have been obtained.

Reaction testing of the M²⁺-containing CIT-6 samples with propylene revealed interesting trends. Most divalent metals (Mn²⁺, Cu²⁺, and Zn²⁺) were completely

inactive for propylene oligomerization. However, Co^{2+} exchanged onto CIT-6 was in fact active for propylene oligomerization, in agreement with previous reports for the Co^{2+} ion on aluminosilicates.⁸⁴ Figure 4.7 shows this reactivity data at 250°C. Conversion and selectivity data for Co-CIT-6 are similar to that of Ni-CIT-6.

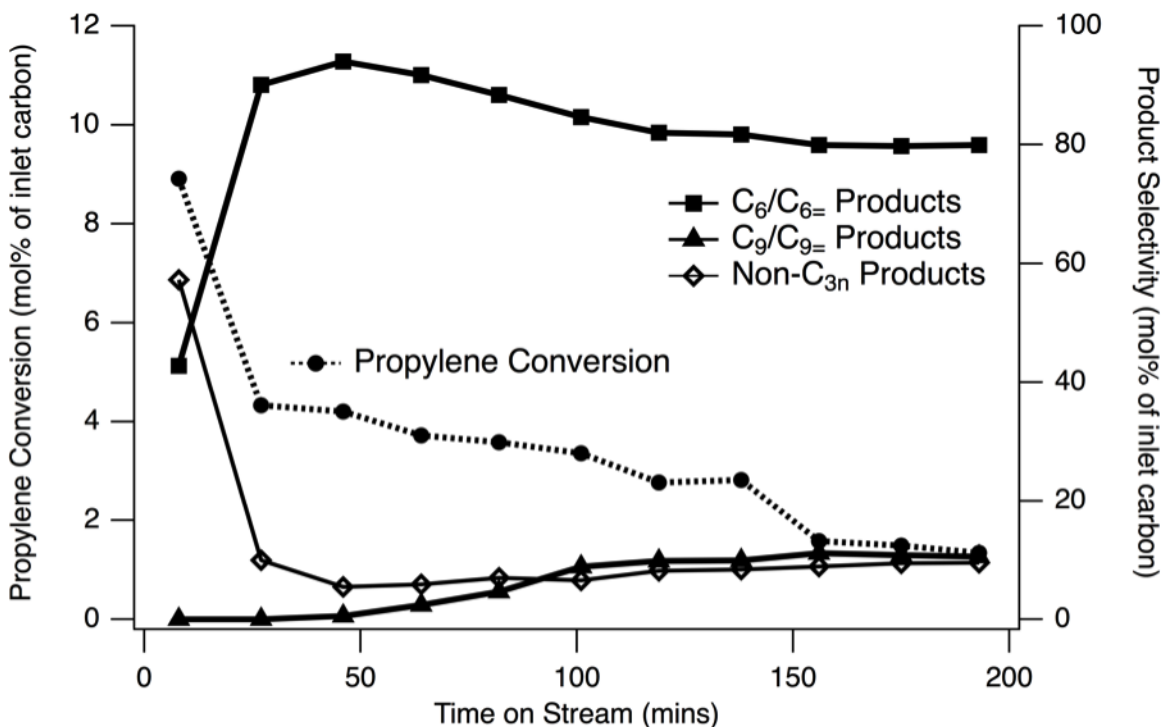


Figure 4.7: Reaction data for Co-CIT-6 with propylene at 250°C.

While mostly inactive for oligomerization, these M-CIT-6 materials may still prove useful in other reactions requiring transition metals, such as deNO_x . Additionally, the method developed to perform the divalent ion exchange onto CIT-6 will likely be useful in creating new zincosilicate *BEA-type catalysts with weaker Brønsted acidity than their aluminosilicate counterparts, leading to more selective products.

4.4 Summary

Ni-CIT-6 and Ni-Zn-MCM-41 underwent reaction testing with several different reactant streams to investigate their ability to oligomerize other light olefins, in addition to

propylene, to simulate more realistic FCC gas conditions. Ni-CIT-6 and Ni-Zn-MCM-41 were both capable of oligomerizing 1-butene into C₈ (and C₁₂ for Ni-Zn-MCM-41) products, as well as forming a range of oligomerization products from an equimolar propylene/1-butene reactant stream. In each case, however, other C₄ products (which had by far the highest selectivities) were formed by double-bond isomerization of the 1-butene feed.

Pt-containing zirconosilicates were inactive for any combined transfer hydrogenation activity by incorporation of *n*-butane. Instead, only simple oligomerization products and resulting cracking products were observed in the reactor effluent. This is likely due to the fact that temperatures were not sufficiently high for Pt to become active as a transfer hydrogenation catalyst and successfully incorporate the *n*-butane into the reaction.

Additionally, several divalent transition metal cations (Mn²⁺, Co²⁺, Cu²⁺, and Zn²⁺) were exchanged onto CIT-6 and reaction tested for oligomerization activity in a feed stream of propylene and inert. Co-CIT-6 demonstrated its effectiveness at oligomerizing propylene, but no other metal-exchanged CIT-6 samples exhibited any oligomerization activity.

While these other samples had no oligomerization activity, they may prove useful in other transition-metal catalyzed reactions. For example, Cu-CIT-6 and Co-CIT-6 could be useful for deNO_x reactions, as both of these cations have proven effective on other zeolite frameworks such as MFI and CHA.^{72, 73, 74, 75, 76, 77, 78, 79} Zn-CIT-6, Cu-CIT-6, and Co-CIT-6 may also be useful for the formation of acetic acid from methane and CO or CO₂, as described by Wu et al.,⁸⁰ Narsimhan et al.,⁸¹ and Huang et al.⁸²

Chapter 5

Conclusions and Suggested Future Work for Part I

This chapter outlines conclusions from the oligomerization work, presenting the key learnings from studying both the nickel-containing zirconosilicates and aluminosilicates. Suggested future work to improve the oligomerization catalyst and the tandem catalysis system are also presented.

5.1 Conclusions

As shown in Chapter 2, the nickel cation exchanged onto aluminosilicates and zirconosilicates can oligomerize propylene under the given reaction conditions, albeit with varying conversions and C_{3n} product selectivities. For all catalysts except Ni-HiAl-BEA, propylene conversion increased with increasing reaction temperature. The opposite trend for Ni-HiAl-BEA may be due to a faster oligomerization site deactivation as temperature increases. Higher selectivities to oligomers are obtained with the zirconosilicate catalysts relative to the aluminosilicates, presumably due to the weaker Brønsted acidity of the zinc heteroatom relative to the aluminum heteroatom at unexchanged framework sites. All catalysts exhibited double-bond isomerization from the hexenes formed directly by propylene dimerization. Cracking reactions of these C_{3n} products were also observed in the aluminosilicates, particularly Ni-USY (this catalyst was the least selective to C_{3n} products tested), but not significantly in the zirconosilicates. Detailed hexene isomer characterization for each oligomerization cata-

lyst revealed that the zincosilicates also typically had much higher linear-to-branched hexene isomer ratios than the aluminosilicates, making them more accessible to the supported Ir-based homogeneous catalysts of the subsequent tandem catalysis system.

The two *BEA topology materials with zinc and aluminum heteroatoms (Ni-CIT-6 and Ni-HiAl-BEA, respectively) exhibit similar propylene conversions, but Ni-HiAl-BEA is not as selective to C_{3n} products as Ni-CIT-6. Cracking products (non- C_{3n}) such as C_{7s} and C_{8s} were also observed with Ni-HiAl-BEA, likely formed by the strong Brønsted acidity of the microporous solid. Hexene selectivity and overall propylene conversion were higher at both reaction temperatures for the mesoporous Ni-Zn-MCM-41 relative to the microporous Ni-CIT-6, likely due to the larger pores within Ni-Zn-MCM-41 which remained unblocked by hydrocarbons for longer periods on stream. Ni-Zn-MCM-41 had the highest stable propylene conversions and selectivities to hexene products. Ni-USY, while it had the highest initial propylene conversions at each temperature, also exhibited the poorest selectivities to C_{3n} products. The wide variety of these products makes this material unsuitable as an oligomerization catalyst under the reaction conditions tested.

These observations validate the hypothesis that matching the framework heteroatom charge with that of the exchanged ion can reduce undesirable side reactions catalyzed by unexchanged, strong Brønsted acid sites, and suggest that the zincosilicates Ni-CIT-6 and Ni-Zn-MCM-41 may well be interesting materials for light olefin oligomerization.

The combined transfer hydrogenation/oligomerization catalyst system using these two new zincosilicate catalysts, while an interesting proposition, does not yet seem to be significantly effective. Ni-CIT-6 and Ni-Zn-MCM-41 are both capable of oligomerizing the propylene in the equimolar propylene/*n*-butane feed streams; however, the Ir-based transfer hydrogenation catalysts appear to be mostly inactive at converting butane to butenes in the gas phase under the given reaction conditions. While mesoporous carbon (one of the Ir-based homogeneous catalyst supports) on its own was capable of forming benzene and toluene from propylene, the conversions were so low at 180°C and 250°C that further study was not warranted.

Further investigation of the Ni-containing zincosilicate oligomerization catalysts was also conducted. Ni-CIT-6 and Ni-Zn-MCM-41 were tested with several different reactant feeds (1-butene and equimolar propylene/1-butene). Oligomerization products were observed in all cases, and, additionally, the tests with 1-butene formed a significant amount of other butene products via double-bond isomerization. An additional attempt to integrate *n*-butane into this reaction process was made by impregnating Ni-CIT-6 and Ni-Zn-MCM-41 with platinum. As platinum exhibits dehydrogenation activity at higher temperatures, it was postulated that some butenes may be formed and incorporated into the products via oligomerization with these Pt-Ni-CIT-6 and Pt-Ni-Zn-MCM-41 samples. Accordingly, the reactions were conducted at 400°C to enhance activity of the Pt, but reactivity at this higher temperature only demonstrated simple propylene oligomerization products, along with some cracking products.

Aside from focus on the tandem catalysis reaction scheme for mixed alkane/alkene feeds, the potential of CIT-6 to form catalysts useful for other reactions was studied. Specifically, several additional divalent metals (Mn^{2+} , Co^{2+} , Cu^{2+} , and Zn^{2+}) were exchanged onto CIT-6, making use of the neutral-pH exchange procedure discovered through this thesis work and first mentioned in Chapter 2. These materials were then tested using the propylene oligomerization reaction, with the same conditions as used for Ni-CIT-6. Only Co-CIT-6 was capable of oligomerizing propylene, but the other transition-metal catalysts may show promise in reactions such as deNO_x and acetic acid synthesis.

5.2 Recommended Future Work

If desired, the Ni-containing oligomerization catalysts may be further explored under other reaction conditions, although the work presented here effectively highlights the main features and differences of the four new materials synthesized. The ability of Ni-CIT-6 to perform oligomerization of both propylene and 1-butene, both isolated and in the presence of other alkanes and alkenes, suggests that it is could be useful for

oligomerizing light olefins, although the isomerization activity observed for 1-butene may produce undesired selectivity issues if specific product isomers are desired.

As for future work with the combined oligomerization/transfer hydrogenation system, focus is most required on the transfer hydrogenation catalyst to enhance its activity. While the oligomerization catalysts appear to be effective at forming dimers and trimers from propylene, the homogeneous transfer hydrogenation catalysts are not as effective in gas-phase reactions to form alkenes from alkanes. In the current system, the oligomerization catalyst far outperforms the deposited homogeneous catalysts' activity, indicating that substantial improvements to the homogeneous catalysts are required before such a system capable of integrating both alkanes and alkenes is feasible. If, however, the reaction apparatus was modified to operate at higher pressure of the reactant gases, the catalyst system could also be revisited, since higher reaction pressures may be more conducive to operation of the supported homogeneous catalysts on these reactants.

The formation of benzene and toluene over mesoporous carbon in the presence of both propylene and *n*-butane, however, is an interesting result. Follow-up work could include additional reaction testing to better understand the necessary temperatures and WHSV values to maximize yields of these products in this system.

Additionally, the other transition metal-exchanged CIT-6 samples may prove to be useful in several different types of reactions. The divalent cation exchange procedure developed in this work will prove invaluable in synthesizing these new catalysts, effectively opening up a new area of zincosilicate-based catalysts for interesting chemistry.

For example, Cu-CIT-6 and Co-CIT-6 could be useful for deNO_x reactions, as both of these cations have proven effective on other zeolite frameworks such as MFI and CHA.^{72, 73, 74, 75, 76, 77, 78, 79} Zn-CIT-6, Cu-CIT-6, and Co-CIT-6 may also be useful for the formation of acetic acid from methane and CO or CO₂, as described by Wu et al.,⁸⁰ Narsimhan et al.,⁸¹ and Huang et al.⁸²

Part II

Organic SDA-Free Materials for the Methanol-to-Olefins Reaction

Chapter 6

Introduction to Part II: The Methanol-to-Olefins (MTO) Reaction

This chapter introduces Part II of my thesis (work on the methanol-to-olefins reaction), with a literature review on the conversion of alcohols into olefinic products, as well as the molecular sieve catalysts commonly employed to perform this reaction. The MTO “hydrocarbon pool” mechanism is outlined, and commercialized catalysts are introduced. Project objectives are outlined, and previous work on the synthesis and modification of MTO catalysts within the Davis lab is explained, setting the stage for the remaining chapters of this thesis.

6.1 Background

Microporous solid acid catalysts such as aluminosilicates (zeolites)⁸⁵ and silicoaluminophosphates (SAPOs),^{86, 87} particularly those with eight-membered ring pores (8MRs) and a cage structure, are capable of converting methanol to light olefins, such as ethylene and propylene. The methanol-to-olefins (MTO) reaction is an industrially viable route for making light olefins from nonpetroleum feedstocks, e.g., natural gas, coal, and biomass,⁸⁸ and is of economic value in times of high petroleum feedstock prices.⁸⁹

In the proposed mechanism for the MTO reaction, the substituted aromatic molecules⁹⁰ create a “hydrocarbon pool”⁹¹ that is instrumental in forming light olefins from methanol via side chain reactions.⁹² These reactive aromatic intermediates (poly-

methylbenzenes) have kinetic diameters ranging from 6.2 Å for *o*-xylene to 7.5 Å for hexamethylbenzene; hence, it is believed that pores or cages of sufficient size and shape to allow formation of these intermediates are critical to the hydrocarbon pool mechanism in these solid acid catalysts.⁹³ Figure 6.1 shows this proposed overall reaction cycle, with the side-chain and paring reactions of carbocations in the hydrocarbon pool serving to form the desired olefin products.² The “Z-H” and “Z⁻” refer to the zeolite in its protonated or deprotonated forms, respectively. Once the initial aromatic species form, methanol continually reacts to methylate these aromatics, releasing water and producing light olefins. These carbocation intermediates are contained within the pore and cage structures of the microporous solid acid catalysts.

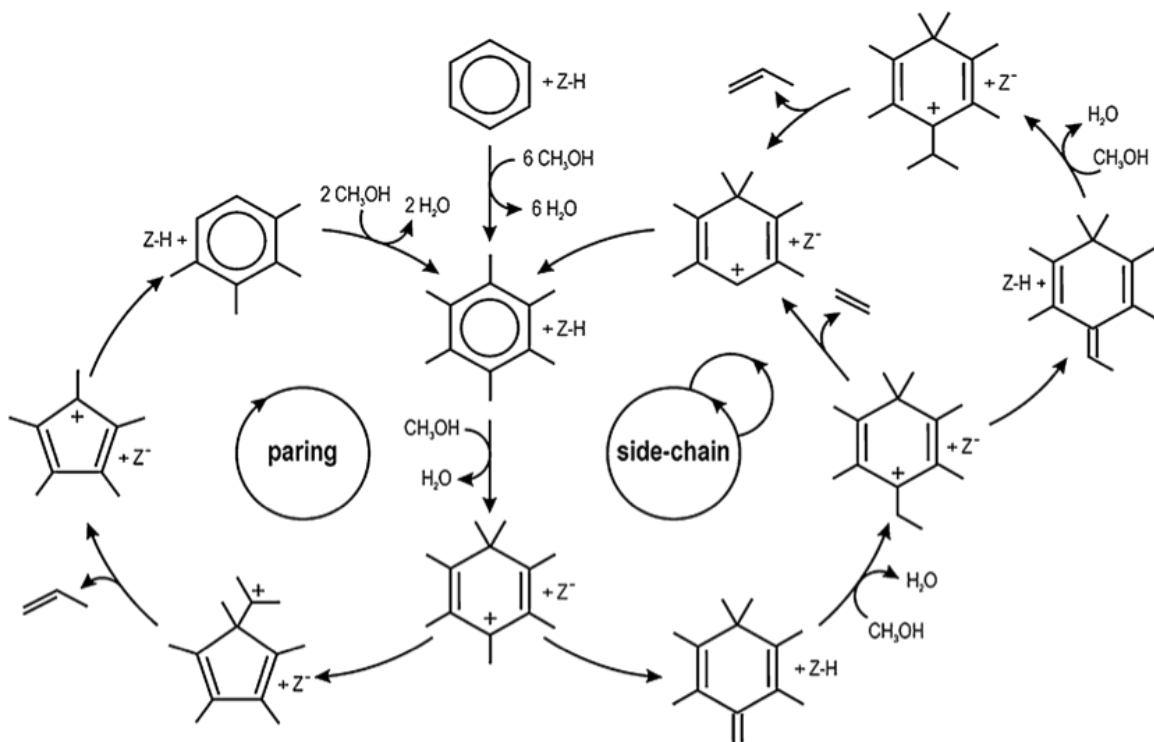


Figure 6.1: MTO hydrocarbon pool mechanism.²

Microporous materials with ten-membered-ring (10MR) or twelve-membered-ring (12MR) pores (such as MFI or *BEA, respectively) may additionally involve the olefin methylation/cracking cycle to form hydrocarbon products from methanol.⁸⁹ The pores of these 10MR and 12MR systems, however, typically cannot retain the aromatic

intermediates of the hydrocarbon pool mechanism, and thus they form significant heavier and/or aromatic products in addition to the desired light olefins.

Small-pore materials (8MRs) with cages, conversely, are more effective in retaining these reactive polymethylbenzene intermediates, and accordingly show increased selectivity to light olefins and other nonaromatic products.⁹⁴ For example, the chabazite (CHA) topology shown in Figure 6.2 consists of relatively large cavities ($8.35 \text{ \AA} \times 8.35 \text{ \AA} \times 8.23 \text{ \AA}$) that are accessible through 8MR pore openings ($3.8 \text{ \AA} \times 3.8 \text{ \AA}$).⁹⁵ Small linear molecules (alcohols and linear alkenes) may diffuse through these 8MR pores; however, the larger branched and aromatic compounds, including the methylated benzene intermediates,^{96, 97} can only form in these cages where they remain trapped. While within the cages, these aromatics react with methanol to form light olefins as part of the reaction cycle shown previously in Figure 6.1.

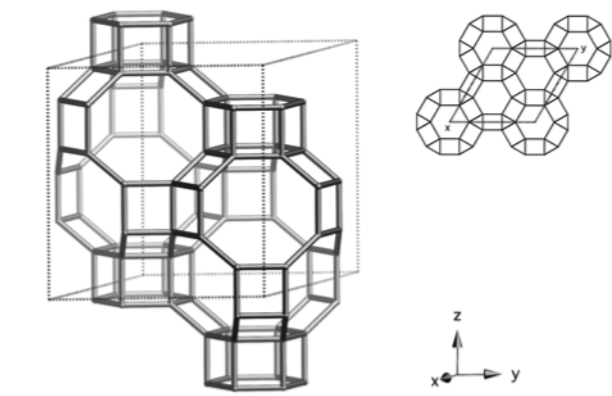


Figure 6.2: CHA cage structure.³

SAPO-34, discovered at Union Carbide (now UOP) in 1984,^{98, 99} is one such 8MR SAPO molecular sieve with CHA framework topology that is preferred for the MTO reaction.^{100, 101} Commercial MTO plants in China currently employ this catalyst, which can exhibit combined ethylene and propylene selectivities as high as 85-90%, depending on reaction conditions.¹⁰² A similar MTO catalyst, SSZ-13,⁷² is the synthetic aluminosilicate analog of SAPO-34. While SSZ-13 also has the CHA topology, it deactivates more rapidly than SAPO-34, in addition to initially producing a significant amount of C_2 - C_4 alkanes.^{103, 104} Aside from these CHA materials, several other

8MR framework topologies such as LEV, AFX, and RTH have also been shown to exhibit MTO activity.^{105, 106}

Typical reaction profiles for SSZ-13 and SAPO-34 are shown in Figure 6.3. Note the high selectivities to ethylene and propylene for each catalyst. With SSZ-13, propylene selectivity initially is higher, while ethylene selectivity slowly increases with increasing time on stream before finally becoming the most selective product at approximately 250 mins. Additionally, high selectivity to light alkanes (mostly propane) is observed initially, but selectivity to these transient products declines quickly. In SAPO-34, both ethylene and propylene are formed at stable selectivities, with no transient behavior observed while methanol conversion is at 100%.

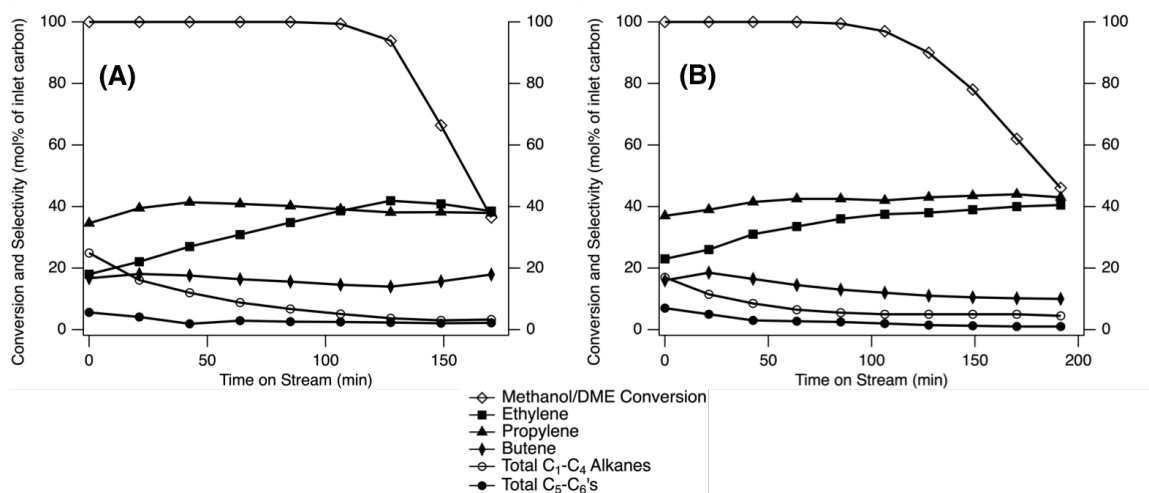


Figure 6.3: Typical reaction data for SSZ-13 (A) and SAPO-34 (B) at 400°C, 1.3 h⁻¹ WHSV (10% MeOH in inert), and atmospheric pressure.

6.2 Motivation and Strategy

While SSZ-13 and SAPO-34 are effective MTO catalysts, they both require the use of organic structure-directing agents (OSDAs) in their respective syntheses. Typically these are quaternary ammonium cations such as N,N,N-trimethyl-1-adamantylammonium hydroxide (shown in Figure 6.4), that are both toxic and expensive.¹⁰⁷ Such OSDAs in fact may be prohibitively expensive, restricting the ability of a material to be com-

mercialized, except in high value-added cases. Therefore, synthesis of such materials in the absence of these OSDAs could provide significant cost savings and improve the commercialization ability of catalysts for the MTO reaction.

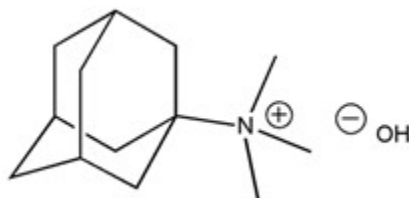


Figure 6.4: N,N,N-trimethyl-1-adamantylammonium hydroxide.

Chabazite, the naturally occurring mineral counterpart to SSZ-13, can easily be made synthetically using only an alkali cation (K^+ , specifically); however, the aluminum content is much higher than SSZ-13, with a typical Si/Al ratio of ~ 2.5 for chabazite, relative to Si/Al ~ 15 for SSZ-13. This higher aluminum content generally leads to faster catalyst deactivation in the MTO reaction, since the acid-site density is greater, causing more hydrocarbon species to react in close proximity within the same intra-crystalline spaces. As these carbocations react, they may deactivate the acid sites or block the pore system as larger polycyclic aromatic species form within the zeolite cages. In fact, an NH_4 -exchanged chabazite sample synthesized with K^+ (Si/Al = 2.4) will deactivate in less than 60 mins under the tested MTO reaction conditions, while SSZ-13 samples (Si/Al ~ 15) will continue to react and selectively form light olefins for hundreds of minutes on stream.

Aluminosilicates with reduced aluminum content (and thus a lower acid-site density) like SSZ-13 tend to have greater catalytic lifetimes and higher olefin selectivities,¹⁰⁸ possibly due to the fact that the reactive species are further apart and may thus deactivate more slowly without interfering with one another. Hence, a method to remove some aluminum from this easily prepared chabazite could alleviate the poor activity and longevity issues, forming an inexpensive, stable MTO catalyst.

One previously employed strategy to reduce the aluminum content of a zeolite is high-temperature steam treatment. The most well-known example of this dea-

lumination technique is its use in the conversion of zeolite Y (faujasite, a mineral with Si/Al of approximately 3) into USY, a stable, highly dealuminated (Si/Al = 50 or higher) catalyst used for catalytic cracking of heavy oils in refineries.¹⁰⁹ To test the transferability of this technique to other zeolite frameworks such as CHA, an SSZ-13 sample synthesized in the presence of an OSDA (Si/Al = 5) was ammonium exchanged, calcined, and steamed at 750°C for 24 h previously in the Davis lab. MTO reaction testing was then performed on this steamed sample, with comparison to the unsteamed H-SSZ-13 (Si/Al = 5) as a control. The results of these MTO reaction tests for the unsteamed and steamed samples are shown in Figures 6.5 and 6.6, respectively.

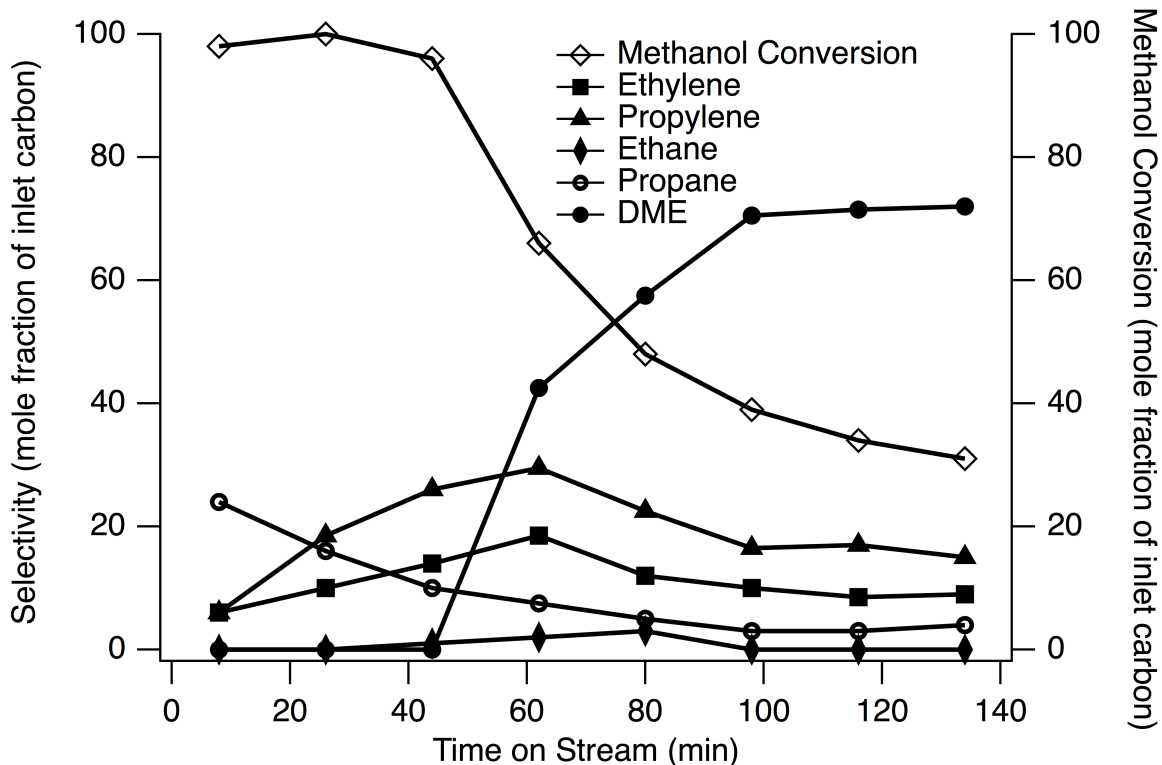


Figure 6.5: Unsteamed H-SSZ-13 sample (Si/Al = 5).

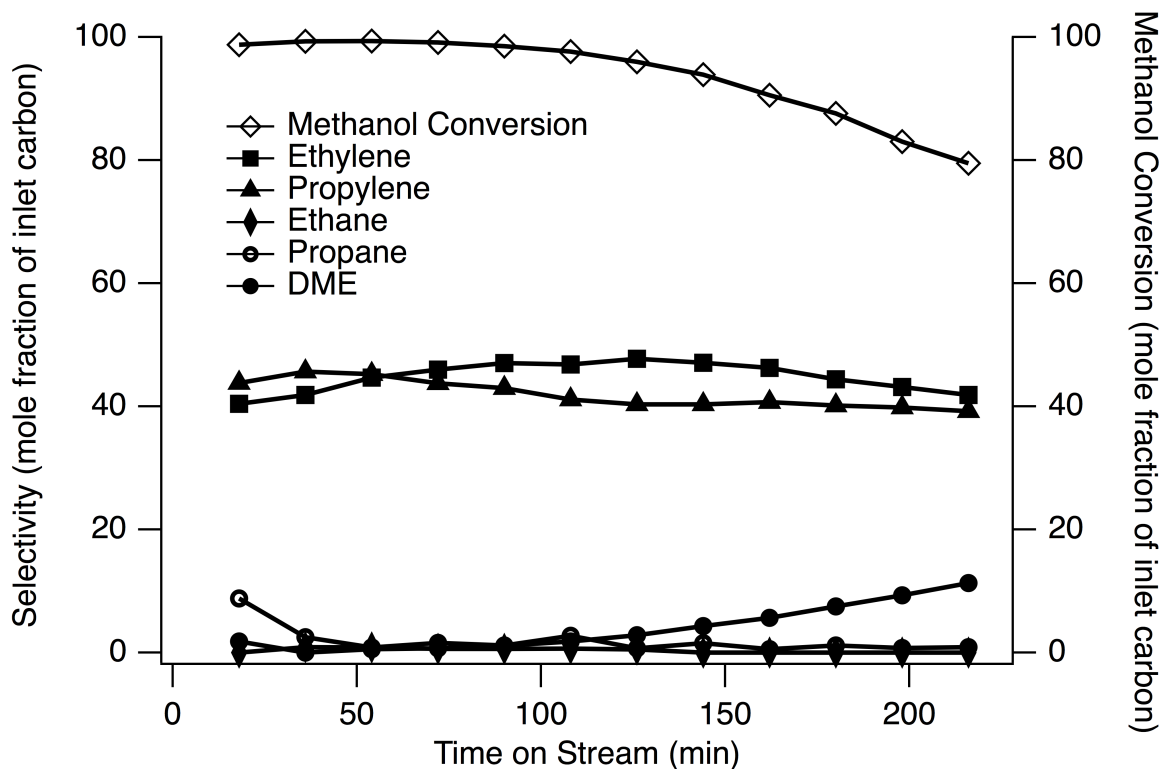


Figure 6.6: Steamed H-SSZ-13 sample (Si/Al = 5).

Clearly, the steamed SSZ-13 exhibited much greater stability in selectivity to light olefins, as well as greatly increased TOS before deactivation, suggesting that the steaming process may be an effective way to bring the catalytic activity of high-aluminum materials closer to that of lower-aluminum materials. Additionally, the activity of this steamed sample begins to resemble that of a traditional SSZ-13 sample, as shown in Figure 6.3A of the previous section. The steaming of the SSZ-13 sample also introduced mesoporosity to the zeolite framework, further improving reactant and product transport into and out of the 8MR pores of the crystalline system.

From this pair of MTO reaction results, we believe that the reduced transient behavior with respect to propane and light olefin selectivities observed from the steamed SSZ-13 sample could be brought about by a reduction of paired Al sites (two adjacent aluminum atoms bonded as $-Al-O-Si-O-Al-$ due to Loewenstein's rule,¹⁸ corresponding to two adjacent Brønsted acid sites) in the framework due to the dealumination of the steaming process, as mild steaming selectively removes one of the framework Al

atoms in paired Al framework sites.¹¹⁰ To further study this transient phenomenon and to test this paired-site hypothesis, a SAPO-34 sample and a series of SSZ-13 samples with varying Al content were synthesized, characterized, and reaction tested to compare their physical and chemical properties with MTO reactivity.

Additionally, while an SSZ-13 with an Si/Al = 5 has twice the aluminum content of a CHA sample with Si/Al = 2.5, the results of the steaming study at this lower Si/Al ratio suggested that steaming OSDA-free CHAs could effectively dealuminate them and improve their MTO activity. This result, along with the ability to synthesize CHA in the absence of OSDAs, suggests that a much less expensive path to selective MTO catalysts may be possible by combining the two techniques.

To test this hypothesis, we synthesized several CHA samples from the hydrothermal conversion of zeolite Y (FAU) following the method of Bourgoigne et al.¹¹¹ and steamed them under a range of conditions. The resulting steamed materials were then subjected to the MTO reaction test, with dramatic increases in light olefin selectivities and catalyst lifetime compared to their unsteamed counterparts. This simple OSDA-free synthesis and steaming treatment combination lends itself to trial on other framework topologies as well. To that end, zeolite RHO was also synthesized in the absence of OSDAs and subjected to high-temperature steam treatment. The results of these steaming studies are presented in the following two chapters.

6.3 Proposed Catalysts and Objectives

Before any steaming work with CHA or RHO catalysts was conducted, a SAPO-34 sample and a series of SSZ-13 samples with varied Al content were synthesized, characterized, and reaction tested. The SAPO-34 sample was ensured to have only “isolated” Si sites (no pairing of Si Brønsted acid sites) by both ²⁹Si MAS NMR and elemental analysis. Such a sample should then behave as has been observed previously, with steady light olefin selectivities and no high initial light alkane selectivity.

The SSZ-13 series consisted of five samples with increasing Si/Al ratios to investigate how Al content (and consequently, paired Al acid site concentrations) affected

MTO reactivity, namely the transient alkane formation noted earlier in Sections 6.1 and 6.2. These two materials series were intended to provide more information about how the acid site concentration and proximity (isolated for the SAPO-34 sample or paired vs. isolated for SSZ-13 samples) affected MTO reactivity, and hence to learn more about the MTO reaction mechanism in materials with the CHA topology. Previous work by Dahl et al. involved synthesis of two SAPO-34 samples and two chabazite samples to study how acid site concentration (simply high or low) affected catalyst deactivation, but this short study was significantly lacking in characterization for each sample and does not address the issue of paired acid sites, instead serving only to prove that materials with higher acid site densities tend to deactivate more rapidly in the MTO reaction, with no explanation as to why.¹⁰⁸ Mechanistic information gained from this proposed study with both SAPO-34 and a range of SSZ-13 samples could then be useful in the subsequent work with steaming of the OSDA-free CHA and RHO catalysts to improve light olefin yields.

For example, as mentioned previously, mild steaming tends to selectively attack one of the Al heteroatoms located at paired Al sites in zeolites, forming a stronger, isolated Brønsted acid site for the remaining heteroatom, which consequently can improve reactivity.¹¹⁰ If the SSZ-13 samples with lower concentrations of paired sites exhibited higher light olefin selectivity and longer times on stream before deactivation in the MTO reaction tests, these data would then suggest that removing paired sites from the zeolite framework for the higher Al-content zeolites (such as the OSDA-free CHA and RHO studied subsequently) by steaming them is indeed an effective way to cheaply improve MTO activity.

To determine paired site content (or lack thereof in SAPO-34 samples), a few techniques are available. For the SSZ-13 series, Cu^{2+} exchange at $\text{pH} = 5$, followed by subsequent elemental analysis, can titrate the paired site content in each sample from the Cu/Al ratio.¹¹² For SAPO-34 samples, a combination of ^{29}Si solid-state NMR and elemental analysis can show that Si atoms are in a single, isolated coordination environment (only one NMR resonance), and that Si has not substituted for Al atoms (another sign of isolated Si sites, as Al should be 0.50 of the T-atom content, with

anything less than 0.5 suggesting Si islanding is occurring).^{113, 114, 115, 116, 117}

To then produce such a simple, inexpensive MTO catalyst, CHA and RHO materials are synthesized using only alkali metal cations (K^+ and Cs^+ , respectively), in the absence of any OSDAs. These catalysts are then steamed and/or acid washed under a wide range of conditions to determine optimal steaming conditions for each material. Steam was produced for these steaming treatments by passing zero-grade air through a water saturator (bubbler) and then sending this moist air into a high-temperature tube furnace, where calcination boats containing the CHA or RHO materials were placed. Steaming times and temperatures could be controlled by the furnace heater controller. By combining the OSDA-free synthesis and steaming process, a stable MTO catalyst can be produced cheaply and efficiently.

An OSDA-free CHA initially underwent steaming to replicate the conditions tested with the initial steamed SSZ-13 sample. MTO reactivity of this steamed sample was then compared to that of the unsteamed material, with marked improvement in olefin selectivity and catalyst lifetime for the steamed sample. Steaming times, temperatures, and steam partial pressures were then varied to further investigate the steaming parameter space for CHA and RHO samples. While these two materials have been thoroughly explored, additional 8MR topologies that can be synthesized without OSDAs, such as LEV, KFI, and MER, have yet to be investigated and may provide interesting catalysts for a myriad of reactions in addition to the conversion of methanol into light olefins.

While the steaming procedure for each material is simple enough to perform, the steaming process itself brings about several physical changes to the zeolites (most notably the change of aluminum coordination environment and introduction of mesoporosity), so characterization techniques to better study and quantify the new properties are needed as well. For example, the dealumination will correspond with changes in the ^{27}Al SS NMR signal as aluminum converts from tetrahedral (framework) to penta- and hexacoordinate coordinations (extraframework). Further, destruction of Brønsted acid sites by removal of this framework aluminum will be reflected and quantified in the NH_3 temperature-programmed desorption (TPD) results. Similarly,

the bulk elemental Si/Al ratio will change for acid-washed samples as aluminum is removed from the materials via the washing process. The observed ^{29}Si SS NMR signal may change as well with the variations in silicon-aluminum connectivity environments caused as the samples undergo dealumination during steaming.

Additionally, the mesoporosity introduced through steaming can be characterized with Ar adsorption and by a new technique for the steamed 8MR systems: *i*-propylamine TPD. Ar adsorption is capable of showing finer detail in adsorption isotherms than N_2 ; hence, it should reveal finer details in pore size and distribution than possible with standard nitrogen adsorption isotherms. In TPD work, this new *i*-propylamine method is useful for two reasons: (i) it reacts at Brønsted sites to form ammonia and propylene, thus proving the reactivity of the acid site, and (ii) it is too large to fit within the 8MR pore structure, thus it can only react at Brønsted acid sites on the crystal surface or in mesoporous areas introduced by the steaming process. Thus, comparison of total Brønsted sites titrated with NH_3 TPD and those observed by *i*-propylamine TPD can provide valuable information about the relative accessibility of acid sites for the MTO mechanism. A higher fraction of accessible sites may lead to increased efficiency of each site (similar to the effect of smaller crystal size and mesoporosity on MTO activity, as has been studied previously), while those acid sites that are further within the intra-crystalline structure may not be as active due to diffusion limitations.^{94, 118, 119, 120, 121}

The methanol-to-olefins reaction reveals some interesting trends with varying steaming treatment for each framework type, and these analytical techniques are invaluable in tracing the sources of these reactivity differences to further reveal the critical parameters and properties of effective MTO catalysts.

Chapter 7

Effect of Heteroatom Concentration in SSZ-13 on the Methanol-to-Olefins Reaction

Work for this chapter was done in collaboration with Luke Harrison of Caltech, as well as Yu Liu, Jonathan Lunn, and Andrzej Malek of The Dow Chemical Company.

7.1 Introduction

The formation of light olefins from methanol provides a commercially feasible route to ethylene and propylene from nonpetroleum sources, such as natural gas, coal, and biomass.^{88, 89, 122, 123} Microporous aluminosilicate (zeolite)⁸⁵ and silicoaluminophosphate (SAPO)^{86, 87} solid acid catalysts are most commonly employed to perform this methanol-to-olefins (MTO) reaction.

Although several zeolite and SAPO framework structures with varying pore sizes and connectivity are capable of performing the MTO reaction (e.g., MFI), microporous materials with pore-and-cage systems, such as the chabazite (CHA) topology, are of particular interest.⁸⁹ The reaction proceeds via a “hydrocarbon pool” mechanism, with polymethylaromatic species remaining trapped in the cages as alcohols and linear alkenes flow into and out of these cages via the eight-membered ring (8MR) pores.^{96, 97, 104, 124, 113}

SAPO-34 and SSZ-13 are two molecular sieves commonly used for the MTO reac-

tion, both with this CHA topology. SAPO-34, discovered in 1984 at Union Carbide (now UOP),^{98, 99} has, in fact, been commercialized for use in the MTO reaction in China, with light olefin selectivities approaching 85-90%.^{100, 101, 102} SSZ-13, discovered by Zonas at Chevron in 1985, is the zeolite analog of SAPO-34, and can exhibit similar ethylene and propylene selectivities.⁷²

In each material, Brønsted acid sites catalyze the methanol-to-olefins transformation. However, despite the identical crystal structure and use of protons as the catalytic sites, the observed reactivities for SAPO-34 and SSZ-13 are quite different in the MTO reaction, both during reaction and deactivation.^{125, 108, 126, 127} When compared to SAPO-34, SSZ-13 typically exhibits differences in light olefin selectivities and higher alkane formation (primarily propane), the magnitudes of which depend on the reaction conditions used. Propane formation is typically associated with formation of aromatic species within the catalyst pore system.^{128, 129} Additionally, SSZ-13 samples with comparable acid site densities to SAPO-34 samples tend to deactivate faster, forming more (and larger) polycyclic species.^{126, 127}

This difference in reaction behavior is commonly attributed to disparities in acid site strength between the two materials,^{127, 130} with the stronger Brønsted acid sites in SSZ-13 leading to increased reaction rates and therefore increased coking and deactivation. However, acid site density has also been shown to play a role in deactivation time and product selectivity for each CHA-type catalyst.¹⁰⁸ Increasing Si/Al ratios in SSZ-13 samples has been shown to increase catalyst stability and reaction time before deactivation.¹⁰⁴

To date, the effect of heteroatom concentration (and accordingly, acid site density/proximity) in these two CHA-type materials has not been well studied to further explore this reactivity difference. In this work, we thus attempt to vary the heteroatom concentrations in these materials (SAPO-34 and SSZ-13) to investigate their effect on the selective conversion of methanol to light olefins. Specifically, we wish to investigate whether paired/adjacent Brønsted acid sites within the cages of these catalysts may contribute to this observed reactivity difference, particularly during the induction period of SSZ-13. In previous work with SAPO-34 and chabazite samples,

Dahl et al. briefly speculated at the possibility of two acid sites interacting within the same CHA cage, but we are not aware of any further follow-up work to test this hypothesis in detail.¹⁰⁸

First, we must compare how the requisite Brønsted acid sites may form in each CHA-type material. With SAPO-34, a cation is required to counterbalance the negative charge introduced when Si^{4+} replaces P^{5+} in the framework.⁹⁸ For SSZ-13, countercations are required to balance the substitution of Al^{3+} for Si^{4+} in the zeolite framework. In as-synthesized materials, these countercations are usually ammonium or alkali metal cations. After post-synthetic modifications (such as ammonium exchange and calcination), these cations are normally protons, thus giving Brønsted acidity to each material.

Typically in SAPO-34 samples, these Si sites (and thus the associated acid sites) will be isolated (surrounded only by 4 Al atoms via oxygen), but syntheses with high Si content may form “islands” of Si in the sample.¹¹³ Islanded Si sites in SAPO-34 form when, in addition to Si replacing P atoms, additional Si-O-Si pairs replace Al-O-P pairs in the framework (resulting in no net addition of framework charge).^{113, 114, 115, 116, 117} This additional substitution may lead to a large area of Si atoms bound only to other Si atoms via oxygen, while the Si atoms on the edge of this island (bound to other Al atoms via oxygen) retain their acidity. Si substitution in SAPO frameworks is limited by the inability of the Si-O-P bond structure to form.^{98, 114} Thus, the only bond structures formed through Si exchanging into the framework are Al-O-P, Si-O-Al, and Si-O-Si.

The type of Si sites present in SAPO-34 can be investigated both by solid-state ^{29}Si NMR and by elemental analysis. ^{29}Si NMR reveals the resonances of all Si sites, Si(4Al) through Si(0Al) (typically -91 to -110 ppm, respectively).^{113, 117} In SAPO-34 samples with Si islands (both P and Al substitutions) all Si resonances will be present, while samples with isolated Si sites (only Si(4Al) sites) will have only a single ^{29}Si NMR resonance from these lone P substitution sites at either -91 ppm or -94 ppm for as-made or calcined samples, respectively.

Elemental analysis can also give clues as to whether islanding is present or not

in SAPOs. Since isolated Si sites in SAPO-34 should only replace P atoms, the Al mole fraction (for T-atoms only) should be 0.5, with Si and P also summing to 0.5, making the (Si+P)/Al ratio equal to 1.0.¹¹³ As Si content increases, Al also begins to be replaced by Si, and the relative fractions change as the Al ratio decreases below 0.5 with the formation of these Si islands.

Similarly in the aluminosilicate SSZ-13, due to Loewenstein's rule,¹⁸ Al atoms cannot be immediately adjacent to one another (connected only via oxygen atoms), but they may be spaced by a single Si atom. This separation forms an -Al-O-Si-O-Al bond, which is known as a "paired site". As Si/Al ratio decreases in SSZ-13 (increasing Al content), the likelihood of paired Al sites occurring increases statistically, although there are no simple, direct methods such as solid-state NMR to measure the fraction of paired sites in aluminosilicates. Exchange of a divalent ion onto these SSZ-13 samples, with subsequent elemental analysis and comparison of the M^{2+}/Al ratio, can, however, serve as one technique to determine the paired site content (and Al sites close enough in the orientation of the crystal to support a divalent cation) by proxy. By synthesizing SSZ-13s in a wide range of Si/Al ratios, the Al content, and thus the probability of a paired site (or two Al sites close enough to accommodate a divalent ion due to orientation of the crystal framework), can be varied.

Thus, changing the relative amounts of Si for SAPO-34 and Al for SSZ-13 in the respective synthesis gels can vary the concentration and type of acid sites within the materials. Figure 7.1 shows diagrams of the isolated, islanded, and paired sites in these materials.

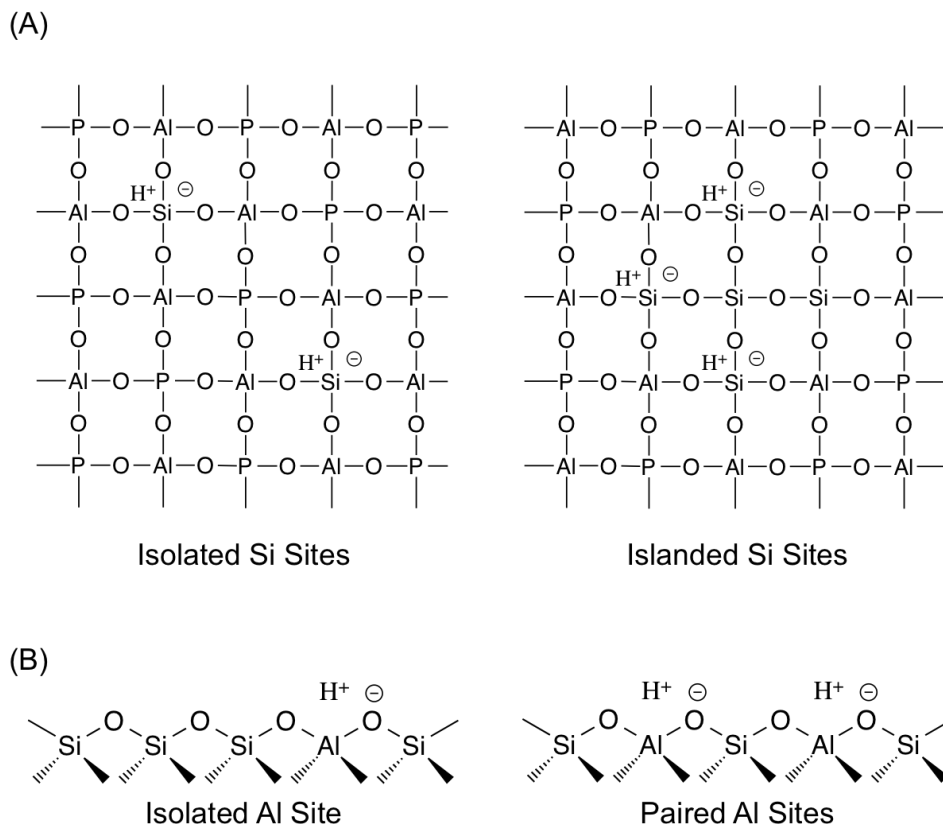


Figure 7.1: Isolated vs. islanded Si sites in SAPO-34 (A) and isolated vs. paired sites in SSZ-13 (B).

To then study the effect of heteroatom concentration (and accordingly, acid site density/proximity) on the methanol-to-olefins reaction in these two CHA-type materials, one SAPO-34 sample and five SSZ-13 samples with varying Al content are prepared to form samples with varying degrees of isolated acid sites. Once synthesized, these materials were calcined (SAPO-34) or calcined, ammonium exchanged, and calcined (SSZ-13s) to convert them to their proton forms. To prove the presence of only isolated Si sites (SAPO-34) or isolated and paired Al sites (SSZ-13), several techniques were employed. For the SAPO-34 material, solid-state ^{29}Si NMR and elemental analysis were performed. For SSZ-13 samples, acid sites were titrated using Cu^{2+} exchange as has been reported by Bates et al. to determine paired site content.¹¹² This exchange technique can also titrate two Al sites close enough to accommodate a divalent ion due to orientation of the crystal framework, even if they are

not simply paired, as shown previously.

All samples were also characterized via powder X-ray diffraction (PXRD), scanning electron microscopy/energy dispersive spectroscopy (SEM/EDS), thermogravimetric analysis (TGA), Ar adsorption, and NH₃ temperature-programmed desorption (TPD).

Each SAPO-34 or SSZ-13 sample then underwent MTO reaction testing in an attempt to discern any differences in reactivity and selectivity, particularly with respect to any transient behavior present for the SSZ-13s.

7.2 Experimental Section

7.2.1 Synthesis of Microporous Materials

7.2.1.1 Isolated Si SAPO-34 Material

The synthesis gel molar composition for the SAPO-34 sample (with only isolated Si sites) was 1 Al₂O₃ / 1 P₂O₅ / 0.075 SiO₂ / 3 TEAOH / 50 H₂O.¹¹³ The alumina source, Catapal B alumina, was dissolved in all the water required before adding Ludox HS-40 to the mixture. This solution was homogenized, and then the phosphoric acid (85wt% solution) was added slowly while stirring. Finally, the tetraethylammonium hydroxide (TEAOH) was added to the gel and stirred until homogeneous. The gel mixture was then poured into a Teflon-lined Parr reactor and heated at 200°C for 24 h.

7.2.1.2 SSZ-13 Materials

The desired synthesis gel molar compositions of the SSZ-13 samples was of the form 1 SiO₂ / x Al₂O₃ / 0.2 SDAOH / 0.2 NaOH / 40 H₂O, where SDAOH is N,N,N-trimethyl-1-adamantylammonium hydroxide.¹³¹ The value for x was varied from 0.0052 to 0.078, as shown in Table 7.2. In a typical synthesis, Mallinckrodt NaOH pellets were dissolved in water, and N,N,N-trimethyl-1-adamantylammonium hydroxide (Sachem, 25wt%) was added to this solution. Reheiss F2000 (55wt% Al₂O₃)

was then added as an alumina source, according to the desired value of x , and stirred together until the solution cleared. Finally, fumed silica (Cab-O-Sil M-5) was added, and the gel was stirred until homogeneous. The solution was placed in a Teflon-lined Parr reactor and heated in a rotating oven at 160°C for approximately 7 days.

7.2.1.3 Product Recovery

Aliquots of each material were taken periodically by first quenching the Parr reactors in water and then removing enough material for powder X-ray diffraction (PXRD). All materials were recovered by centrifugation. Once the syntheses were completed, each material was washed three times with water and once with acetone before drying in air overnight at 100°C.

7.2.2 Calcination and Ammonium Exchange

All materials were calcined in flowing breathing-grade air in a Nabertherm DKN400 muffle furnace. Materials were initially heated to 150°C at a heating rate of 1°C/min and held for 3 h before being heated to 580°C (again at a heating rate of 1°C/min) and held for 12 h to assure complete combustion of any remaining organic structure directing agents.

The calcined SSZ-13 materials were then converted to the ammonium form by ion exchanging them three times with 1 M aqueous NH_4NO_3 solution at 90°C for 2 h. The solid product from each exchange was again recovered by centrifugation, washed with water and acetone, and dried overnight at 100°C. These SSZ-13 samples were then calcined using the method described above to convert them to the proton form.

7.2.3 Characterization

PXRD patterns were obtained with a Rigaku MiniFlex II instrument using Cu $K\alpha$ radiation ($\lambda=1.54184 \text{ \AA}$) to determine structure type and purity. Crystallite sizes were calculated for each peak using the Scherrer equation with a shape factor of 0.9.¹³² The reported crystallite sizes are the average of the crystallite sizes calculated

from each peak. Morphology and elemental composition were also determined via scanning electron microscopy/energy dispersive spectroscopy (SEM/EDS) on a ZEISS 1550VP instrument equipped with an Oxford X-Max SDD energy dispersive X-ray spectrometer.

Thermogravimetric analysis (TGA) was conducted using a Netzsch STA-449C Jupiter instrument for the SAPO-34 sample and a Perkin Elmer STA-6000 instrument for the SSZ-13 materials. The SAPO-34 sample was ramped to 150°C at 1°C/min and held 3 h before ramping to 600°C (again at 1°C/min) followed by a final hold for 1 h at 600°C. SSZ-13 samples were heated to 900°C at a steady ramp rate of 10°C/min. Each sample exhibited two distinct mass loss regions, corresponding to water loss and organic loss, with organic mass loss reported as the second region (typically above 250°C).

To determine micropore volume (using the t-plot method), Ar adsorption was performed on each sample at 87.45 K with a Quantachrome Autosorb iQ adsorption instrument using a constant-dose method. Samples were off-gassed at 80°C for 1 h, followed by holds for 3 h at 120°C and 10 h at 350°C prior to adsorption measurements.

NH₃ temperature-programmed desorption (TPD) experiments were performed on the proton form of each material using an Altamira Instruments AMI-200 apparatus with an online Dymaxion Dycor mass spectrometer to quantify desorbed species. Once loaded into the quartz reactor tube, samples were heated to 150°C for 1 h at 10°C/min, followed by heating to 600°C for 1 h at 10°C/min in flowing argon (50 sccm) to remove any adsorbed species. Samples were then cooled to 160°C, and NH₃ was dosed onto each sample at a flow rate of 5 sccm in 50 sccm argon until no further NH₃ uptake was observed via the mass spectrometer. After a 2 h purge in flowing argon (50 sccm) to remove any physisorbed NH₃, the sample was heated to 600°C at rate of 10°C/min in 30 sccm argon while the mass spectrometer monitored desorbing products, namely $m/z = 17$ fragments corresponding to NH₃. The sample was held at 600°C for 2 h to ensure all species had fully desorbed.

Room temperature ²⁹Si NMR spectra were obtained on a Bruker Avance 500 MHz spectrometer with a triple resonance probehead using 4 mm ZrO₂ rotors. The ²⁹Si

MAS NMR spectra with high power proton decoupling were obtained at 99.33 MHz using a 4.0 μs $\pi/2$ pulse. To allow for experiments with shorter delay times, the samples were evacuated under heating, and O_2 was adsorbed into the materials. This allowed useable spectra to be obtained with a delay time of 10 s. The spinning speed was 8 kHz, and chemical shift was referenced to tetrakis(trimethylsilyl)silane (TKTMS).

To determine the number of paired sites present in SSZ-13 samples, the Cu^{2+} cation was exchanged onto each sample, and the resulting copper content (Cu/Al ratio) of each sample was determined via SEM/EDS. Copper cation exchange was performed by liquid-phase ion-exchange of a $\text{Cu}(\text{NO}_3)_2$ solution (0.01 M-0.001 M, approximately 100 mL of solution per 1 g of solids) at 25°C for 5 h. The solution pH was adjusted to 5 using a 0.1M NH_4OH solution to prevent formation and/or precipitation of $\text{Cu}(\text{OH})_n$ species. The materials were then separated from the $\text{Cu}(\text{NO}_3)_2$ solution via centrifugation, washed with distilled water and acetone, and dried.

7.2.4 MTO Reaction Testing

Catalyst evaluation was carried out in a fixed bed reactor at ambient pressure. 200 mg catalyst (35-60 mesh size) were loaded between layers of 35-60 mesh quartz chips in a $\frac{1}{4}$ " I.D. X 6" stainless steel reactor tube. Methanol flow rate was controlled by an ISCO pump (100DM, Teledyne Technologies Inc.) to achieve a weight-hourly space velocity (WHSV) of $\sim 1.3\text{h}^{-1}$. The methanol was diluted in 30 cc/min He to a concentration of 10%. The temperature in each experiment was set at 400°C and was controlled using a brass heating block around the reactor tube. Prior to reaction, the catalyst was pretreated at 500°C for 2 hours in He. Product evaluation was performed using a Siemens Maxum Process GC. Conversions and selectivities were computed on a carbon mole basis.

7.3 Results and Discussion

7.3.1 Characterization

Figure 7.2 contains the PXRD pattern for the SAPO-34 sample. The PXRD patterns of the proton-form SSZ-13 samples are shown in Figure 7.3. Additionally, for each material the elemental compositions (by SEM/EDS), organic content (by TGA), micropore volumes (Ar adsorption), and acid site counts (by NH_3 TPD) are shown in Table 7.1 for the SAPO-34 sample and Table 7.2 for SSZ-13 samples.

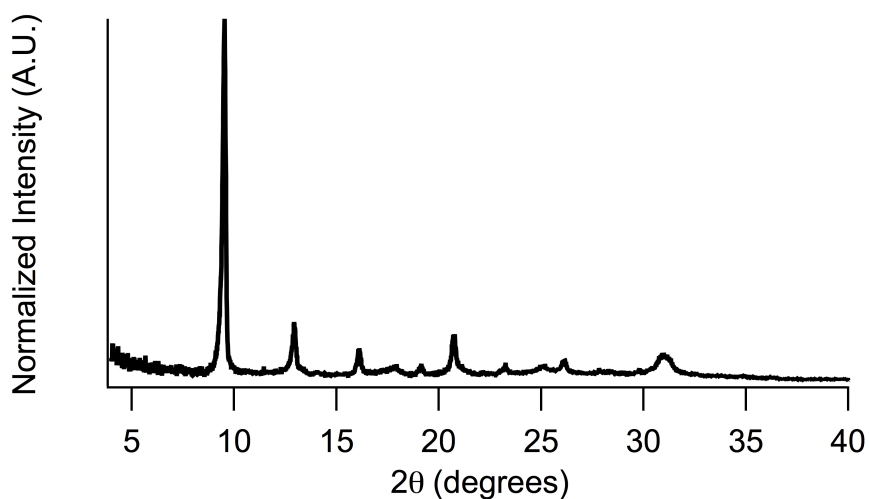


Figure 7.2: Powder XRD pattern of the proton form of the SAPO-34 sample with isolated Si sites.

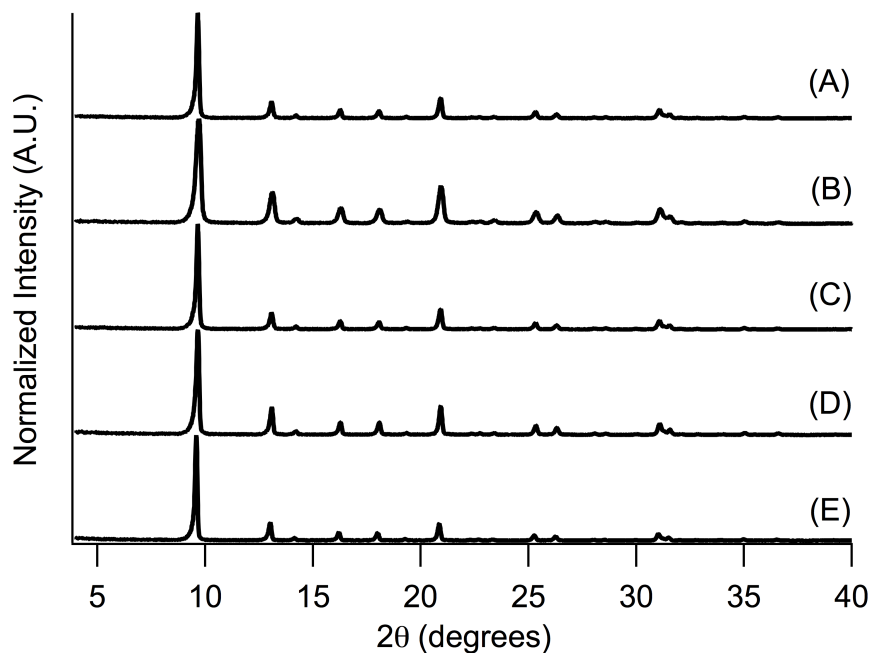


Figure 7.3: Powder XRD patterns of the proton forms of (A) SSZ-13A, (B) SSZ-13B, (C) SSZ-13C, (D) SSZ-13D, and (E) SSZ-13E.

As calculated by the Scherrer equation and shown in Table 7.2, the SSZ-13 samples have primary crystallite sizes increasing from 0.025 μm to 0.058 μm as Si/Al increases from 4.7 to 54.5 for samples SSZ-13A through SSZ-13E, respectively. Table 7.1 shows the average primary crystallite size for the SAPO-34 sample is similar to that of the lower Si/Al SSZ-13 samples.

Similarly, organic mass losses determined by TGA reveal a trend for the SSZ-13 samples with organic mass loss increasing from 12.6% to 23.3% as Si/Al ratio increases, while the SAPO-34 sample again is similar to the lower Si/Al SSZ-13 samples at approximately 15% organic mass loss.

Micropore volumes for both the SAPO-34 and SSZ-13 samples as determined by Ar adsorption and the t-plot method are consistent with the CHA topology.

The NH_3 TPDs reveal that as Si/Al increases for each SSZ-13 material, the Brønsted acid site count decreases, corresponding to the reduced aluminum content in each sample and in general agreement with the elemental Si/Al ratios determined.

Material	Synthesis Gel SiO_2 x Value	Si Mole Fraction	P Mole Fraction	Al Mole Fraction	(Si+P)/Al Molar Ratio	Primary Crystallite Size (μm)	Organic Mass Loss (TGA)	Micropore Volume (cc/g)	Acid Site Count by NH_3 (mmol/g)
SAPO-34	0.075	0.06	0.44	0.50	1.00	0.035	15.1%	0.21	0.63

Table 7.1: SAPO-34 characterization data.

Material	Synthesis Gel Al_2O_3 x Value	Si/Al Ratio	Primary Crystallite Size (μm)	Organic Mass Loss (TGA)	Micropore Volume (cc/g)	Acid Site Density by NH_3 (mmol/g)	Theoretical Acid Site Density (mmol/g)	Cu/Al Molar Ratio
SSZ-13A	0.078	4.7	0.025	12.6%	–	0.65	2.19	0.19
SSZ-13B	0.026	17.0	0.034	19.6%	–	0.49	0.69	0.08
SSZ-13C	0.0156	21.2	0.049	21.9%	0.23	0.47	0.57	0.06
SSZ-13D	0.0078	45.9	0.055	22.5%	–	0.26	0.27	0.03
SSZ-13E	0.0052	54.5	0.058	23.3%	0.21	0.18	0.22	–

Table 7.2: SSZ-13 characterization data.

For the SAPO-34 sample, NH_3 TPD demonstrates that Brønsted acid sites are indeed present and in a density near that of the lower Si/Al SSZ-13 samples.

Further, the SAPO-34 sample contains only isolated Si sites, as shown by the single resonance observable from ^{29}Si solid-state NMR in Figure 7.4.

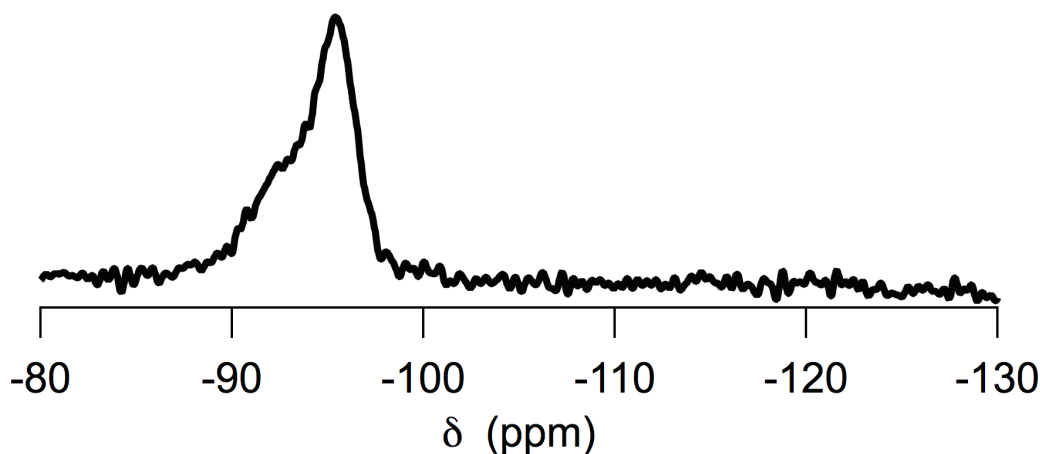


Figure 7.4: ^{29}Si NMR spectra for the calcined SAPO-34 sample.

Elemental analysis corroborates these ^{29}Si solid-state NMR results for the SAPO sample, as the sample has an Al mole fraction of exactly 0.5 and an (Si+P)/Al ratio of 1, consistent with Si substituting only for P in the SAPO framework and creating only isolated Si sites.

For the SSZ-13 samples, Si/Al ratios from 4.7-54.5 were obtained. Paired site fractional probabilities range from approximately 0.25 to 0.025 for this Si/Al ratio range, as computed by Bates et al. for SSZ-13 samples.¹¹² Copper exchange confirms these paired site values decrease with increasing Si/Al, as shown in Table 7.2. As Si/Al increases (Al content decreases), the fraction of paired Al sites decreases, with the corresponding fraction of isolated Al sites increasing. This range of values is sufficient to investigate a wide range of compositions and Al site proximities for the MTO reaction.

7.3.2 MTO Reaction Testing

Figure 7.5 shows the reaction profile for the SAPO-34 sample. Time on stream until deactivation began was approximately 100 mins, with relatively steady light olefin selectivities and a low initial alkane formation observed for this sample.

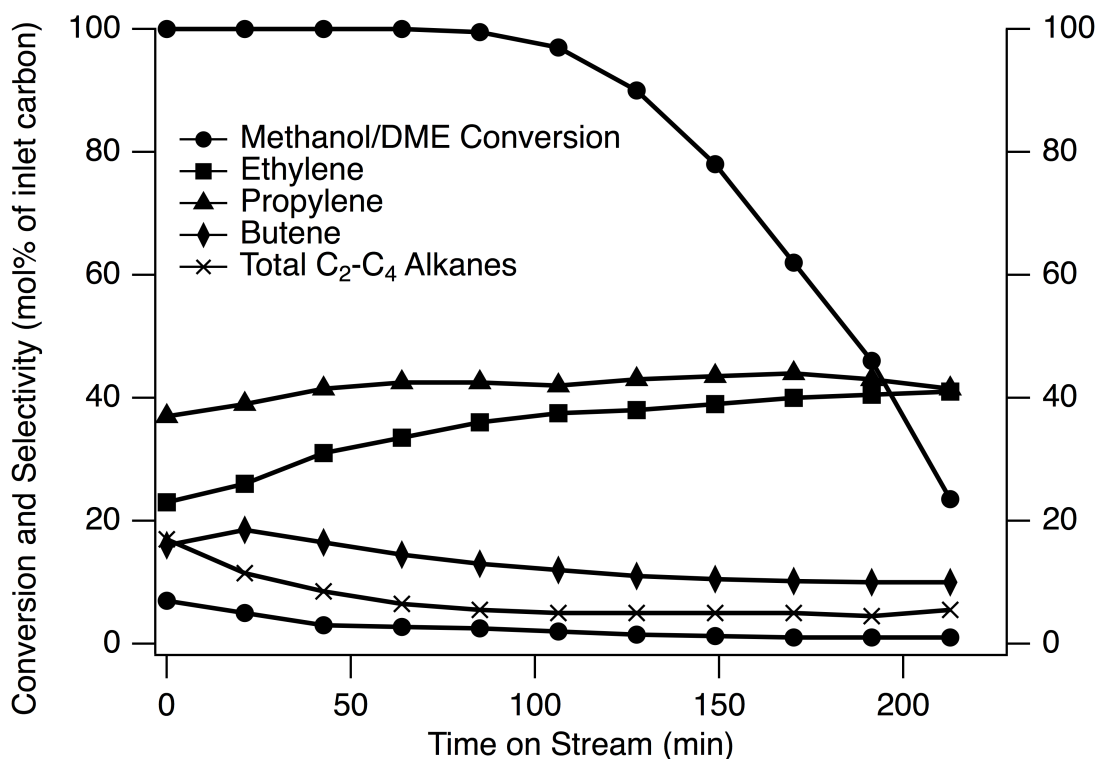


Figure 7.5: Representative MTO reaction data obtained at 400°C for the calcined SAPO-34.

Figure 7.6 illustrates representative time-on-stream reaction data obtained at 400°C for the ammonium-exchanged and calcined SSZ-13 samples. Each of the SSZ-13 catalysts is active in producing C₂-C₄ olefins when methanol conversion is at or near 100%. As time on stream increases, methanol conversion eventually decreases, with catalyst longevity differing for each sample. No significant trends in aggregate crystallite size were noted for the SSZ-13 samples. Catalyst lifetimes varied drastically with Si/Al ratio for the SSZ-13 samples, with higher Si/Al ratios having the longest lifetimes and most stable olefin selectivities, as also noted by Zhu et al.¹⁰⁴ and Dahl et al.¹⁰⁸

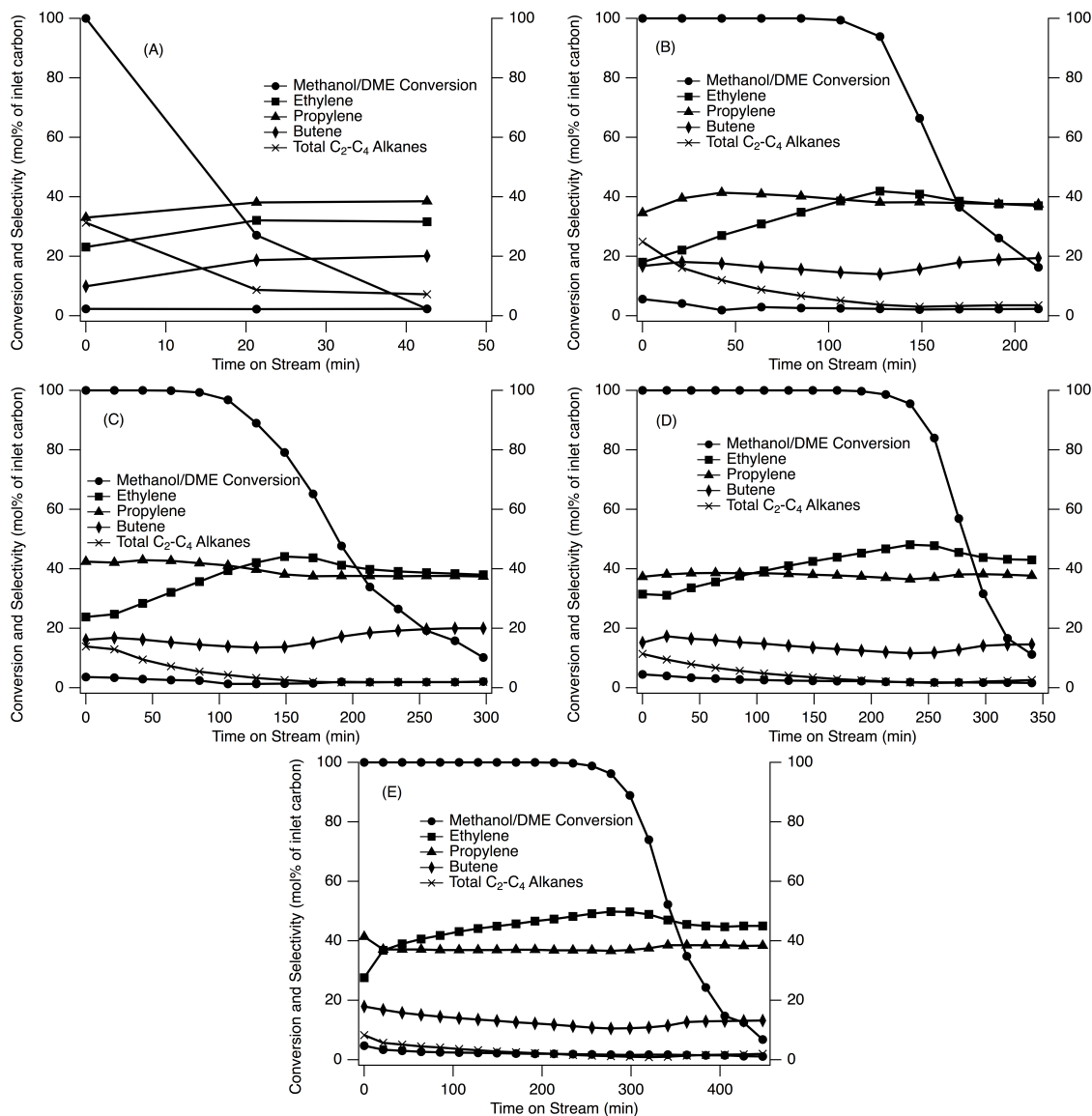


Figure 7.6: Representative MTO reaction data obtained at 400°C for the ammonium-exchanged and calcined: (A) SSZ-13A, (B) SSZ-13B, (C) SSZ-13C, (D) SSZ-13D, and (E) SSZ-13E.

Light alkanes, mainly propane, are observed among the products at the start of the reaction for all of the SSZ-13s, with selectivities to these alkanes decreasing with time on stream. Samples with lower Si/Al ratios (and consequently, higher paired site content from Table 7.2) exhibit higher initial selectivities to these transient light alkane products. Additionally, as Si/Al ratio increases for the SSZ-13 samples,

the crossover point where ethylene selectivity surpasses propylene selectivity occurs at decreasing TOS values. Both of these observations in the transient behavior of SSZ-13 suggest that mechanistically, the MTO reaction in CHA is being affected by the acid site concentration (and potentially proximity), thus producing the differing selectivities to alkanes and light olefins observed.

Interestingly, as Si/Al ratio increases, the SSZ-13 samples begin to resemble SAPO-34 in their reactivity. In fact, the activity of SSZ-13E very closely resembles that of the SAPO-34 sample, both in total light olefin selectivities and catalyst lifetime. The key difference observed is the higher ethylene selectivity in the SSZ-13 samples, compared to the higher propylene selectivity for the SAPO-34 sample shown here, although ethylene selectivity in SAPO-34s has been reported to increase relative to propylene with sufficient time on stream.^{108, 133} This similarity in reactivity between SSZ-13 and SAPO-34 could be due to the increasing isolation of Al sites in higher Si/Al SSZ-13s, analogous to the more-isolated Brønsted acid sites in the SAPO-34s.

In fact, if we plot both the initial propane selectivities from each MTO reaction and the Cu/Al ratios as a function of framework Si/Al ratio for each SSZ-13 sample, as shown in Figure 7.7, we observe that they each exhibit a similar decreasing trend with increasing framework Si/Al ratio. Additionally, Cu/Al ratios obtained for the SSZ-13 samples match well with the calculated theoretical values for paired framework Al sites, suggesting that we have fully titrated each paired Al site with Cu^{2+} in these samples.¹¹² Thus, it becomes apparent that higher Al content (and thus, higher paired Al site content) in the SSZ-13 materials has some significant effect on the observed transient behavior of these materials in the MTO reaction.

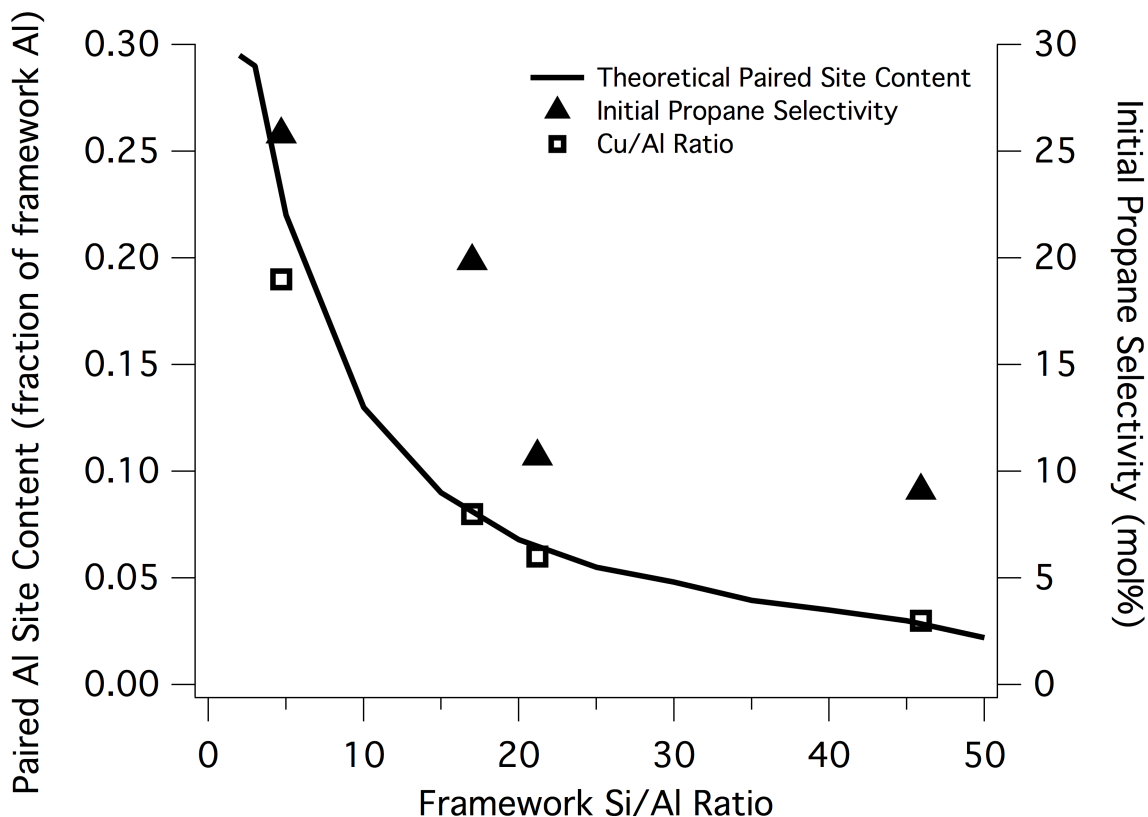


Figure 7.7: Cu/Al ratio, initial propane selectivity, and theoretical paired framework Al site content, as a function of framework Si/Al ratio for the SSZ-13 samples.

7.4 Summary

A SAPO-34 sample was synthesized with only isolated Si sites, as shown by ^{29}Si solid-state NMR and elemental analysis. When tested for the MTO reaction, this SAPO-34 sample exhibited relatively stable light olefin selectivities before beginning to deactivate at approximately 100 mins TOS.

SSZ-13 samples were also synthesized in a wide range of Si/Al ratios to vary the paired Al site content, with several trends appearing. As Si/Al increased, crystallite size and organic mass loss (by TGA) increased, while Brønsted acid site density (by NH_3 TPD) and paired Al site content (by Cu^{2+} exchange and SEM/EDS) decreased.

Furthermore, as the Si/Al ratio of the SSZ-13s varied, the MTO reactivity changed markedly. In these materials, samples with a higher probability of having paired acid

sites (lower Si/Al ratios) have very different MTO reactivity compared to materials with a high probability of having only isolated acid sites (higher Si/Al ratios). This is best illustrated in the quicker deactivation times and initial transient product selectivities (such as high initial propane selectivities) for the lower Si/Al ratio materials.

Increasing the Si/Al of the SSZ-13 samples reduced these transient selectivities. In fact, as the Si/Al ratios of the SSZ-13 samples increased, the MTO product selectivities began to resemble those observed for the SAPO-34 sample. This difference in reactivity among the SSZ-13 samples could potentially be attributed to the decreasing paired Al site content as Si/Al ratio increases. When overlaid with the Cu/Al ratios of each SSZ-13 sample, the initial propane selectivities decreased in a similar fashion with increasing framework Si/Al ratio. Cu/Al ratios were also very near the calculated theoretical paired site values, suggesting good titration of paired Al sites in the SSZ-13 framework.

In conclusion, SAPO-34 appears to exhibit stable MTO reactivity due to its isolated Brønsted acid sites. As paired Brønsted site content is reduced in the SSZ-13 samples (increasing isolated site content), these samples begin to have more stable olefin selectivities and on-stream behavior, similar to the SAPO-34 sample with isolated acid sites. Hence, to form an MTO catalyst with stable light olefin selectivities and with lower initial alkane formation (MTO behavior similar to the commercial SAPO-34 catalyst), it seems that isolated Brønsted acid sites are preferable. This also suggests that steaming low Si/Al materials (to selectively reduce paired acid sites) will be effective in increasing the catalytic lifetime and olefin selectivity of these materials. Further investigation of catalyst steaming is then outlined in the subsequent chapters.

As follow-up to this investigation, detailed hydrocarbon analysis of the coke species present on each spent catalyst in this study is underway currently at The Dow Chemical Company. Identification and quantification of these hydrocarbon species can then help provide more mechanistic details for deactivation pathways based on this paired site observation.

Chapter 8

Post-Synthetic Treatments on CHA and RHO to Enhance Methanol-to-Olefins Activity¹

Work for this chapter was done in collaboration with Lucy Ji.

In this chapter, the techniques of steaming and subsequently acid washing high-aluminum OSDA-free zeolite samples (CHA and RHO) are explored as a means to increase olefin selectivity and catalyst lifetime. New analytical techniques (namely Ar adsorption and reactive TPD) are developed to study these steamed and acid-washed materials, primarily as methods to characterize the pore structure differences and quantify the types of acid sites present in each material. Additionally, conventional techniques such as powder X-ray diffraction, ²⁹Si and ²⁷Al SS NMR, and SEM/EDS are employed to learn more about the acid site environment and crystal structure of each sample. Differences in each material brought about via steaming are highlighted and explained.

8.1 Introduction

The methanol-to-olefins (MTO) reaction is an industrially viable route for making light olefins, ethylene and propylene, using feedstocks other than petroleum, e.g.,

¹Information contained in this chapter has been submitted as a manuscript to *ACS Catalysis* and is currently under revision before publication (Ji, Y.; Deimund, M.A.; Bhawe, Y.; Davis, M.E. Submitted to *ACS Catal.* 24 Feb. 2015).

natural gas, coal, and biomass.⁸⁸ The reaction can be carried out over solid acid catalysts such as aluminosilicate¹³⁴ and silicoaluminophosphate (SAPO)^{86, 87} molecular sieves. The industrial catalyst for the MTO reaction is SAPO-34,^{100, 101} a small-pore SAPO molecular sieve with the chabazite (CHA) framework topology, that is currently utilized in commercial MTO plants in China. Depending upon reaction conditions, SAPO-34 can convert methanol to ethylene and propylene at 85-90% selectivity.¹⁰² The high selectivity towards light olefins is attributed to the material's optimal acidity (acid site strength and density)¹²⁷ as well as the topology of the CHA framework,^{96, 135} consisting of relatively large cavities (8.35 Å x 8.35 Å x 8.23 Å) that are accessible through 8 membered ring (8MR) pore openings (3.8 Å x 3.8 Å).⁹⁵ Only small linear molecules (alcohols and linear alkenes) can diffuse through the 8MR pores, while larger branched and aromatic compounds, including methylated benzene intermediates,^{96, 97} remain trapped inside the cages.

Despite its success, SAPO-34 suffers the shortcoming of requiring the use of an organic structure-directing agent (OSDA) to crystallize. Aluminosilicates (zeolites) also catalyze the reaction, but synthesizing them at high Si/Al ratios that are desirable for catalytic applications typically requires the use of OSDAs as well. The high cost and environmental concerns associated with removal of the OSDA from the materials prior to use has generated considerable interest in developing OSDA-free synthesis methods. While the earliest synthetic zeolites were prepared in the absence of OSDAs, using only inorganic cations as the structure-directing species produces materials with high aluminum content ($\text{Si/Al} < 5$) and thus limited use, particularly in applications requiring solid acidity.

CHA-type zeolites can be prepared in the absence of OSDAs, but their Si/Al ratios are too low to be of use in reactions like MTO. However, it may be possible to remove aluminum from the framework through post-synthetic treatments, thereby modifying the acidity and catalytic behavior of the materials. Since CHA is an 8MR zeolite, the extracted aluminum cannot be removed from intact cages. However, if mesoporosity is formed during the dealumination, then it may be possible to extract the extra-framework aluminum via the larger pores. Here, we show that CHA-type

zeolites synthesized without OSDAs can be subjected to dealumination to provide active MTO catalysts. This strategy may enable the preparation of low cost MTO catalysts. Additionally, there are a number of other framework topologies that may be interesting catalysts for the MTO reaction that have yet to be evaluated because of their low Si/Al. The dealumination strategy provided here will allow for investigation of other framework types (we are currently exploring several other zeolites and the results will be reported at a later time).

SSZ-13⁷² is the synthetic aluminosilicate analog of SAPO-34 and can be synthesized over a wide range of Si/Al ratios using the N,N,N-trimethyl-1-adamantylammonium OSDA. While also active for converting methanol to olefins, SSZ-13 deactivates more rapidly than SAPO-34 and initially produces a significant amount of C₂-C₄ alkanes.^{103, 104} Recently, our research group showed that an SSZ-13 synthesized with high aluminum content (Si/Al = 5) could be dealuminated via steaming to obtain a catalyst with improved olefin selectivities and lifetime, comparable to that of an SSZ-13 with Si/Al = 15. Reaction data from this study is provided in the Appendix (Figures C.1 and C.2, with H-SAPO-34 data shown for comparison in Figure C.3). In a similar study, Cartlidge et al.¹³⁶ prepared CHA-type zeolites at Si/Al ratios of greater than 2.5 using the hexamethylenetetramine OSDA, dealuminated the samples by steam and acid treatments, and observed improved olefin selectivities.

Based on these results, we hypothesized that a dealumination strategy could be applied to aluminum-rich CHA-type zeolites prepared without the use of an OSDA to create a selective catalyst for converting methanol to light olefins. CHA-type zeolite is prepared from the hydrothermal conversion of zeolite Y (FAU) and then steamed at temperatures of 500°C, 600°C, or 700°C to partially extract the framework aluminum. CHA steamed at 600°C is additionally acid washed to remove the extra-framework aluminum.

Similarly, zeolite RHO, another aluminum-rich zeolite that could be prepared in the absence of an OSDA, also underwent steaming as a means of testing whether this steaming procedure was effective only for CHA, or for 8MR zeolites in general. RHO exhibited better hydrothermal stability than CHA, and thus was steamed at

temperatures of 600°C, 700°C, and 800°C to partially extract framework aluminum; however, the RHO framework collapsed during the subsequent acid-washing under the given conditions. Zeolites CHA and RHO exhibit similar but not identical trends in their responses to steam treatment.

The effects of the dealumination treatments on the solids are analyzed by powder X-ray diffraction (XRD), energy-dispersive X-ray spectroscopy (EDS), and Ar physisorption. Removal of aluminum from the zeolite framework is observed by ^{27}Al and ^{29}Si solid-state MAS NMR. The acid site densities of the samples were measured by temperature programmed desorption (TPD) using NH_3 and *i*-propylamine. NH_3 is able to titrate all Brønsted acid sites (both within and outside the crystal), while *i*-propylamine, being too large to fit inside intra-crystalline areas bounded by 8MRs, can only react with Brønsted acid sites on the crystal surface or within mesoporous regions introduced by steaming. The catalytic performance of the materials is evaluated by the use of the MTO reaction.

8.2 Experimental Section

8.2.1 CHA Synthesis

CHA-type zeolites were prepared from the hydrothermal conversion of zeolite Y (FAU) following the method of Bourgoigne et al.¹¹¹ In a typical synthesis, 238 mL of deionized water was mixed with 32.2 mL of 45wt% aqueous potassium hydroxide solution (Aldrich), to which 30 g of zeolite Y (Zeolyst, CBV712, $\text{SiO}_2/\text{Al}_2\text{O}_3 = 12$) was added. The mixture was shaken for about 30 s and heated in a sealed polypropylene vessel at 100°C for 4 days under static conditions. The solid product was recovered by centrifugation, washed with water and acetone, and dried overnight at 100°C. The as-synthesized product, which had potassium as the countercation (designated K-CHA), was ion-exchanged three times with 1 M aqueous ammonium nitrate solution at 90°C for 2 h at a ratio of 100 mL of liquid per gram of solid to obtain the NH_4^+ form (designated NH_4 -CHA).

8.2.2 RHO Synthesis

RHO-type zeolites were prepared according to the method of Robson described in the patent literature.¹³¹ A synthesis gel was prepared with molar composition $0.3 \text{ Na}_2\text{O} / 0.1 \text{ Al}_2\text{O}_3 / 1 \text{ SiO}_2 / 0.04 \text{ Cs}_2\text{O} / 8 \text{ H}_2\text{O}$ using Catapal B as the alumina source, Ludox HS-40 as the silica source, Mallinckrodt NaOH pellets as the NaOH source, and Aldrich 50wt% CsOH aqueous solution as the Cs source. In a typical synthesis, the alumina source was added to a solution containing NaOH and water. The mixture was heated at 110°C until the alumina was dissolved, forming a clear solution. The CsOH was then added to the solution, followed by addition of the silica source. The reaction mixture was covered and stirred for 72 h at room temperature before being transferred to a Teflon-lined autoclave and heated for 1-3 days at 100°C. The crystallized product was recovered by centrifugation, washed with water and acetone, and dried overnight at 100°C. The NH_4^+ form of the product was obtained via NH_4^+ exchange in the same manner as that described for CHA.

8.2.3 Steaming and Acid Washing Treatments

Table 8.1 provides a summary of the steaming and acid washing treatments for CHA. Steaming was conducted under atmospheric pressure in an MTI OTF-1200X horizontal tube furnace fitted with a 3" ID mullite tube. NH_4 -CHA samples (approximately 1.2 g in a typical experiment) were loaded in ceramic calcination boats and placed in the center of the tube furnace. The furnace was ramped at 1°C/min to the desired steaming temperature, held at temperature for 8 h, and then allowed to cool. The entire process was carried out under a flow of moist air created by bubbling zero-grade air at 50 cc/min through a heated water saturator (bubbler) upstream of the furnace. Samples were steamed at temperatures of 500°C, 600°C, and 700°C with the bubbler held at 80°C (water saturation pressure of 47.3 kPa), and the resulting CHA materials were designated CHA-S500B80, CHA-S600B80, and CHA-S700B80, respectively.

The effect of the partial pressure of steam on CHA was investigated by two additional steaming experiments at 600°C where the bubbler temperature was changed

to 60°C and 90°C (water saturation pressures of 19.9 kPa and 70.1 kPa, respectively). For each of the bubbler temperatures tested (60°C, 80°C, and 90°C), the air was approximately 50% saturated with water vapor. A dry calcination of NH₄-CHA was conducted in the same tube furnace for 8 h at 600°C (1°C/min ramp) under 50 cc/min of zero-grade air, and the product was designated CHA-C600. A portion of the CHA steamed at 600°C with the bubbler held at 80°C was additionally acid washed with 0.1 N aqueous hydrochloric acid at a liquid-to-solid ratio of 100:1 (w/w) for 2 h at 100°C in a sealed vessel. The product, designated CHA-S600B80A, was recovered by filtering, washed extensively with water, and dried overnight at 100°C.

Sample	Steaming Temp. ^a	Bubbler Temp.	Si/Al Bulk	Si/Al _T ^b	Acid Site Concentration by NH ₃ TPD [mmol/g]	Acid Site Concentration by <i>i</i> -propylamine TPD [mmol/g]
CHA-S500B80	500°C	80°C	2.4	11	1.07	0.24
CHA-S600B80	600°C	80°C	2.4	16	0.94	0.30
CHA-S600B80A	600°C	80°C	7.8	12	0.80	0.39
CHA-S700B80	700°C	80°C	2.3	17	0.72	0.20
CHA-S600B60	600°C	60°C	2.4	15	0.92	0.16
CHA-S600B90	600°C	90°C	2.5	16	0.84	0.29
CHA-C600	600°C	N/A	2.7	38	0.09	0.08

Table 8.1: Summary of steaming conditions, Si/Al ratios, and acid site concentrations for dealuminated CHA samples.

^a Furnace was held at temperature for 8 h for all samples

^b Calculated from ²⁷Al NMR

Similarly, the RHO materials were subjected to the same steam treatment, although it was determined that RHO samples were more resilient to higher steaming temperatures than CHA. Accordingly, RHO samples were steamed at the higher tem-

peratures of 600°C, 700°C, and 800°C with the bubbler held at 80°C (corresponding to a steam partial pressure of 47.3 kPa), and the resulting RHO materials were designated RHO-S600B80, RHO-S700B80, and RHO-S800B80, respectively. The effect of steam partial pressure on RHO was also investigated by two additional steaming experiments at 800°C where the bubbler temperature was changed to 60°C (steam partial pressure of 19.9 kPa) and 90°C (steam partial pressure of 70.1 kPa). A dry calcination of NH₄-RHO was also conducted in the same tube furnace for 8 h at 800°C (1°C/min ramp) under 50 cc/min of zero-grade air, and the product was designated RHO-C800. Acid washing work with steamed RHO is currently ongoing. Table 8.2 provides a summary of the steaming treatments for these RHO samples.

Sample	Steaming Temp. ^a	Bubbler Temp.	Si/Al Bulk	Si/Al _T ^b	Acid Site	Acid Site
					Concentration by NH ₃ TPD [mmol/g]	Concentration by <i>i</i> -propylamine TPD [mmol/g]
RHO-S600B80	600°C	80°C	3.2	25	0.30	0.28
RHO-S700B80	700°C	80°C	3.2	28	0.26	0.14
RHO-S800B60	800°C	60°C	3.1	39	0.28	0.14
RHO-S800B80	800°C	80°C	3.2	27	0.45	0.15
RHO-S800B90	800°C	90°C	3.1	32	0.30	0.22
RHO-C800	800°C	N/A	3.1	53	0.11	0.11

Table 8.2: Summary of steaming conditions, Si/Al ratios, and acid site concentrations for dealuminated RHO samples.

^a Furnace was held at temperature for 8 h for all samples

^b Calculated from ²⁷Al NMR

8.2.4 Characterization

Powder X-ray diffraction (XRD) patterns were obtained on a Rigaku MiniFlex II instrument with Cu K α radiation ($\lambda = 1.54184 \text{ \AA}$) at a sampling window of 0.01° and scan speed of $0.05^\circ/\text{min}$. Scanning electron microscopy/energy dispersive spectroscopy (SEM/EDS) was used to determine the morphology and bulk elemental composition of the materials and was conducted on a ZEISS 1550VP instrument equipped with an Oxford X-Max SDD energy dispersive X-ray spectrometer. Powder patterns were normalized to the highest intensity peak.

Solid-state ^{27}Al MAS NMR spectra were acquired on a Bruker AM 300 MHz spectrometer operated at 78.2 MHz using a 90° pulse length of $2 \mu\text{s}$ and a cycle delay time of 1 s. Samples were loaded in a 4 mm ZrO_2 rotor and spun at 12 kHz. Chemical shifts were referenced to 1 M aqueous aluminum nitrate solution. Solid-state ^{29}Si MAS NMR spectra were acquired on a Bruker Avance 200 MHz spectrometer operated at 39.78 MHz with ^1H decoupling. A 90° pulse length of $4 \mu\text{s}$ and a cycle delay time of 60 s was used for recording. Samples were loaded in a 7 mm ZrO_2 rotor and spun at 4 kHz, and chemical shifts were referenced to tetramethylsilane. Reported spectra are scaled to the same maximum intensity.

Ar physisorption was conducted on a Quantachrome Autosorb iQ instrument. Prior to adsorption measurements, samples were outgassed by heating the sample at $10^\circ\text{C}/\text{min}$ to 80°C , holding for 1 h, then heating at $10^\circ\text{C}/\text{min}$ to 120°C , holding for 3 h followed by heating at $10^\circ\text{C}/\text{min}$ to 350°C and holding for 10 h. Adsorption isotherms were collected using Ar at 87.45 K using the constant dose (quasi-equilibrium) method. Micropore volumes were obtained from the adsorption branch of the isotherms using the t-plot method ($0.1 < P/P_0 < 0.3$). Pore size analyses were obtained from the adsorption branches using the non-local density functional theory (NLDFT) model provided by Micromeritics (based on model of Ar at 87 K on a zeolite with cylindrical pores).

To quantify the number and accessibility of the Brønsted acid sites present, NH_3 and *i*-propylamine TPD were performed on each ammonium-exchanged, steamed

CHA and RHO sample. NH_3 TPD allows access to all acid sites both external to and within the 8MR pore system, while *i*-propylamine only accesses acid sites external to the 8MR pore system (and in areas of mesoporosity created by the steam treatment), as *i*-propylamine is too large to fit within the 8MR pores. When *i*-propylamine desorbs from a Brønsted acid site, it reacts with the site to form propylene and ammonia. This propylene desorption peak can be integrated to determine the number of Brønsted acid sites accessible to the sterically hindered *i*-propylamine.

The materials were pelletized, crushed, and sieved, with particles between 0.6 mm and 0.18 mm being retained and loaded between quartz wool beds in a continuous-flow quartz-tube reactor (part of an Altamira AMI-200 reactor). A thermocouple inserted directly into the bed monitored temperature, and a Dymaxion mass spectrometer monitored desorbing products. Once loaded, samples were heated to 150°C for 1 h at 10°C/min and then to 600°C for 1 h at 10°C/min in flowing helium (50 sccm) to remove any adsorbed species.

For NH_3 TPD, samples were then cooled to 160°C, and NH_3 was dosed onto each sample. After a 6 h purge in flowing helium (50 sccm) to remove any physisorbed NH_3 , the sample was heated to 600°C at rate of 10°C/min in 30 sccm helium while the mass spectrometer monitored desorbing products, namely $m/z = 17$ fragments corresponding to NH_3 . The sample was held at 600°C for 2 h to ensure all species had fully desorbed.

For *i*-propylamine TPD, after the initial heating to 600°C, samples were cooled to 50°C, and *i*-propylamine was dosed onto each sample by means of a vapor saturator. The sample was then purged in a flow of helium (50 sccm) for 6 h before heating to 600°C at 10°C/min, with the mass spectrometer monitoring the main propylene and NH_3 signals ($m/z = 41$ and 17, respectively) formed by the decomposition reaction of the *i*-propylamine at a Brønsted acid site in the sample. Acid site count was determined by integration of the propylene peak.

8.3 Results and Discussion

8.3.1 Characterization

Tables 8.1 and 8.2 show the results of the elemental analysis, Si/Al_T ratios, and TPD results (both NH₃ and *i*-propylamine) for the CHA and RHO samples, respectively. All samples before and after steaming have similar bulk Si/Al ratios, with the exception of the acid-washed chabazite, CHA-S600B80A, which had extracted alumina removed in the washing procedure. Si/Al_T ratios (determined from ²⁷Al NMR) show the amount of tetrahedrally coordinated aluminum in each sample. As this ratio increases, more aluminum is changing coordination and presumably being extracted from the zeolite framework. Acid-washing is effective in removing this extraframework aluminum, as demonstrated by CHA-S600B80A, which has a much higher bulk Si/Al (7.84 vs 2.38 for the steamed sample, CHA-S600B80) than the samples that were only steamed.

8.3.2 Effect of Steaming Temperature and Acid Washing for CHA

The powder XRD patterns of the as-synthesized NH₄-CHA and the CHA samples steamed at 500°C-700°C under the same steam partial pressure (47.3 kPa) are shown in Figure 8.1. These XRD data indicate that partial degradation of the structure takes place during steaming. The baseline signal increases relative to the peaks for the steamed samples, indicating the presence of amorphous material and a loss of crystallinity upon steaming. Increasing the steaming temperature, and thus the severity of steaming, results in increasingly greater structural degradation, with the 700°C steamed sample showing the greatest loss in crystallinity. Further, the XRD peaks are shifted to lower d-spacings for the steamed samples, which can be attributed to contractions of the unit cell due to extraction of framework aluminum. The bulk Si/Al ratios of the steamed samples (Table 8.1) are essentially the same as that of the starting CHA (Si/Al = 2.4), accommodating for minor deviations that are within

measurement error. Acid washing the 600°C steamed CHA sample results in additional degradation and produces an increase in the bulk Si/Al ratio from 2.4 to 7.8.

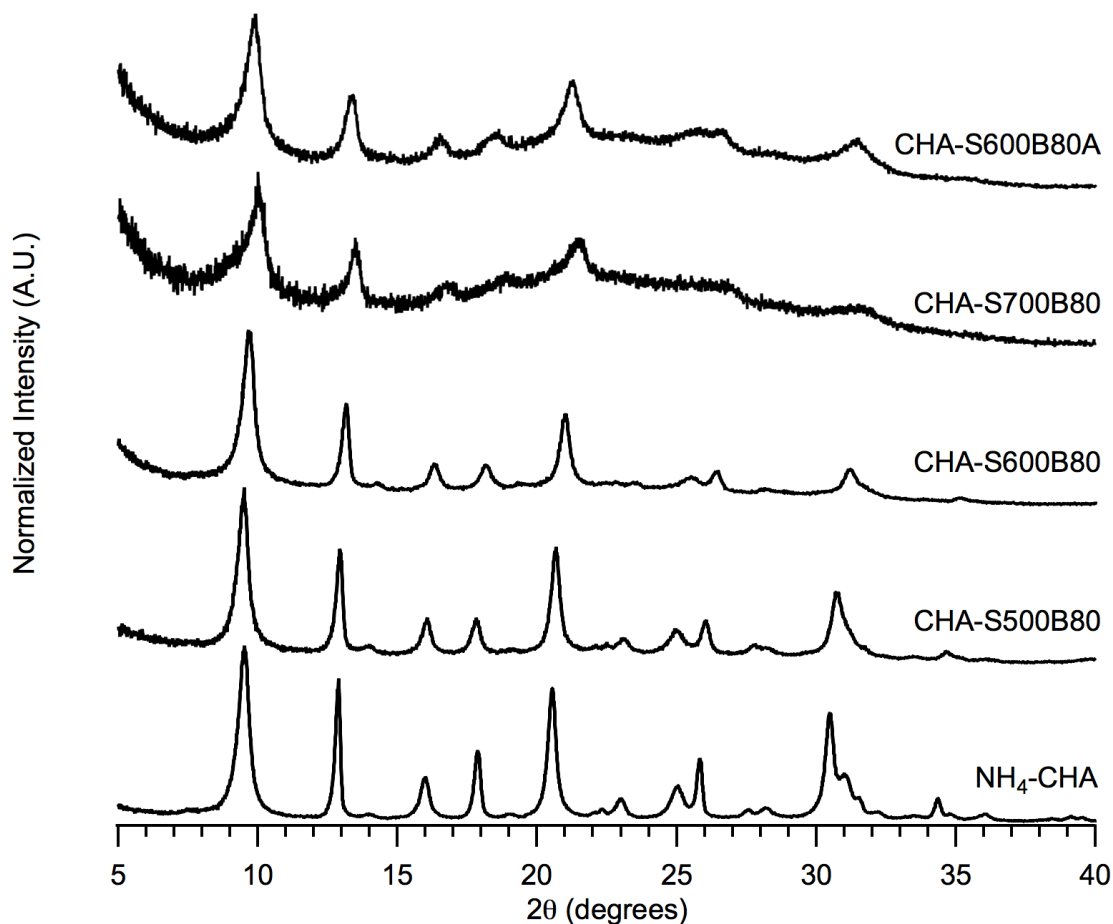


Figure 8.1: Powder XRD patterns of the as-synthesized CHA, CHA samples steamed at 500°C, 600°C, and 700°C at a steam partial pressure of 47.3 kPa, and the CHA sample steamed at 600°C and acid washed (bottom to top).

Indications that aluminum is extracted from the zeolite framework after the steam and acid treatments are provided by the ^{27}Al NMR spectra that are shown in Figure 8.2. The spectra of both the as-synthesized K-CHA (Figure C.4) and NH_4^+ -exchanged CHA show a single sharp resonance centered at approximately 55 ppm, corresponding to tetrahedral, framework aluminum. In addition to this resonance, the spectra of

the steamed samples show two additional resonances centered at approximately 30 ppm and 0 ppm, that are attributed to pentacoordinated and hexacoordinated aluminum species, respectively. As the steaming temperature is raised from 500°C to 700°C, an increasing fraction of aluminum is converted from tetrahedral to penta- and hexacoordination (indicated by increases in the intensities of the resonances centered at 30 ppm and 0 ppm relative to the resonance centered at 55 ppm). Accordingly, the silicon to tetrahedral aluminum (Si/Al_T) ratios (Table 8.1) calculated from the ^{27}Al NMR increase with increasing steaming temperature. The intensities of the resonances associated with penta- and hexacoordinated aluminum were reduced after acid washing the 600°C steamed CHA, with nearly complete removal of the pentacoordinated aluminum species. These NMR data for the acid treated sample are consistent with the elemental analyses in that the Si/Al increases after acid treatment. These results also suggest that the bulk of the higher-coordinated (above 4) aluminum is extra-framework.

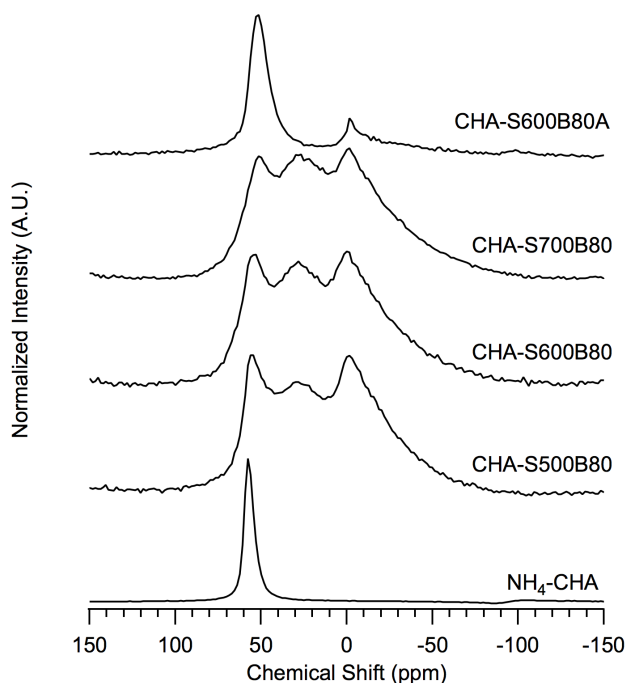


Figure 8.2: ^{27}Al MAS NMR spectra of the as-synthesized CHA, the CHA samples steamed at 500°C, 600°C, and 700°C at a steam partial pressure of 47.3 kPa, and the CHA sample steamed at 600°C and acid washed (bottom to top).

Further indication that the aluminum content of the zeolite framework changes after steaming is provided by the ^{29}Si NMR spectra (Figure 8.3) of the steamed CHA. The spectrum of the as-synthesized $\text{NH}_4\text{-CHA}$ shows four resonances centered at approximately -109 ppm, -104 ppm, -98 ppm, and -93 ppm, that can be attributed to Si(0Al), Si(1Al), Si(2Al), and Si(3Al) environments, respectively. The silicon environment changes to predominantly Si(0Al) and Si(1Al) after steaming, with the Si(0Al) resonance becoming the largest peak.

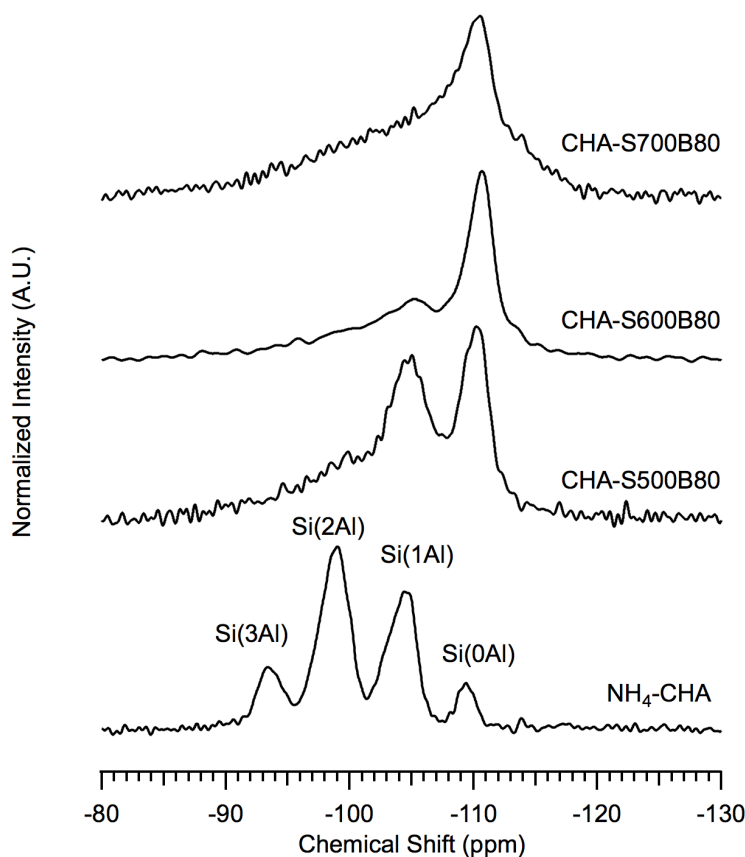


Figure 8.3: ^{29}Si MAS NMR spectra of the as-synthesized CHA, the CHA samples steamed at 500°C, 600°C, and 700°C at a steam partial pressure of 47.3 kPa, and the CHA sample steamed at 600°C and acid washed (bottom to top).

Figure 8.4A shows the full Ar physisorption isotherms of the as-synthesized $\text{NH}_4\text{-CHA}$ and steamed CHA samples along with the isotherm of a pure silicon dioxide sample (Si CHA) that is used as a control for illustrating the adsorption isotherm

for a pure (cation-free) CHA material. The steamed CHA samples show decreased micropore adsorption volumes (Table 8.3) compared to the NH_4 -CHA due to partial collapse of the framework. The micropore filling region is illustrated in Figure 8.1B that shows the adsorption branches of the isotherms (on a semi-logarithmic scale) normalized by the adsorption volume of Si CHA at $P/P_0 = 0.1$.

Acid washing the 600°C steamed CHA produces a significant increase in the adsorption volume that can be attributed to the removal of extra-framework aluminum localized within the channels and pores of the sample prior to acid leaching. This treatment, however, does not produce an increase in the micropore volume (Figure 8.4B).

At pressures above the micropore filling P/P_0 range, the adsorption isotherms of the steamed samples differ in shape from that of the NH_4 -CHA and Si CHA in that the adsorption volumes of the steamed samples increase continuously and at a higher rate per P/P_0 compared to the unsteamed samples. The NLDFT analyses of pore size distributions are illustrated in Figure 8.4C and show the cumulative pore volumes as a function of pore diameter. All of the samples show an initial steep increase in cumulative pore volume corresponding to micropore filling. While the NH_4 -CHA does not show any additional pore filling in pores larger than approximately 0.5 nm in diameter, the steamed samples show a second step increase in cumulative pore volume for pores between 2-4 nm in diameter. These data suggest that mesopores are created by the steam treatments.

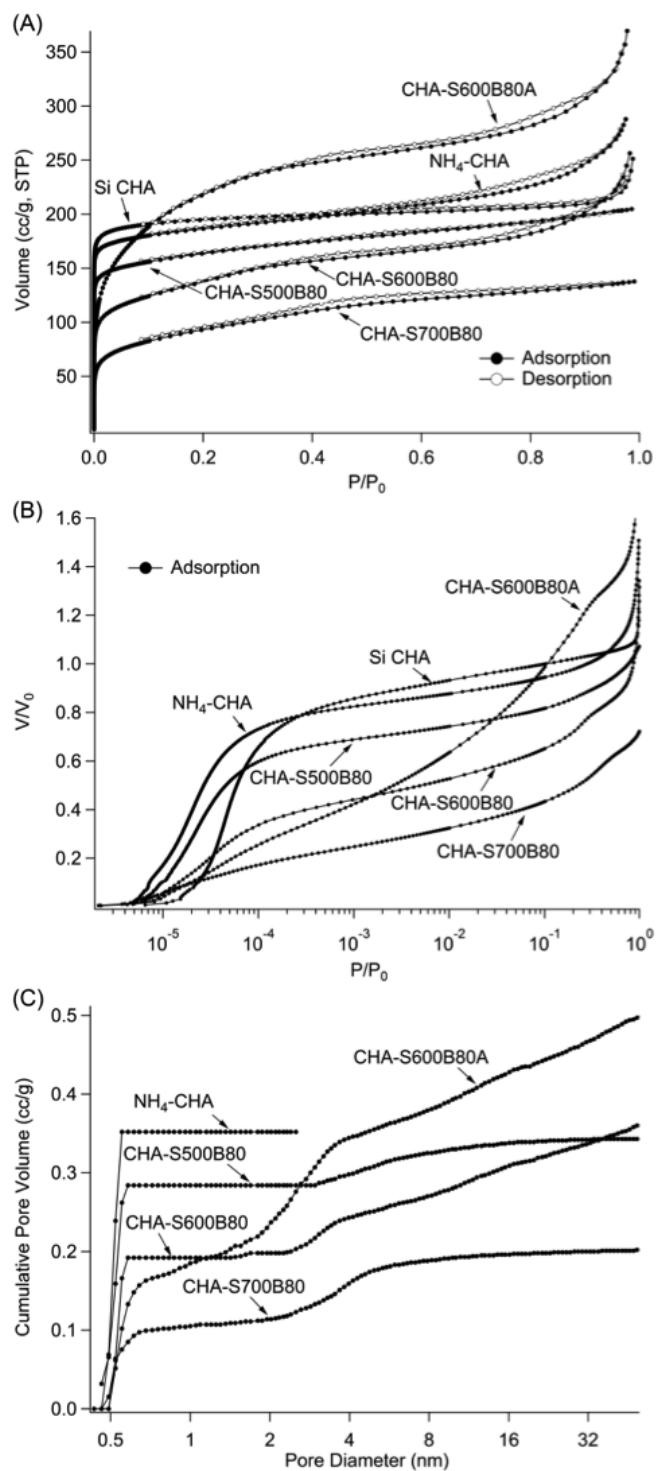


Figure 8.4: Ar physisorption isotherms of the as-synthesized and 500°C -700°C steamed CHA samples, and 600°C steamed and acid-washed CHA: (A) full isotherms, (B) normalized adsorption isotherms plotted on a semi-logarithmic scale, and (C) NLDFT cumulative pore volume vs. pore diameter.

Sample	Micropore Volume (cc/g)
Pure Si CHA	0.221
NH ₄ -CHA	0.190
CHA-S500B80	0.149
CHA-S600B80	0.077
CHA-S700B80	0.038
CHA-S600B60	0.047
CHA-S600B90	0.075

Table 8.3: Micropore volumes of the as-synthesized and steamed CHA samples.

Entries 1, 2, and 4 of Table 8.1 also demonstrate how steaming decreases the total number of Brønsted acid sites from 3.75 mmol/g for the unsteamed material (NH₄-CHA by NH₃ TPD) to 1.07 mmol/g, 0.94 mmol/g, and 0.72 mmol/g for the CHAs steamed at 500°C, 600°C, and 700°C, respectively. The number of Brønsted acid sites decreases as steaming temperature increases, consistent with increasing framework aluminum removal and degradation. These total acid site densities also correlate well with the predicted numbers based on the amount of tetrahedral aluminum remaining in each sample by ²⁷Al NMR.

The sites accessible by *i*-propylamine (presumably accessible via the mesopores introduced by steaming) exhibit a maximum with increasing steaming temperature at CHA-S600B80. This result suggests that the steaming process has an optimal temperature (600°C for CHA) before framework degradation becomes too severe and access to acid sites decreases. For reference, the unsteamed NH₄-CHA has 0.08 mmol/g of acid sites by *i*-propylamine TPD.

Acid washing of the steamed CHA-S600B80 sample (Entry 3 in Table 8.1) reveals the presence of fewer total Brønsted acid sites, but a higher fractional accessibility, as indicated by the reduced NH₃ and increased *i*-propylamine acid site counts, respectively, from the TPDs.

These TPD results are consistent with the other characterization data for the samples that suggest steaming converts tetrahedral framework Al to pentacoordinate

or hexacoordinate Al, consequently destroying Brønsted acid sites (as seen via ^{27}Al NMR and NH_3 TPD), and introduces mesoporosity (as seen via Ar adsorption and *i*-propylamine TPD). The samples steamed at 600°C demonstrate the best balance of access to Brønsted acid sites without excessive framework degradation.

8.3.3 Effect of Steaming Temperature for RHO

The powder XRD patterns of the as-synthesized NH_4 -RHO and the RHO samples steamed at 600°C-800°C under the same steam partial pressure (47.3 kPa) are shown in Figure 8.5. As with the CHA samples, these XRD data indicate that partial degradation of the structure takes place during steaming, albeit at higher temperatures than the CHA materials. Increasing the steaming temperature again results in increasingly greater structural degradation, with the 800°C steamed sample showing the greatest loss of crystallinity under these conditions.

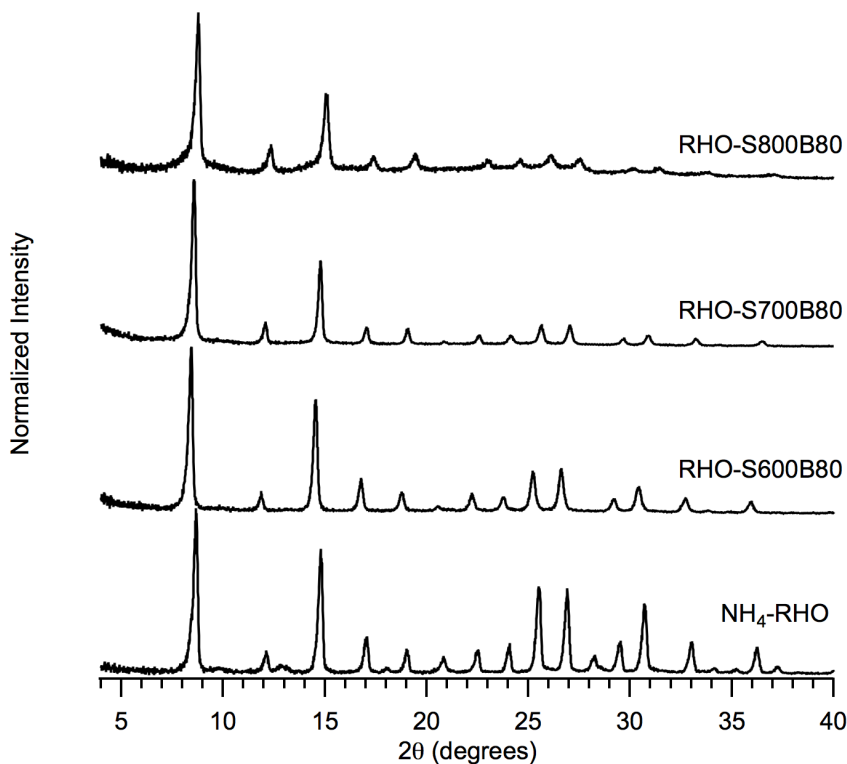


Figure 8.5: Powder XRD patterns of the as-synthesized RHO, RHO samples steamed at 600°C, 700°C, and 800°C at a steam partial pressure of 47.3 kPa (bottom to top).

The ^{27}Al NMR spectra shown in Figure 8.6 again confirm that aluminum is removed from the zeolite framework during the steam treatment, as with CHA. The spectrum of the NH_4^+ -exchanged RHO also shows a single sharp resonance centered at approximately 55 ppm, corresponding to tetrahedral, framework aluminum. The spectra of the steamed samples also show two additional resonances centered at approximately 30 ppm and 0 ppm, corresponding again to pentacoordinated and hexacoordinated aluminum species, respectively. As the steaming temperature is raised from 600°C to 800°C, more aluminum is converted from tetrahedral to penta- and hexacoordination (indicated by increases in the intensities of the resonances centered at 30 ppm and 0 ppm relative to the resonance centered at 55 ppm). Accordingly, the silicon to tetrahedral aluminum ($\text{Si}/\text{Al}_\text{T}$) ratios (Table 8.2) calculated from the ^{27}Al NMR increase with increasing steaming temperature.

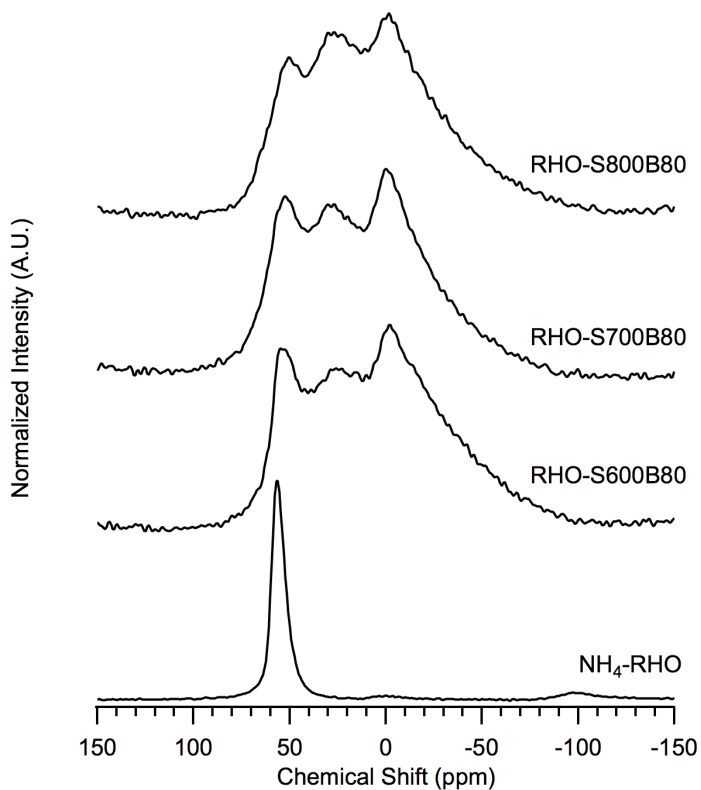


Figure 8.6: ^{27}Al MAS NMR spectra of the as-synthesized RHO and the RHO samples steamed at 600°C, 700°C, and 800°C at a steam partial pressure of 47.3 kPa (bottom to top).

Further indication that the aluminum content of the zeolite framework changes after steaming is provided by the ^{29}Si NMR spectra (Figure 8.7) of the steamed RHO. The spectrum of the as-synthesized $\text{NH}_4\text{-RHO}$ shows the same four resonances (centered at approximately -109 ppm, -104 ppm, -98 ppm, and -93 ppm) that can be attributed to Si(0Al), Si(1Al), Si(2Al), and Si(3Al) environments, respectively. The silicon environment changes to predominantly Si(0Al) and Si(1Al) after steaming, with the Si(0Al) resonance becoming the largest peak.

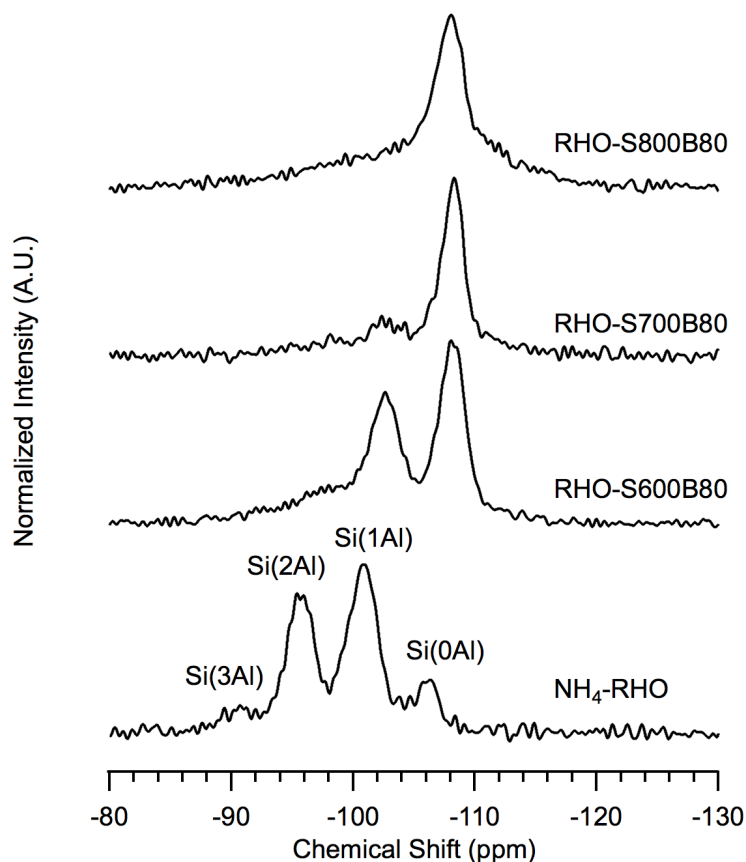


Figure 8.7: ^{29}Si MAS NMR spectra of the as-synthesized RHO and the RHO samples steamed at 600°C, 700°C, and 800°C at a steam partial pressure of 47.3 kPa (bottom to top).

Entries 1, 2, and 4 of Table 8.2 also demonstrate how steaming decreases the total number of Brønsted acid sites in RHO from 0.55 mmol/g for the unsteamed material ($\text{NH}_4\text{-RHO}$ by NH_3 TPD) to 0.30 mmol/g, 0.26 mmol/g, and 0.45 mmol/g

for the RHO samples steamed at 600°C, 700°C, and 800°C, respectively. As steaming temperature increases, the number of accessible Brønsted acid sites remains nearly constant and then increases, exhibiting a maximum at 800°C (RHO-S800B80). The acid sites titrated for this RHO-S800B80 sample are the closest to the theoretical value for the tetrahedral Al present (0.46 mmol/g for $\text{Si}/\text{Al}_T = 27.2$), while NH_3 TPD for the samples steamed at lower temperatures show far fewer Brønsted sites than are expected. This suggests that accessibility to the acid sites for the samples steamed at 600°C and 700°C may be restricted due to framework collapse.

The sites accessible by *i*-propylamine (presumably accessible via the mesopores introduced by steaming) exhibit the opposite behavior with increasing steaming temperature, with acid site counts decreasing as steaming temperature increases. The RHO-S800B80 sample has one of the lowest values for *i*-propylamine TPD, which could suggest that the micropore structure remains the most intact at this higher steaming temperature. Ar micropore analysis is needed to follow up on these results and provide confirmation. (For reference, the unsteamed NH_4 -RHO has 0.33 mmol/g of acid sites by *i*-propylamine TPD.)

As observed with CHA, these TPD results are consistent with the other characterization data for the samples that suggest steaming converts tetrahedral framework Al to pentacoordinate or hexacoordinate Al, consequently destroying Brønsted acid sites (as seen via ^{27}Al NMR and NH_3 TPD), causing framework collapse, and introducing mesoporosity (as seen via *i*-propylamine TPD) to the RHO samples.

8.3.4 Effect of Steam Partial Pressure for CHA

Figure 8.8 shows the XRD patterns of the samples steamed at 600°C with varying partial pressures of steam. The XRD patterns show that lowering the steam partial pressure results in increased amorphization, as indicated by an increasing baseline intensity relative to the peak intensities. Almost complete collapse of the structure was observed when NH_4 -CHA is calcined under dry air for 8 h at 600°C.

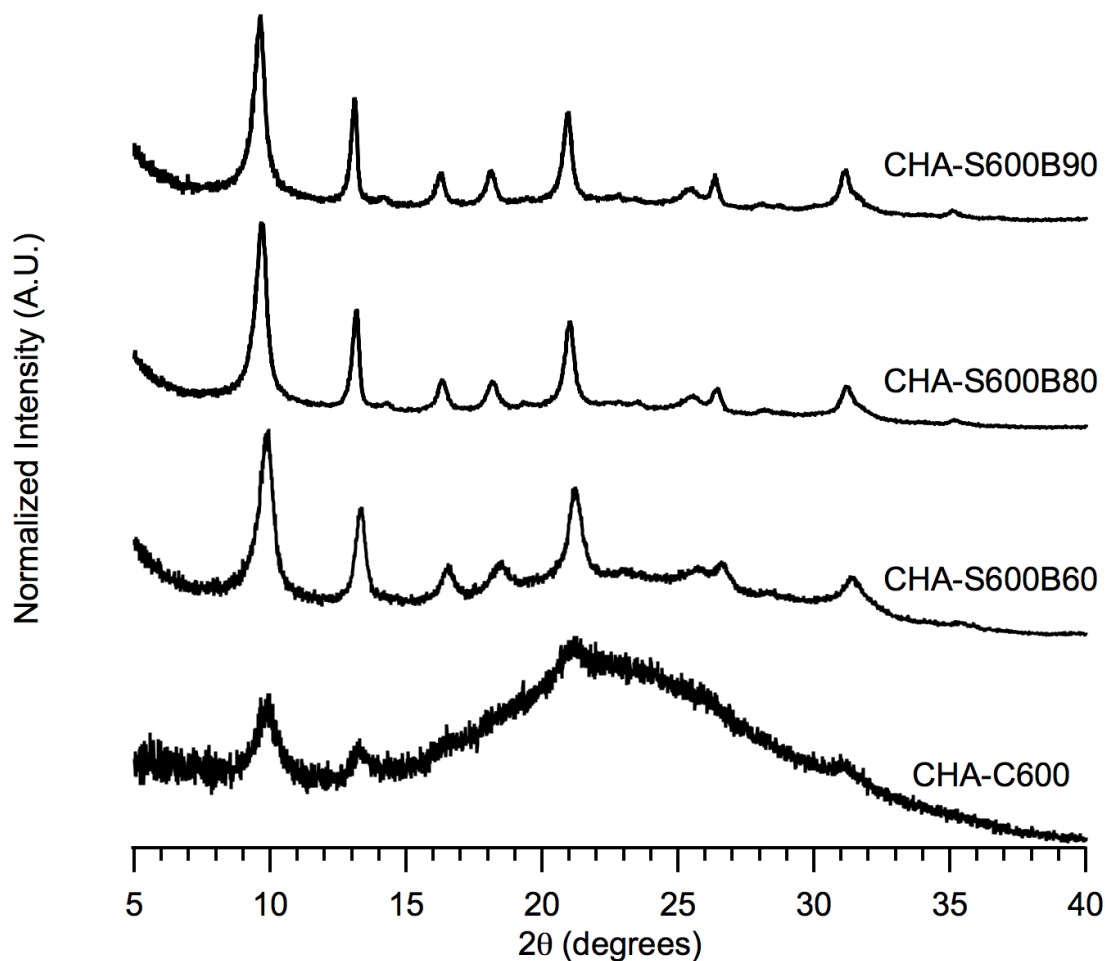


Figure 8.8: Powder XRD patterns of CHA samples steamed at 600°C with varying partial pressures of steam.

The ^{27}Al NMR spectra of the steamed samples (Figure 8.9), however, do not show significant differences in the relative intensities of the tetrahedral, pentacoordinated, and hexacoordinated aluminum signals, although the intensity of the tetrahedral aluminum signal relative to the higher coordinated aluminum was the lowest for the CHA calcined under dry conditions. ^{29}Si NMR spectra of the samples steamed under varying steam partial pressures are shown in Figure 8.10 and show differences in the silicon environments for the samples steamed under varying water vapor pressures.

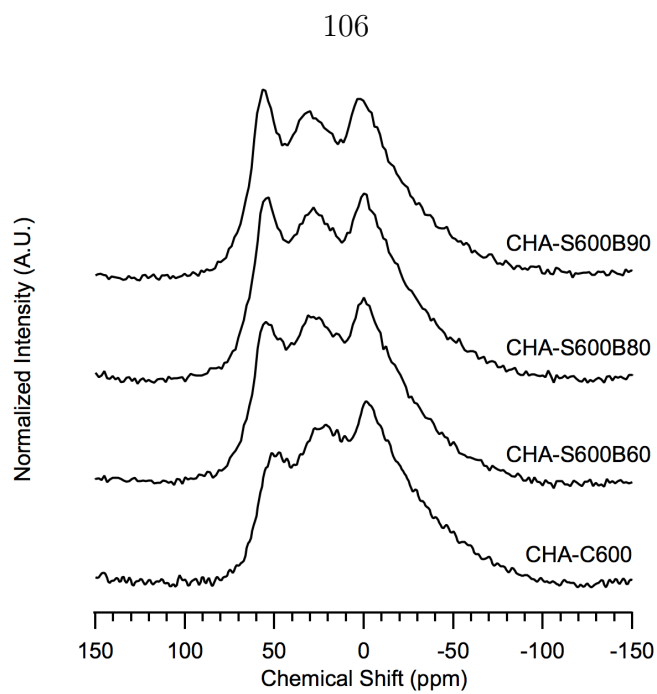


Figure 8.9: ^{27}Al MAS NMR spectra of CHA samples steamed at 600°C with varying partial pressures of steam.

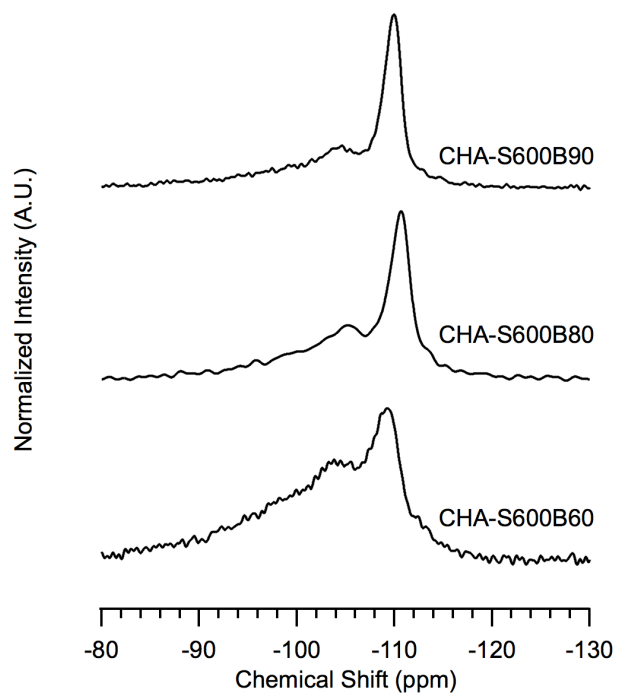


Figure 8.10: ^{29}Si MAS NMR spectra of CHA samples steamed at 600°C with varying partial pressures of steam.

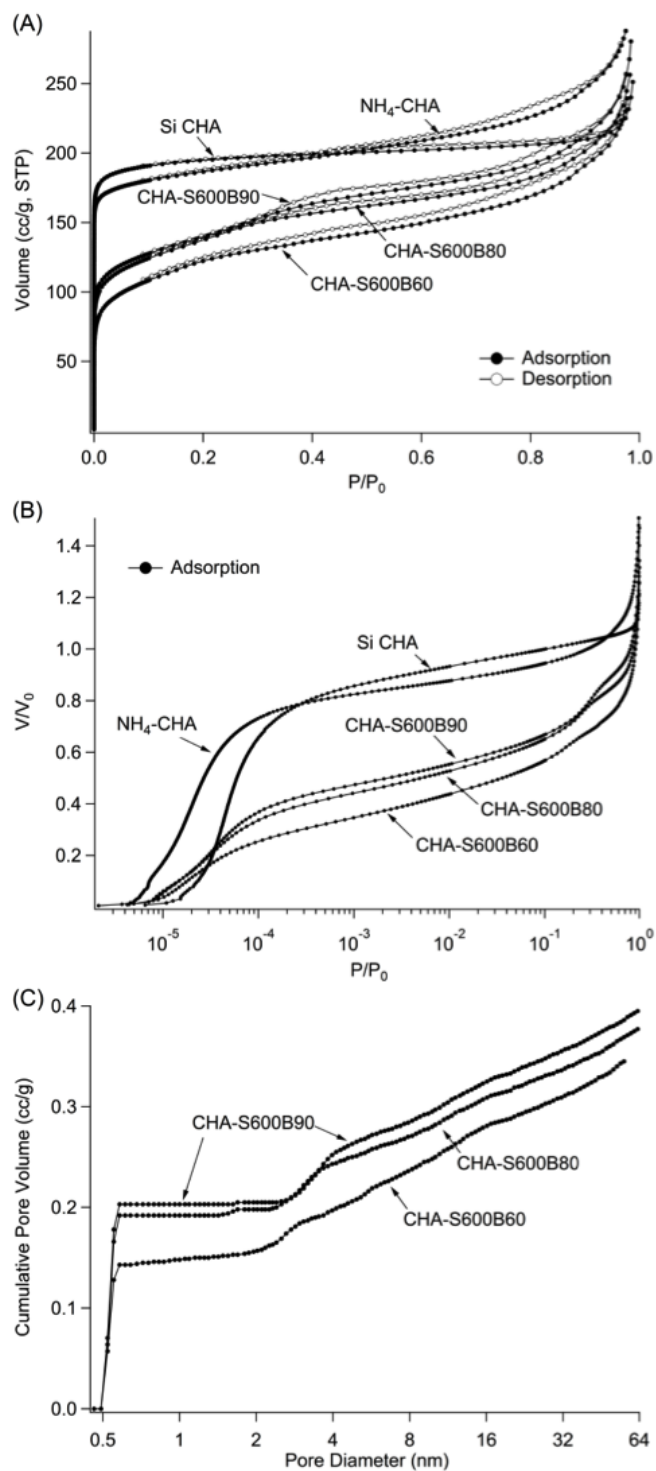


Figure 8.11: Ar physisorption isotherms of the as-synthesized and 600°C steamed CHA samples under varying steam partial pressures: (A) full isotherms, (B) normalized adsorption isotherms plotted on a semi-logarithmic scale and (C) NLDFT cumulative pore volume vs. pore diameter.

Ar physisorption measurements on the steamed samples (Figure 8.11) show that with decreasing steam partial pressure, the samples show decreasing adsorption volume. This trend is also observed in the micropore filling region of the isotherms (Figure 8.11B) and corroborated by the intact micropore volumes (Table 8.3). Figure 8.11C indicates that the steamed samples have essentially the same pore size distribution, showing a large step increase in cumulative pore volume for pores of 2 nm in diameter and larger.

Interestingly, as steam partial pressure decreases, the total Brønsted acid sites titrated by NH_3 TPD remain relatively similar (Entries 2, 5, and 6 in Table 8.1, consistent with the ^{27}Al NMR results), with a maximum value at CHA-S600B80. The *i*-propylamine TPD results are quite different, however, with the greatest accessibility observed for the two samples at steam partial pressures of 47.3 kPa and 70.1 kPa (CHA-S600B80 and CHA-S600B90, respectively). The sample with the lowest steam partial pressure, CHA-S600B60, had approximately half the *i*-propylamine accessibility of these samples.

8.3.5 Effect of Steam Partial Pressure for RHO

Figure 8.12 shows the XRD patterns of the samples steamed at 800°C for 8 h with varying partial pressures of steam. The XRD patterns show that the samples steamed with the water saturator held at 80°C and 90°C (corresponding to steam partial pressures of 47.3 kPa and 70.1 kPa, respectively) are very similar to each other, as with CHA. However, lowering the bubbler temperature from 80°C to 60°C (17.7 kPa of steam) results in increased structural degradation. Almost complete collapse of the structure is observed when NH_4 -RHO is calcined under dry air for 8 h at 800°C.

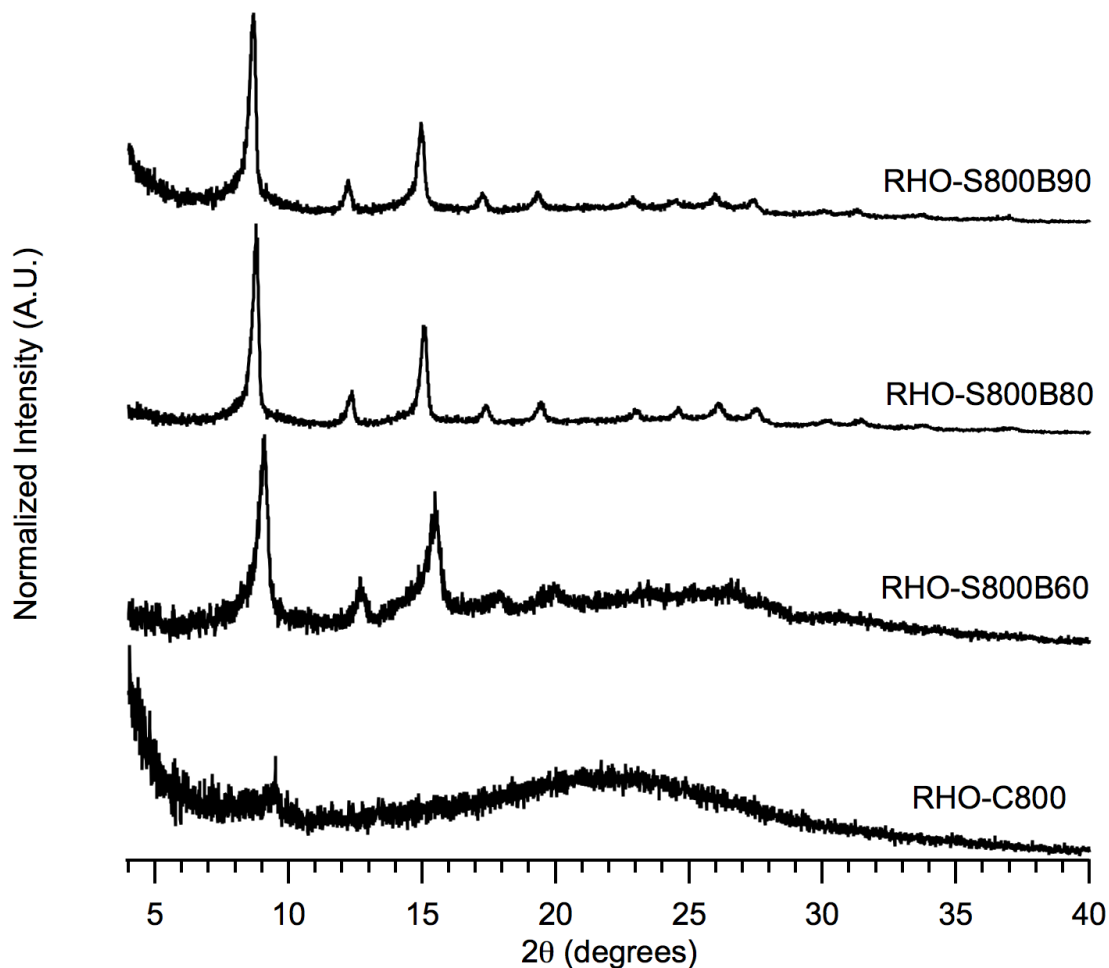


Figure 8.12: Powder XRD patterns of RHO samples steamed at 800°C with varying partial pressures of steam.

As with the CHA samples, the ^{27}Al NMR spectra of the steamed samples (Figure 8.13) do not show significant differences in the relative intensities of the tetrahedral, pentacoordinated, and hexacoordinated aluminum signals. ^{29}Si NMR spectra of the samples steamed under varying steam partial pressures is shown in Figure 8.14, that shows differences in the silicon environments for the samples. As with the CHA samples, the ^{29}Si NMR data for the steamed RHO samples suggest that with increasing steam partial pressure, an increasing portion of the silicon exists in the $\text{Si}(0\text{Al})$ environment.

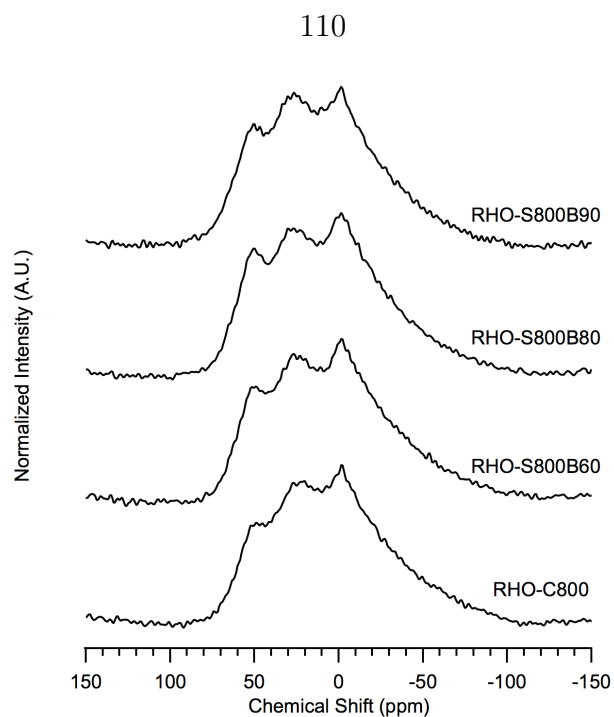


Figure 8.13: ^{27}Al MAS NMR spectra of RHO samples steamed at 800°C with varying partial pressures of steam.

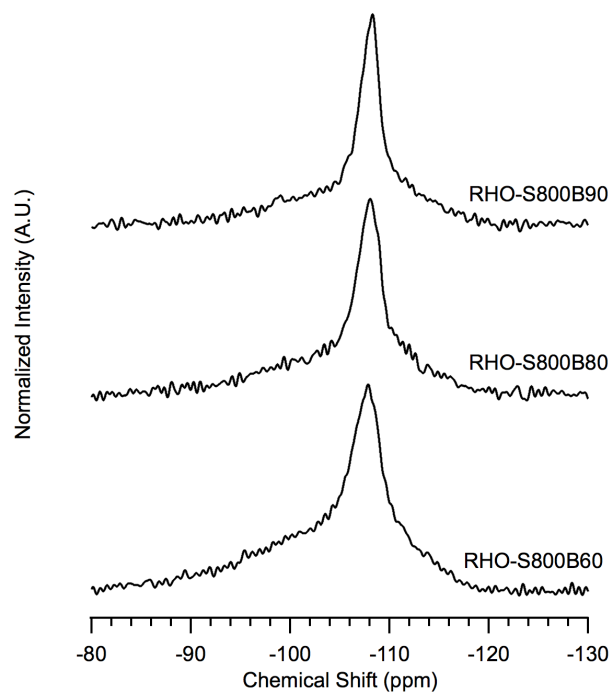


Figure 8.14: ^{29}Si MAS NMR spectra of RHO samples steamed at 800°C with varying partial pressures of steam.

As steam partial pressure decreases, the total Brønsted acid sites titrated by NH_3 TPD (Entries 3, 4, and 5 in Table 8.2) experience a maximum at the 800°C-steamed sample (RHO-S800B80). The *i*-propylamine TPD results are different, however, with the greatest accessibility observed for the sample at the highest steam partial pressure (70.1 kPa for RHO-S800B90). The two samples with the lowest steam partial pressure, RHO-S800B60 and RHO-S800B80, had approximately 75% of the *i*-propylamine accessibility of this sample.

The trend of increased degradation with decreasing steam partial pressure observed for both materials is the opposite of what has been reported for larger pore zeolites such as zeolite Y (FAU)^{137, 138} and ZSM-5 (MFI).¹¹⁰ Our steaming experiments with zeolite Y at 550°C and 650°C using a similar steam procedure to those reported by Wang et al.,¹³⁸ who investigated the effect of steam partial pressure on the steaming of Y, are consistent with the literature results in that Y samples calcined in the presence of steam undergo greater dealumination compared to samples calcined in dry air. Characterizations (powder XRD patterns and ²⁷Al NMR) for the 550°C and 650°C steamed Y samples are provided in the Appendix (Table C.1 and Figures C.5-C.8). However, when zeolite Y is steamed under more severe conditions (8 h at 800°C) using the same steaming procedure that was used with the CHA zeolites, the results (Table C.1 and Figures C.9-C.10) show the reversed trend of greater degradation with decreasing steam partial pressure, consistent with the behavior of the CHA zeolites. Furthermore, steam treatment of CHA at milder conditions (3 h at 500°C) using the 550°C and 650°C Y steaming procedure produces increasing dealumination with increasing steam partial pressure (Table C.1 and Figures C.11-C.12), consistent with the behavior of Y at the lower steaming temperatures. The similar behaviors between CHA and Y at these steaming conditions suggest that the trend reported here is not unique to CHA.

It has been proposed that the steaming involves hydrolyses of Al-O-Si bonds by water vapor at high temperatures, resulting in extra-framework aluminum species and the formation of vacant silanol nests.^{138, 139, 140} As an increasing number of the framework aluminum is extracted, portions of the zeolite collapse, forming amorphous

regions. Investigations on the steam dealumination of Y zeolites further suggest that in the presence of steam, silicon may migrate in the form of ortho-silicic acid (H_4SiO_4) to fill in the aluminum vacancies and thus “heal” the structure so that the resulting structure shows increased thermal stability.^{140, 141}

It is likely that a similar stabilization process may be occurring during the heating period for the zeolites studied here. When heated to temperatures at which the zeolite normally becomes amorphous under dry conditions (600°C for CHA and 800°C for Y in this study), the presence of steam provides stabilization of the structure. Due to the slow ramp rate (1°C/min) used during the steaming experiments for CHA and Y where the reversed trend of increased degradation with decreasing steam partial pressure was observed, the samples spend approximately the first half of the duration of the steaming experiment in heating under a steam atmosphere. A significant portion of the steaming process would thus occur in the heating period, during which the dealumination and healing steps described above are occurring at the same time. Under the higher steam partial pressures tested, healing of the framework may be facilitated and occurs at a rate that is fast enough to compensate for the dealumination process, and thus the structure is stabilized during the heating period. At a low steam partial pressure, the rate of healing could be too slow to compensate for dealumination and dehydroxylation and thus significant loss of crystallinity occurs. The ^{29}Si NMR of the samples steamed under varying steam partial pressures suggest that as the steam partial pressure is increased, the Si(0Al) peak grows in intensity relative to the downfield peaks, which would be consistent with increasing formation of Si-O-Si bonds with increasing availability of water during steaming.

8.4 Summary

CHA-type and RHO-type zeolites were prepared from the hydrothermal conversion of zeolite Y, NH_4^+ -exchanged, and dealuminated post-synthetically by steam and acid treatments to create selective catalysts for converting methanol to olefins. Characterizations by XRD and Ar physisorption of the steamed samples showed that

partial collapse of the framework occurs during the steaming process with the degree of degradation increasing with steaming temperature. ^{27}Al MAS NMR spectra of the steamed samples revealed the presence of tetrahedral, pentacoordinate, and hexacoordinate aluminum species. NH_3 and *i*-propylamine TPD results further corroborated that steaming converted tetrahedral aluminum to pentacoordinate and hexacoordinate species while also introducing pores larger than 8MR pores to the samples (simultaneously reduced the number of total Brønsted acid sites, but made them more accessible). As steaming temperature increases, the total Brønsted acid sites decreased, but accessibility via mesopores exhibited a maximum when samples were steamed at 600°C for CHA and 800°C for RHO.

Chapter 9

Effect of Post-Synthetic Treatments on MTO Reactivity for CHA-Type and RHO-Type Materials¹

Work for this chapter was done in collaboration with Lucy Ji.

9.1 Introduction

This chapter presents and explains MTO reaction data observed for each of the steamed and acid-washed samples from the previous chapter, highlighting important trends in product selectivities and catalytic lifetimes from each set of steaming and/or acid washing conditions. The effect of reaction temperature on steamed CHA and RHO samples is also studied (at 350°C, 400°C, and 450°C). From the combination of characterization data and reaction data, a new process to synthesize cheaper and comparably selective MTO catalysts becomes defined.

¹Information contained in this chapter has been submitted as a manuscript to *ACS Catalysis* and is currently under revision before publication (Ji, Y.; Deimund, M.A.; Bhawe, Y.; Davis, M.E. Submitted to *ACS Catal.* 24 Feb. 2015).

9.2 Experimental Section

9.2.1 MTO Reaction Testing

The CHA and RHO samples described in the previous chapter were used for reaction testing. For each sample, approximately 200 mg of pure zeolite was pelletized, crushed, and sieved to obtain particles between 0.6 mm and 0.18 mm. This material was then supported between glass wool beds in a tubular, continuous flow reactor. Prior to reaction, all samples were calcined in-situ under a flow of breathing-grade air, during which the temperature was ramped at 1°C/min to 150°C, held for 3 h, then ramped at 1°C/min to 580°C and held for 12 h. The reaction was conducted at 350°C, 400°C, or 450°C with a feed of 10% methanol/inert at a WHSV of 1.3 h⁻¹. Reaction testing of unsteamed CHA or RHO was conducted on a sample in the H⁺ form (H-CHA or H-RHO), which was obtained by calcining the NH₄-CHA or NH₄-RHO in-situ. Regeneration of spent catalysts was conducted in-situ by heating at 1°C/min from the reaction temperature to 580°C, holding for 6 h, and then cooling at 1°C/min back to the reaction temperature, all under a flow of breathing-grade air. Conversions and selectivities are computed on a carbon mole basis, and reported selectivities are normalized by the total selectivity of the products observed. Carbon mole balances were near 100% in all cases.

9.3 Results and Discussion

9.3.1 Effect of Steaming Temperature and Acid Washing for CHA

Figure 9.1 illustrates representative TOS reaction data obtained at 400°C for the as-synthesized CHA and CHA steamed at 500°C-700°C with the water saturator at 80°C, and a SAPO-34. Each of the catalysts is initially active in producing C₂-C₄ olefins when methanol conversion is close to 100%. With increasing TOS, methanol conversion decreases, and is accompanied by a decrease in olefin selectivities and a

simultaneous increase in dimethyl ether (DME) production. C_3 - C_5 alkanes, mainly propane and butane, are also observed among the products at the start of the reaction, with selectivities decreasing with increasing TOS. Lower alkanes (methane and ethane) are not observed among the products.

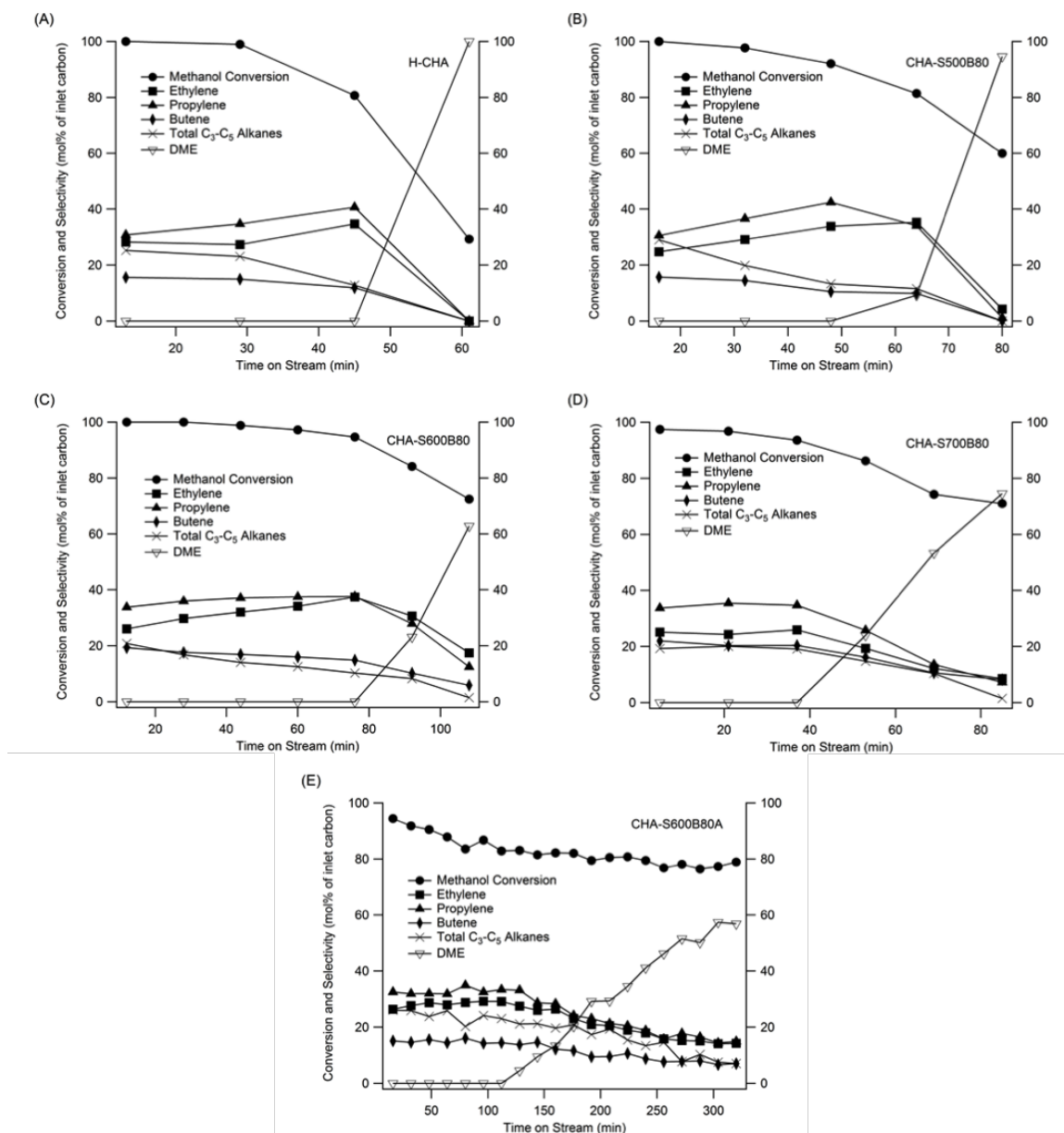


Figure 9.1: Representative MTO reaction data obtained at 400°C for: as-synthesized H-CHA (A), 500°C steamed CHA (B), 600°C steamed CHA (C), 700°C steamed CHA (D), and 600°C steamed and acid washed CHA (E).

Sample	Reaction Temperature	Maximum Methanol Conversion	Combined	Time to Deactivation (g-MeOH/g-cat) ^a
			C ₂ -C ₃ Olefin Selectivity at Maximum Methanol Conversion	
H-CHA	400°C	100.0%	59.0%	1.3
CHA-S500B80	400°C	100.0%	55.3%	1.6
CHA-S600B80	350°C	98.6%	58.6%	1.2
CHA-S600B80	400°C	100.0%	65.6%	2.3
CHA-S600B80	450°C	100.0%	74.2%	3.2
CHA-S700B80	400°C	97.4%	58.8%	1.4
CHA-S600B80A	400°C	94.4%	58.9%	5.0
CHA-S600B80A	450°C	100.0%	71.4%	>9.0

Table 9.1: Maximum combined C₂-C₃ olefin selectivities for CHA near complete conversion and deactivation times of catalysts tested.

^a First time point where methanol conversion drops below 80%

Table 9.1 provides a summary of the reaction data that includes the maximum methanol conversion, maximum combined C₂-C₃ olefin selectivity at or very near 100% conversion, and the approximate time to deactivation (arbitrarily defined as the first time point where the conversion drops below 80%). The as-synthesized CHA, while initially active in producing ethylene and propylene, has the shortest catalyst lifetime. Methanol conversion starts at 100%, but decreases rapidly after approximately 45 min (0.93 g-MeOH/g-cat) TOS, and DME becomes the main reaction product. The fast deactivation may be attributed to the high framework aluminum content of the as-synthesized CHA (Si/Al = 2.4) that leads to rapid coke deposition.

Whereas deactivation occurs abruptly for the as-synthesized CHA, the steamed materials show more gradual deactivation profiles that vary depending on the severity

of steaming. CHA steamed at 500°C has a slightly improved lifetime compared to the as-synthesized CHA. Methanol is initially completely converted and remains above 80% conversion for 64 min (1.3 g-MeOH/g-cat) TOS. However, olefin selectivities for CHA-S500B80 are comparable to the unsteamed CHA.

CHA steamed at 600°C shows the most stable reaction profile and longest lifetime among the steamed samples. Methanol conversion starts at 100% and remains above 80% for more than 92 min (2.0 g-MeOH/g-cat) TOS before deactivation occurs, with DME becoming the main product. Importantly, improved olefin selectivities are also observed for this sample. C₂ and C₃ olefin selectivities increase gradually with increasing TOS when conversion is near 100% and reach maximum selectivities of 29.7% and 35.9%, respectively, at complete conversion. Upon regeneration of the spent catalyst, similar olefin selectivities are observed with only a slight decrease in catalyst lifetime (Figures C.13 and C.14).

The lifetime of the 600°C steamed CHA is improved further after acid washing (Figure 9.1E). Methanol conversion decreases slowly and remains steady around 80% until approximately 240 min (5.0 g-MeOH/g-cat) TOS. The combined ethylene and propylene selectivity remains steady at approximately 61% for 100 min TOS before gradually declining.

Increasing the steaming temperature further to 700°C gives poorer MTO activity compared to CHA-S600B80, likely due to the increased severity of steaming at 700°C. Ethylene and propylene reach selectivities of 24.3% and 35.4%, respectively, at 96.8% methanol conversion (21 min TOS). Conversion drops below 80% by approximately 60 min TOS, giving a reaction profile similar to the 500°C steamed CHA.

The improvements in selectivities and catalyst lifetime of the 600°C steamed CHA may be attributed to modifications in the acidity of the catalysts resulting from the extraction of framework aluminum. It is also likely that the mesoporosity created by steaming plays a role in the extended lifetimes. It has been observed that the introduction of mesopores in microporous zeolite catalysts facilitates mass transport to the micropores and leads to longer catalyst lifetimes.¹²⁰ This trend has been reported by Wu et al.,¹²¹ who evaluated mesoporous SSZ-13 that was synthesized using the

N,N,N-trimethyl-1-adamantylammonium OSDA in combination with a mesoporegen. These introduced mesopores result in improved lifetimes for the MTO reaction by allowing greater utilization of the micropore volume. As demonstrated by the NH_3 and *i*-propylamine TPD data, the 600°C-steamed CHA sample appears to have the best balance of intact Brønsted acid sites and access to those sites via the mesoporosity introduced by the steaming process, that could account for the excellent reaction behavior observed.

9.3.2 Effect of Reaction Temperature for CHA

The effects of reaction temperature on the activity of CHA-S600B80 and CHA-S600B80A are illustrated in Figure 9.2. The most apparent trend in the reaction profiles for CHA-S600B80 when the reaction temperature is increased from 350°C to 450°C is the increase in catalyst lifetime. At 350°C, methanol conversion is initially near 100%, but declines below 80% after approximately 59 min (1.3 g-MeOH/g-cat) of TOS, while at 400°C, the lifetime was 108 min (2.3 g-MeOH/g-cat). Increasing the reaction temperature further to 450°C results in the longest lifetime at 152 min (3.2 g-MeOH/g-cat). Further, the maximum combined ethylene and propylene selectivity increases at 450°C to 74.2% at 100% MeOH conversion.

Similarly, the acid washed sample shows increases in lifetime and olefin selectivities at 450°C. CHA-S600B80A converts methanol to ethylene and propylene steadily at an average of 69% combined selectivity for almost 200 min (4.1 g-MeOH/g-cat) TOS before DME becomes the main product. Further, ethylene selectivities increase for both CHA-S600B80 and CHA-S600B80A when the reaction temperature is increased from 400°C to 450°C so that more ethylene than propylene is produced at 450°C. Regeneration of CHA-S600B80A at 450°C results in some loss in olefin selectivities and lifetime (Figures C.15 and C.16).

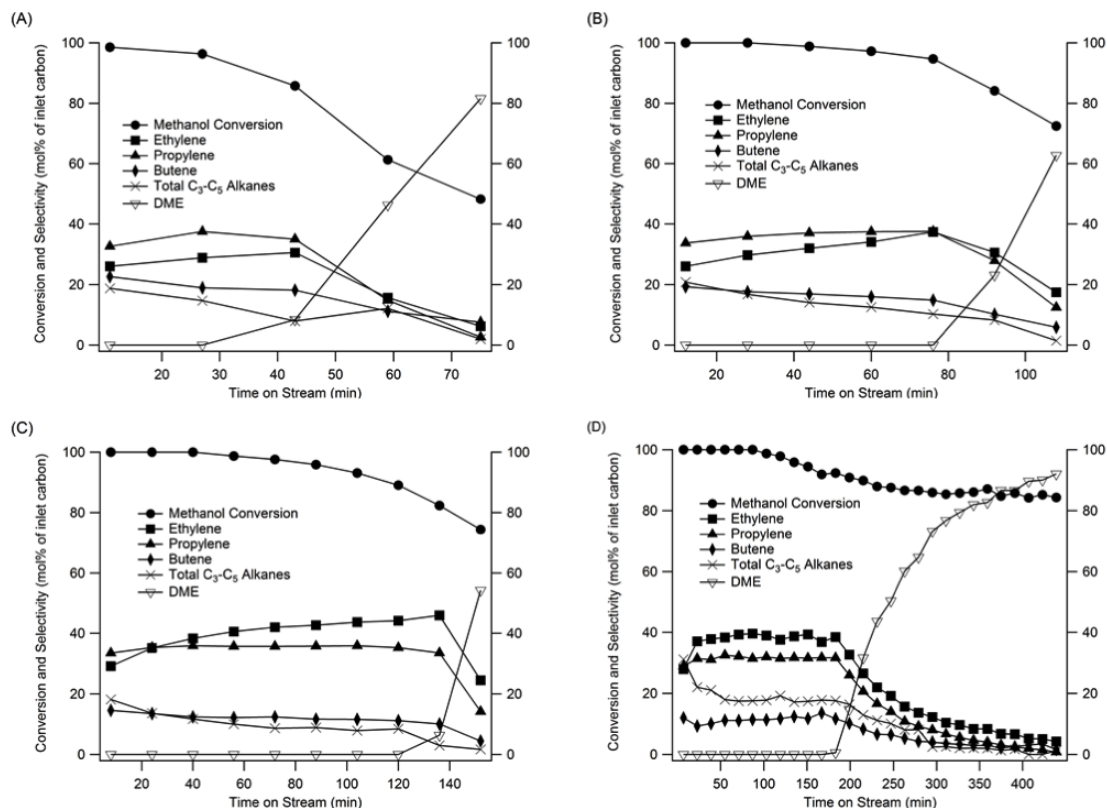


Figure 9.2: MTO reaction data for CHA-S600B80 obtained at reaction temperatures of 350°C (A), 400°C (B), 450°C (C), and CHA-S600B80A at 450°C (D).

9.3.3 Effect of Steaming Temperature for RHO

Figure 9.3 illustrates representative TOS reaction data obtained at 400°C for the as-synthesized RHO and RHO steamed at 600°C-800°C under a steam partial pressure of 47.3 kPa. As with CHA, each of the catalysts initially produces C₂-C₄ olefins when methanol conversion is close to 100%. With increasing TOS, methanol conversion decreases, and is accompanied by a decrease in olefin selectivities. For the H-RHO and RHO-S600B80 samples, DME production also increases with deactivation, while for RHO-S700B80 and RHO-S800B80, DME production does not increase as methanol conversion decreases; instead, olefin selectivities remain steady. This result suggests that a different mechanism of deactivation may be at play in CHA as compared to RHO. C₃-C₅ alkanes, mainly propane and butane, are also observed among the

products at the start of the reaction in the H-RHO and RHO-S600B80 samples, with selectivities decreasing with increasing TOS. The RHO-S700B80 and RHO-S800B80 samples have very stable selectivities to the alkanes and light olefins for all points on stream. Lower alkanes (methane and ethane) are not observed among the products for any samples.

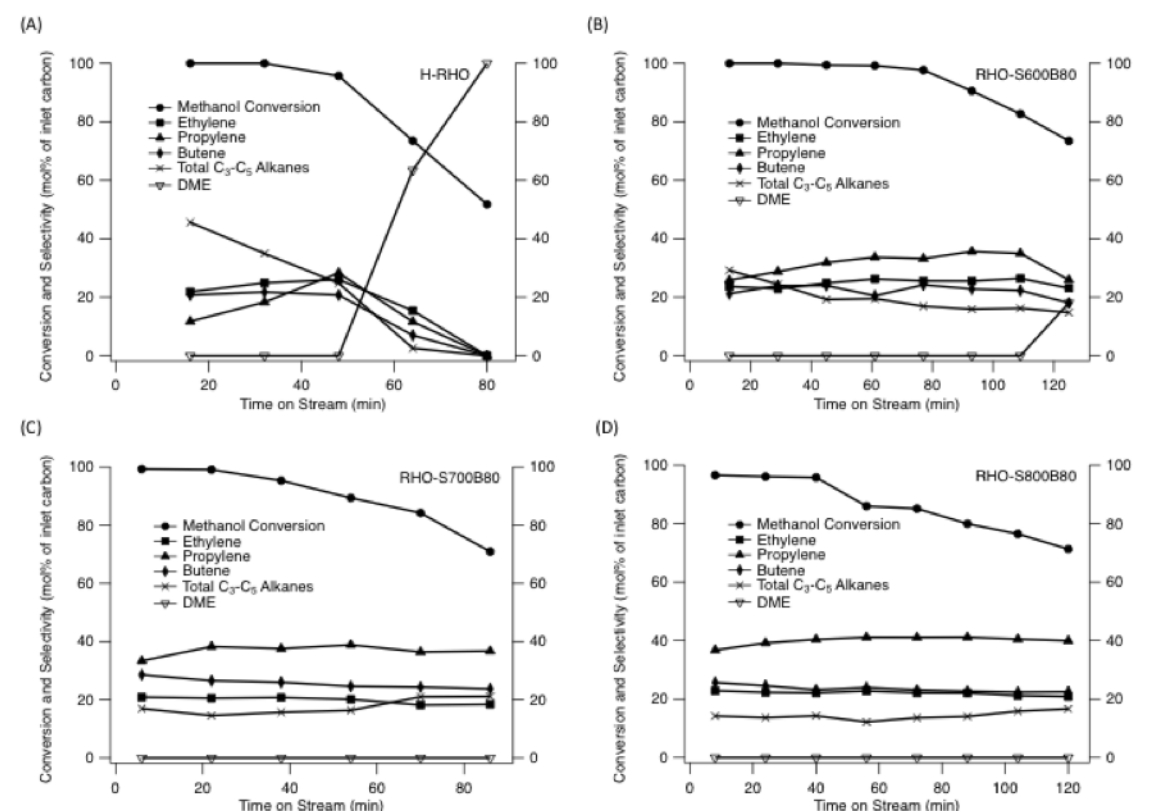


Figure 9.3: Representative MTO reaction data obtained at 400°C for as-synthesized H-RHO (A), 600°C steamed RHO (B), 700°C steamed RHO (C), and 800°C steamed RHO (D).

Sample	Reaction Temperature	Maximum Methanol Conversion	Combined	Time to Deactivation (g-MeOH/g-cat) ^a
			C ₂ -C ₃ Olefin Selectivity at Maximum Methanol Conversion	
H-RHO	400°C	100.0%	43.2%	1.0
RHO-S600B80	400°C	100.0%	51.6%	2.3
RHO-S700B80	400°C	99.1%	58.8%	1.5
RHO-S800B80	350°C	91.9%	50.2%	0.5
RHO-S800B80	400°C	96.1%	61.5%	1.2
RHO-S800B80	450°C	100.0%	66.1%	1.8

Table 9.2: Maximum combined C₂-C₃ olefin selectivities for RHO near complete conversion and deactivation times of catalysts tested.

^a First time point where methanol conversion drops below 80%

Table 9.2 provides a summary of the reaction data for the RHO samples. The as-synthesized RHO, while initially active in producing ethylene and propylene, has the shortest catalyst lifetime, as was also observed for the as-made CHA.

Methanol conversion for this as-made RHO starts at 100%, but decreases rapidly after approximately 60 min (1.3 g-MeOH/g-cat) TOS, and DME becomes the main reaction product. This fast deactivation may again be attributed to rapid coke formation from the high framework aluminum content of the as-synthesized RHO (Si/Al = 2.8).

Despite rapidly deactivating in the as-made form, the steamed RHO samples deactivate more gradually and depend upon steaming severity. When RHO is steamed at 600°C, the methanol conversion remains higher for longer on stream, staying above 80% for 109 min (2.3 g-MeOH/g-cat) TOS. Additionally, the olefin selectivities become much more stable with less DME formed during deactivation, and initial alkane

formation is greatly reduced.

The RHO sample steamed at 700°C also has very stable olefin selectivities, as was observed for the RHO sample steamed at 600°C. Methanol conversion falls below 80% sooner on this material (70 mins TOS, 1.5 g-MeOH/g-cat) than the sample steamed at 600°C, and in fact it has the shortest catalytic lifetime of all the steamed samples. Interestingly, the initial transient alkane behavior is totally absent in this sample, and no significant DME is observed as the catalyst deactivates. This is in contrast to CHA samples, wherein DME production takes over as soon as the catalyst deactivates, suggesting that differing MTO reaction and/or deactivation mechanisms are at play in the steamed CHA and RHO samples. Further study into these differences could provide significant insight into the MTO mechanism, and more research is warranted.

When steamed at 800°C, RHO has the highest combined C₂-C₃ olefin selectivity and a relatively long catalytic lifetime, with no significant DME formation and no initial transient alkane formation (similar to that observed when steamed at 700°C, but with improved lifetime). The improvements in selectivities and catalyst lifetime of the steamed RHO are likely due to changes in the framework aluminum content (and thus acidity) in the material, as well as the mesoporosity introduced, which contributes to improved mass transport of reactants and products within the zeolite.

9.3.4 Effect of Reaction Temperature for RHO

The effects of reaction temperature on the activity of RHO-S800B80 is illustrated in Figure 9.4. At 350°C, RHO-S800B80 only achieves a maximum of 92% MeOH conversion and deactivates very quickly, dropping below 80% MeOH conversion after 26 min (0.5 g-MeOH/g-cat). When reaction temperature is increased to 400°C or 450°C, catalyst lifetime and MeOH conversion both increase dramatically. At 400°C, catalyst lifetime is 72 mins (1.5 g-MeOH/g-cat), and olefin selectivities are very stable. Further increase in reaction temperature to 450°C results in the longest time before MeOH conversion drops below 80% (89 min, 1.8 g-MeOH/g-cat). C₂-C₃ olefin selectivities at 400°C and 450°C are both very similar, but the RHO-S800B80 at 450°C

slightly edges out the 400°C sample and has longer TOS before deactivation.

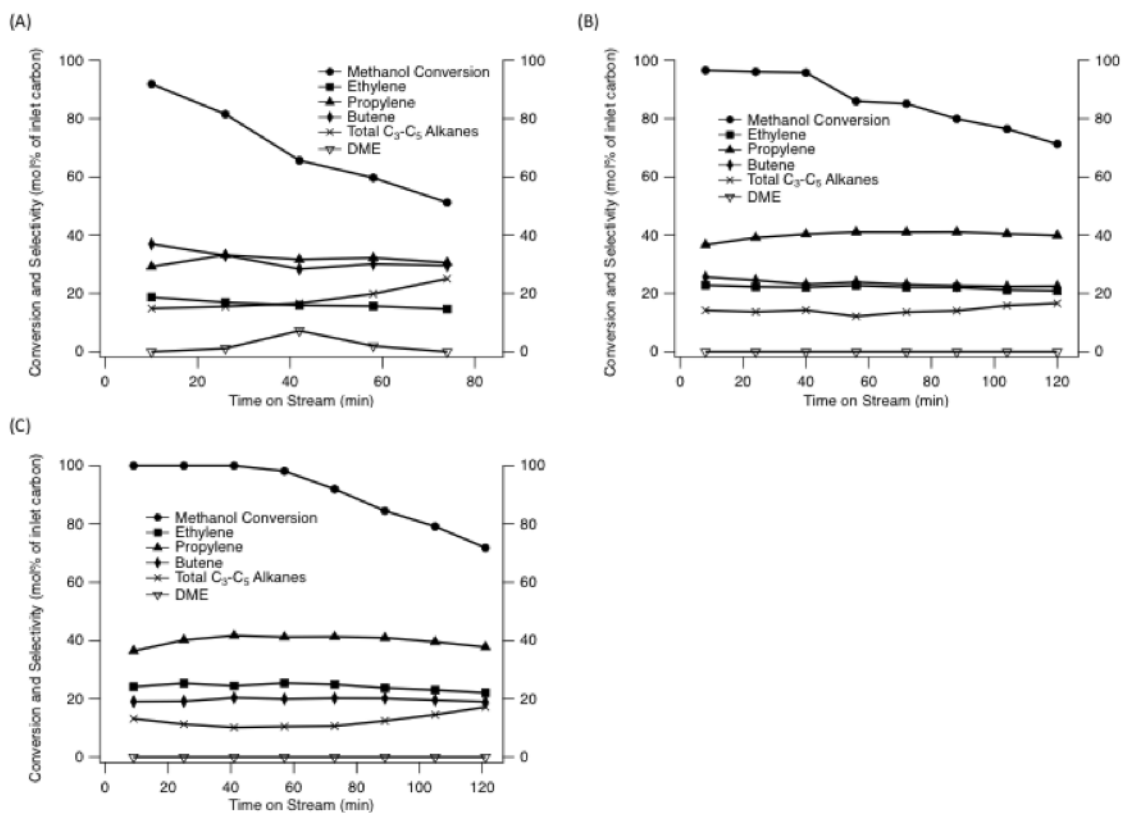


Figure 9.4: MTO reaction data for RHO-S800B80 obtained at reaction temperatures of 350°C (A), 400°C (B), and 450°C (C).

9.4 Summary

When evaluated for the MTO reaction, the unsteamed H-CHA (Si/Al = 2.4) and H-RHO (Si/Al = 2.8) samples deactivated quickly whereas the steamed samples showed longer lifetimes and increased olefin selectivities. CHA steamed at 600°C achieved the highest olefin selectivities (comparable to that of the commercial catalyst) and lifetime among the steamed samples, and the activity was retained upon regeneration of the spent catalyst. The results presented here show that the acidity and catalytic behavior of an aluminum-rich CHA zeolite prepared without using an OSDA can be modified by post-synthetic dealumination treatments to create a selective catalyst for converting methanol to olefins. Steaming of OSDA-free RHO samples also improved both the

catalytic lifetime and light olefin selectivity. As it has been demonstrated for two different 8MR zeolites, it is likely that this dealumination strategy may be effective for preparing useful catalysts starting from small-pore zeolites of other topologies that are currently of interest for applications such as MTO and deNO_x.

Chapter 10

Conclusions and Suggested Future Work for Part II

The final chapter on MTO work summarizes the effects of heteroatom concentrations and post-synthetic treatments and draws general conclusions from the frameworks studied. Additionally, discussion of the reactivity of the OSDA-free MTO catalysts and potential directions for future research to improve their industrial viability are outlined and explained.

10.1 Conclusions

Chapter 7 demonstrates the effects of heteroatom concentration by synthesizing two zeotype materials with CHA topology (SAPO-34 and SSZ-13) commonly employed for the MTO reaction. The SAPO-34 sample is synthesized with only isolated Si sites. This sample began to deactivate after approximately 100 mins TOS, but had relatively stable light olefin selectivities and low initial alkane formation, as is typical with SAPO-34 samples.

SSZ-13 samples are synthesized in a range of Si/Al ratios, from 4.7 to 54.5. The physical properties and MTO reaction differences are much more significant with these samples. As Si/Al increased, crystallite size and organic mass loss (by TGA) increase, while Brønsted acid site density (by NH_3 TPD) and paired Al site content (by Cu^{2+} exchange and SEM/EDS) decrease.

Additionally, the MTO reactivity for these SSZ-13 samples varies drastically. The

samples with lower Si/Al ratios exhibit shorter catalytic lifetimes and significant initial selectivities to light alkanes as transient products. As Si/Al ratio increases, these transient selectivities are reduced, while catalytic lifetime increases. In fact, the MTO activity of the SSZ-13 sample with an Si/Al ratio of 54.5 begins to resemble that of the SAPO-34 sample. This difference in reactivity among the SSZ-13 samples could likely be attributed to the decreasing paired Al site content as Si/Al ratio increases, with SSZ-13 samples ultimately becoming more like the SAPO-34 sample with essentially isolated Brønsted acid sites.

As demonstrated in the two previous chapters, zeolites CHA and RHO can be synthesized quickly and reliably in the absence of organic SDAs. Furthermore, steaming of these 8MR materials has been shown to drastically improve their activity and selectivity to light olefins in the MTO reaction.

From the characterization and reaction testing work, several trends have appeared. Primarily, for both CHA and RHO, as steaming temperature increases, the degradation of the framework increases (as shown by powder XRD). Interestingly, as water content decreases, framework crystallinity decreases as well. This trend has, however, also been observed for faujasite (FAU) at elevated temperatures, as discussed in Section 8.3 of Chapter 7 and in the Appendix.

During these steaming processes, ^{27}Al SS NMR confirms that pentacoordinate and hexacoordinate (extraframework) aluminum species are formed in each material. ^{29}Si SS NMR corroborates this change in Al coordination, as all samples exhibit primarily Si(0Al) and Si(1Al) sites after steaming. Ar adsorption isotherms of all samples also reveal the formation of mesopores after steaming, in agreement with the removal of framework aluminum species (by ^{27}Al SS NMR) and degradation of the microporous crystal structure (as shown by powder XRD). The combination of NH_3 TPD and reactive *i*-propylamine TPD further show that the introduction of mesopores by steaming occurs, as the acid sites titrated by *i*-propylamine TPD (and thus accessible to this larger molecule) increase with increasing steaming severity. Sites titrated by NH_3 similarly decrease with increasing steaming severity, as the crystalline framework degrades and Brønsted acid sites are destroyed. These mesopores, in combination with

framework Al removal, are thought to enhance MTO activity by improving transport into the crystal structure and reducing the framework Al content (and thus effective Si/Al ratio) within the samples, respectively.

With both CHA and RHO, there is an optimum temperature for steaming before the framework degradation becomes too severe and MTO activity suffers. Typically, increasing the steaming temperature for both topologies serves to improve the catalyst lifetime and olefin stability. However, CHA experiences a maximum in MTO activity improvement when steamed at 600°C, before declining in performance when steamed at 700°C (while still remaining crystalline), while RHO is capable of withstanding steaming temperatures of up to 800°C while continually improving TOS and light olefin selectivities until its total framework collapse at 850°C.

Acid washing of CHA samples appears to remove the extraframework (pentacoordinate and hexacoordinate) aluminum generated by the steaming process, thereby improving catalyst lifetime and olefin stabilities relative to the samples that were not acid-washed. For zeolite RHO, the acid-washing work to determine optimal conditions for removal of extraframework aluminum is still in progress.

As reaction temperature increases from 350°C to 450°C, TOS before deactivation increases for both CHA and RHO. To produce the highest light olefin selectivities and longest TOS before deactivation, CHA should be steamed at 600°C for 8 h in a steam partial pressure of 47.3 kPa, with the MTO reaction run at 450°C. This steamed sample may also be acid-washed to remove additional extraframework aluminum, and the resulting product will exhibit longer TOS before deactivation. For zeolite RHO, steaming conditions of 800°C for 8 h at a steam partial pressure of 47.3 kPa should be used, again with the MTO reaction run at 450°C, to produce the highest light olefin selectivities.

10.2 Recommended Future Work

For the SAPO-34 and SSZ-13 samples, a detailed hydrocarbon characterization of the coke remaining on each catalyst after reaction could provide valuable information

about how each catalyst deactivates. Identifying and quantifying each species, particularly the polycyclic species, could give mechanistic insight into how deactivation may be occurring at these paired site locations, as the samples with higher paired site concentrations may exhibit unusually high content of certain species. The Dow Chemical Company is in the process of performing this analysis on the post-reaction catalysts currently.

Much work has been done to develop a robust synthesis and steaming treatment process for both CHA and RHO. Now that both materials have been investigated under a wide variety of steaming temperatures and partial pressures, this methodology may be expanded to other zeolites (both 8MR and larger-pore materials) to discover additional useful catalysts. Zeolites KFI, LEV, and MER are other interesting 8MR materials that can be synthesized OSDA-free and should be initially studied. Further expansion to other frameworks may be desired if new OSDA-free syntheses are discovered. The combination of OSDA-free syntheses and steam treatments is a simple method that can result in useful catalysts at greatly reduced costs compared to existing methods.

While both CHA and RHO exhibited similar trends in stability, such as increased degradation with both increasing steaming temperature and reduced steam partial pressure, observed trends in MTO reaction data showed some differences. Most notably, as CHA deactivates and MeOH conversion declines, it becomes more and more selective to DME, while RHO tends to have steady olefin selectivities and little to no DME formation, regardless of MeOH conversion. This difference in selectivities during deactivation suggests that there may be some differences in the MTO reaction and/or deactivation mechanism on CHA when compared to RHO. Such differences could be a result of the effect steaming has on each framework type, or simply as a result of the differences in the 8MR frameworks during the reaction itself.

To study how these two materials may differ during the MTO reaction, some of the acid sites for each zeolite after steaming could be selectively deactivated using a trimethyl phosphite exchange, followed by calcination, as has been done for ZSM-5.¹⁴² Trimethyl phosphite, which is too large to fit into the 8MR pores, will bind to and

deactivate Al sites (after calcination) in the mesopores or external crystal surface, leaving Al acid sites within the 8MR pore system intact. Correct exchange of the trimethyl phosphite can be verified by ^{31}P SS NMR.

Once only the Al sites within the 8MR pores are active, the zeolites can undergo MTO reaction testing again to determine if reactivity and selectivity to DME change. If the same DME selectivity behavior is observed for the CHA and RHO samples with and without the presence of the trimethyl phosphite, it then suggests that the different DME selectivities are a result of the unique 8MR pore structures for each material. However, if DME selectivity differences are noted for each sample before and after the exchange, this suggests that DME may be forming on the external/mesoporous acid sites created during steaming, rather than in the 8MR pore system. In any case, further study of these two materials and their mechanisms of reaction and deactivation is warranted.

Chapter 11

Summary and Future Direction

Overall conclusions of both thesis parts will be briefly presented, and suggested future directions will be highlighted.

11.1 Overall Conclusions

As Part I shows, the Ni^{2+} cation exchanged onto zincosilicates is capable of oligomerizing propylene and is more selective to C_{3n} products than nickel-containing aluminosilicate catalysts. These zincosilicate catalysts are additionally capable of oligomerizing 1-butene and mixed alkene feeds such as equimolar propylene and 1-butene. When exposed to mixed alkane/alkene feeds (such as equimolar propylene and *n*-butane), however, they can only oligomerize the olefin and do not react with the alkane at all.

In an attempt to activate the alkane in such a mixed feed, a series of supported homogeneous Ir-based transfer hydrogenation catalysts were synthesized. These catalysts were reaction tested both on their own and in physical mixtures with the zincosilicate oligomerization catalysts in reactant feed streams of equimolar propylene and *n*-butane, but did not exhibit any significant dehydrogenation/hydrogenation activity. Similarly, catalysts formed by depositing Pt on Ni-CIT-6 and Ni-Zn-MCM-41 were reaction tested at higher temperatures (400°C) in an equimolar alkane/alkene feed (propylene and *n*-butane), but the materials were not capable of forming dehydrogenated products or incorporating these dehydrogenated alkanes into the oligomers formed.

Through development of the Ni-containing zincosilicate catalysts, the capability to exchange other divalent transition metals onto CIT-6 without removal of the framework Zn or destruction of the crystal structure was developed. This ability may lead to several new catalysts based on the zincosilicate *BEA structure of CIT-6, such as Mn-CIT-6, Co-CIT-6, Cu-CIT-6, and Zn-CIT-6. For example, Cu-CIT-6 may prove useful in deNO_x applications, while Co-CIT-6 and Zn-CIT-6 may be effective in forming acetic acid from methane and carbon dioxide. Additional applications with these and other divalent transition metals exchanged onto CIT-6 will likely continue to appear as catalysis research progresses.

The second part of this thesis has explored two avenues of the MTO reaction: first, by synthesizing materials with differing heteroatom concentrations to learn more about MTO reaction behavior as acid site type and concentration changes, and second, by synthesizing OSDA-free materials and post synthetically treating them as a path to cheaper MTO catalysts.

Initially, the effect of heteroatom (and consequently, Brønsted acid site) distribution on the physical properties and MTO reactivity of the two conventional MTO catalysts, SAPO-34 and SSZ-13, was studied. A SAPO-34 sample with isolated Si sites exhibited typical MTO reactivity, with stable light olefin selectivities and low initial alkane selectivity. SSZ-13 samples, however, showed drastic differences as Si/Al ratio was increased. Most notably, as Si/Al ratio increases, the initial selectivity to light alkanes decreases and catalyst lifetime increases. This change in reactivity with changing Al content can be correlated with the concentration of paired Al sites in these SSZ-13 samples. Additionally, as Si/Al increases for the SSZ-13s, reactivity begins to resemble that of SAPO-34s, which typically have only isolated Brønsted acid sites.

Cheaper MTO catalysts may be manufactured by first synthesizing CHA-type and RHO-type zeolites in the absence of OSDAs and subsequently steam-treating these materials. While steaming conditions to produce the optimal MTO activity vary for each material, several trends are noted. Most notably, as steaming temperature increases, framework damage also increases for the zeolites, until the materials

eventually become amorphous above a certain upper temperature limit. Additionally, as water partial pressure increases during steaming, the extent of degradation of the framework decreases, as has been observed for FAU at elevated temperatures (800°C). After steam treatment, Al is extracted from the zeolite frameworks, forming penta-coordinate and hexacoordinate aluminum species, as demonstrated by ^{27}Al SS NMR. Ar adsorption isotherms also reveal introduction of mesoporosity after steaming, and *i*-propylamine TPD work shows an increase in the number of accessible acid sites outside of the 8MR pore systems.

Reaction testing demonstrates that steam treatment dramatically improves olefin selectivity and time on stream before deactivation for both CHA and RHO. In fact, at specific steaming conditions (600°C for 8 h with the water bubbler held at 80°C), CHA can exhibit selectivities to light olefins (C_2 and C_3) of nearly 75%, approaching the selectivities reported with commercial SAPO-34 MTO catalysts. Similarly, a RHO sample steamed at 800°C for 8 h with the water bubbler held at 80°C can exhibit combined C_2 - C_3 selectivities over 65% when undergoing the MTO reaction at 450°C.

11.2 Future Directions

Although the combined catalyst system does not appear to be effective with the current supported homogeneous catalyst, the idea may be revisited if improved homogeneous transfer hydrogenation catalysts are developed. Focus on improving the homogeneous catalyst loading onto a support and its activity in gas phase reactions are of the utmost importance to making the tandem catalysis system capable of oligomerizing mixed alkane/alkene feeds. If the reaction apparatus was modified to operate at higher pressure of the reactant gases, the catalyst system could be revisited as well, since this higher pressure may be more conducive to operation of the supported homogeneous catalysts.

While Ni-CIT-6 has been extensively studied in this work, the new M-CIT-6 catalysts are relatively unexplored outside of propylene oligomerization. They may provide interesting new activity and should be considered for future reaction testing

where divalent transition metals are involved. Example reactions such as deNO_x and acetic acid synthesis should be pursued, but they should not serve as limiting cases. It is quite likely that the divalent ion exchange procedure for CIT-6 (with pH balancing and/or heteroatom protection via Mg²⁺ or Ca²⁺ exchange) may in fact be translatable to other zincosilicate frameworks or in materials where the heteroatom is somewhat unstable in the framework.

Post-MTO reaction SAPO-34 and SSZ-13 catalysts should undergo a detailed hydrocarbon characterization of the coke present to gain more information about each catalyst. Identifying and quantifying each species, particularly the polycyclic species, could give insight into the deactivation mechanism, particularly as it may change with paired site content. Currently, The Dow Chemical Company is performing this analysis.

The CHA and RHO materials examined here for their MTO activity are already useful as catalysts in their own right, but improved understanding of the MTO mechanisms at play in these two materials would be desirable. Steamed CHA and RHO exhibit very different light olefin selectivities and on-stream behavior, particularly during deactivation. The suite of characterization tools (such as Ar adsorption, NH₃ TPD, and *i*-propylamine TPD) that have become available to the Davis lab over the past few years could provide valuable insight into the physical and chemical properties of these steamed catalysts. Further investigation of these specific MTO mechanisms and selectivity differences by targeted deactivation of Al acid sites within the mesopores of each material with phosphite compounds (such as trimethylphosphite) may shed more light on how olefins are formed in CHA and RHO. Along this same vein, expansion of the steam treatment technique to other OSDA-free 8MR zeolite framework types, such as MER, LEV, and KFI, might reveal other interesting trends in light olefin selectivities.

Bibliography

- [1] Gary, J. H.; Handwork, G. E.; Kaiser, M. J. *Petroleum Refining: Technology and Economics*, 5th ed.; CRC Press: Boca Raton, FL, 2007.
- [2] Lesthaeghe, D.; Horr , A.; Waroquier, M.; Marin, G. B.; Van Speybroeck, V. *Chem. Eur. J.* **2009**, *15*, 10803–10808.
- [3] International Zeolite Association; *Framework Type CHA*; 2015 (Accessed February 2, 2015). http://izasc-mirror.la.asu.edu/fmi/xsl/IZA-SC/Atlas_pdf/CHA.pdf.
- [4] International Zeolite Association; *Framework Type *BEA*; 2015 (Accessed February 2, 2015). http://izasc-mirror.la.asu.edu/fmi/xsl/IZA-SC/Atlas_pdf/BEA.pdf.
- [5] Haber, J. *Pure Appl. Chem.* **1991**, *63*, 1227–1246.
- [6] Tschernich, R. W. *Zeolites of the World*; Geoscience Press: Phoenix, AZ, 2007.
- [7] U.S. Energy Information Administration; *U.S. Downstream Processing of Fresh Feed Input by Catalytic Cracking Units*; 2015 (Accessed February 2, 2015). <http://www.eia.gov/dnav/pet/hist/LeafHandler.ashx?n=PET&s=MCRCCUS2&f=A>.
- [8] O’Connor, C. T.; Kojima, M. *Catal. Today* **1990**, *6*, 329–349.
- [9] Heveling, J.; van der Beek, A.; de Pender, M. *Appl. Catal.* **1988**, *42*, 325–336.
- [10] Ng, F. T. T.; Creaser, D. C. *Appl. Catal. A.* **1994**, *119*, 327–339.
- [11] Bonneviot, L.; Olivier, D.; Che, M. *J. Mol. Catal.* **2001**, *21*, 415–430.

- [12] Maxwell, I. E. In *Advances in Catalysis*; Eley, D. D.; H, P.; Weisz, P. B., Eds.; Academic Press: New York, 1982; Vol. 31, pp 24–38.
- [13] Garwood, W. E.; Krambeck, F. J.; Kushnerick, J. D.; *US 4,740,645: Multistage Conversion of Lower Olefins with Interreactor Quenching*; US Patent Office; 1988.
- [14] Hogan, J. P.; Banks, R. L.; Lanning, W. C.; Clark, A. *Ind. Eng. Chem.* **1955**, *47*, 752–757.
- [15] Matsuda, T.; Miura, H.; Sugiyama, K.; Ohno, N. *J. Chem. Soc.* **1979**, *75*, 1513–1520.
- [16] Tabak, S. A.; *US 4,433,185: Two-Stage System for Catalytic Conversion of Olefins with Distillate and Gasoline Modes*; US Patent Office; 1984.
- [17] Keil, F. J. *Microporous Mesoporous Mater.* **1999**, *29*, 49–66.
- [18] Lowenstein, W. *Am. Mineral.* **1954**, *39*, 92–96.
- [19] Dědeček, J.; Sobalík, Z.; Wichterlová, B. *Cat. Rev.* **2012**, *54*, 135–223.
- [20] Serrano, D. P.; van Grieken, R.; Melero, J. A.; Garcia, A. *Appl. Catal. A.* **2004**, *269*, 137–146.
- [21] Takewaki, T.; Beck, L. W.; Davis, M. E. *Top. Catal.* **1999**, *9*, 35–42.
- [22] Takewaki, T.; Beck, L. W.; Davis, M. E. *J. Phys. Chem. B.* **1999**, *103*, 2674–2679.
- [23] Takewaki, T.; Davis, M. E.; *US 6,117,411: Molecular Sieve CIT-6*; US Patent Office; 2000.
- [24] Takewaki, T.; Hwang, S.-J.; Yamashita, H.; Davis, M. E. *Microporous Mesoporous Mater.* **1999**, *32*, 265–278.
- [25] Hartmann, M.; Racouchot, S.; Bischof, C. *Chem. Commun.* **1997**, 2367–2368.

- [26] Hartmann, M.; Racouchot, S.; Bischof, C. *Microporous Mesoporous Mater.* **1999**, *27*, 309–320.
- [27] Tosoh Corporation; *Zeolite for Catalysts*; 2015 (Accessed February 2, 2015).
<http://www.tosoh.com/our-products/advanced-materials/zeolite-for-catalysts>.
- [28] Zeolyst International; *Zeolite Beta*; 2015 (Accessed February 2, 2015).
<http://zeolyst.com/our-products/standard-zeolite-powders/zeolite-beta.aspx>.
- [29] Lam, Y. C.; *Update on Progress Towards Light Alkane Upgrading by Tandem Olefin Dimerization and Transfer Hydrogenation*; BP Teleconference Presentation; 2012.
- [30] Andy, P.; Davis, M. E. *Ind. Eng. Chem. Res.* **2004**, *43*, 2922–2928.
- [31] Pellet, R. *J. Catal.* **1998**, *177*, 40–52.
- [32] Mlinar, A. N.; Baur, G. B.; Bong, G. G.; Getsoian, A. B.; Bell, A. T. *J. Catal.* **2012**, *296*, 156–164.
- [33] Mlinar, A. N.; Ho, O. C.; Bong, G. G.; Bell, A. T. *ChemCatChem* **2013**, *5*, 3139–3147.
- [34] Kiessling, D.; Froment, G. F. *Appl. Catal.* **1991**, *71*, 123–138.
- [35] Hartmann, M.; Pöppel, A.; Kevan, L. *J. Phys. Chem.* **1996**, *100*, 9906–9910.
- [36] Mlinar, A. N.; Shylesh, S.; Ho, O. C.; Bell, A. T. *ACS Catal.* **2014**, *4*, 337–343.
- [37] Hulea, V.; Fajula, F. *J. Catal.* **2004**, *225*, 213–222.
- [38] Tanaka, M.; Itadani, A.; Kuroda, Y.; Iwamoto, M. *J. Phys. Chem. C.* **2012**, *116*, 5664–5672.
- [39] Majano, G.; Delmotte, L.; Valtchev, V.; Mintova, S. *Chem. Mater.* **2009**, *21*, 4184–4191.

- [40] Kamimura, Y.; Chaikittisilp, W.; Itabashi, K.; Shimojima, A.; Okubo, T. *Chem. Asian J.* **2010**, *5*, 2182–2191.
- [41] Chaikittisilp, W.; Yokoi, T.; Okubo, T. *Microporous Mesoporous Mater.* **2008**, *116*, 188–195.
- [42] Ghosh, A. K.; Kydd, R. A. *J. Catal.* **1986**, *100*, 185–195.
- [43] U.S. Energy Information Administration; *Table 2. Natural Gas Production, Transmission, and Consumption, by State, 2013*; 2015 (Accessed March 3, 2015). http://www.eia.gov/naturalgas/annual/pdf/table_002.pdf.
- [44] de Klerk, A. *Fischer-Tropsch Refining*; Wiley-VCH Verlag Press: Weinheim, Germany, 2011.
- [45] Basset, J.-M.; Coperet, C.; Soulivong, M., D. and Taoufik; Cazat, J. T. *Acc. Chem. Res.* **2010**, *43*, 323–334.
- [46] Haibach, M. C.; Kundu, S.; Brookhart, M.; Goldman, A. S. *Acc. Chem. Res.* **2012**, *45*, 947–958.
- [47] Chen, C. Y.; O’Rear, D. J.; Leung, P. *Top. Catal.* **2012**, *55*, 1344–1361.
- [48] Goldman, A. S.; Roy, A. H.; Huang, Z.; Ahuja, R.; Schinski, W.; Brookhart, M. *Science* **2006**, *312*, 257–261.
- [49] Bailey, B. C.; Schrock, R. R.; Kundu, S.; Goldman, A. S.; Huang, Z.; Brookhart, M. *Organometallics* **2009**, *28*, 355–360.
- [50] Dobereiner, G. E.; Yuan, J.; Schrock, R. R.; Goldman, A. S.; Hackenberg, J. D. *J. Am. Chem. Soc.* **2013**, *135*, 12572–12575.
- [51] Fogg, D. E.; dos Santos, E. N. *Coord. Chem. Rev.* **2004**, *248*, 2365–2379.
- [52] Wasilke, J. C.; Obrey, S. J.; Baker, R. T.; Bazan, G. C. *Chem. Rev.* **2005**, *105*, 1001–1020.

- [53] Leitch, D. C.; Lam, Y. C.; Labinger, J. A.; Bercaw, J. E. *J. Am. Chem. Soc.* **2013**, *135*, 10302–10305.
- [54] Leitch, D. C.; Labinger, J. A.; Bercaw, J. E. *Organometallics* **2014**, *33*, 3353–3365.
- [55] Choi, J.; MacArthur, A. H. R.; Brookhart, M.; Goldman, A. S. *Chem. Rev.* **2011**, *111*, 1761–1779.
- [56] Gupta, M.; Hagen, C.; Flesher, R. J.; Kaska, W. C.; Jensen, C. M. *Chem. Commun.* **1996**, 2083–2084.
- [57] Jensen, C. M. *Chem. Commun.* **1999**, 2443–2449.
- [58] Liu, F.; Goldman, A. S. *Chem. Commun.* **1999**, 655–656.
- [59] Göttker-Schnetmann, I.; Brookhart, M. *J. Am. Chem. Soc.* **2004**, *126*, 9330–9338.
- [60] Huang, Z.; Brookhart, M.; Goldman, A. S.; Kundu, S.; Ray, A.; Scott, S. L.; Vicente, B. C. *Adv. Synth. Catal.* **2009**, *351*, 188–206.
- [61] Punji, B.; Emge, T. J.; Goldman, A. S. *Organometallics* **2010**, *29*, 2702–2709.
- [62] Nawara-Hultsch, A. J.; Hackenberg, J. D.; Punji, B.; Supplee, C.; Emge, T. J.; Bailey, B. C.; Schrock, R. R.; Brookhart, M.; Goldman, A. S. *ACS Catal.* **2013**, *3*, 2505–2514.
- [63] McLain, S. J.; Wood, C. D.; Schrock, R. R. *J. Am. Chem. Soc.* **1979**, *101*, 4558–4570.
- [64] McLain, S. J.; Sancho, J.; Schrock, R. R. *J. Am. Chem. Soc.* **1979**, *101*, 5451–5453.
- [65] Haenel, M. W.; Oevers, S.; Angermund, K.; Kaska, W. C.; Fan, H.-J.; Hall, M. B. *Angew. Chem. Int. Ed.* **2001**, *40*, 3596–3600.

- [66] Chao, S. T.; Lara, N. C.; Lin, S.; Day, M. W.; Agapie, T. *Angew. Chem. Int. Ed.* **2011**, *50*, 7529–7532.
- [67] Tanaka, R.; Yamashita, M.; Chung, L. W.; Morokuma, K.; Nozaki, K. *Organometallics* **2011**, *30*, 6742–6750.
- [68] Avent, A. G.; Bedford, R. B.; Chaloner, P. A.; Dewa, S. Z.; Hitchcock, P. B. *J. Chem. Soc., Dalton Trans.* **1996**, 4633.
- [69] McInturff, E. L.; Mowat, J.; Waldeck, A. R.; Krische, M. J. *Angew. Chem. Int. Ed.* **2013**, *53*, 1390–1394.
- [70] Zhan, B.; Moden, B.; Dakka, J.; Santiesteban, J.; Iglesia, E. *J. Catal.* **2007**, *245*, 316–325.
- [71] Li, Y.; Armor, J. N. *Appl. Catal. B* **1993**, *2*, 239.
- [72] Zones, S. I.; *US 4,544,538: Zeolite SSZ-13 and its Method of Preparation*; US Patent Office; 1985.
- [73] Iwamoto, M.; Furukawa, H.; Mine, Y.; Uemura, F.; Mikuriya, S.-i.; Kagawa, S. *J. Chem. Soc., Chem. Commun.* **1986**, 1272–1273.
- [74] Iwamoto, M.; Yahiro, H.; Torikai, Y.; Yoshioka, T. *Chem. Lett.* **1990**, 1967–1970.
- [75] Sato, S.; Yu-u, Y.; Yahiro, H.; Mizuno, N.; Iwamoto, M. *Appl. Catal.* **1991**, *70*, L1–L5.
- [76] Zones, S. I.; *US 5,194,235: Synthesis of SSZ-16 Zeolite Catalyst*; US Patent Office; 1993.
- [77] Andersen, P. J.; Bailie, J. E.; Casci, J. L.; Chen, H.-Y.; Fedeyko, J. M.; Foo, R. K. S.; Rajaram, R. R.; *US 2010/0290963 A1: Transition Metal/Zeolite SCR Catalysts*; US Patent Office; 2010.
- [78] Rak, Z. S.; Veringa, H. J. *React. Kinet. Catal. Lett.* **1997**, *60*, 303–312.

- [79] Ciambelli, P.; Corbo, P.; Gaudino, M. C.; Migliardini, F.; Sannino, D. *Top. Catal.* **2001**, *16/17*, 413–417.
- [80] Wu, J.-F.; Yu, S.-M.; Wang, W. D.; Fan, Y.-X.; Bai, S.; Zhang, C.-W.; Gao, Q.; Huang, J.; Wang, W. *J. Am. Chem. Soc.* **2013**, *135*, 13567–13573.
- [81] Narsimhan, K.; Michaelis, V. K.; Mathies, G.; Gunther, W. R.; Griffin, R. G.; Román-Leshkov, Y. *J. Am. Chem. Soc.* **2015**, *137*, 1825–1832.
- [82] Huang, W.; Sun, W. Z.; Li, F. *AIChE J.* **2010**, *56*, 1279–1284.
- [83] Mole, T.; Anderson, J. R.; Creer, G. *Appl. Catal.* **1985**, *17*, 141–154.
- [84] Inui, T.; Kim, J. B.; Takeguchi, T. *Zeolites* **1996**, *17*, 354–360.
- [85] Froment, G. F.; Dehertog, W. J. H.; Marchi, A. J. In *Catalysis: Vol 9*; Spivey, J. J., Ed.; Royal Society of Chemistry: Cambridge, UK, 1992; pp 1–64.
- [86] Dai, W.; Wang, X.; Wu, G.; Guan, N.; Hunger, M.; Li, L. *ACS Catal.* **2011**, *1*, 292–299.
- [87] Kaiser, S. W.; *US 4,499,327: Using Silicoaluminophosphate Molecular Sieve Catalyst*; US Patent Office; 1985.
- [88] Vora, B.; Chen, J. Q.; Bozzano, A.; Glover, B.; Barger, P. *Catal. Today* **2009**, *141*, 77–83.
- [89] Olsbye, U.; Svelle, S.; Bjørgen, M.; Beato, P.; Janssens, T. V. W.; Joensen, F.; Bordiga, S.; Lillerud, K.-P. *Angew. Chem. Int. Ed.* **2012**, *51*, 5810–5831.
- [90] Hereijgers, B. P. C.; Bleken, F.; Nilsen, M. H.; Svelle, S. *J. Catal.* **2009**, *264*, 77–87.
- [91] Dahl, I. M.; Kolboe, S. *Catal. Lett.* **1993**, *20*, 329–336.
- [92] Bjørgen, M.; Svelle, S.; Joensen, F.; Nerlov, J.; Kolboe, S.; Bonino, F.; Palumbo, L.; Bordiga, S.; Olsbye, U. *J. Catal.* **2007**, *249*, 195–207.

- [93] Zhu, Q.; Kondo, J. N.; Tatsumi, T.; Inagaki, S.; Ohnuma, R.; Kubota, Y.; Shimodaira, Y.; Kobayashi, H.; Domen, K. *J. Phys. Chem. C* **2007**, *111*, 5409–5415.
- [94] Chen, D.; Moljord, K.; Fuglerud, T.; Holmen, A. *Microporous Mesoporous Mater.* **1999**, *29*, 191–203,.
- [95] Baerlocher, C.; McCusker, L. B.; Olson, D. H. *Atlas of Zeolite Framework Types*, 6th ed.; Elsevier: Amsterdam, 2007.
- [96] Haw, J. F.; Marcus, D. M. *Top. Catal.* **2005**, *34*, 41–48.
- [97] Arstad, B.; Nicholas, J. B.; Haw, J. F. *J. Am. Chem. Soc.* **2004**, *126*, 2991–3001.
- [98] Lok, B. M.; Messina, C. A.; Patton, R. L.; Gajek, R. T.; Cannan, T. R.; Flanigen, E. M. *J. Am. Chem. Soc.* **1984**, *106*, 6092–6093.
- [99] Lok, B. M.; Messina, C. A.; Patton, R. L.; Gajek, R. T.; Cannan, T. R.; Flanigen, E. M.; *US 4,440,871: Crystalline Silicoaluminophosphates*; US Patent Office; 1984.
- [100] Liang, J.; Li, H.; Zhao, S.; Guo, W.; Wang, R.; Ying, M. *Appl. Catal.* **1990**, *64*, 31–40.
- [101] Vora, B. V.; Marker, T. L.; Barger, P. T.; Nilsen, H. R.; Kvisle, S.; Fuglerud, T. *Stud. Surf. Sci. Catal.* **1997**, *107*, 87–98.
- [102] Chen, J. Q.; Bozzano, A.; Glover, B.; Fuglerud, T.; Kvisle, S. *Catal. Today* **2005**, *106*, 103–107.
- [103] Yuen, L.-T.; Zones, S. I.; Harris, T. V.; Gallegos, E. J.; Auroux, A. *Microporous Mater.* **1994**, *2*, 105–117.
- [104] Zhu, Q.; Kondo, J. N.; Ohnuma, R.; Kubota, Y.; Yamaguchi, M.; Tatsumi, T. *Microporous Mesoporous Mater.* **2008**, *112*, 153–161.

- [105] Bhawe, Y.; Moliner-Marin, M.; Lunn, J. D.; Liu, Y.; Malek, A.; Davis, M. *ACS Catal.* **2012**, *2*, 2490–2495.
- [106] Schmidt, J. E.; Deimund, M. A.; Davis, M. E. *Chem. Mater.* **2014**, *26*, 7099–7105.
- [107] Zones, S. I. *Microporous Mesoporous Mater.* **2011**, *144*, 1–8.
- [108] Dahl, I. M.; Mostad, H.; Akporiaye, D.; Wendell, R. *Microporous Mesoporous Mater.* **1999**, *29*, 185–190.
- [109] Ward, J. W.; *US 3,929,672: Ammonia-Stable Y Zeolite Compositions*; US Patent Office; 1975.
- [110] Lago, R. M.; Haag, W. O.; Mikovsky, R. J.; Olson, D. H.; Hellring, S. D.; Schmitt, K. D.; Kerr, G. T. In *Proceedings of the 7th Annual International Zeolite Conference*; Murakami, Y.; Ijima, A.; Ward, J. W., Eds.; Elsevier: Amsterdam, 1986; Vol. 28, pp 677–684.
- [111] Bourgoigne, M.; Guth, J. L.; Wey, R.; *US 4,503,024: Process for the Preparation of Synthetic Zeolites, and Zeolites Obtained by Said Process*; US Patent Office; 1985.
- [112] Bates, S. A.; Verma, A. A.; Paolucci, C.; Parekh, A. A.; Anggara, T.; Yezerets, A.; Schneider, W. F.; Miller, J. T.; Delgass, W. N.; Ribeiro, F. H. *J. Catal.* **2014**, *312*, 87–97.
- [113] Xu, L.; Du, A.; Wei, Y.; Wang, Y.; Yu, Z.; He, Y.; Zhang, X.; Liu, Z. *Microporous Mesoporous Mater.* **2008**, *115*, 332–337.
- [114] Ashtekar, S.; Chilukuri, S. V. V.; Chakrabarty, D. K. *J. Phys. Chem.* **1998**, *98*, 4878–4883.
- [115] Zibrowius, B.; Löffler, E.; Hunger, M. *Zeolites* **1992**, *12*, 167–174.

- [116] Vomscheid, R.; Briend, M.; Peltre, M. J.; Massiani, P.; Man, P. P.; Barthomeuf, D. *J. Chem. Soc., Chem. Commun.* **1993**, 544–546.
- [117] Tan, J.; Liu, Z.; Bao, X.; Liu, X.; Han, X.; He, C.; Zhai, R. *Microporous Mesoporous Mater.* **2002**, *53*, 97–98.
- [118] Nishiyama, N.; Kawaguchi, M.; Hirota, Y.; Van Vu, D.; Egashira, Y.; Ueyama, K. *Appl. Catal. A.* **2009**, *362*, 193–199.
- [119] Dai, W.; Wu, G.; Li, L.; Guan, N.; Hunger, M. *ACS Catal.* **2013**, *3*, 588–596.
- [120] Hartmann, M. *Angew. Chem. Int. Ed.* **2004**, *43*, 5880–5882.
- [121] Wu, L.; Degirmenci, V.; Magusin, P. C. M. M.; Lousberg, N. J. H. G. M.; Hensen, E. J. M. *J. Catal.* **2013**, *298*, 27–40.
- [122] Ilias, S.; Bhan, A. *ACS Catal.* **2013**, *3*, 18–31.
- [123] Stöcker, M. *Microporous Mesoporous Mater.* **2005**, *82*, 257–292.
- [124] Schulz, H. *Catal. Today* **2010**, *154*, 183–194.
- [125] Yuen, L.-T.; Zones, S.; Harris, T. V.; Gallegos, E. J.; Auroux, A. *Microporous Mater.* **1994**, *2*, 105–117.
- [126] Barger, P. In *Zeolites for Cleaner Technologies*; Guisnet, M.; Gilson, J.-P., Eds.; Imperial College Press: London, UK, 2002; Vol. 3, pp 239–260.
- [127] Bleken, F.; Bjørgen, M.; Palumbo, L.; Bordiga, S.; Svelle, S.; Lillerud, K.-P.; Olsbye, U. *Top. Catal.* **2009**, *52*, 218–228.
- [128] Dahl, I. M.; Kolboe, S. *J. Catal.* **1994**, *149*, 458–464.
- [129] Dahl, I. M.; Kolboe, S. *J. Catal.* **1996**, *161*, 304–309.
- [130] Guisnet, M.; Costa, L.; Ribeiro, F. R. *J. Mol. Catal. A: Chem.* **2009**, *305*, 69–83.

- [131] Robson, H. E.; *US 3,904,738: Zeolite RHO*; US Patent Office; 1975.
- [132] Burton, A. W.; Ong, K.; Rea, T.; Chan, I. Y. *Microporous Mesoporous Mater.* **2009**, *117*, 75–90.
- [133] Song, W.; Fu, H.; Haw, J. F. *J. Am. Chem. Soc.* **2001**, *123*, 4749–4754.
- [134] Froment, G. F.; Dehertog, W. J. H.; Marchi, A. J.; Royal Society of Chemistry: Cambridge, 1992; pp 1–64.
- [135] Wilson, S.; Barger, P. *Microporous Mesoporous Mater.* **1999**, *29*, 117–126.
- [136] Cartlidge, S.; Patel, R. In *Zeolites: Facts, Figures, Future*; Jacobs, P. A.; van Santen, R. A., Eds.; Elsevier: Amsterdam, 1989; pp 1151–1161.
- [137] Engelhardt, G.; Lohse, U.; Patzelova, V.; Mägi, M.; Lippmaa, E. *Zeolites* **1983**, *3*, 233–238.
- [138] Wang, Q. L.; Gianetto, G.; Torrealba, M.; Perot, G.; Kappenstein, C.; Guisnet, M. *J. Catal.* **1991**, *130*, 459–470.
- [139] Malola, S.; Svelle, S.; Bleken, F. L.; Swang, O. *Angew. Chem. Int. Ed.* **2011**, *51*, 652–655.
- [140] Lutz, W. *Adv. Mat. Sci. Eng.* **2014**, *2014*, 1–20.
- [141] Scherzer, J. In *Catalytic Materials: Relationship Between Structure and Reactivity*; E., W. T.; A., D. B. R.; G., D. E.; K., B. R. T., Eds.; American Chemical Society: Washington, D.C., 1984; Chapter 11, pp 157–200.
- [142] Tynjälä, P.; Pakkanen, T. T. *Microporous Mesoporous Mater.* **2004**, *20*, 363–369.

Appendix A

Oligomerization Catalyst Characterization and Reaction Data

A.1 Characterization of Materials Used as Catalysts

All materials (with the exception of USY) were synthesized in-house. The powder X-ray diffraction (XRD) patterns for each of these materials as made, after nickel exchange, and after calcination are shown in the following figures.

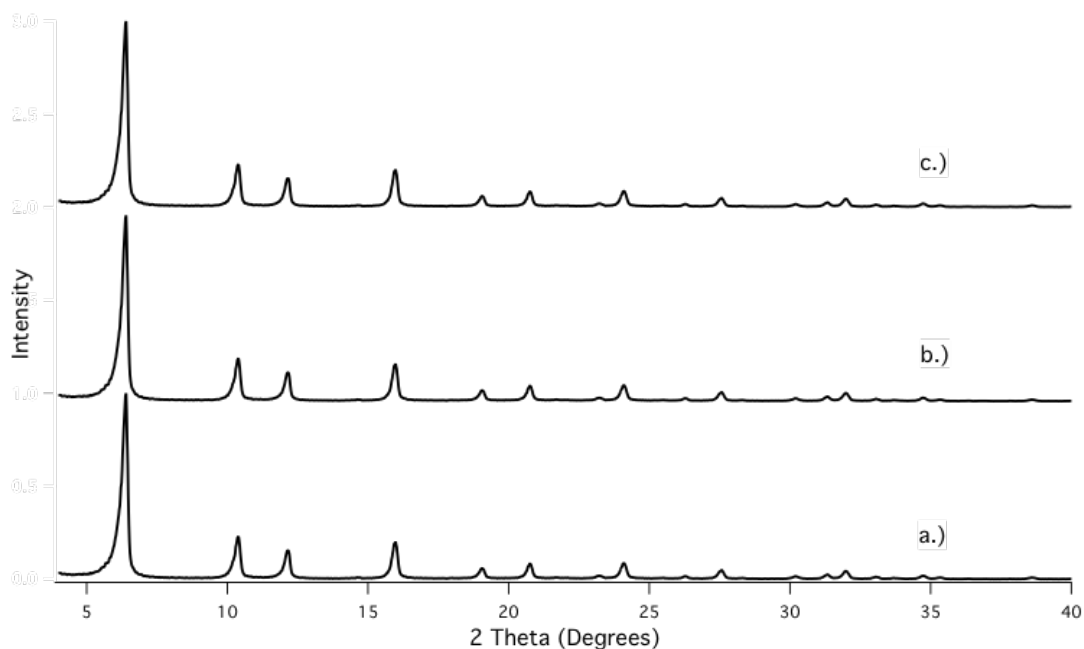


Figure A.1: Patterns of a.) as-received USY, b.) Ni-USY, and c.) calcined Ni-USY.

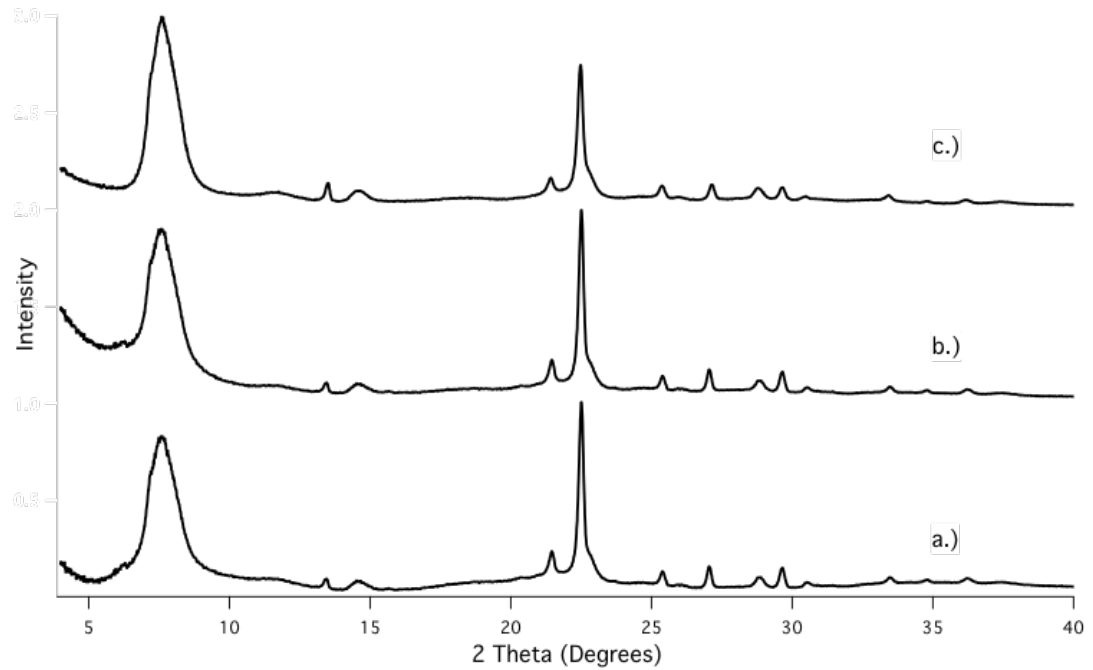


Figure A.2: XRD patterns of a.) as-made CIT-6, b.) Ni-CIT-6, and c.) calcined Ni-CIT-6.

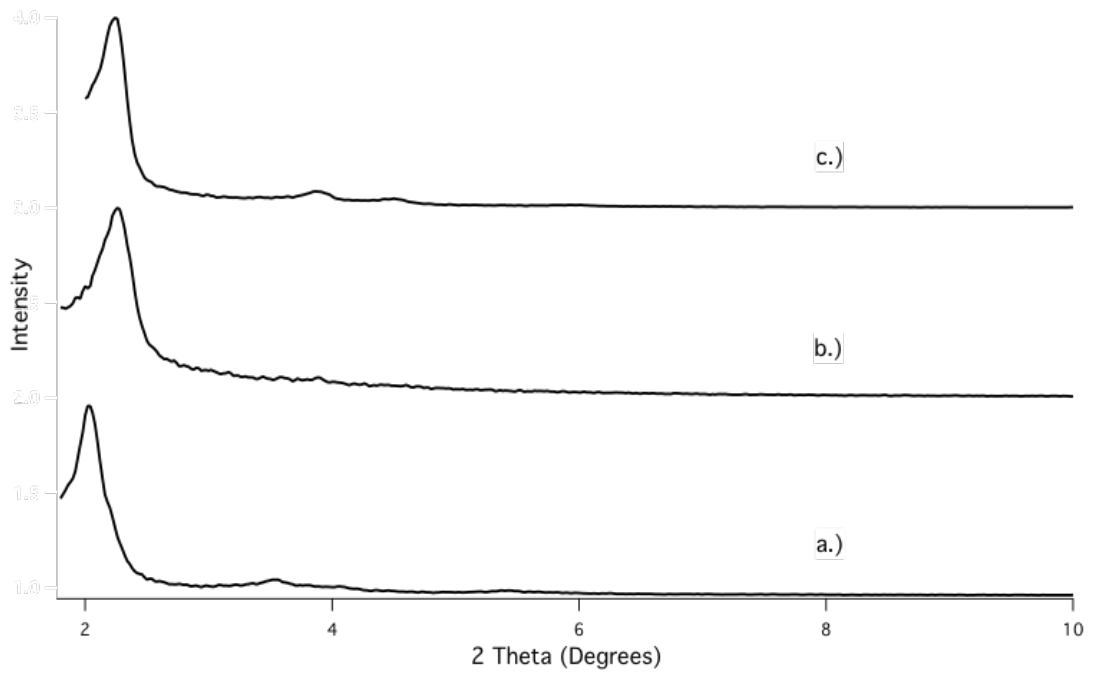


Figure A.3: XRD patterns of a.) as-made Zn-MCM-41, b.) Ni-Zn-MCM-41, and c.) calcined Ni-Zn-MCM-41.

The high-aluminum zeolite beta (HiAl BEA) was synthesized according to a seeded procedure similar to that described by Majano et al.³⁹ The XRD pattern for the zeolite beta seeds is shown in Figure A.4 below. Additionally, the XRD pattern for the resulting solids as made, after nickel exchange, and after calcination are shown below in Figure A.5.

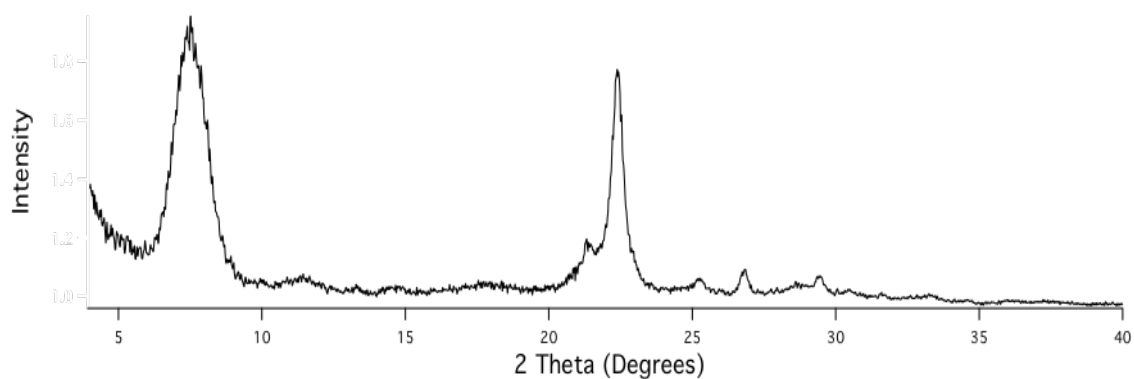


Figure A.4: XRD pattern of Tosoh zeolite beta used as seeds.

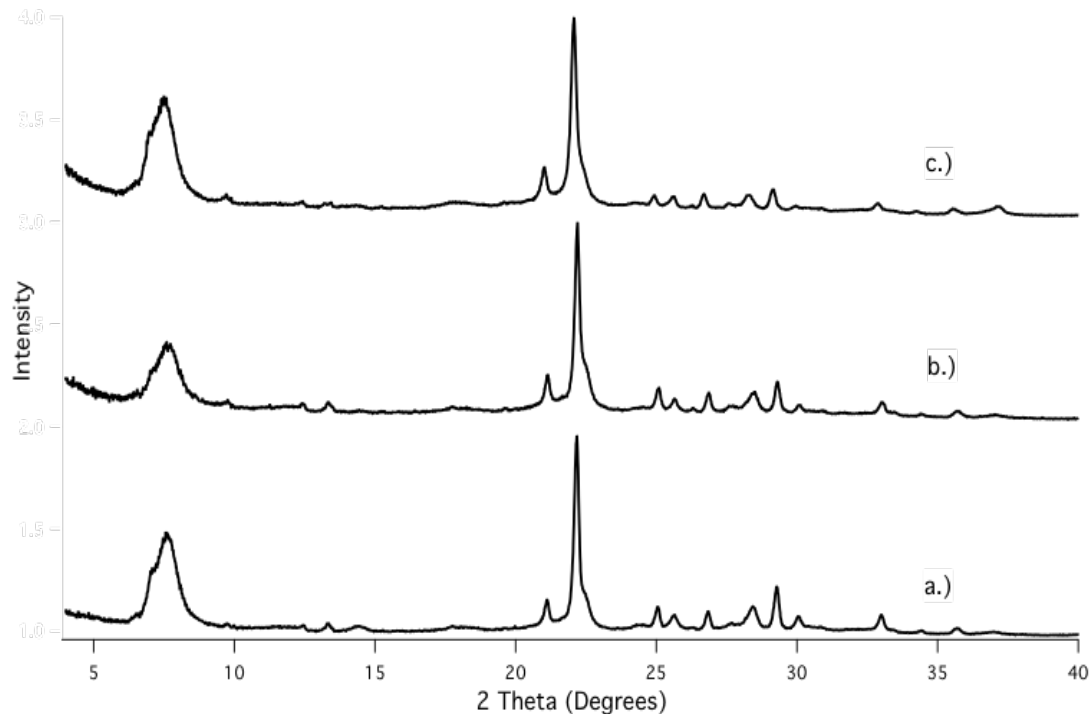


Figure A.5: XRD patterns of a.) as-made HiAl-BEA, b.) Ni-HiAl-BEA, and c.) calcined Ni-HiAl-BEA.

Additionally, a solid-state ^{27}Al NMR experiment was conducted to confirm that all aluminum atoms in HiAl BEA were tetrahedrally coordinated within the zeolite framework. The NMR spectrum is shown in Figure A.6.

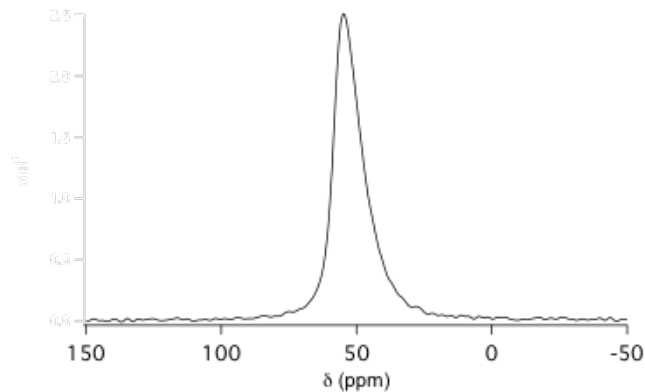


Figure A.6: ^{27}Al NMR of HiAl BEA.

The peak centered near 50 ppm is characteristic of aluminum atoms in tetrahedral coordination, suggesting all aluminum was incorporated into the zeolite framework.^{39, 40, 41} No other peaks were observed in the ^{27}Al NMR spectrum.

To determine micropore volume, Ar adsorption was performed on each sample at 87.45 K with a Quantachrome Autosorb iQ adsorption instrument using a constant-dose method. Samples were off-gassed at 80°C for 1 h, followed by 3 h at 120°C and 10 h at 350°C prior to adsorption measurements. Table A.1 displays the pore volumes for each material in the Ni^{2+} -exchanged, calcined form (determined using the t-plot method).

Material	Micropore Volume [cc/g]
Ni-CIT-6	0.18
Ni-HiAl-BEA	0.16
Ni-USY	0.22
Pore Volume [cc/g]	
Ni-Zn-MCM-41	0.53

Table A.1: Pore volumes for porous materials.

Argon adsorption isotherms for each material after Ni²⁺ exchange and calcination are shown in Figures A.7, A.8, A.9, and A.10.

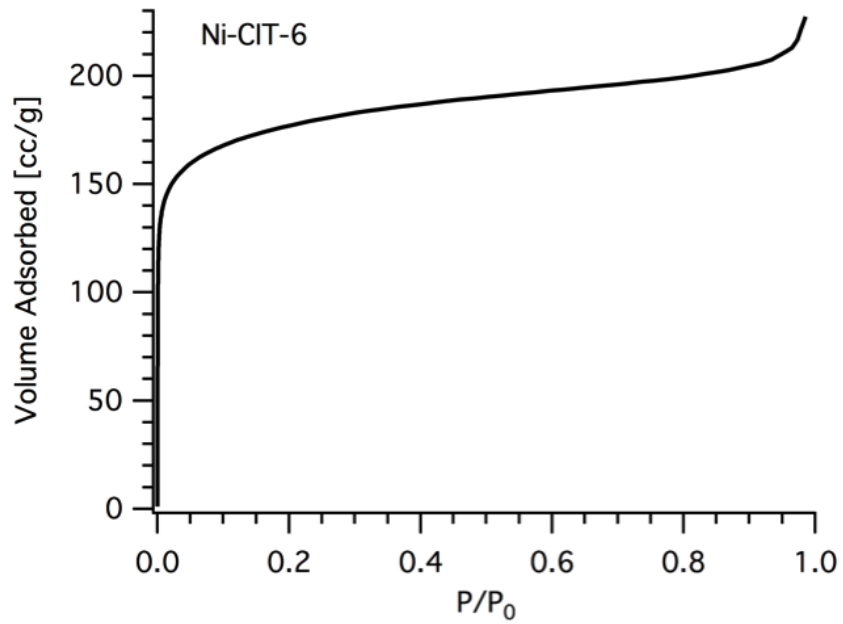


Figure A.7: Argon adsorption isotherm for Ni-CIT-6.

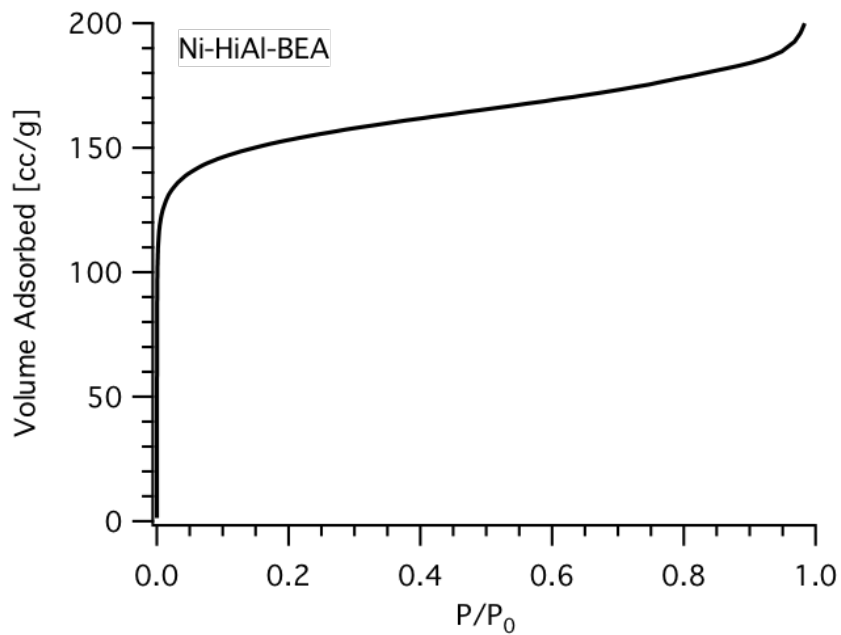


Figure A.8: Argon adsorption isotherm for Ni-HiAl-BEA.

The calculated micropore volume for Ni-HiAl-BEA (0.16 cc/g) is lower than expected for a typical *BEA sample, although this micropore volume is consistent with that reported by Kamimura et al. for a calcined high-aluminum *BEA sample.⁴⁰

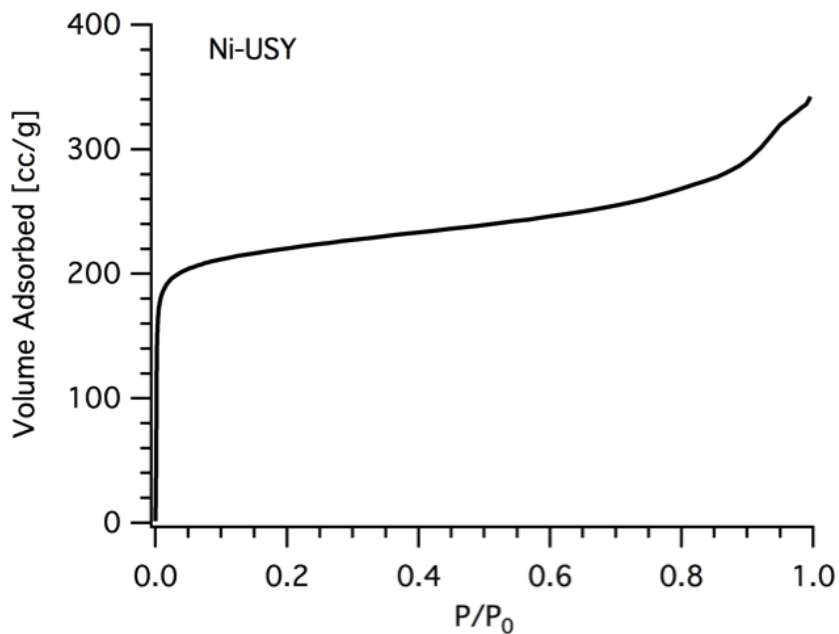


Figure A.9: Argon adsorption isotherm for Ni-USY.

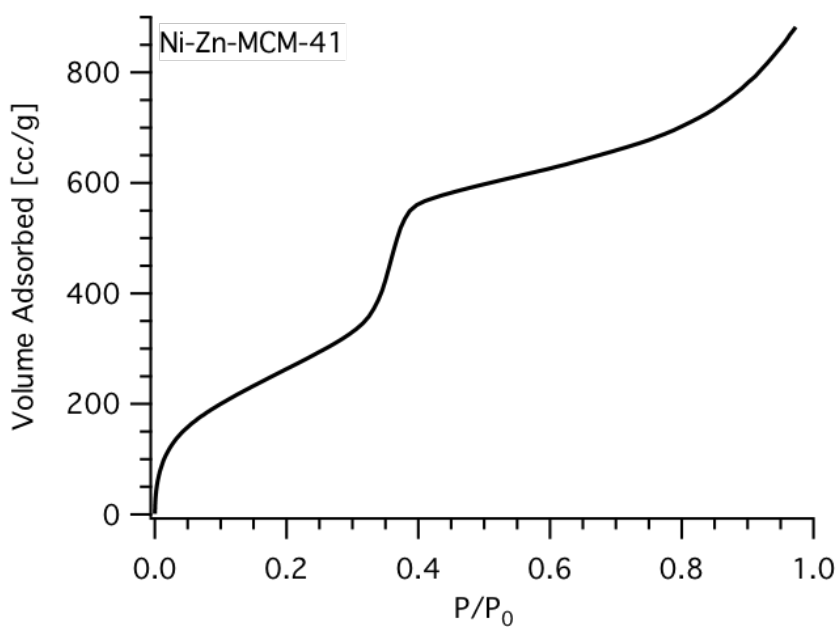


Figure A.10: Argon adsorption isotherm for Ni-Zn-MCM-41.

The results of the NH_3 TPD experiments are also shown for each nickel-exchanged, calcined material in Figure A.11.

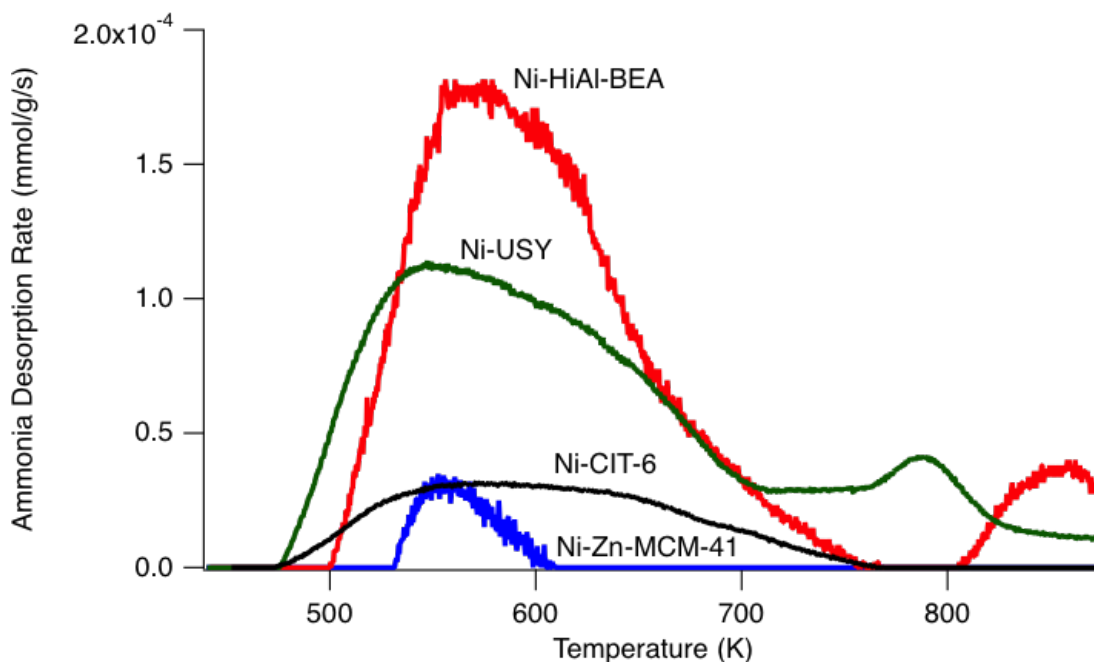


Figure A.11: Ammonia TPD for nickel-exchanged, calcined samples.

Mass-spectrometer signal quantification also allowed for determination of the Brønsted acid site concentration for each material. Table A.2 below shows these acid site concentrations, which are consistent with the elemental analyses determined previously.

Material	Acid Site Concentration [mmol/g]
Ni-CIT-6	0.18
Ni-Zn-MCM-41	0.04
Ni-HiAl-BEA	0.73
Ni-USY	0.68

Table A.2: Brønsted acid site concentrations for the nickel-containing materials.

A.2 Reaction Data at Two Reaction Temperatures

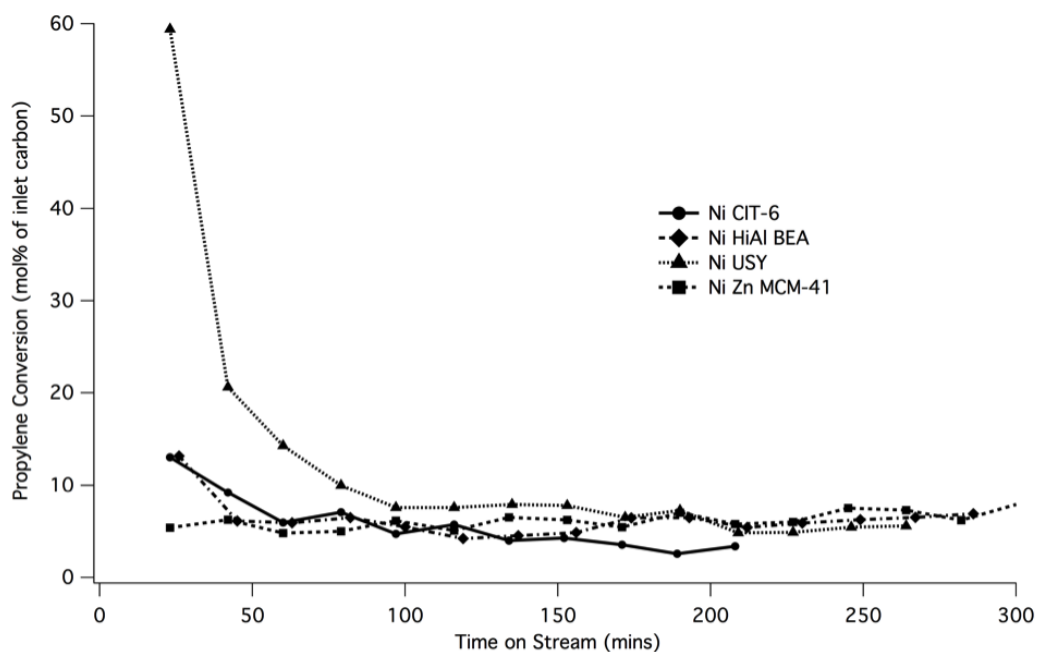


Figure A.12: Propylene conversion vs. TOS for all catalysts at 180°C.

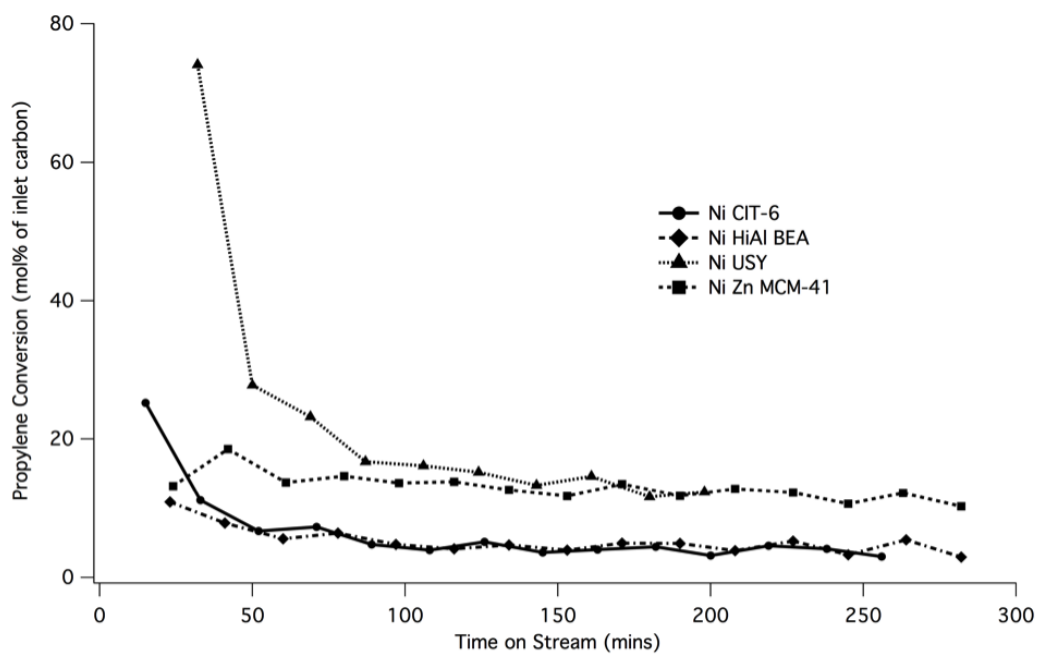


Figure A.13: Propylene conversion vs. TOS for all catalysts at 250°C.

A.3 Complete Selectivity Graphs for All Reaction Runs

Note: Run 1 and Run 2 designate catalyst testing before and after regeneration by calcination in air, respectively.

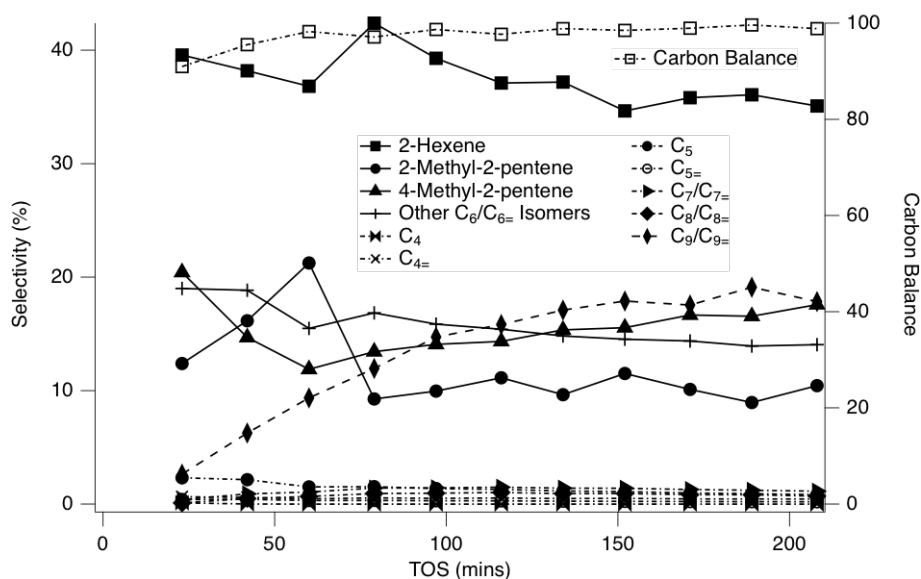


Figure A.14: All selectivities vs. TOS for Run #1 Ni-CIT-6 at 180°C.

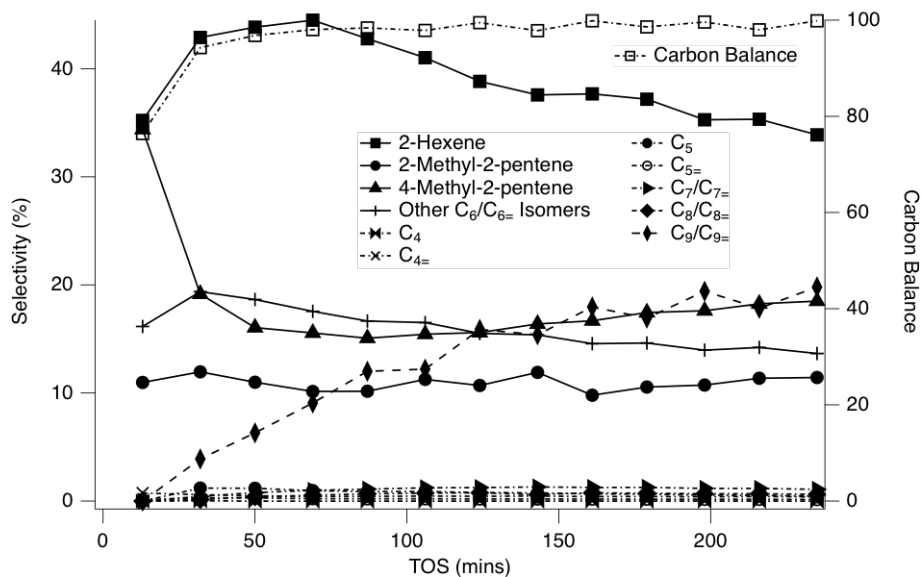


Figure A.15: All selectivities vs. TOS for Run #2 Ni-CIT-6 at 180°C.

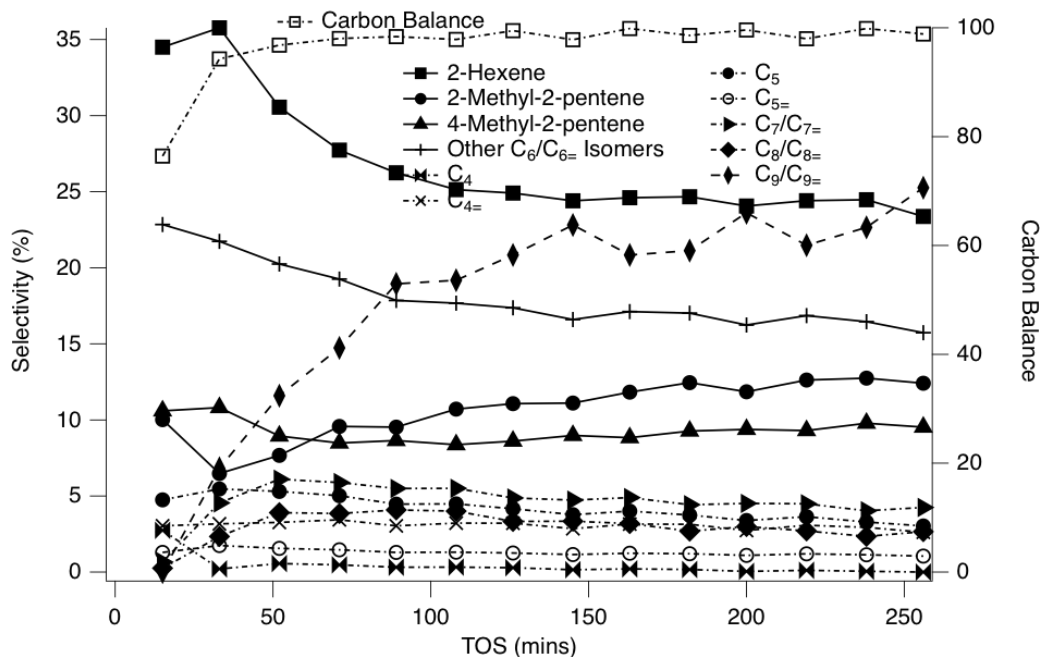


Figure A.16: All selectivities vs. TOS for Run #1 Ni-CIT-6 at 250°C.

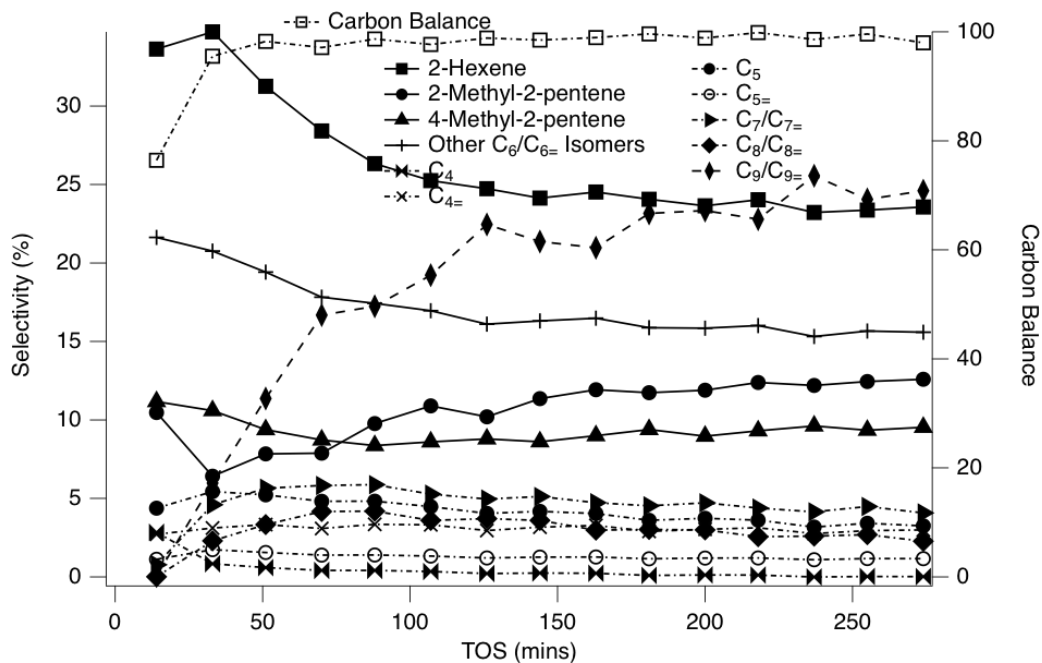


Figure A.17: All selectivities vs. TOS for Run #2 Ni-CIT-6 at 250°C.

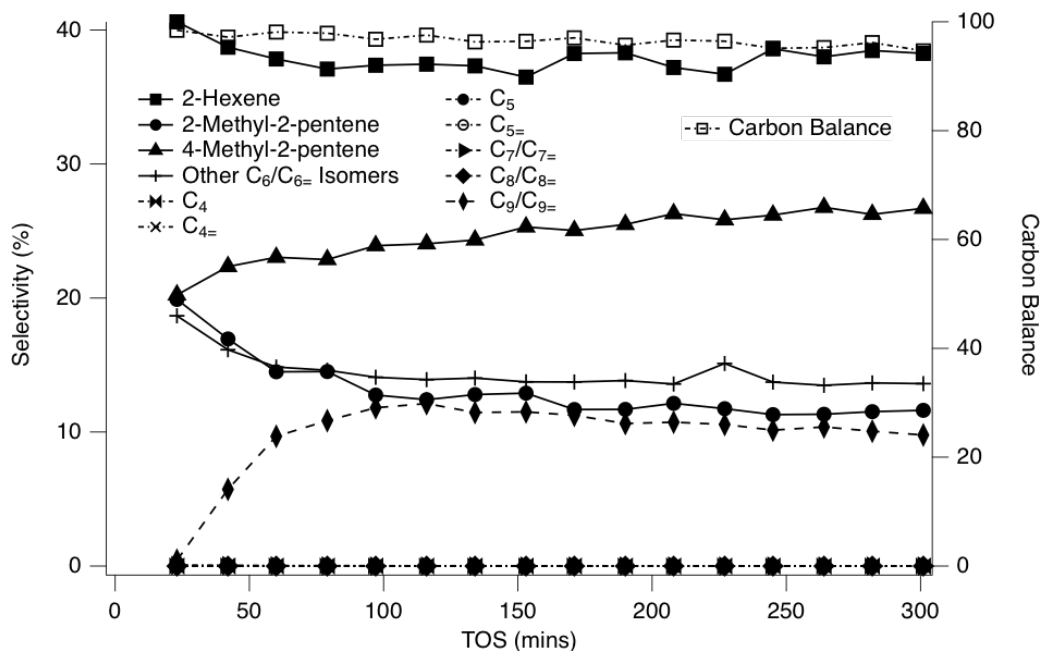


Figure A.18: All selectivities vs. TOS for Run #1 Ni-Zn-MCM-41 at 180°C.

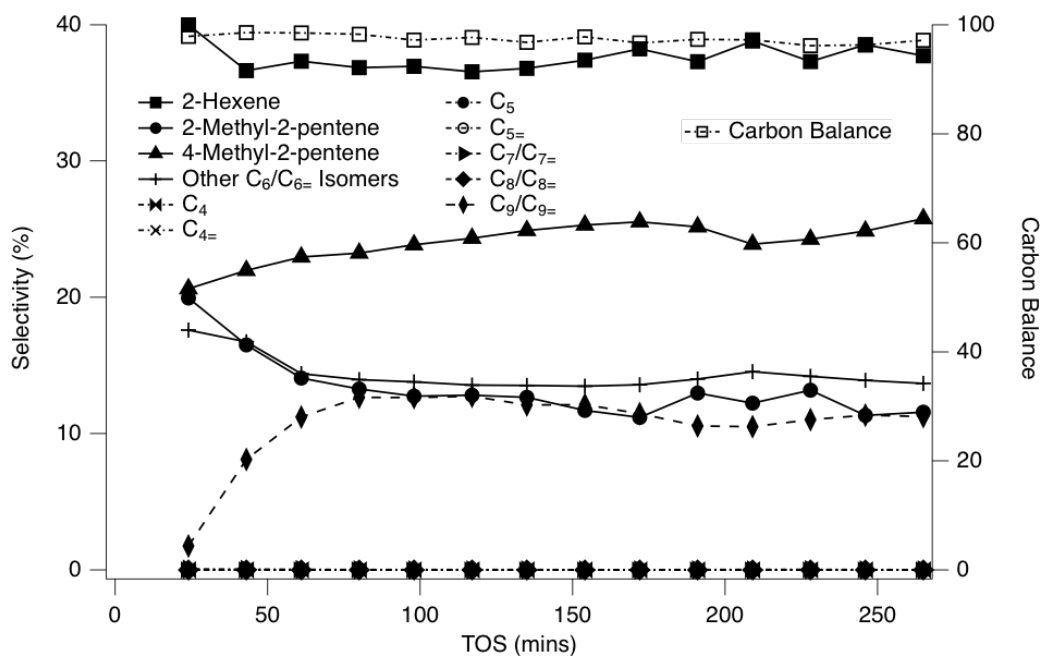


Figure A.19: All selectivities vs. TOS for Run #2 Ni-Zn-MCM-41 at 180°C.

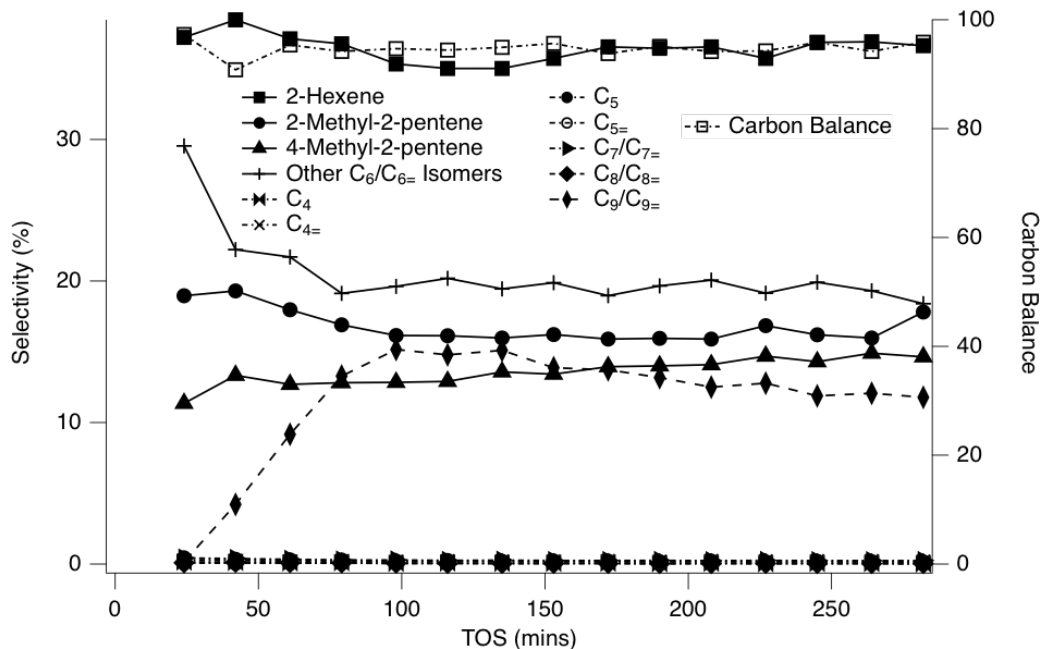


Figure A.20: All selectivities vs. TOS for Run #1 Ni-Zn-MCM-41 at 250°C.

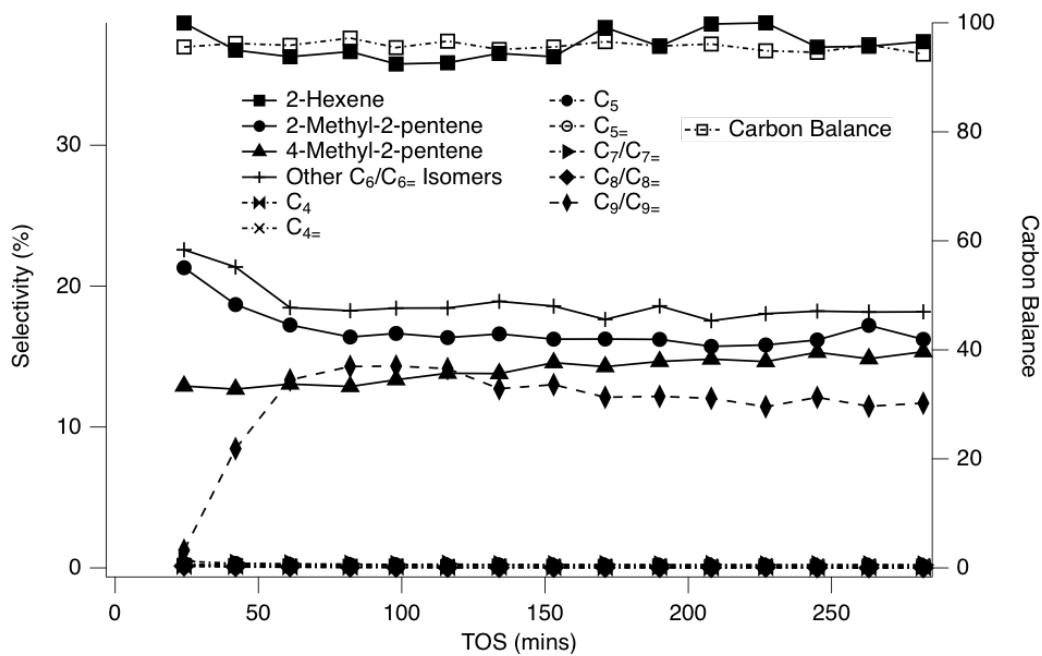


Figure A.21: All selectivities vs. TOS for Run #2 Ni-Zn-MCM-41 at 250°C.

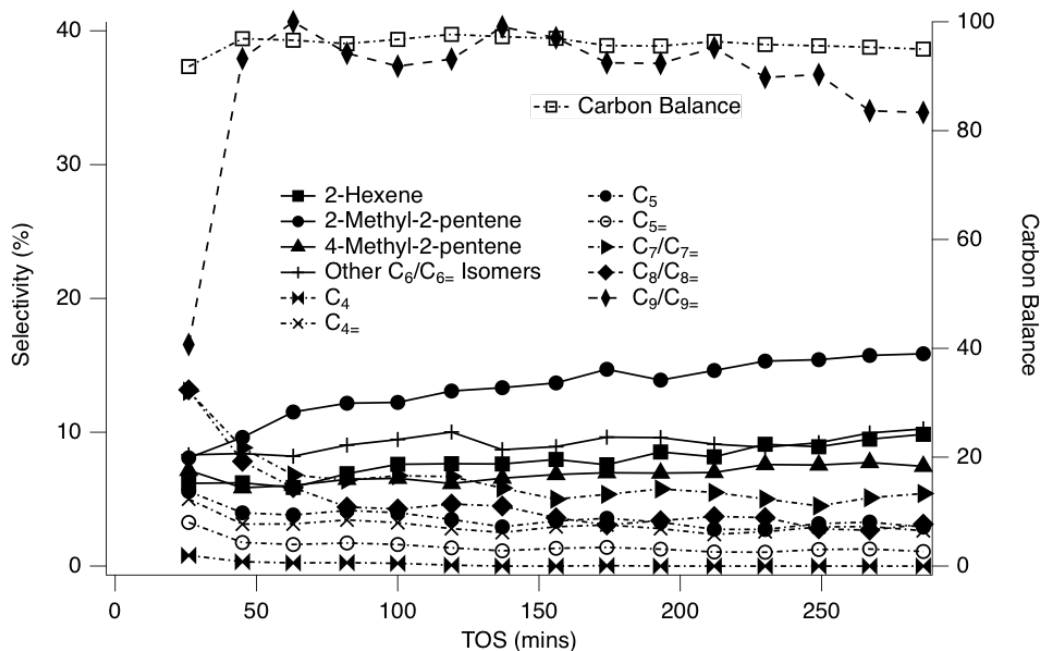


Figure A.22: All selectivities vs. TOS for Run #1 Ni-HiAl-BEA at 180°C.

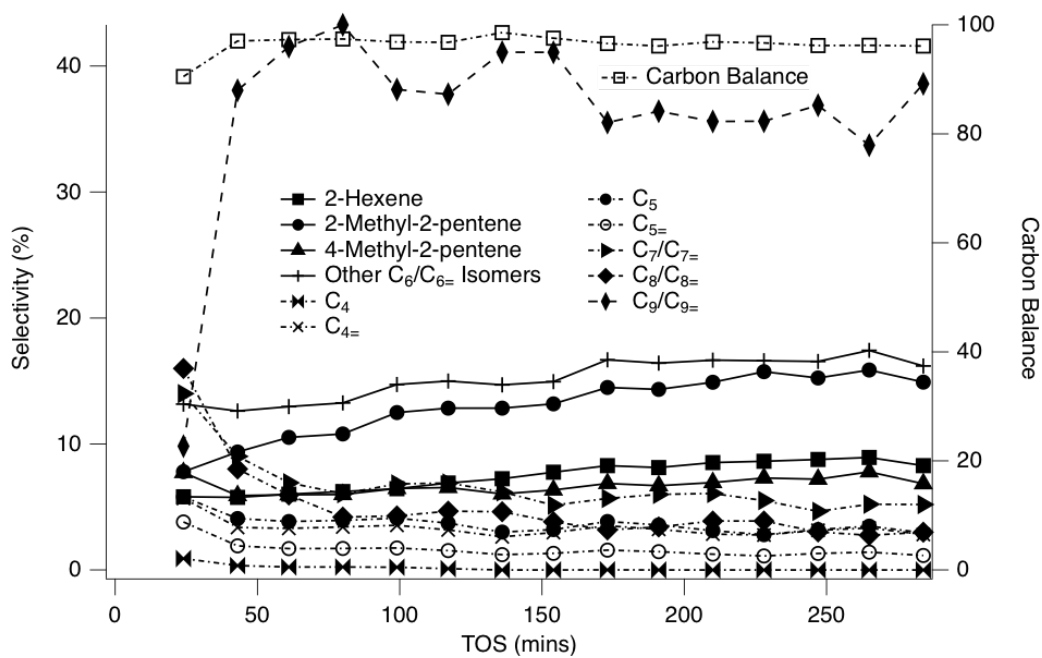


Figure A.23: All selectivities vs. TOS for Run #2 Ni-HiAl-BEA at 180°C.

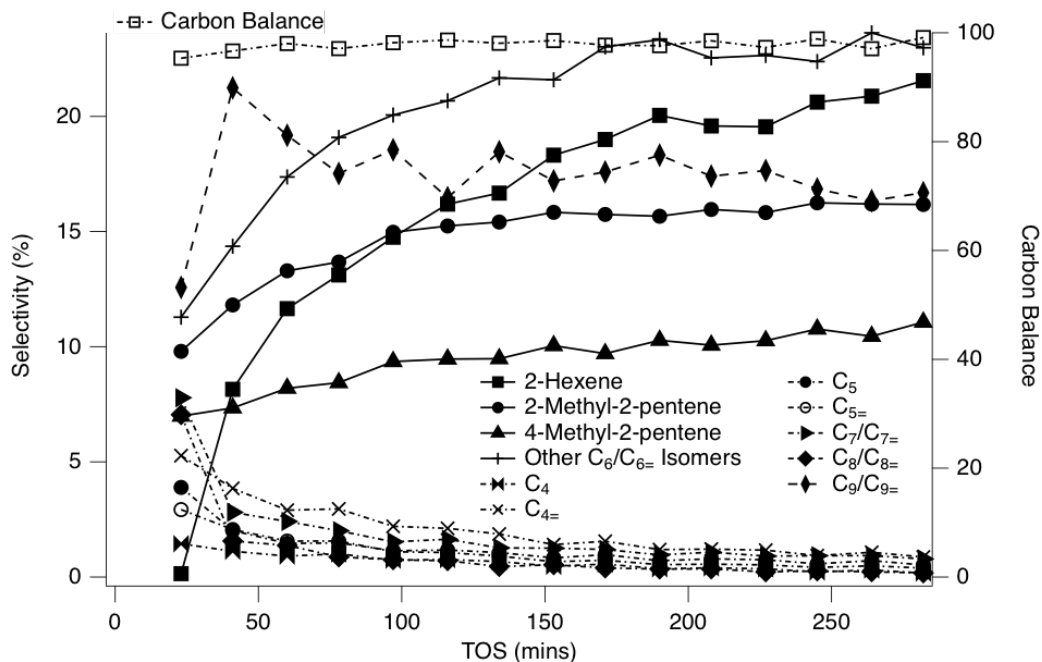


Figure A.24: All selectivities vs. TOS for Run #1 Ni-HiAl-BEA at 250°C.

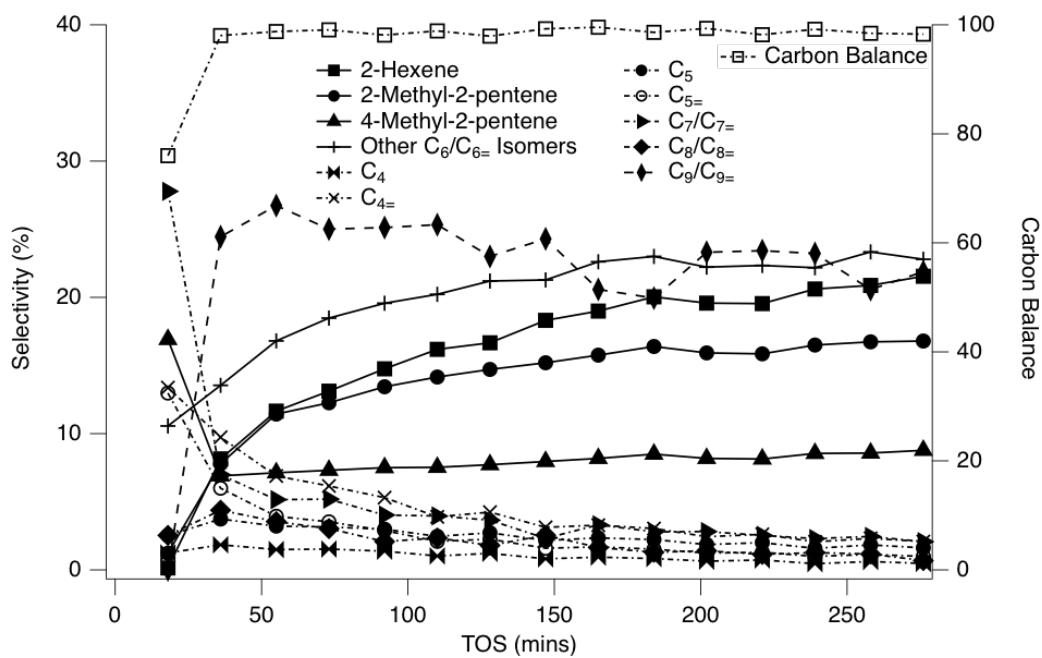


Figure A.25: All selectivities vs. TOS for Run #2 Ni-HiAl-BEA at 250°C.

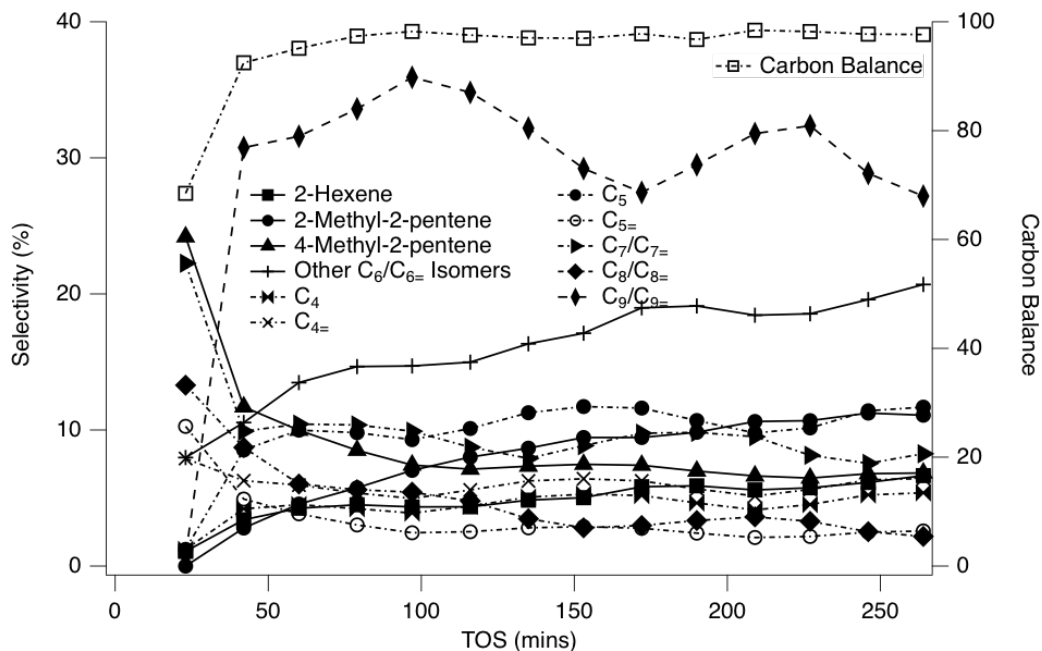


Figure A.26: All selectivities vs. TOS for Run #1 Ni-USY at 180°C.

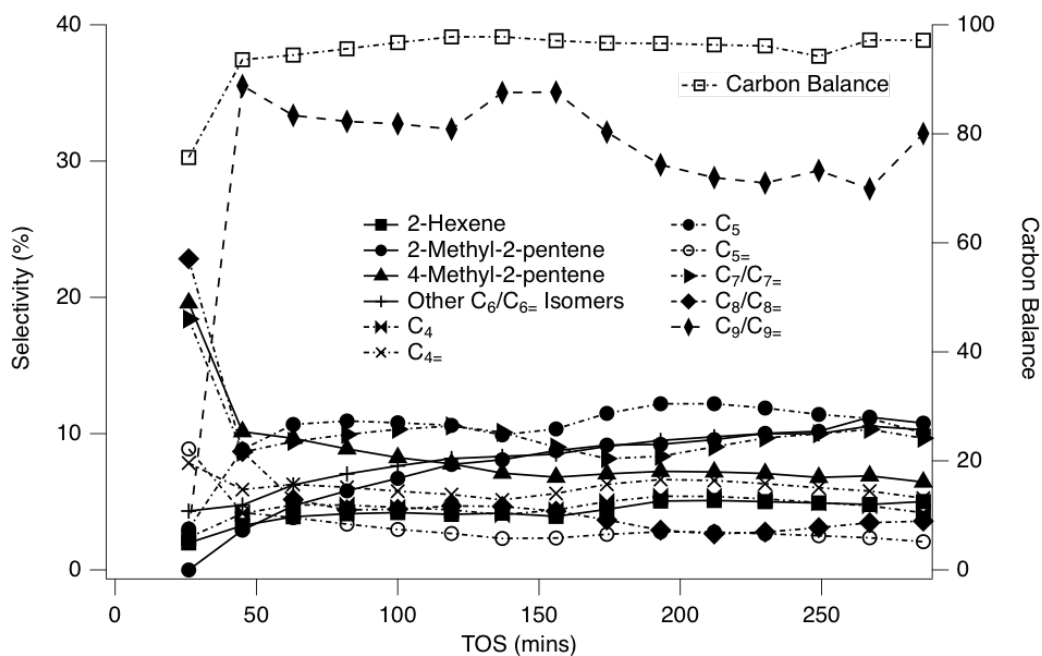


Figure A.27: All selectivities vs. TOS for Run #2 Ni-USY at 180°C.

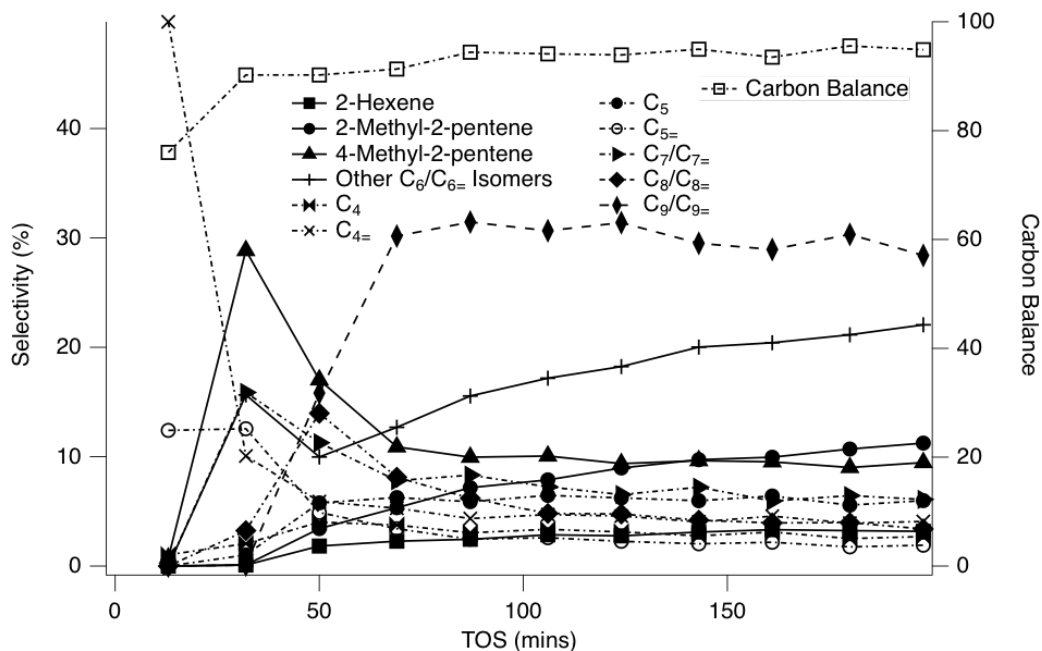


Figure A.28: All selectivities vs. TOS for Run #1 Ni-USY at 250°C.

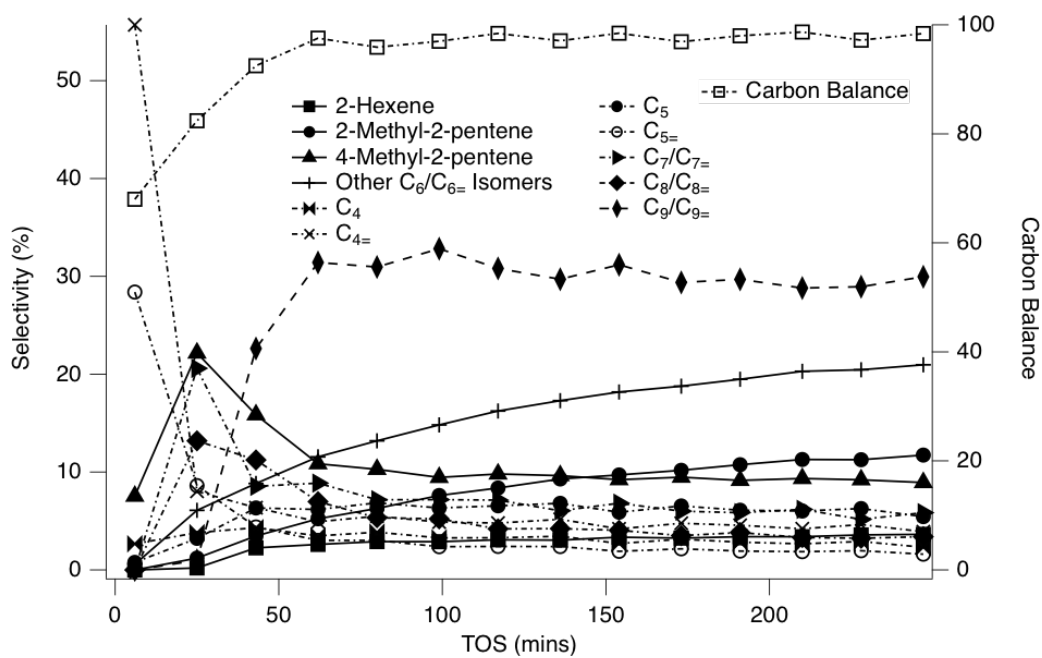


Figure A.29: All selectivities vs. TOS for Run #2 Ni-USY at 250°C.

A.4 Comparisons of Reaction Data at 180°C and 250°C For Ni-CIT-6 and Samples Exchanged with Mg^{2+} or Ca^{2+} , Calcined, and Ni^{2+} -Exchanged

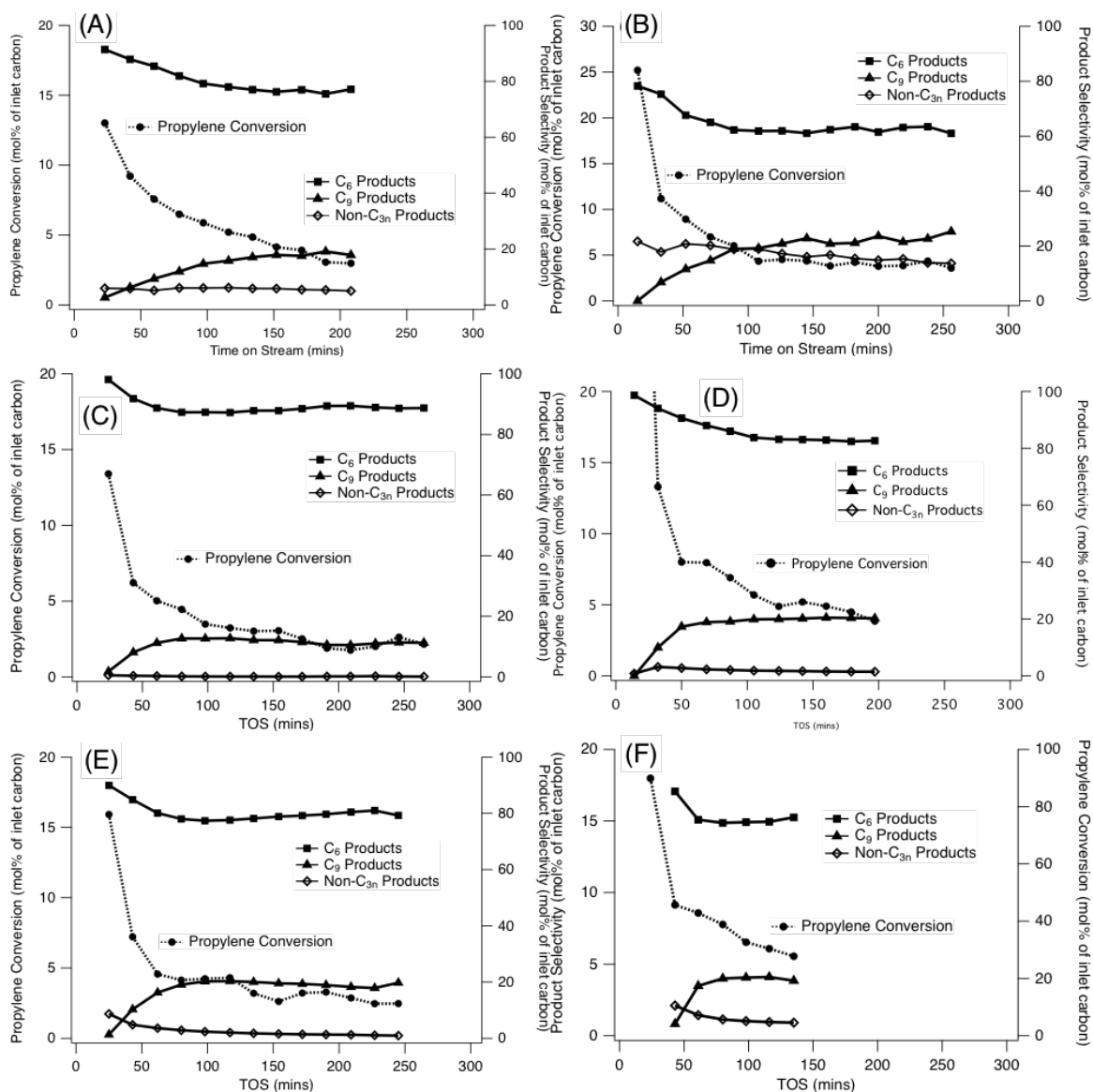


Figure A.30: Reaction comparisons for Ni-CIT-6 at 180°C (A), Ni-CIT-6 at 250°C (B), Ni-Mg-CIT-6 at 180°C (C), Ni-Mg-CIT-6 at 250°C (D), Ni-Ca-CIT-6 at 180°C (E), and Ni-Ca-CIT-6 at 250°C (F).

A.5 Post-Reaction Powder XRDs

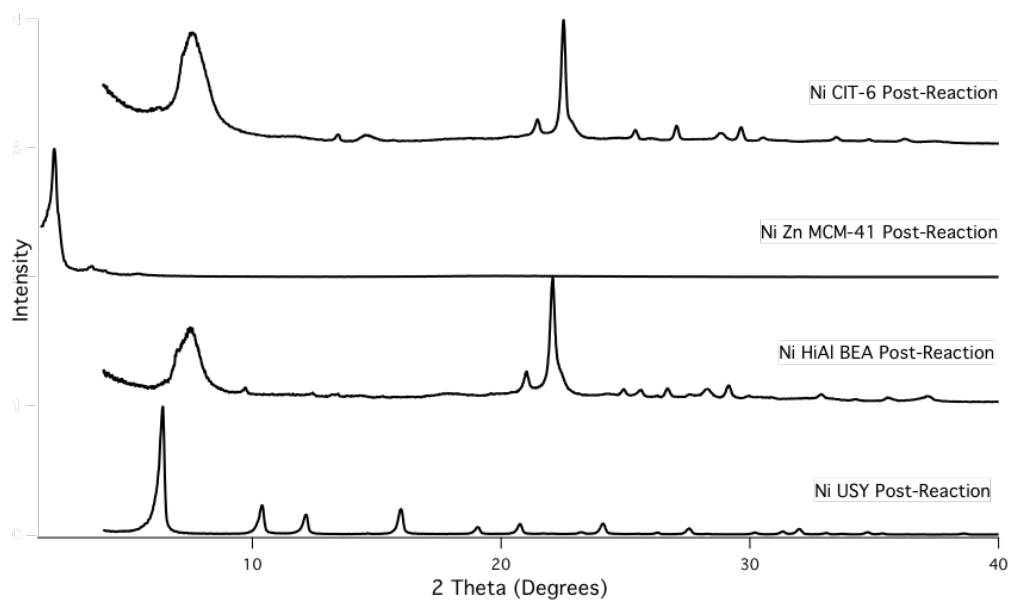


Figure A.31: XRD patterns for all catalysts post-reaction.

A.6 Post-Reaction TGAs of Spent Catalysts

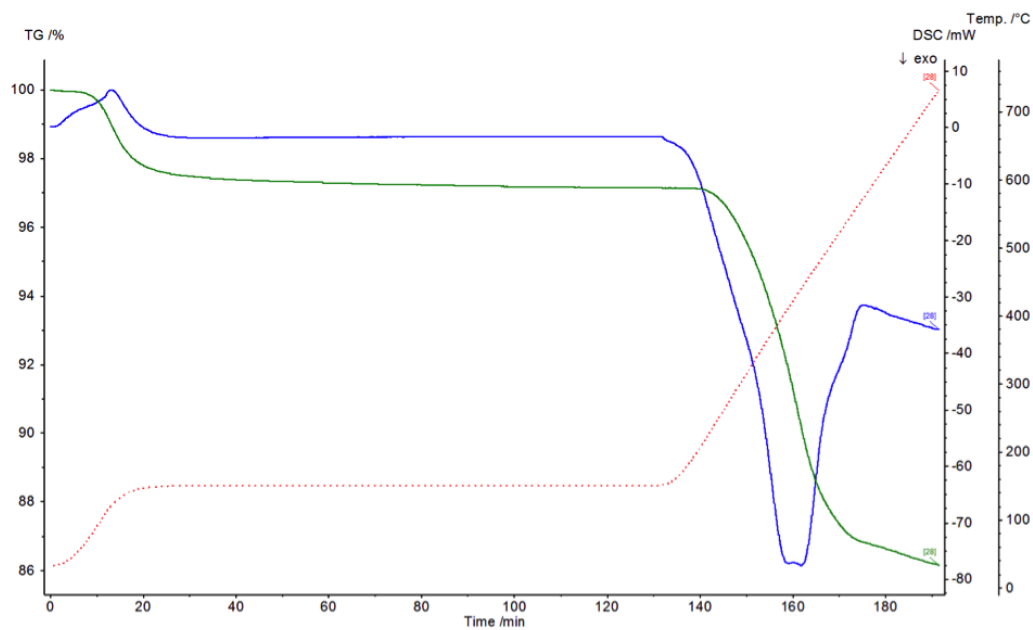


Figure A.32: TGA for Ni-CIT-6 at 180°C post-reactions.

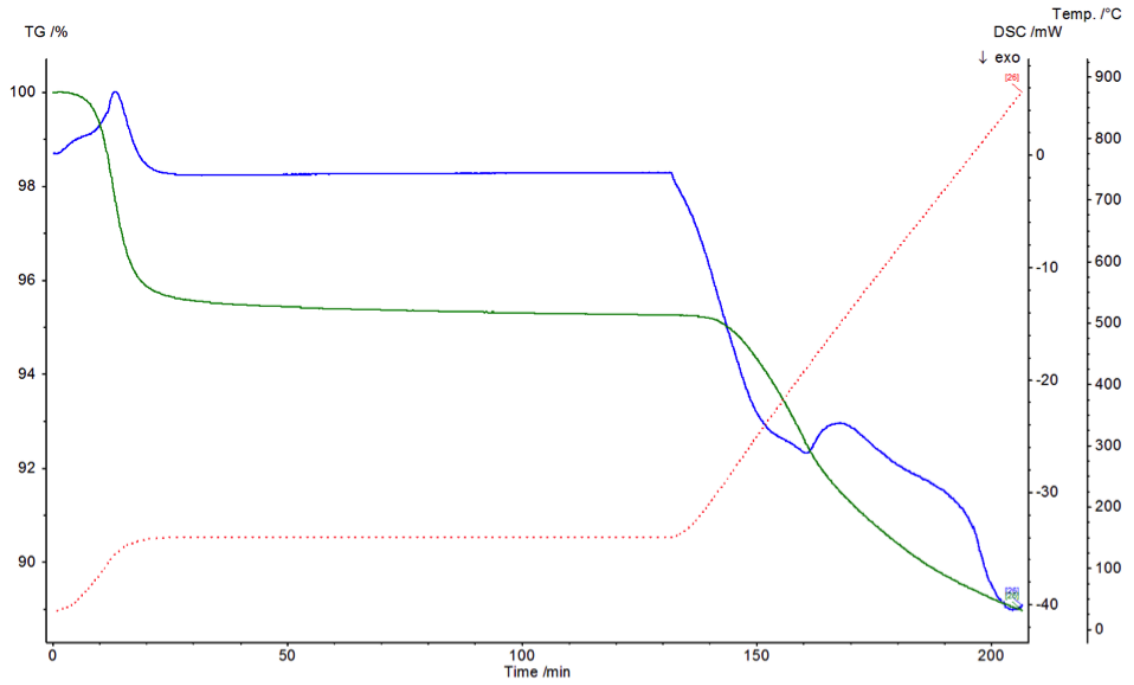


Figure A.33: TGA for Ni-Zn-MCM-41 at 180°C post-reactions.

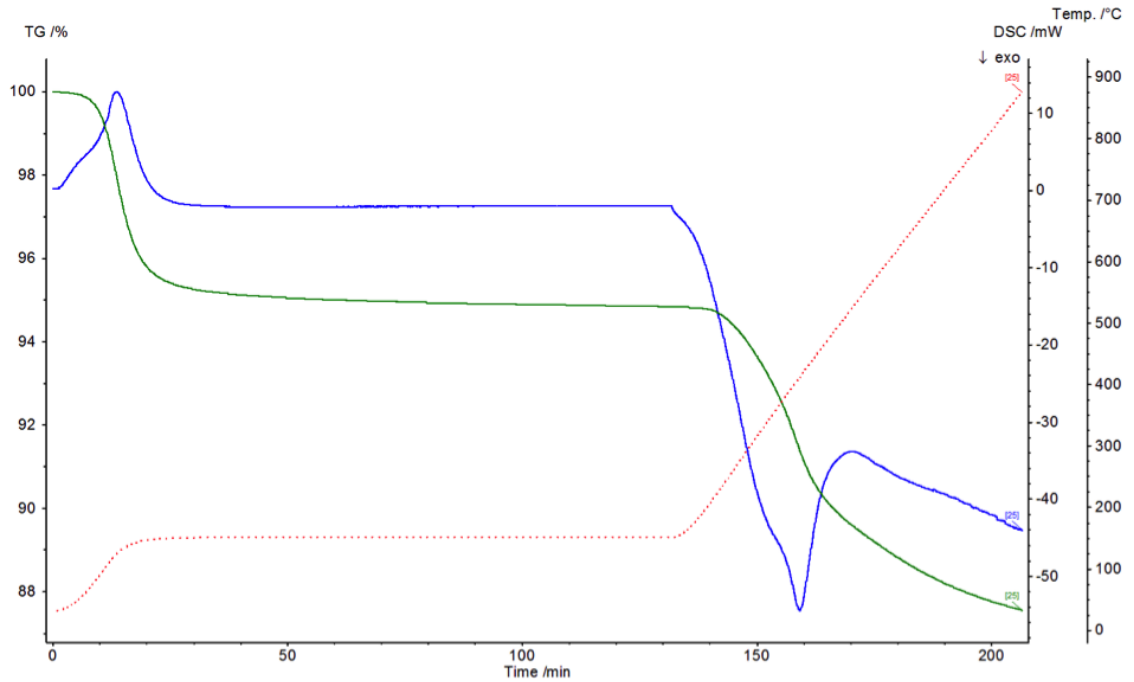


Figure A.34: TGA for Ni-Zn-MCM-41 at 250°C post-reactions.

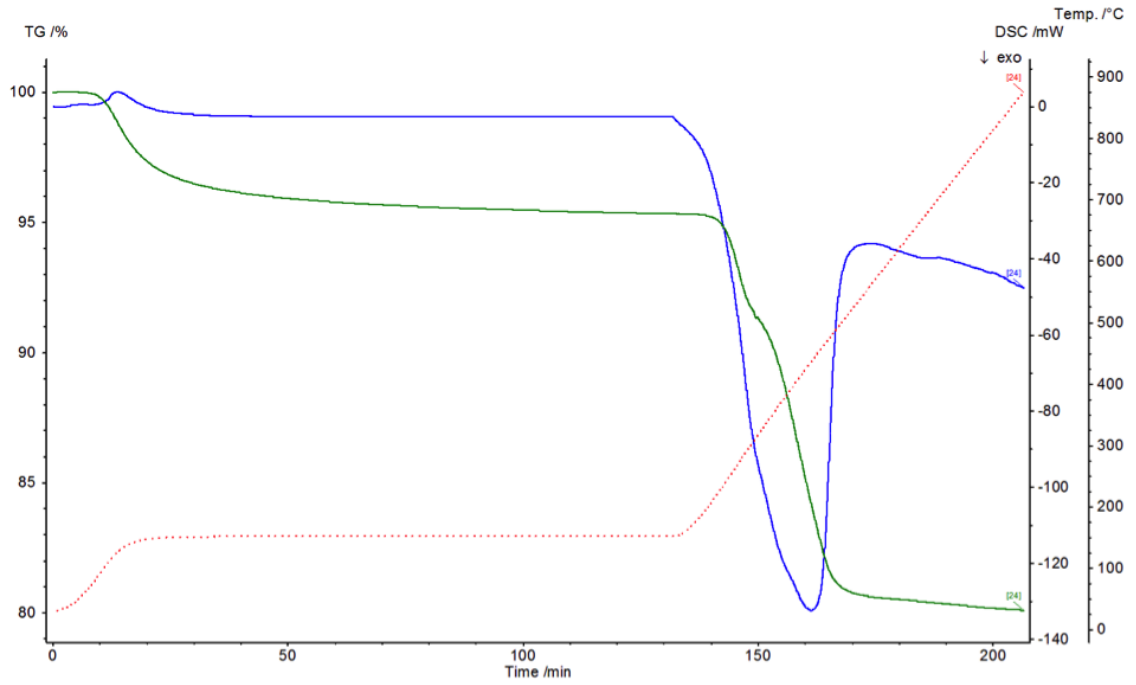


Figure A.35: TGA for Ni-HiAl-BEA at 180°C post-reactions.

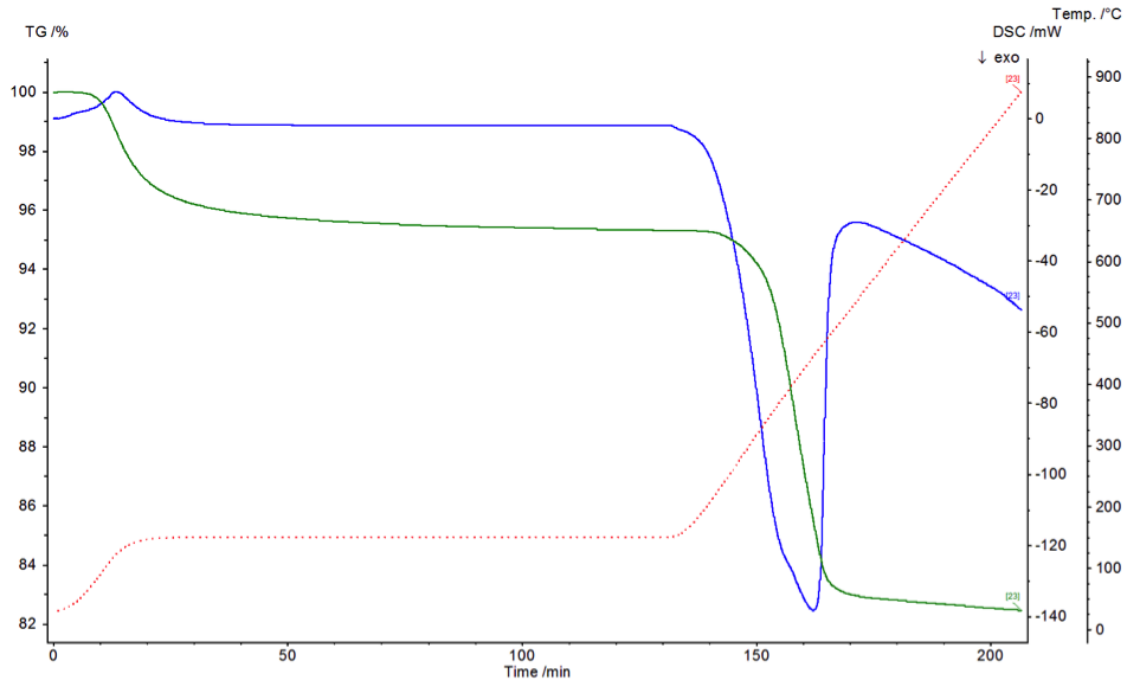


Figure A.36: TGA for Ni-HiAl-BEA at 250°C post-reactions.

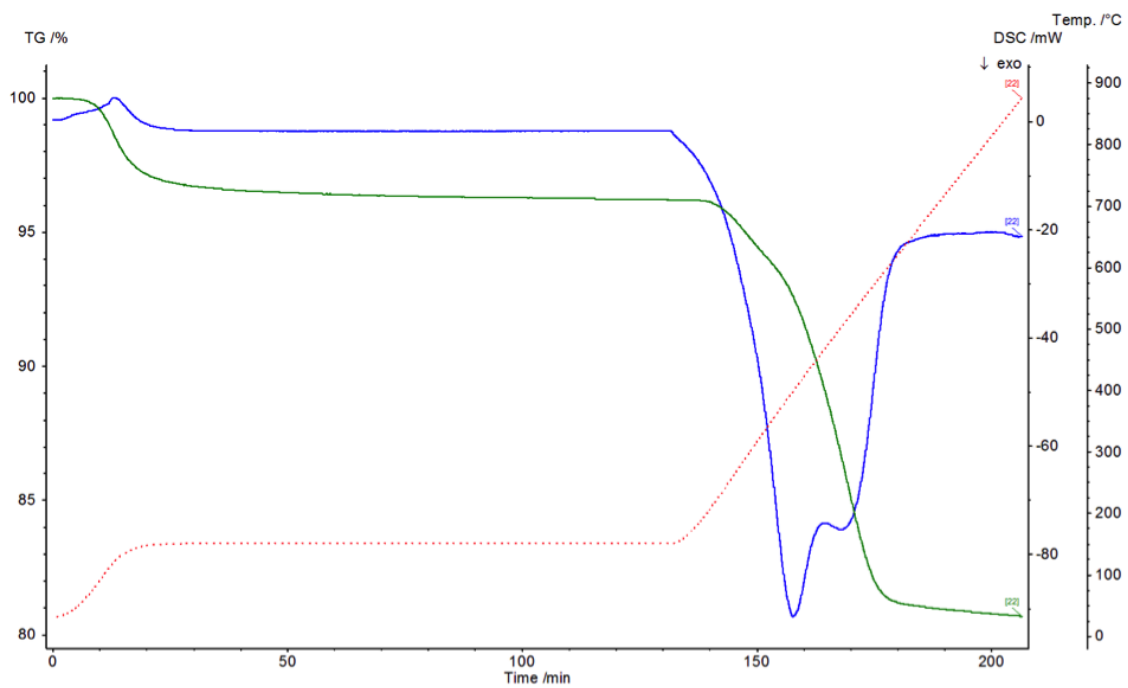


Figure A.37: TGA for Ni-USY at 250°C post-reactions.

Appendix B

Mixed Catalysts Characterization

B.1 Characterization of Materials Used as Catalysts

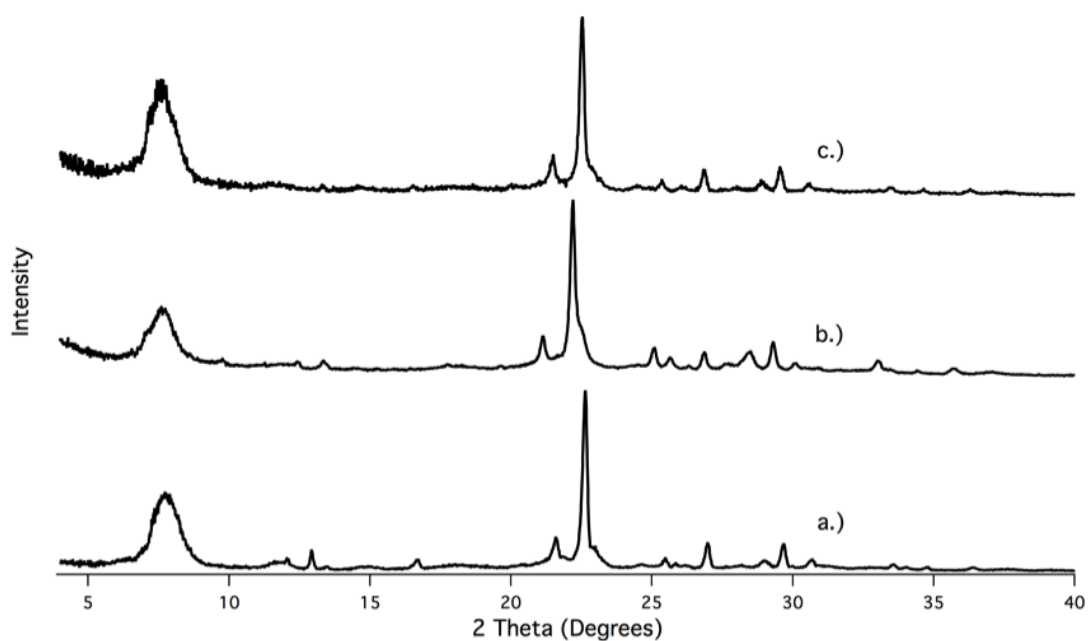


Figure B.1: XRD patterns of a.) as-made CIT-6, b.) Ni-CIT-6, and c.) calcined Ni-CIT-6 for use in the tandem catalyst system.

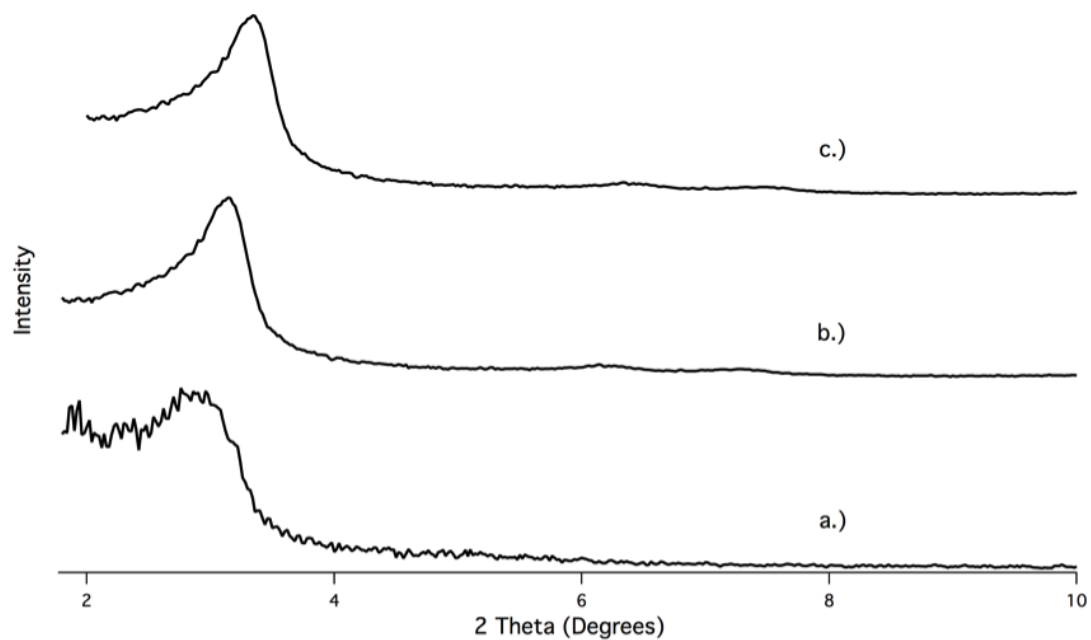


Figure B.2: XRD patterns of a.) as-made Zn-MCM-41, b.) Ni-Zn-MCM-41, and c.) calcined Ni-Zn-MCM-41 for use in the tandem catalyst system.

Appendix C

Post-Synthetic Treatment Characterization and Reaction Data

Work for this section was done in collaboration with Lucy Ji.

C.1 Study on the Effect of Steam Treatment on SSZ-13 for MTO

SSZ-13 was synthesized following the method reported in literature⁷² at a Si/Al ratio of 5 using the N,N,N-trimethyl-1-adamantylammonium hydroxide SDA. The SSZ-13 with Si/Al = 5 was calcined, NH₄⁺-exchanged, and then steamed for 24 h at 750°C under a flow of water vapor/inert mixture, which was accomplished by bubbling inert through a water saturator held at 75°C. Reaction testing of the samples was conducted at 400°C using a 10% methanol/inert feed at a WHSV of 1.3 h⁻¹. The MTO reaction profiles for the fresh (unsteamed) SSZ-13 with Si/Al = 5 and steamed SSZ-13 are shown in Figures C.1 and C.2, respectively. The unsteamed SSZ-13 initially converts methanol at 100% but deactivates rapidly after approximately 45 min TOS. Both the catalyst lifetime and olefin selectivities are improved after steam treatment. Methanol conversion remains above 80% for more than 200 min TOS for the steamed SSZ-13. Further, whereas the unsteamed SSZ-13 shows a transient period at the start of the reaction in which a significant amount of propane is observed in addition to rising olefin selectivities, the steamed material has a more stable reaction profile, similar to

SAPO-34. For comparison, the reaction data for a SAPO-34 that was synthesized in-house is graphed in Figure C.3.

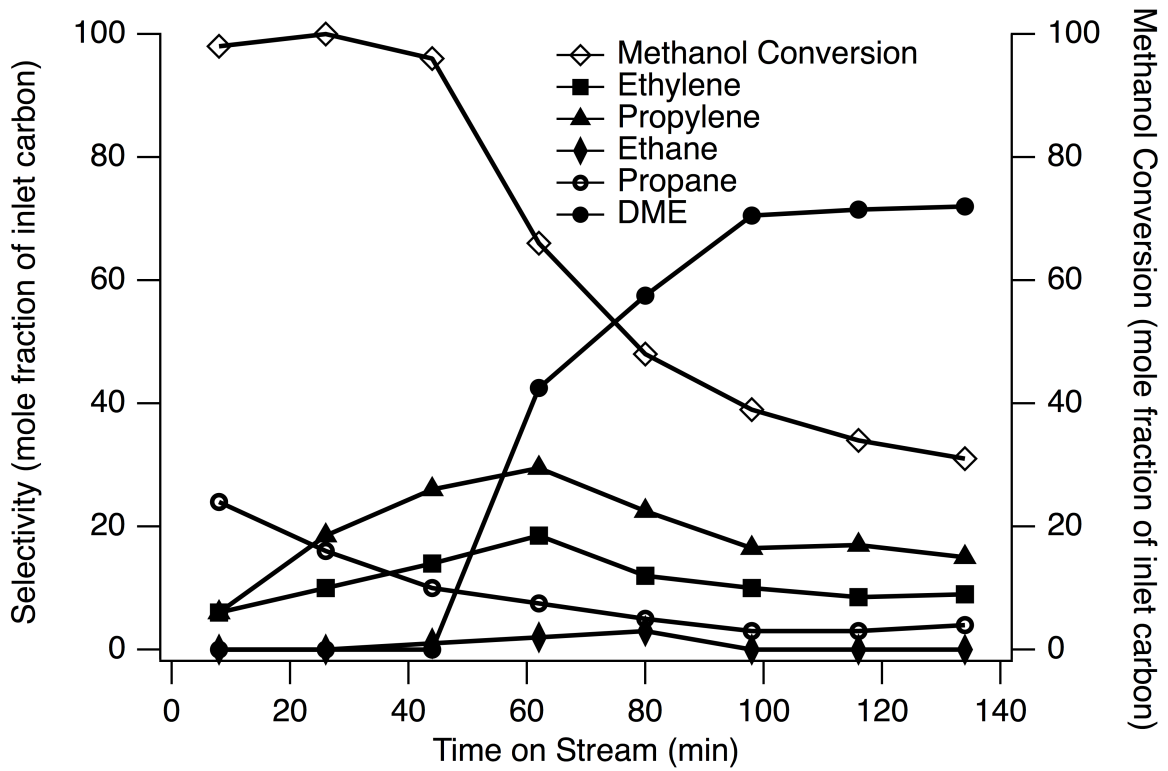


Figure C.1: MTO reaction data for fresh (unsteamed) H-SSZ-13 Si/Al = 5.

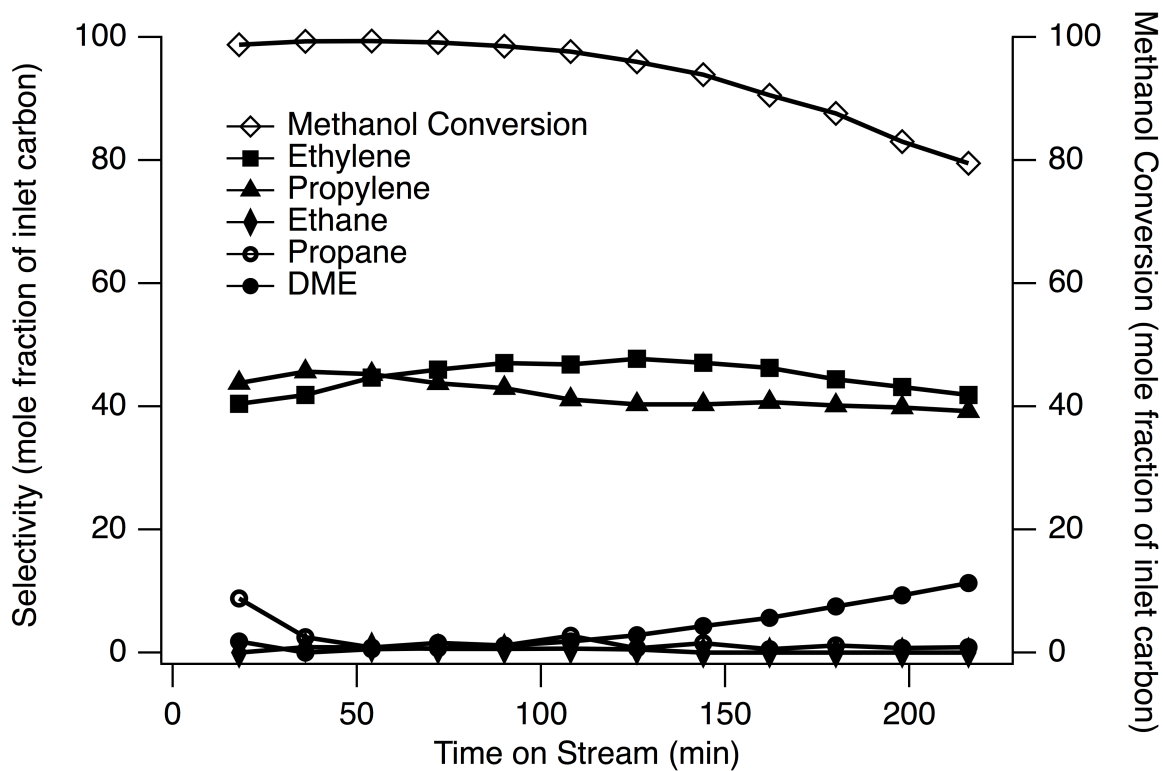


Figure C.2: MTO reaction data for steamed H-SSZ-13 Si/Al=5.

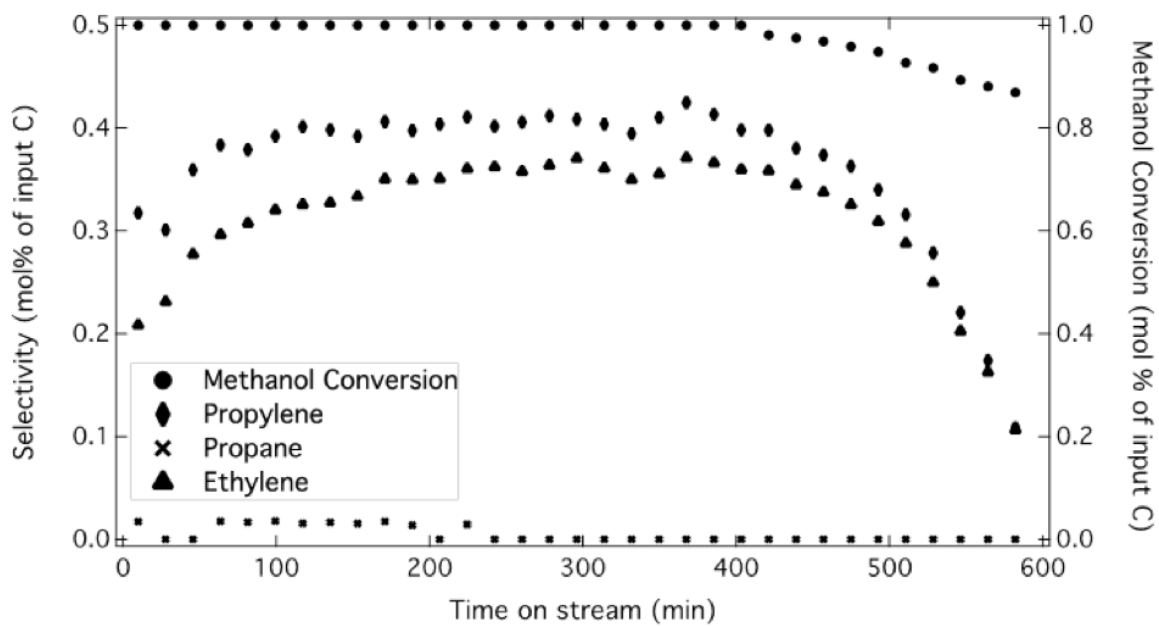


Figure C.3: MTO reaction data for H-SAPO-34.

C.2 Further Catalyst Characterization

A ^{27}Al MAS NMR spectrum of the as-synthesized K-CHA was obtained and is shown in Figure C.4. The spectrum contains only a single sharp peak centered at approximately 55 ppm, corresponding to tetrahedral aluminum, and indicates that all aluminum is initially incorporated in the framework.

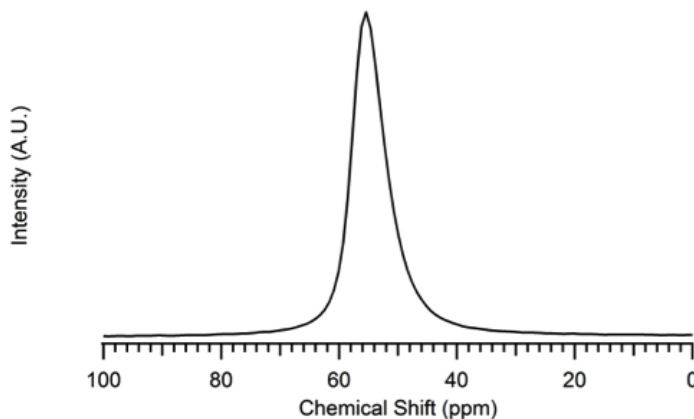


Figure C.4: ^{27}Al NMR of as-synthesized K-CHA.

C.3 Steaming Experiments with Zeolite Y and CHA

Three series of steaming experiments were conducted using zeolite Y (FAU) for the purposes of verifying that the steaming and dry calcination results previously reported in the literature on Y can be reproduced as well as determining whether the trend observed with CHA under varying partial pressures is also observed in Y when steamed using the same procedure. For all of the Y steaming experiments, the starting zeolite was a commercial NaY with $\text{Si}/\text{Al} = 2.97$ that had been NH_4^+ exchanged three times for 2 h at 90°C with 1 M NH_4NO_3 . The NH_4^+ -exchanged Y, designated NH_4NaY , had a Na/Al ratio of 0.28 (measured by EDS) and was steamed using the same tube furnace apparatus as that used for the CHA samples.

A summary of the steaming conditions is provided in Table C.1. Two sets of steaming experiments were conducted at 550°C and 650°C under similar conditions reported by Wang et al.,¹³⁸ who investigated the effect of the water partial pressure on

steaming of zeolite Y. Samples were heated at 5°C/min to the steaming temperature (550°C or 650°C) under 50 cc/min of dry air and then subjected to flowing steam (created by bubbling 50 cc/min of dry air through a heated water saturator) for 3 h at the steaming temperature. Samples were cooled under 50 cc/min of dry air flow at the end of the 3 h steaming period. Steaming experiments were conducted with the bubbler held at 60°C, 80°C, and 90°C, corresponding to steam partial pressures of 19.9 kPa, 47.3 kPa, and 70.1 kPa, respectively. An additional dry calcination was carried out on the NH₄NaY using the same temperature profile under flowing dry air (50 cc/min).

In the third set of steaming experiments, NH₄NaY samples were steamed under more severe conditions using the same procedure that was used for the CHA samples steamed at 600°C under varying steam partial pressures. Samples were heated at 1°C/min to 800°C and held for 8 h at the steaming temperature. The entire process, including heating and cooling, was carried out under flowing air. An additional dry calcination was conducted under 50 cc/min of dry air using the same temperature profile.

To determine whether CHA would also show the same trend that was observed with Y steamed at 550°C and 650°C, an additional series of steaming experiments was conducted with CHA using the same steaming procedures that were used for the 550°C and 650°C zeolite Y steaming experiments. NH₄-CHA samples were steamed for 3 h at 500°C under varying steam partial pressures. The furnace was ramped at 5°C/min to 500°C under 50 cc/min of dry air, steam was introduced for 3 h at 500°C only, and the sample was then allowed to cool under flowing dry air (50 cc/min).

Figures C.5 and C.6 show the powder XRD patterns of the NH₄NaY samples steamed at 550°C and 650°C, respectively. ²⁷Al MAS NMR spectra of the 550°C and 650°C steamed samples are shown in Figures C.7 and C.8. At both steaming temperatures, the ²⁷Al NMR indicates that a greater fraction of tetrahedral aluminum is converted to pentacoordinated and hexacoordinated aluminum for the steamed NH₄NaY samples compared to the dry calcined samples, consistent with what has been reported by Wang et al.¹³⁸

Sample	Heating Ramp Rate	Steaming Time	Steaming Temperature	Bubbler Temperature	Duration of Flowing Steam	Al_T/Al_{Total}
$NH_4NaY-S550B90$	5°C/min	3 h	550°C	90°C	At steaming temperature only	0.144
$NH_4NaY-S550B80$	5°C/min	3 h	550°C	80°C	At steaming temperature only	0.288
$NH_4NaY-S550B60$	5°C/min	3 h	550°C	60°C	At steaming temperature only	0.387
$NH_4NaY-C550$	5°C/min	3 h	550°C	-	Dry calcination	0.822
$NH_4NaY-S650B90$	5°C/min	3 h	650°C	90°C	At steaming temperature only	0.394
$NH_4NaY-S650B80$	5°C/min	3 h	650°C	80°C	At steaming temperature only	0.325
$NH_4NaY-S650B60$	5°C/min	3 h	650°C	60°C	At steaming temperature only	0.308
$NH_4NaY-C650$	5°C/min	3 h	650°C	-	Dry calcination	0.444
$NH_4NaY-S650B90$	1°C/min	8 h	800°C	90°C	Entire period	0.230
$NH_4NaY-S650B80$	1°C/min	8 h	800°C	80°C	Entire period	0.670
$NH_4NaY-S650B60$	1°C/min	8 h	800°C	60°C	Entire period	0.713
$NH_4NaY-C650$	1°C/min	8 h	800°C	-	Dry calcination	0.234
CHA-S500B90	5°C/min	3 h	500°C	90°C	At steaming temperature only	0.139
CHA-S500B60	5°C/min	3 h	500°C	60°C	At steaming temperature only	0.156
CHA-C500	5°C/min	3 h	500°C	-	Dry calcination	0.201

Table C.1: Summary of zeolite Y and CHA steaming conditions.

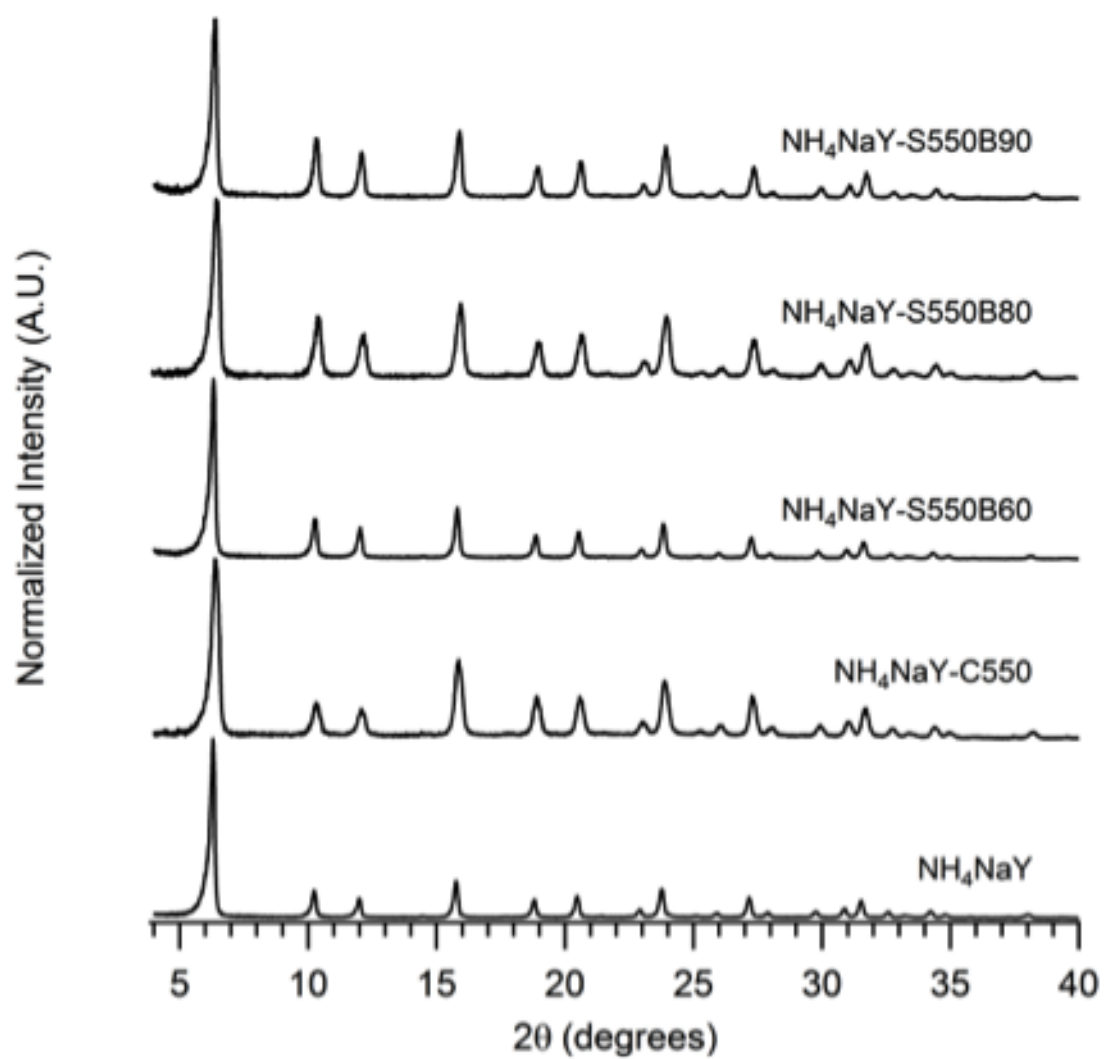


Figure C.5: Powder XRD patterns of unsteamed NH₄NaY and NH₄NaY samples steamed for 3 h at 550°C in order of increasing steam partial pressure (bottom to top).

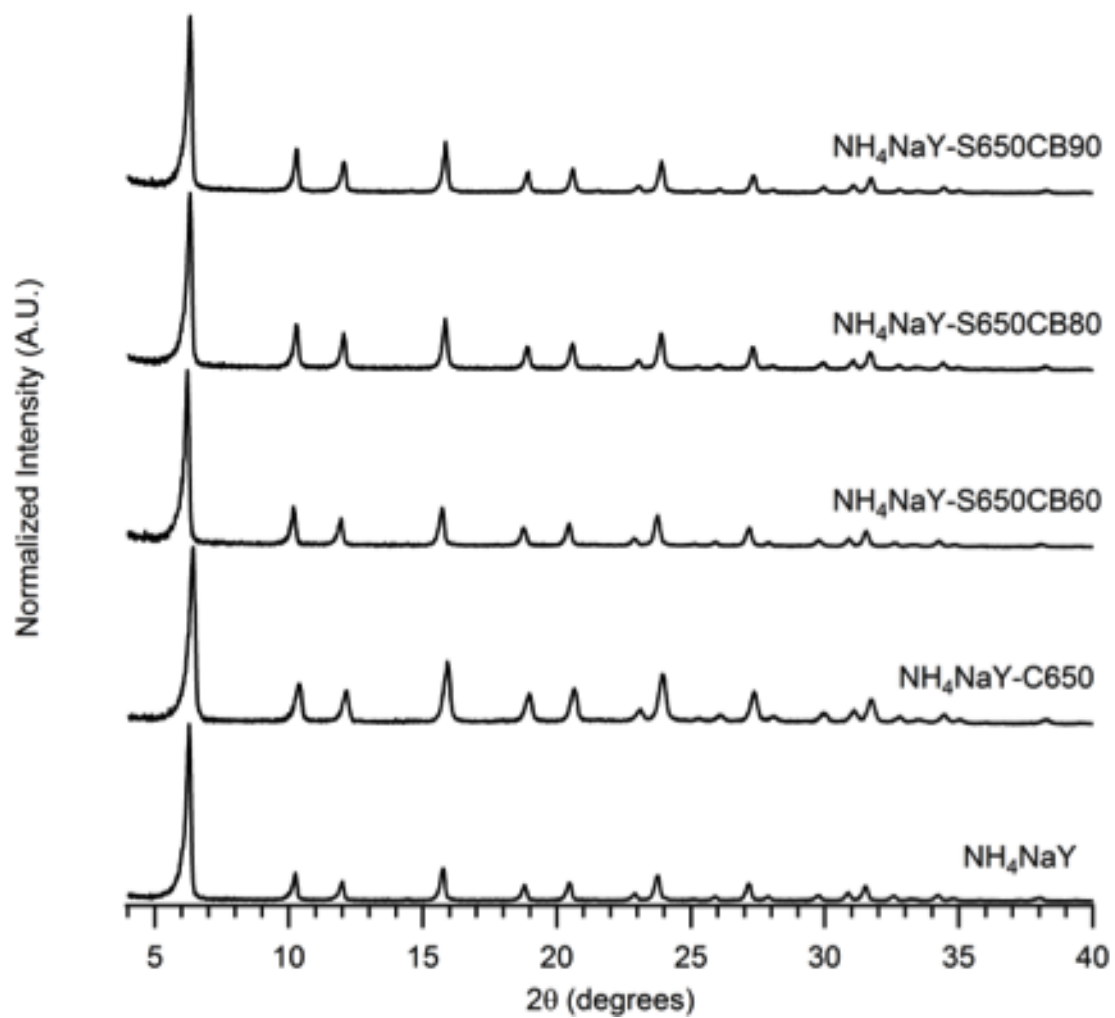


Figure C.6: Powder XRD patterns of NH_4NaY samples steamed for 3 h at 650°C in order of increasing steam partial pressure (bottom to top).

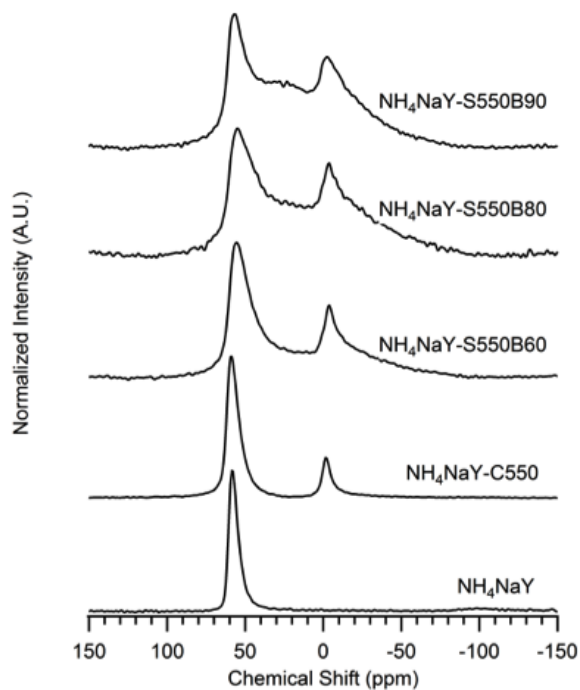


Figure C.7: ^{27}Al NMR spectra of unsteamed NH_4NaY and NH_4NaY samples steamed for 3 h at 550°C in order of increasing steam partial pressure (bottom to top).

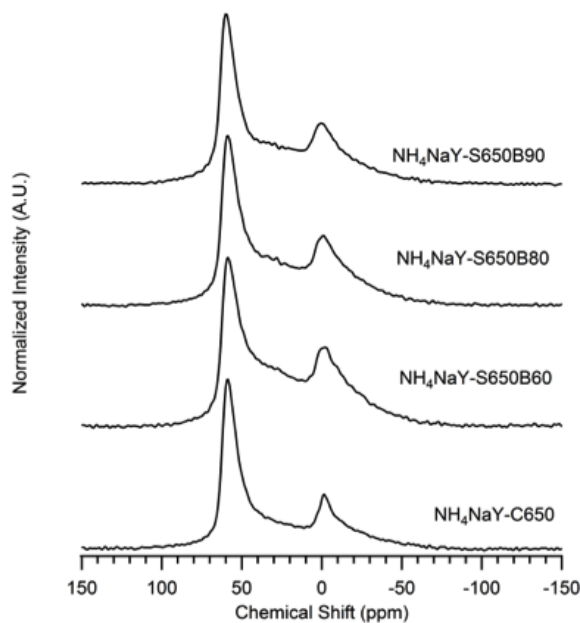


Figure C.8: ^{27}Al NMR spectra of NH_4NaY samples steamed for 3 h at 650°C in order of increasing steam partial pressure (bottom to top).

The powder XRD patterns and ^{27}Al NMR spectra of the $\text{NH}_4\text{Na-Y}$ samples steamed at 800°C are shown in Figures C.9 and C.10, respectively. At these conditions, the NH_4NaY samples show increased degradation when the water partial pressure is lowered, with the sample calcined under dry air showing the greatest degradation. The ^{27}Al NMR is consistent with the XRD data in that the amount of pentacoordinated and hexacoordinated aluminum increase relative to the tetrahedral aluminum as the water partial pressure is lowered. This trend is opposite of what was observed for the 550°C and 650°C steamed NH_4NaY but consistent with the behavior of CHA steamed at 600°C under varying steam partial pressures. The similarity in the behavior of steamed Y compared to CHA at these conditions suggests that the trend of increased degradation with decreasing steam partial pressure is not unique to CHA.

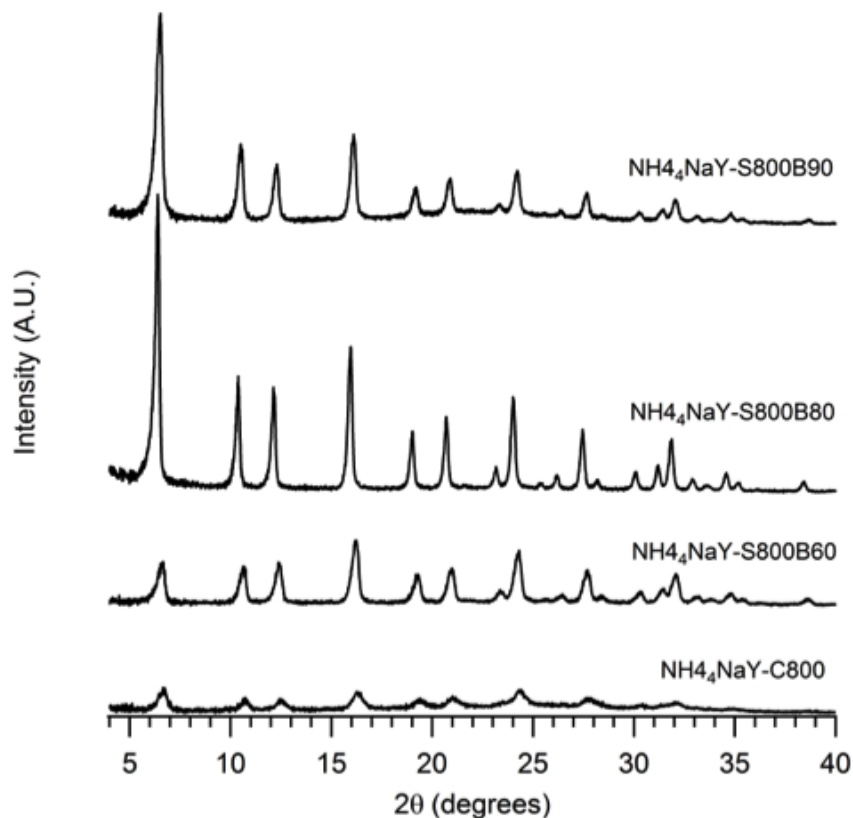


Figure C.9: Powder XRD patterns of $\text{NH}_4\text{Na-Y}$ samples steamed for 8 h at 800°C in order of increasing steam partial pressure (bottom to top).

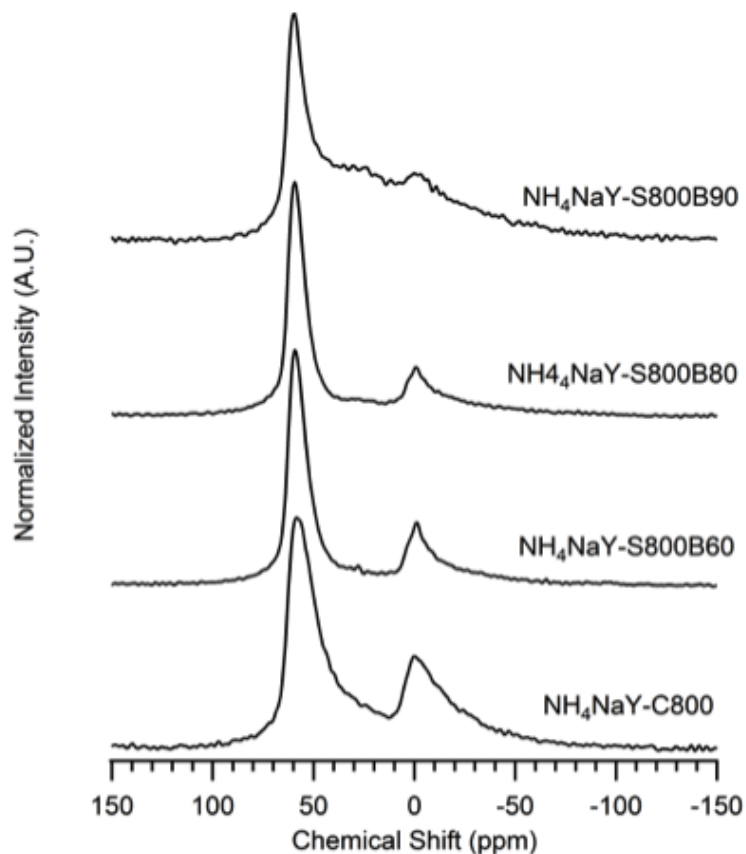


Figure C.10: ^{27}Al MAS NMR of $\text{NH}_4\text{Na-Y}$ samples steamed for 8 h at 800°C in order of increasing steam partial pressure (bottom to top).

Figures C.11 and C.12 show the powder XRD patterns and ^{27}Al NMR, respectively, of the CHA samples steamed at 500°C where steam is introduced at 500°C only. While the powder XRD patterns of the steamed samples are very similar to each other, the ^{27}Al NMR spectra indicate that as the steam partial pressure is increased, an increasing portion of the tetrahedral aluminum is converted to penta-coordinate and hexacoordinate aluminum and is consistent with what was observed for the 550°C and 650°C steamed Y.

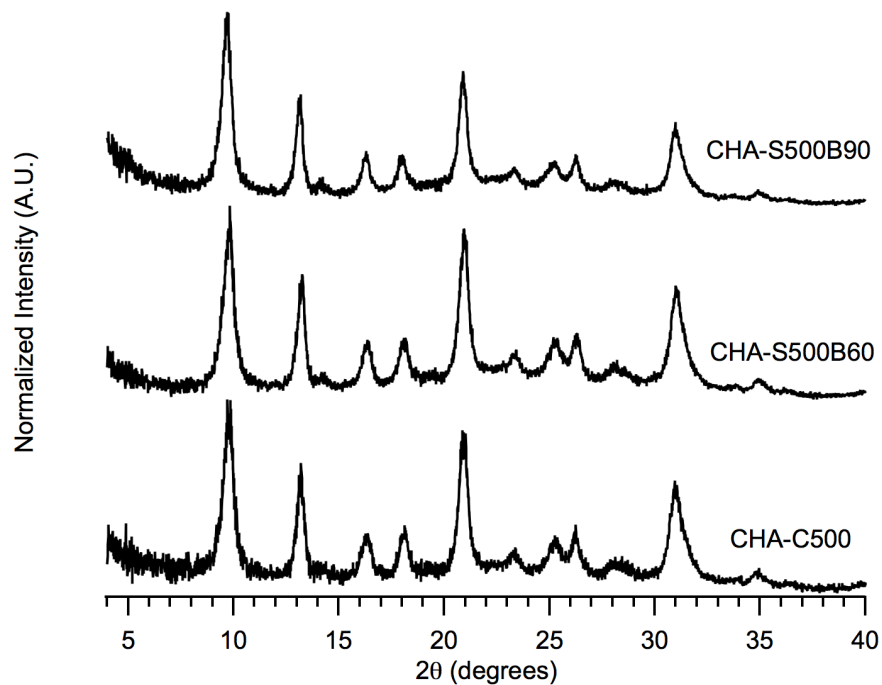


Figure C.11: Powder XRD patterns of CHA samples steamed for 3 h at 500°C in order of increasing steam partial pressure (bottom to top).

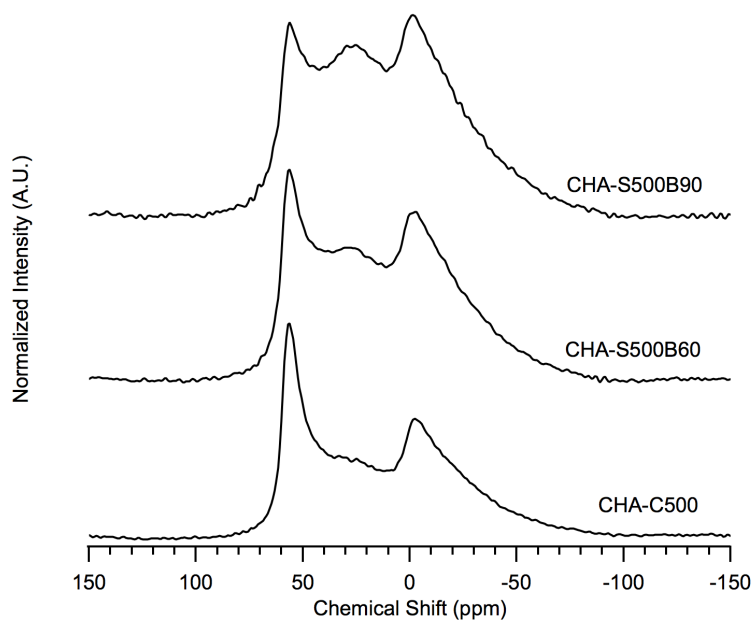


Figure C.12: ^{27}Al MAS NMR of CHA samples steamed for 3 h at 500°C in order of increasing steam partial pressure (bottom to top).

C.4 MTO Reaction Data for Fresh and Regenerated Steamed CHA

An additional batch of steamed CHA was prepared to determine whether the activity could be recovered by regeneration. CHA was steamed for 8 h at 600°C under a steam partial pressure of 47.3 kPa, and a portion of the steamed material was acid washed in the same manner as described in the Experimental section. Reaction testing was conducted using a 10% methanol/inert feed at a WHSV of 1.3 h⁻¹. The reaction profiles at 400°C of the fresh and regenerated 600°C steamed CHA are shown in Figures C.13 and C.14, respectively. The activity of the 600°C steamed and acid washed CHA was evaluated over two reaction cycles at 450°C and the reaction profiles are shown in Figures C.15 and C.16.

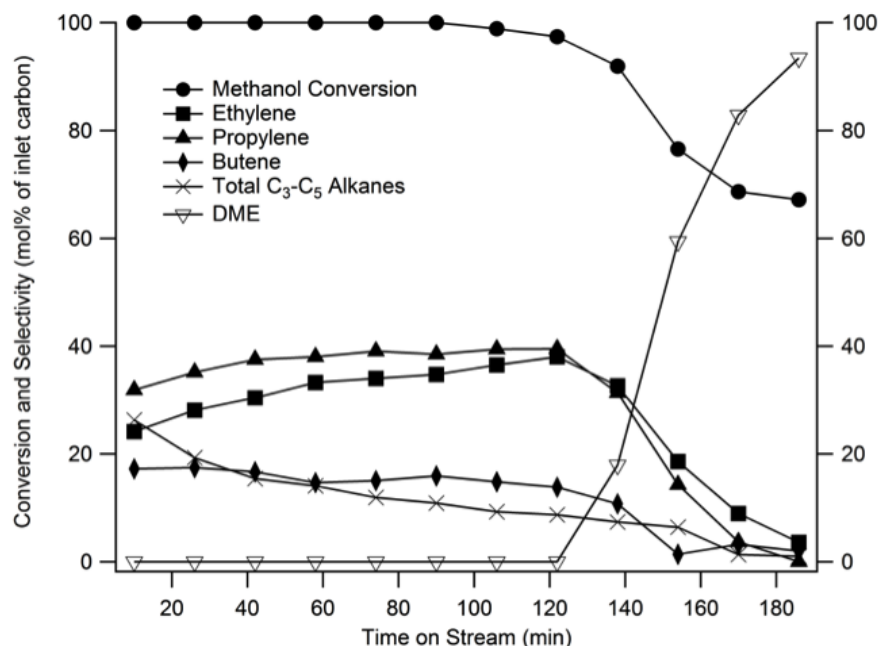


Figure C.13: MTO reaction data obtained at 400°C for 600°C steamed CHA during the initial reaction run.

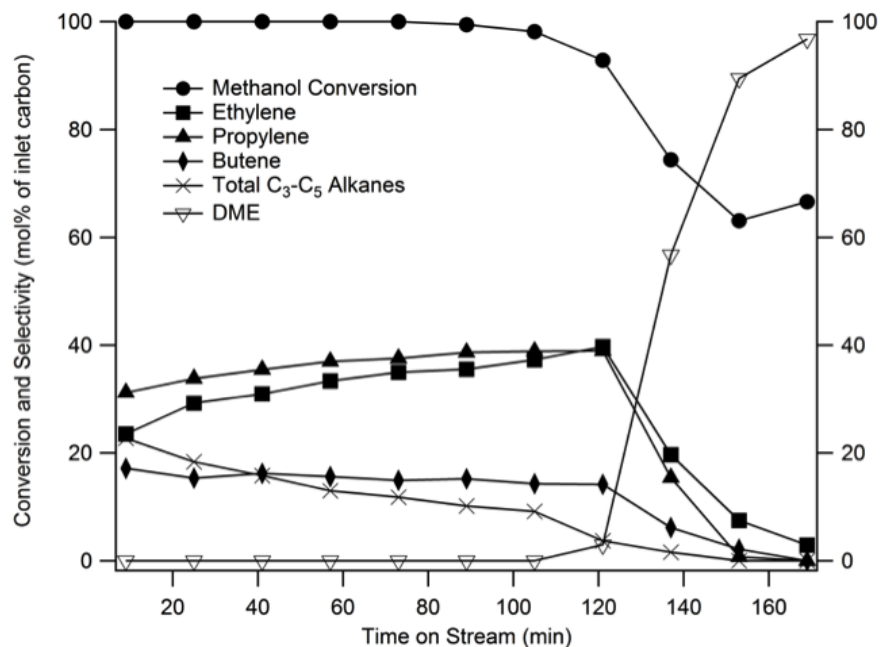


Figure C.14: MTO reaction data obtained at 400°C for 600°C steamed CHA after regeneration of spent catalyst.

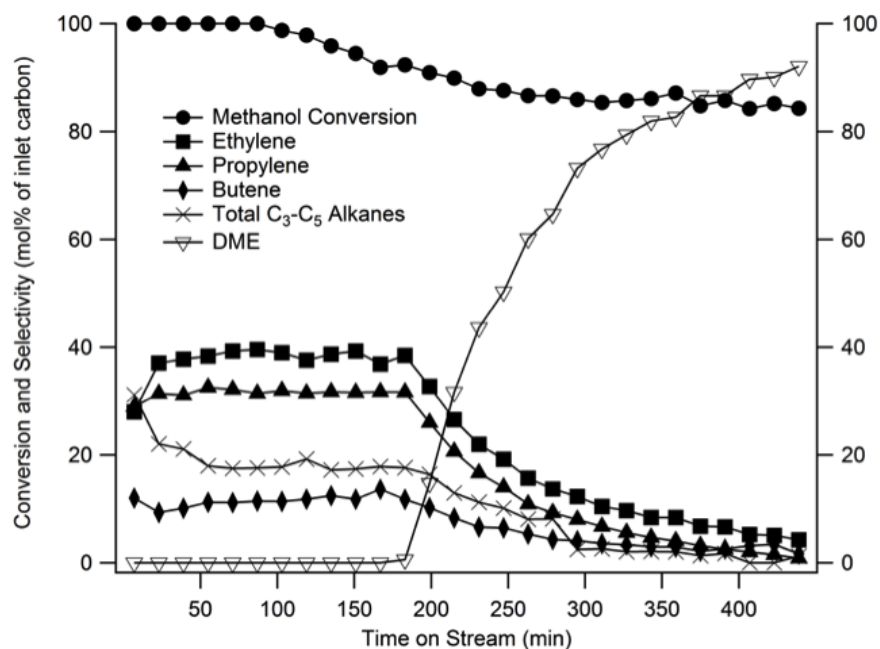


Figure C.15: MTO reaction data obtained at 450°C for 600°C steamed and acid washed CHA during the initial reaction test.

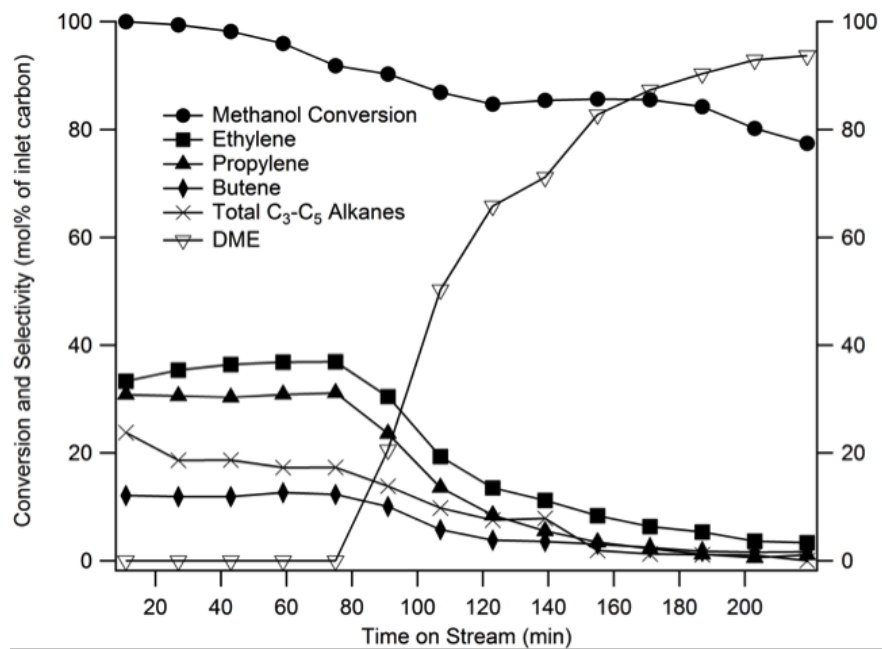


Figure C.16: MTO reaction data obtained at 450°C for 600°C steamed and acid washed CHA after regeneration of spent catalyst.

Appendix D

Additional Publications

D.1 Highly Active Mixed-Metal Nanosheet Water Oxidation Catalysts Made by Pulsed-Laser Ablation in Liquids

Hunter, B.M.; Blakemore, J.D.; Deimund, M.A.; Gray, H.B.; Winkler, J.R.; Müller, A.M. *J. Am. Chem. Soc.* 2014, *136*, 13118-13121. DOI: 10.1021/ja506087h.

D.2 The Facile Preparation of Aluminosilicate RTH Across a Wide Composition Range Using a New Organic Structure Directing Agent

Schmidt, J.E.; Deimund, M.A.; Davis, M.E. *Chem. Mater.* 2014, *26*, 7099-7105. DOI: 10.1021/cm503625u.

D.3 Synthesis of RTH-type Zeolites Using a Diverse Library of Imidazolium Cations

Schmidt, J.E.; Deimund, M.A.; Xie, D.; Davis, M.E. *Chem. Mater.* 2015. DOI: 10.1021/acs.chemmater.5b01003.

D.4 Effect of Pore and Cage Size on the Formation of Aromatic Intermediates During the Methanol-to-Olefins Reaction

Deimund, M.A.; Schmidt, J.E.; Davis, M.E. *Top. Catal.* 2015, 58, 426-423. DOI: 10.1007/s11244-015-0384-y.

D.5 Upgrading Light Hydrocarbons: A Tandem Catalytic System for Alkane/Alkene Coupling

Labinger, J.A.; Leitch, D.C.; Bercaw, J.E.; Deimund, M.A., Davis, M.E. *Top. Catal.* 2015, 58, 494-501. DOI: 10.1007/s11244-015-0380-2.

Highly Active Mixed-Metal Nanosheet Water Oxidation Catalysts Made by Pulsed-Laser Ablation in Liquids

Bryan M. Hunter, James D. Blakemore, Mark Deimund, Harry B. Gray, Jay R. Winkler, and Astrid M. Müller*

Beckman Institute and Division of Chemistry and Chemical Engineering, California Institute of Technology, M/C 139-74, Pasadena, California 91125.

Supporting Information Placeholder

ABSTRACT: Surfactant-free mixed-metal hydroxide water oxidation nanocatalysts were synthesized by pulsed-laser ablation in liquids. In a series of [Ni-Fe]-layered double hydroxides with intercalated nitrate and water, $[\text{Ni}_{1-x}\text{Fe}_x(\text{OH})_2](\text{NO}_3)_y(\text{OH})_{x-y}\cdot n\text{H}_2\text{O}$, higher activity was observed as the amount of Fe decreased to 22%. Addition of Ti^{4+} and La^{3+} ions further enhanced electrocatalysis, with a lowest overpotential of 260 mV at 10 mA cm^{-2} . Electrocatalytic water oxidation activity increased with the relative proportion of a 405.1 eV N 1s (XPS binding energy) species in the nanosheets.

Conversion of solar energy into storable fuels in a sustainable way will be essential to meet future global energy demands. Worldwide scalability requires materials to be made from earth-abundant elements. Splitting water into oxygen and hydrogen with only sunlight as energy input is seen as a particularly attractive route.¹ But such systems for the production of solar fuels will require robust, highly active catalysts.²⁻⁴

Most widely used water oxidation catalysts are based on rare metals such as Ru and Ir.^{5,6} First-row transition metal oxides and hydroxides continue to attract attention because of their low cost and stability in base.⁷⁻¹⁴ The overpotentials of earth-abundant catalysts at 10 mA cm^{-2} typically range from 350 to 430 mV in pH 14 aqueous electrolytes.^{15,16} In recent work, Yan showed that hollow spheres of α -Ni(OH)₂ catalyzed water oxidation in base with an overpotential of 331 mV at 10 mA cm^{-2} on glassy carbon working electrodes.¹⁷

Here we report surfactant-free, highly active $[\text{Ni}_{1-x}\text{Fe}_x(\text{OH})_2](\text{NO}_3)_y(\text{OH})_{x-y}\cdot n\text{H}_2\text{O}$ nanosheet water oxidation catalysts with admixed ions. Our best catalyst had an overpotential of 260 mV at 10 mA cm^{-2} on flat highly-ordered pyrolytic graphite working electrodes. We attribute the higher activity to unique morphological and structural

properties, which were synthetically accessible by the use of pulsed-laser ablation in liquids (PLAL). In PLAL, nanoparticles are formed by very rapid cooling of a plasma comprised of elements from the solid ablation target and the surrounding liquid. This condensation process, which is kinetically controlled, produces predominantly crystalline nanomaterials.¹⁸ PLAL offers size and composition control through a wide range of tunable experimental parameters.¹⁹

With PLAL, mixed-metal nanomaterials with tailored compositions can be prepared readily by adding metal ions into the aqueous ablation liquid. We intentionally incorporated different amounts of Fe into our α -Ni(OH)₂ nanocatalysts, as variable concentrations of Fe in electrodeposited nickel (oxy)hydroxides have been shown to improve electrocatalytic activity.²⁰⁻²⁵ We also added Ti^{4+} and La^{3+} ions to the ablation liquid and screened the resulting materials for water oxidation activity.

Eight mixed-metal catalysts were synthesized using PLAL by varying ablation targets, metal ion type and concentrations, and laser pulse energies (see SI for experimental details, all ablation solutions contained nitrate). The nanomaterials were prepared with Fe concentrations ranging from 22 to 95% of the total metal content (Table 1). We identified their compositions spectroscopically; and, notably, they all exhibited high electrocatalytic oxygen-evolution activities in basic solutions.

Powder X-ray diffraction (XRD) measurements (SI) indicate that the Fe-rich nanoparticles **1-3** are poorly crystalline; the Ni-rich nanoparticles **4-8** display diffraction patterns consistent with layered double hydroxide (LDH) structures. XRD data indicate minor contributions from Fe(O)OH;²⁶ **6** also contained the crystalline spinel NiFe₂O₄,²⁷ and Ti-based oxides were present in **7** and **8**. LDHs have the general formula $[\text{M}_{1-x}\text{M}'_x(\text{OH})_2](\text{A}^{m-})_{x/m}\cdot n\text{H}_2\text{O}$; the structures are comprised of sheets of $[\text{M}_{1-x}\text{M}'_x(\text{OH})_2]^{x+}$ edge-shared octahedra. Cationic charges arising from M'^{3+} in the sheets are balanced by intercalated hydrated anions (A^{m-}).²⁸⁻³⁰

Table 1: Preparation conditions of catalysts **1** to **8** and concentrations of Fe with respect to total metal content.

Catalyst	Solid target	Added ions	Ion concentration (M)	Pulse energy (mj)	Fe (% metal content) ^a
1	Ni	Fe	0.1	90	95
2	Ni	Fe	0.01	90	86
3	Fe	Ni	0.1	90	70
4	Fe	Ni	1.0	90	36
5	Fe	Ni	3.0	90	22
6	Fe	Ni	3.0	210	30
7	Fe	Ni Ti	3.0 0.015	210	23
8	Fe	Ni Ti La	3.0 0.015 0.023	210	29

^a Determined by XPS.

X-ray photoelectron spectroscopy (XPS) was employed to obtain binding energies of Ni 2p and Fe 2p core levels in **1-8**; these energies are indicative of Ni(OH)₂ and (hydrated) iron oxides (SI). In addition, Mössbauer^{31,29} and x-ray absorption³²⁻³⁴ spectroscopic data indicate that Fe is incorporated as Fe³⁺ in place of Ni²⁺ in [Ni-Fe]-LDHs. Two well-resolved N 1s peaks appear in the XP spectra of nanoparticles **4-8**, with binding energies of 407.3 and 405.1 eV. The higher binding-energy feature (407.3 eV) is assigned to nitrate.³⁵⁻⁴⁰ The 2.2 eV reduction in N 1s binding energy for the second feature could arise from nitrate in an unusual electronic environment, although nitrogen in a lower oxidation state (e.g., NO₂, NO₂⁻) cannot be ruled out. Infrared spectra are consistent with the presence of a second type of NO_x species (SI). Infrared and Raman data (SI) support the presence of intercalated nitrate anions in the LDH structure.⁴¹ On the basis of these data, the predominant crystalline material in **4-8** can be assigned to the [Ni-Fe]-LDH [Ni_{1-x}Fe_x(OH)₂](NO₃)_y(OH)_{x-y}•nH₂O (Figure 1).

Nanoparticle sizes were obtained from transmission electron micrographs (TEM), and crystalline domain sizes were determined by Scherrer analysis of XRD data. Lateral sizes ranged from ~7 to 22 nm (Table S1). Catalysts **1** to **5** consisted of nanosheets, as expected for layered structures. Analysis of TEM and XRD data for **6** revealed that two types of nanoparticles were formed; smaller, more spherical (6.5 ± 0.8) nm particles are attributed to the spinel NiFe₂O₄, and larger (13 ± 1) nm sheets are assigned to the LDH [Ni_{1-x}Fe_x(OH)₂](NO₃)_y(OH)_{x-y}•nH₂O. Also, differences in TEM contrast, shape, and size were found for **7** and **8** (SI).⁴² Specific surface areas of catalysts **5** to **8** determined by Brunauer-Emmett-Teller (BET) measurements are in agreement with particle sizes derived from TEM data. Catalysts **6** to **8**, which were synthesized at 210 mJ pulse energy, had similar BET surface areas (193 ± 1 m² g⁻¹), whereas **5**, prepared at 90 mJ/pulse, exhibited a slightly higher surface area (220 m² g⁻¹) (SI).⁴³

187

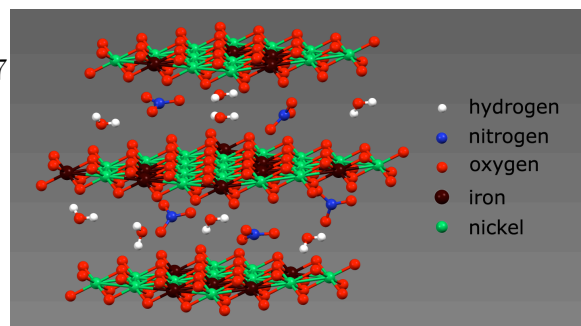


Figure 1. Schematic structural representation of the [Ni-Fe]-LDH [Ni_{1-x}Fe_x(OH)₂](NO₃)_y(OH)_{x-y}•nH₂O.

We assessed electrocatalytic oxygen-evolution activity in 1 M aqueous KOH.⁴⁴ Faradaic yields of oxygen evolution for **5**, **6** and **8** were all essentially 100%. Steady-state Tafel data were measured to obtain overpotentials; virtually identical mass loadings were used in all electrochemical experiments (all current densities are reported per geometric area). Importantly, chronoamperometry data showed that the catalytic activity of nanoparticles **5-8** was maintained for more than 5 hours (SI).

The electrocatalytic activities of materials **1** to **5**, synthesized at virtually the same pulse energy, steadily increased with decreasing Fe content (Figure S13). Catalyst **5** (22% Fe relative to total metal content) performed best in the [Ni-Fe]-LDH materials, with an overpotential of 280 mV at 10 mA cm⁻². Incorporation of less than 22% Fe relative to total metal content was limited by the solubility of Ni nitrate in the aqueous ablation liquid. XRD data for **5**, collected before and after 30 min of anodic polarization, confirmed that the crystallinity of the [Ni-Fe]-LDH material was retained (Figure S5). The Fe content of our best performing catalyst is in agreement with Dai's report.³⁴ It differs, however, from findings for amorphous materials, which performed best with 40% Fe.⁴⁵

We made catalyst **6** employing virtually the same precursor conditions as for **5**, but with a pulse energy of 210 instead of 90 mJ. We have shown before with cobalt oxide that pulse energy can be used to control particle size.¹⁹ Varying pulse energy in the synthesis of more complex mixed-metal materials led to particles with different compositions (Figure 2). While **5** consisted mainly of crystalline [Ni-Fe]-LDH, **6** was mixed crystalline [Ni-Fe]-LDH/NiFe₂O₄. Catalyst **6** showed inferior activity for water oxidation relative to **5**, presumably because the active [Ni-Fe]-LDH was diluted by the spinel oxide. This finding suggests that crystalline [Ni_{1-x}Fe_x(OH)₂](NO₃)_y(OH)_{x-y}•nH₂O is the more active species in our materials for catalytic water oxidation. IR spectra of **5** and **6** are consistent with [Ni_{1-x}Fe_x(OH)₂](NO₃)_y(OH)_{x-y}•nH₂O with high interstitial water and nitrate content.⁴⁶⁻⁴⁸ The positions of peaks in the IR spectrum of catalyst **5** indicated the incorporation of Fe into the *α*-Ni(OH)₂ lattice (SI).⁴⁹

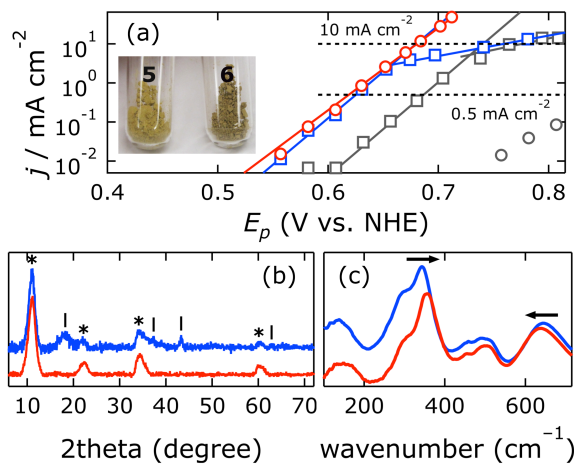


Figure 2. (a) Tafel plots of current density (j) as a function of electrode polarization potential (E_p) (red, **5**; blue, **6**; gray squares, Ni oxide electrodeposited according to ref. ⁵⁰; gray circles, bare electrode), and a photograph of **5** and **6**; (b) XRD data * $[\text{Ni}_{1-x}\text{Fe}_x(\text{OH})_2](\text{NO}_3)_y(\text{OH})_{x-y}\cdot n\text{H}_2\text{O}$, | NiFe_2O_4 spinel; (c) far-IR spectra (red, **5**; blue, **6**).

The precise nature of the electrocatalytically active species in Fe–Ni–O catalysts has been much discussed.^{51,52,45,53} In work on crystalline Fe–Ni–O thin films, Boettcher suggested $(\text{Fe,Ni})(\text{O})\text{OH}$ was the catalytically active phase.^{24,25} Whereas Dai found that crystalline $\alpha\text{-(Fe,Ni)(OH)}_2$ had highest activity with an Fe:Ni ratio of 5:1,^{34,54} Hu demonstrated higher intrinsic activity of exfoliated LDHs with a nominal Fe:Ni ratio of 1:3.⁵⁵ In other work of note, O'Hare demonstrated that NiTi layered double hydroxide nanosheets were effective visible-light-driven water oxidation photocatalysts with AgNO_3 as sacrificial electron acceptor.⁵⁶

We found that addition of Lewis-acidic Ti^{4+} and La^{3+} ions to the ablation liquid improved catalytic activity relative to our most active $[\text{Fe-Ni}]$ -LDH catalyst (**5**). We synthesized catalysts **7** and **8** using virtually the same precursor conditions as for **5**, but with Ti^{4+} (**7**) or Ti^{4+} and La^{3+} (**8**) added to the ablation solution (Table 1). XRD data revealed that both catalysts were primarily $[\text{Ni-Fe}]$ -LDH materials (SI). Oxides containing added elements were also present; TiO_2 and Fe_2TiO_4 were found in **7**, whereas crystalline Ni_3TiO_5 and $\text{La}(\text{Ni,Fe})\text{O}_3$ were detected in **8**. The spinel oxide NiFe_2O_4 was absent from both **7** and **8**. XPS data showed that **8** contained 1% La relative to total metal content. Both catalysts were more active than LDHs **5** and **6**, with **7** and **8** exhibiting the lowest overpotentials at 10 mA cm^{-2} of 270 and 260 mV, respectively (SI).

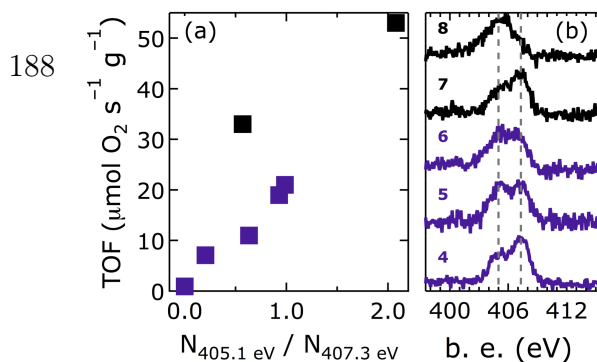


Figure 3. (a) TOF vs. $\text{N}_{405.1 \text{ eV}}/\text{N}_{407.3 \text{ eV}}$ (purple, neat Fe–Ni-based catalysts; black, **7** and **8**); (b) XPS data of catalysts **4** to **8** (the gray dashed lines mark the N 1s binding energies (405.1 and 407.3 eV)).

Highly active, surfactant-free, mixed transition metal hydroxide water oxidation nanoparticle catalysts can be made by PLAL. We spectroscopically identified a crystalline $[\text{Ni-Fe}]$ -LDH as the catalytically most active material. We discovered that turnover frequency (TOF) correlated with the ratio of two nitrogen species detected by XPS in the as-synthesized catalysts (Figure 3). Addition of Ti^{4+} and La^{3+} ions further enhanced activity (reaching 10 mA cm^{-2} at an overpotential of 260 mV). On a flat electrode, this is the lowest overpotential reported to date for mixed metal oxide catalysts.

ASSOCIATED CONTENT

Supporting Information. General experimental conditions and apparatus; physical characterization; electrochemical characterization. This material is available free of charge via the Internet at <http://pubs.acs.org>.

AUTHOR INFORMATION

Corresponding Author

astridm@caltech.edu

Notes

No competing financial interests have been declared.

The authors' institution (California Institute of Technology) has filed a provisional U.S. patent application directly relating to the work described in the manuscript (provisional patent application no. 62/013,976; filed on June 18, 2014).

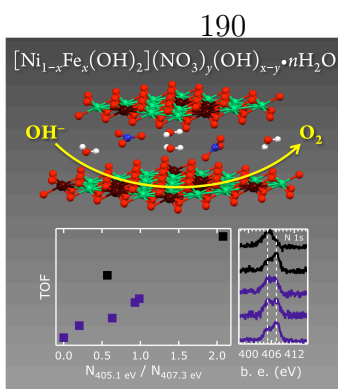
ACKNOWLEDGMENT

We thank Richard Gerhart for fabrication of an electrochemical cell, Alasdair McDowall for help with TEM, and George Rossman for help with solid-state Raman and IR spectroscopies. Research was carried out in the Laser Resource Center and the Molecular Materials Research Center of the Beckman Institute of the California Institute of Technology. This work was supported by the NSF CCI Solar Fuels Program (CHE-1305124) and the Arnold and Mabel Beckman Foundation.

REFERENCES

- (1) Gray, H. B. *Nature Chem.* **2009**, *1*, 7.
- (2) Lewis, N. S.; Nocera, D. G. *Proc. Natl. Acad. Sci. U. S. A.* **2006**, *103*, 15729.
- (3) Walter, M. G.; Warren, E. L.; McKone, J. R.; Boettcher, S. W.; Mi, Q.; Santori, E. A.; Lewis, N. S. *Chem. Rev.* **2010**, *110*, 6446.
- (4) McKone, J. R.; Lewis, N. S.; Gray, H. B. *Chem. Mater.* **2013**, *26*, 407.
- (5) Trasatti, S. *Electrochim. Acta* **1984**, *29*, 1503.
- (6) Man, I. C.; Su, H.-Y.; Calle-Vallejo, F.; Hansen, H. A.; Martínez, J. L.; Inoglu, N. G.; Kitchin, J.; Jaramillo, T. F.; Nørskov, J. K.; Rossmeisl, J. *ChemCatChem* **2011**, *3*, 1159.
- (7) Gilbert, J. A.; Eggleston, D. S.; Murphy, W. R.; Geselowitz, D. A.; Gersten, S. W.; Hodgson, D. J.; Meyer, T. J. *J. Am. Chem. Soc.* **1985**, *107*, 3855.
- (8) Limburg, J.; Brudvig, G. W.; Crabtree, R. H. *J. Am. Chem. Soc.* **1997**, *119*, 2761.
- (9) Ruettinger, W.; Yagi, M.; Wolf, K.; Bernasek, S.; Dismukes, G. C. *J. Am. Chem. Soc.* **2000**, *122*, 10353.
- (10) Dau, H.; Limberg, C.; Reier, T.; Risch, M.; Roggan, S.; Strasser, P. *ChemCatChem* **2010**, *2*, 724.
- (11) Yin, Q.; Tan, J. M.; Besson, C.; Geletii, Y. V.; Musaev, D. G.; Kuznetsov, A. E.; Luo, Z.; Hardcastle, K. I.; Hill, C. L. *Science* **2010**, *328*, 342.
- (12) Wiechen, M.; Zaharieva, I.; Dau, H.; Kurz, P. *Chem. Sci.* **2012**, *3*, 2330.
- (13) Du, P.; Eisenberg, R. *Energy Environ. Sci.* **2012**, *5*, 6012.
- (14) Singh, A.; Spiccia, L. *Coord. Chem. Rev.* **2013**, *257*, 2607.
- (15) McCrory, C. C. L.; Jung, S.; Peters, J. C.; Jaramillo, T. F. *J. Am. Chem. Soc.* **2013**, *135*, 16977.
- (16) Yang recently reported a highly active graphene FeNi double hydroxide hybrid on Ni foam working electrodes (Long, X.; Li, J.; Xiao, S.; Yan, K.; Wang, Z.; Chen, H.; Yang, S. *Angew. Chem., Int. Ed. Engl.* **2014**, *53*, 7584), although the high porosity of the electrode substrate leads to a surface area enlargement, inflating current densities that were normalized to the geometric electrode area; this makes a performance comparison impossible.
- (17) Gao, M.; Sheng, W.; Zhuang, Z.; Fang, Q.; Gu, S.; Jiang, J.; Yan, Y. *J. Am. Chem. Soc.* **2014**, *136*, 7077.
- (18) Yang, G. W. *Prog. Mater. Sci.* **2007**, *52*, 648.
- (19) Blakemore, J. D.; Gray, H. B.; Winkler, J. R.; Müller, A. M. *ACS Catal.* **2013**, *3*, 2497.
- (20) Corrigan, D. A. *J. Electrochem. Soc.* **1987**, *134*, 377.
- (21) Risch, M.; Klingan, K.; Heidkamp, J.; Ehrenberg, D.; Chernev, P.; Zaharieva, I.; Dau, H. *Chem. Commun.* **2011**, *47*, 11912.
- (22) Li, X.; Walsh, F. C.; Pletcher, D. *Phys. Chem. Chem. Phys.* **2011**, *13*, 1162.
- (23) Lyons, M. E. G.; Cakara, A.; O'Brien, P.; Godwin, I.; Doyle, R. L. *Int. J. Electrochem. Sci.* **2012**, *7*, 11768.
- (24) Trotochaud, L.; Ranney, J. K.; Williams, K. N.; Boettcher, S. W. *J. Am. Chem. Soc.* **2012**, *134*, 17253.
- (25) Trotochaud, L.; Young, S. L.; Ranney, J. K.; Boettcher, S. W. *J. Am. Chem. Soc.* **2014**, *136*, 6744.
- (26) Powder diffraction file no. 00-029-0713 (ICDD, 2012).
- (27) Powder diffraction file no. 01-076-6119 (ICDD, 2012).
- (28) Demourgues-Guerlou, L.; Fournès, L.; Delmas, C. *J. Solid State Chem.* **1995**, *114*, 6.
- (29) Axmann, P.; Glemser, O. *J. Alloys Compd.* **1997**, *246*, 232.
- (30) Trolard, F.; Bourrié, G. In *Clay Minerals in Nature - Their Characterization, Modification and Application*; Valaskova, M., Ed.; InTech: 180strava, Czech Republic, 2012.
- (31) Corrigan, D. A.; Conell, R. S.; Fierro, C. A.; Scherson, D. A. *J. Phys. Chem.* **1987**, *91*, 5009.
- (32) Balasubramanian, M.; Melendres, C. A.; Mini, S. J. *Phys. Chem. B* **2000**, *104*, 4300.
- (33) Landon, J.; Demeter, E.; İnoğlu, N.; Keturakis, C.; Wachs, I. E.; Vasić, R.; Frenkel, A. I.; Kitchin, J. R. *ACS Catal.* **2012**, *2*, 1793.
- (34) Gong, M.; Li, Y.; Wang, H.; Liang, Y.; Wu, J. Z.; Zhou, J.; Wang, J.; Regier, T.; Wei, F.; Dai, H. *J. Am. Chem. Soc.* **2013**, *135*, 8452.
- (35) Wagner, C. D. R. W. M. D., L.E.; Moulder, J.F.; Mullenberg, G. E. *Handbook of X-Ray Photoelectron Spectroscopy*; Perkin-Elmer Corporation: Eden Prairie, MN, 1979.
- (36) Bandis, C.; Scudiero, L.; Langford, S. C.; Dickinson, J. T. *Surf. Sci.* **1999**, *442*, 413.
- (37) Wei, M.; Xu, X.; Wang, X.; Li, F.; Zhang, H.; Lu, Y.; Pu, M.; Evans, D. G.; Duan, X. *Eur. J. Inorg. Chem.* **2006**, *2006*, 2831.
- (38) Baltrusaitis, J.; Jayaweera, P. M.; Grassian, V. H. *Phys. Chem. Chem. Phys.* **2009**, *11*, 8295.
- (39) Wang, X.; Deng, R.; Kulkarni, S. A.; Wang, X.; Pramana, S. S.; Wong, C. C.; Gratzel, M.; Uchida, S.; Mhaisalkar, S. G. *J. Mater. Chem. A* **2013**, *1*, 4345.
- (40) Nanayakkara, C. E.; Jayaweera, P. M.; Rubasinghe, G.; Baltrusaitis, J.; Grassian, V. H. *J. Phys. Chem. A* **2013**, *118*, 158.
- (41) Frost, R. L.; Erickson, K. L.; Klopogge, T. J. *Spectrochim. Acta A* **2005**, *61*, 2919.
- (42) Co-crystallization of several crystal phases cannot be excluded in such small size domains.
- (43) We note that, strictly speaking, BET surface areas are not necessarily equivalent to electroactive surface areas.
- (44) Pourbaix, M. *Atlas of Electrochemical Equilibria in Aqueous Solutions*; Pergamon Press: New York, 1966.
- (45) Louie, M. W.; Bell, A. T. *J. Am. Chem. Soc.* **2013**, *135*, 12329.
- (46) Oliva, P.; Leonardi, J.; Laurent, J. F.; Delmas, C.; Braconnier, J. J.; Figlarz, M.; Fievet, F.; Guibert, A. d. *J. Power Sources* **1982**, *8*, 229.
- (47) Kermarec, M.; Carriat, J. Y.; Burattin, P.; Che, M.; Decarreau, A. *J. Phys. Chem.* **1994**, *98*, 12008.
- (48) Hall, D. S.; Lockwood, D. J.; Poirier, S.; Bock, C.; MacDougall, B. R. *J. Phys. Chem. A* **2012**, *116*, 6771.
- (49) Hannyer, B.; Ristić, M.; Popović, S.; Musić, S.; Petit, F.; Foulon, B.; Dalipi, S. *Mater. Chem. Phys.* **1998**, *55*, 215.
- (50) Dincă, M.; Surendranath, Y.; Nocera, D. G. *Proc. Natl. Acad. Sci. U. S. A.* **2010**, *107*, 10337.
- (51) Bediako, D. K.; Lassalle-Kaiser, B.; Surendranath, Y.; Yano, J.; Yachandra, V. K.; Nocera, D. G. *J. Am. Chem. Soc.* **2012**, *134*, 6801.
- (52) Smith, R. D. L.; Prévot, M. S.; Fagan, R. D.; Trudel, S.; Berlinguette, C. P. *J. Am. Chem. Soc.* **2013**, *135*, 11580.
- (53) Chen, J. Y. C.; Miller, J. T.; Gerken, J. B.; Stahl, S. S. *Energy Environ. Sci.* **2014**, *7*, 1382.
- (54) For a comparison of activities see Table S3.
- (55) Song, F.; Hu, X. *Nat. Commun.* **2014**, *5*.
- (56) Zhao, Y.; Li, B.; Wang, Q.; Gao, W.; Wang, C. J.; Wei, M.; Evans, D. G.; Duan, X.; O'Hare, D. *Chem. Sci.* **2014**, *5*, 951.

TOC graphic:



The Facile Preparation of Aluminosilicate RTH Across a Wide Composition Range Using a New Organic Structure Directing Agent

Joel E. Schmidt, Mark A. Deimund and Mark E. Davis*

Chemical Engineering, California Institute of Technology, Pasadena, CA 91125

RTH-type zeolite (aluminosilicate) is a potentially useful catalytic material that is limited by the inability to easily prepare the material over a wide composition range. Here, we report the use of pentamethylimidazolium to prepare aluminosilicate RTH across a wide range of compositions in both fluoride and hydroxide inorganic systems. RTH-type zeolites are crystallized with a calcined product Si/Al of 7-27 from fluoride media and 6-59 from hydroxide media. The use of this new, simple organic structure directing agent that can be prepared in one step, allows for dramatic improvement in the compositional space where aluminosilicate RTH can be formed. RTH is tested as a catalyst for the methanol-to-olefins reaction, and at complete conversion shows a high propylene to ethylene ratio of 3.9 at a propylene selectivity of 43%.

1. Introduction

Molecular sieves have diverse applications including catalysis, ion exchange and adsorption, where their utility depends on the properties of each material, such as pore size, composition and hydrothermal stability.¹⁻³ In many applications, there is only a single structure and composition to achieve optimal performance, motivating much of the research directed at creating new materials.⁴ Currently, most discovery of new materials is based on trial and error, although there are a growing number of guiding principles and advances in methodologies that attempt to computationally predict materials.^{5,6} One of the most important methods of discovery has been the use of organic structure directing agents (OSDAs), that are normally alkylammonium cations. The use of OSDAs began with the work of Barrer and Denny to incorporate alkylammonium cations in reactions,⁷ and since that time, numerous mono-, di-, and polyquaternary OSDAs have been examined.⁸⁻¹⁸ OSDAs have been instrumental in the discovery of new frameworks, and they have also expanded the composition range for many materials, that has allowed for enhanced material properties, e.g., catalytic activity and stability.

Recently, microporous materials with 8-membered rings (MRs, number of tetrahedral atoms in the ring) have received considerable interest as catalysts for the methanol-to-olefins reaction (MTO) and NO_x reduction. MTO is of high economic demand due to the increasing price of petroleum feedstocks.¹⁹ Many different frameworks have been considered for this application, but microporous materials with 8MRs have been found to give good yields of olefins,²⁰ and selecting materials with the right number and location of acid sites can limit the formation of coke.²⁰ SAPO-34 (CHA framework topology) has been commercialized for MTO, and shows good performance with high selectivity to light olefins and a suppressed rate of coke formation.^{19,20} SSZ-13 (aluminosilicate CHA) is also promising for MTO, as its high silica to alumina ratio helps prevent the severe coking found on CHA with a lower silica to alumina ratio.²⁰ One limitation of CHA type materials is the high cost of the OSDA used to prepare them.²¹

A second, high-demand application of 8MR materials is for NO_x reduction, as these small-pore materials exhibit long-term hydrothermal stability under demanding conditions.²² The CHA framework exchanged with either Cu²⁺ or Fe²⁺ is promis-

ing,²³ and both Cu-SSZ-13 and Cu-SAPO-34 function well as catalysts for this reaction.^{24,25} In order to accommodate the charge of the copper, these materials generally have lower silica to alumina ratios (one Cu²⁺ requires two closely spaced aluminum atoms to balance the charge). As with the MTO reaction, limitations of using CHA type materials for NO_x reduction include the high cost of the OSDA required to make these materials as well as catalyst lifetime. Another promising material for NO_x reduction is SSZ-39 (AEI framework), that has a three-dimensional, 8MR system and shows superior activity and hydrothermal stability to Cu-CHA, but is limited in that it can only be produced at very narrow Si/Al ratios.²⁶ The results from SSZ-39 demonstrate that improvement is possible for NO_x reduction applications with new, 8MR materials with specific Si/Al ratios.

A promising zeolite type for the aforementioned catalytic applications is the RTH framework, a graphical representation of the structure can be found on the IZA website.²⁷⁻³¹ RTH has 8MRs with openings of 4.1 x 3.8 Å and 5.6 x 2.5 Å along the *a* and *c* axes, respectively, and a free volume of 408 Å³ (smaller than that of CHA, 415 Å³).²⁹ The geometry of the cages is different, as the largest sphere that can be occluded in the CHA framework is 7.37 Å in diameter while in RTH it is 8.18 Å in diameter. As RTH has a unique framework structure, it may exhibit catalytic properties indicative of an 8MR system but with specific new attributes. RTH was first disclosed as a borosilicate (RUB-13) in 1995 using 1,2,2,6,6-pentamethylpiperidine as the OSDA.^{23,32} The aluminosilicate version of this material (SSZ-50) was first reported in 2002 (date of first publication, first patent application filed in 1999), and is made using the N-ethyl-N-methyl-5,7,7-trimethylazoniumbicyclo[4.1.1]octane cation.^{28,33} This OSDA was found to be strongly directing to SSZ-50, as it directed its formation across a wide synthesis gel composition range. Small changes to the organic were found to alter the product selectivity, thus demonstrating the specificity of this organic for SSZ-50. It was reported that pure-phase SSZ-50 could be prepared in gel compositions ranging from Si/Al=15 all the way to the pure-silica material, but product compositions were not reported.^{15,28,34} Unfortunately, this organic is not commercially available and must be prepared through an elaborate, multi-step synthesis, limiting the potential applications of SSZ-50 unless other preparation methods can be found.

Recently, methods to prepare RTH without an OSDA have been reported, and draw upon methods employed to find OSDA-free methods for other frameworks such as *BEA.^{29,30,35,36} It was reported that RTH could be synthesized without any organics by using RUB-13 as seeds and carefully controlling the amount of sodium hydroxide and water in the synthesis.²⁹ Using this method, the product Si/Al ratio was limited to the range of 37 to 57.^{29,35} It was also found that a wide variety of amines could be used in the synthesis of aluminoborosilicate RTH to give products with Si/Al=48-259 and Si/B=18-66.³⁵ The catalytic activity of aluminosilicate RTH prepared without OSDAs (TTZ-1) was evaluated for the MTO reaction, and it showed a higher selectivity to propylene than SAPO-34 or ZSM-5, as well as a longer catalyst lifetime.²⁹ While these OSDA-free methods do show promise for the production of aluminosilicate RTH, they suffer from a limited composition range. The relatively high Si/Al values reported for OSDA-free RTH are unusual for organic free syntheses and are higher than those generally used for MTO and NO_x reduction.

In order to fully evaluate the catalytic potential of RTH, a method to easily produce this material across a wide composition range with an OSDA that is easy to prepare (if an OSDA is necessary) is needed. Recently, we have been exploring substituted imidazoles in fluoride-mediated, low-water systems (pioneered by Corma and Cambor).^{14,15,17} While several substituted imidazoles have been previously evaluated, there are many permutations of carbon atoms around the imidazole ring that remain to be explored, as well as their combinations with different inorganic conditions. In particular, we have been investigating fluoride-mediated syntheses of aluminosilicates in order to produce materials with catalytic activity. In some known synthetic systems, it is possible to add aluminum to obtain catalytically active materials, though a change in zeolite product selectivity can sometimes be observed.³⁷⁻³⁹ We recently reported using a computational method to predict chemically synthesizable OSDAs for desired microporous material frameworks, and used pure-silica STW (HPM-1) as the test case for this method.⁴⁰ Pentamethylimidazolium was predicted to be the most strongly directing OSDA for STW, and this was confirmed experimentally. In attempting to prepare aluminosilicate STW in fluoride media, we found that the RTH framework formed instead. Here, we use this OSDA for the preparation and characterization of aluminosilicate RTH (in both fluoride and hydroxide mediated syntheses) that has a wide composition range. Included in the product characterizations are results from MTO reaction testing.

2. Experimental Section

2.1 Synthesis

OSDA Synthesis

Pentamethylimidazolium was synthesized by dissolving 1,2,4,5-tetramethylimidazole (TCI Chemicals) in methanol and then cooling in a dry ice bath. A three-fold molar excess of iodomethane (Aldrich) was then slowly added (Caution: Highly exothermic reaction!), and the mixture was then slowly warmed to room temperature and stirred for one day. The solvent and excess iodomethane were then removed using rotary evaporation (Caution: Highly toxic vapors present, use appropriate precautions), and the product was recrystallized from acetone and washed with ether. The structure was verified

using ¹H and ¹³C NMR (D₂O, methanol added as internal standard) and the product was converted from the iodide to the hydroxide form using hydroxide exchange resin (Dowex Marathon A, hydroxide form) in water, and the product was titrated using a Mettler-Toledo DL22 autotitrator using 0.01 M HCl as the titrant. ¹H-NMR (500 MHz, D₂O): δ 3.60 (s, 6H), 2.54 (s, 3H), 2.20 (s, 6H). ¹³C-NMR (125 MHz, D₂O): δ 7.99, 9.76, 31.58, 125.42, 142.21.

Microporous Materials Synthesis

Fluoride mediated reactions

A general synthesis procedure was as follows. Tetraethylorthosilicate (Aldrich) and aluminum isopropoxide (Aldrich) were added to the organic in its hydroxide form in a Teflon Parr reactor liner. The container was closed and stirred for at least 12 hours to allow for complete hydrolysis. The lid was then removed, and the alcohol and appropriate amount of water were allowed to evaporate under a stream of air. Composition was monitored gravimetrically. Additional water was added as necessary, and then aqueous HF (Aldrich) was added and the mixture was stirred by hand until a homogenous gel was obtained. (Caution: Use appropriate personal protective equipment, ventilation and other safety measures when working with HF.) The final molar ratios of the gel were:



The parameters x and y were varied depending on the synthesis and the desired composition. For low water syntheses, a final evaporation step was used after the addition of HF to reach the desired water ratio. The Teflon-lined Parr reactor was sealed and placed in a rotating oven at 160°C. Aliquots of the material were taken periodically by first quenching the reactor in water and then removing enough material for powder X-ray diffraction (PXRD).

Hydroxide Mediated Syntheses

For the hydroxide syntheses, several variations on gel Si/Al as well as the sources of silica and alumina were used. Specific synthesis preparations are below. For all hydroxide reactions, seeds were added after 1 day at reaction temperature, once a decrease in pH was observed. Normally seeds were added as a homogeneous aliquot of the contents of a previous, completed reaction (less than 0.3 mL) as these were found to be more active than seeds that had been washed. The use of seeds was found to speed the formation of RTH and to help avoid the formation of dense phases, but this influence was not extensively investigated. Aliquots were taken periodically, and crystallization was monitored by both PXRD and pH, as an increase in pH was generally observed when the product crystallized. After the product crystallized, the material was washed with DI water and then collected via centrifugation. This process was repeated at least three times, and a final wash was performed using acetone. The product was dried at 100°C in air.

Sodium aluminate (or Reheiss F-2000) and Ludox AS-40 (or Cabosil)

The OSDA in its hydroxide form, sodium hydroxide (if necessary), any necessary water and sodium aluminate (Pfaltz & Bauer) were combined in a Teflon Parr reactor liner and stirred until the sodium aluminate completely dissolved. Ludox AS-40 (Aldrich) was then added and stirred until a homogenous gel was obtained. In sodium-free syntheses, Reheiss F-2000 (55wt% Al₂O₃) was used as the source of aluminum

instead of sodium aluminate, and Cabosil M-5 was used instead of Ludox AS-40. The gel pH was measured, and then the Teflon-lined Parr reactor was placed in a rotating oven at 160°C.

Si/Al=15 (NH₄-Y and Sodium Silicate)

Following the method of Wagner et al.⁴¹ 2 mmol of OSDA was mixed with 0.20 g of 1 M NaOH, and water was added to give a total mass of 6 g. Then 2.5 grams of sodium silicate (PQ Corporation, 28.6wt% SiO₂ and 8.9wt% Na₂O) was added to the mixture and finally 0.25 g of NH₄-Y (Zeolyst CBV 500, Si/Al=2.55) was added. The solution was heated at 140°C in a rotating oven.

Si/Al=15 (CBV 720)

3 mmol of OSDA was mixed with 1 g of 1 M NaOH and water was added to bring the total mass to 7 g. Then 1 g of CBV 720 (Zeolyst, Si/Al=15) was added. The solution was heated at 175°C in a rotating oven.

Si/Al=30 (CBV 760)

3 mmol of OSDA was mixed with 1 g of 1 M NaOH and water was added to bring the total mass to 7 g. Then 1 g of CBV 760 (Zeolyst, Si/Al=30) was added. The solution was heated at 175°C in a rotating oven.

SSZ-13 Synthesis

SSZ-13 was synthesized using a standard method.⁴² In a typical preparation, 3.33 g of 1 M NaOH was mixed with 2.81 g of N,N,N-trimethyl-1-adamantammonium hydroxide (Sachem, 1.18 mmol OH/g) and 6.62 g of water. Then 0.077 g of Reheiss F-2000 (55wt% Al₂O₃) was added and stirred until the solution cleared. Finally, 1.00 g of Cabosil M-5 was added and stirred until a homogeneous solution was obtained. The solution was heated at 160°C in a rotating oven for approximately 6 days.

SAPO-34 Synthesis

SAPO-34 was prepared from the following gel composition: 0.5(TEA)₂O:1.5Pr₂NH:0.6SiO₂:1Al₂O₃:1P₂O₅:70H₂O. In a typical preparation, 11.5 g of 85 wt% phosphoric acid were dissolved in 4.35 g of water and stirred for 5 minutes. Then 6.875 g of Catapal B alumina were added to 20 g of water and stirred for 10 minutes. The mixtures were then slowly combined and stirred for 1 hour at room temperature. Next 4.48 g of Ludox HS-40 was added and stirred by hand until a homogeneous gel was obtained. Then 20.8 g of 35 wt% TEOH and 7.61 g of dipropylamine were added and the gel was homogenized by manual stirring. Then the gel was stirred at room temperature for 2 hours. Finally, the gel was added to a Teflon-lined Parr reactor and heated at 200°C without stirring for 24 hours.

Calcination

All products were calcined in breathing grade air. The material was heated to 150°C at 1°C/min, held for three hours, then heated to 580°C at 1°C/min and held for six hours to assure complete combustion of the organic.

2.2 Characterization

The ¹³C CP-MAS NMR spectra were recorded using a Bruker Avance 200 MHz spectrometer with a 7 mm rotor at a spinning rate of 4 kHz and were conducted in a 4.7 T magnetic field, corresponding to Larmor frequencies of 200 MHz and 50.29 MHz for ¹H and ¹³C respectively. The ¹³C spectra are referenced to adamantane as a secondary external standard

relative to tetramethylsilane. The ²⁷Al MAS NMR were recorded using a Bruker AM 300 MHz spectrometer with a 4 mm rotor at a spinning rate of 8 kHz, and were conducted in a 7.0 T magnetic field corresponding to a Larmor frequency of 78.172 MHz. The ²⁷Al spectra are referenced to 1.1 M Al(NO₃)₃ as an external standard. All argon adsorption isotherms were performed at 87.45 K using a Quantachrome Autosorb iQ and were conducted using a quasi-equilibrium, volumetric technique.⁴³ All powder X-ray diffraction (PXRD) characterization was conducted on a Rigaku MiniFlex II with Cu K_α radiation. SEM images were acquired on a ZEISS 1550 VP FESEM, equipped with in-lens SE. EDS spectra were acquired with an Oxford X-Max SDD X-ray Energy Dispersive Spectrometer system.

2.3 Reaction Testing

Prior to reaction testing, all materials were calcined as described in section 2.1. After calcination they were exchanged to ammonium form using 1 M NH₄NO₃ (100 mL of solution per gram of catalyst) at 95°C with stirring for three hours, this was done a total of three times per sample. After ammonium exchange the materials were washed with water and dried and then calcined using the method in section 2.1. The calcined materials were then pelletized, crushed, and sieved. Particles between 0.6 mm and 0.18 mm were supported between glass wool beds in an Autoclave Engineers BTRS, Jr. SS-316 tubular, continuous flow reactor.

All catalysts were dried at 150°C in situ in a 30 cm³/min flow of 5% Ar/95% He for 4 h prior to the reaction. The reactions were conducted at 400°C in a 10% methanol/inert flow. Methanol was introduced via a liquid syringe pump at 5.4 μL/min, into a gas stream of the inert blend at 30 cm³/min. The reactant flow had a weight hourly space velocity of 1.3 h⁻¹. In a typical run, 200 mg of dry catalyst was loaded. Effluent gases were evaluated using an on-stream GC/MS (Agilent GC 6890/MSD5793N) with a Plot-Q capillary column installed. Conversions and selectivities were computed on a carbon mole basis. Catalyst regeneration between reaction tests was done in-situ by exposing the catalyst to breathing grade air at reaction temperature, ramping to 580°C at 1°C/min, holding at 580°C for 6 hours, and then cooling to reaction temperature.

3. Results and Discussions

3.1 Fluoride-Mediated Reactions

We recently reported a computational method to construct chemically synthesizable OSDAs for desired frameworks that successfully identified pentamethylimidazolium as an OSDA for producing pure-silica STW.⁴⁰ After the successful synthesis of pure-silica STW using this OSDA, fluoride-mediated aluminosilicate reactions were then conducted with pentamethylimidazolium. These reactions produced aluminosilicate RTH (SSZ-50). This is the first report of aluminosilicate RTH produced in fluoride media (Zones and co-workers reported pure-silica RTH in fluoride media¹⁵). This result highlights the influence that small amounts of aluminum can have on low-water, fluoride-mediated syntheses.³⁹

A representative PXRD of the calcined material produced in fluoride media (sample F3) is shown in the upper diffraction pattern in Figure 1, and a summary of all synthetic results is

presented in Table 1. The fluoride method was able to produce RTH across a wide range of compositions, but at the highest Si/Al ratios tested, STW appeared as a competitive phase (sample F9). This phase competition is an expected result based on work using pentamethylimidazolium to make pure-silica STW.⁴⁰ A representative SEM of the material produced in the fluoride method is shown in Figure 2a (sample F4). The crystal size and morphology are consistent with pure-silica RTH produced in fluoride media,¹⁵ and the large crystal size is what is generally observed for low-water, fluoride-mediated syntheses. It was determined that pentamethylimidazolium, and not a decomposition product, led to the formation of aluminosilicate RTH using ¹³C CP-MAS NMR, and the spectrum compared to the ¹³C liquid NMR of pentamethylimidazolium is shown in Figure 3. In order to determine the coordination of the aluminum in the material, ²⁷Al MAS NMR was performed on the calcined sample containing the highest amount of aluminum (sample F2), and the spectrum is shown in Figure 4. The single resonance in this sample at 54 ppm is consistent with tetrahedrally coordinated aluminum, and there is no evidence of octahedrally coordinated aluminum, normally found around 0 ppm.

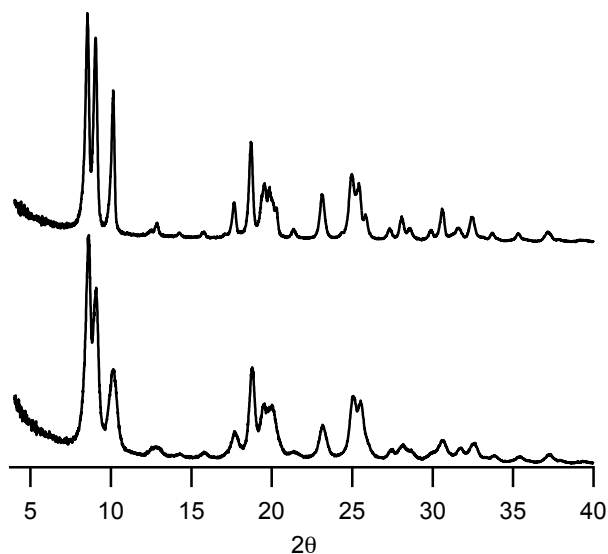


Figure 1. Calcined aluminosilicate RTH prepared in fluoride (upper, sample F3) and hydroxide media (lower, sample H4).

Table 1. Synthesis of RTH in fluoride media

Gel Si/Al	Product Si/Al ^a	Gel H ₂ O/SiO ₂	Time (days)	Sample
5	--	7	No product	F1
10	7	7	29	F2
15	10	14	46	F3
20	16	14	22	F4
20	18	4	10	F5
33	22	14	20	F6
40	26	14	17	F7
50	27	14	20	F8
150	STW impurity	7	7	F9

^aReported Si/Al is of calcined material

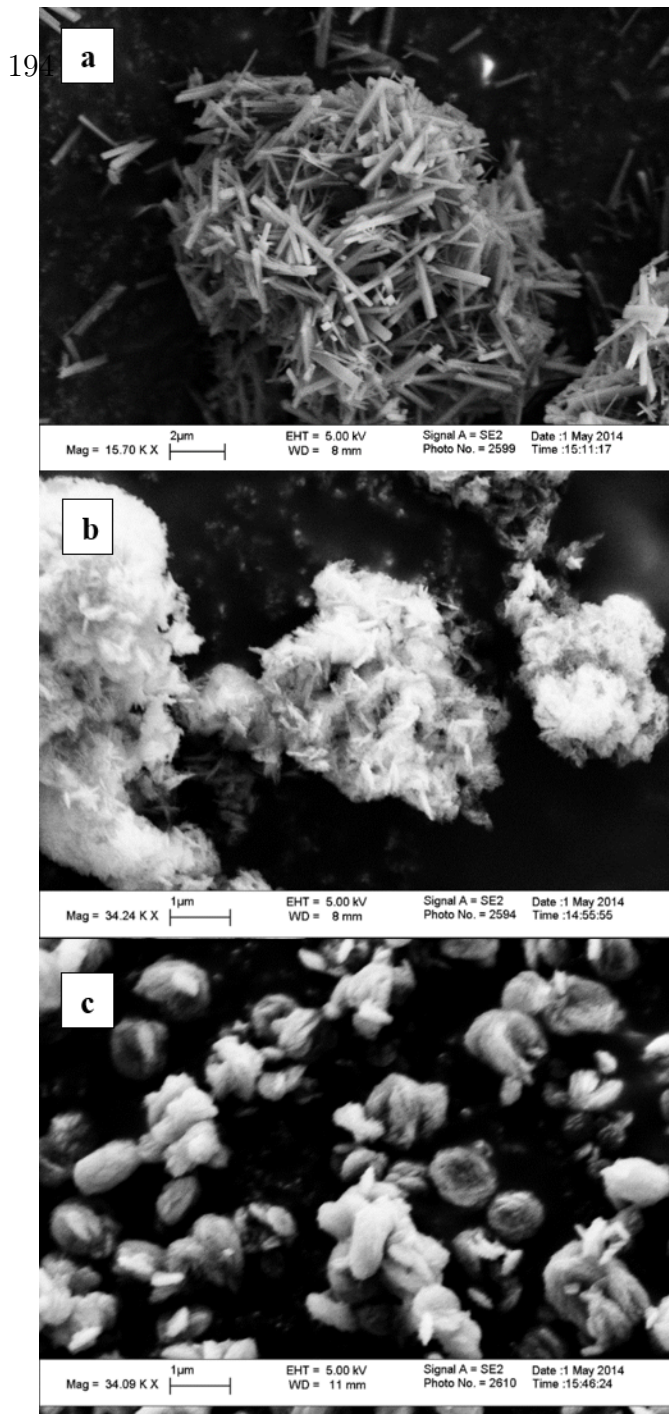


Figure 2. SEM images: (a) Calcined RTH prepared in fluoride media (sample F4), (b) calcined RTH synthesized in hydroxide media with sodium (sample H4), (c) calcined RTH synthesized in hydroxide media without sodium (sample H5).

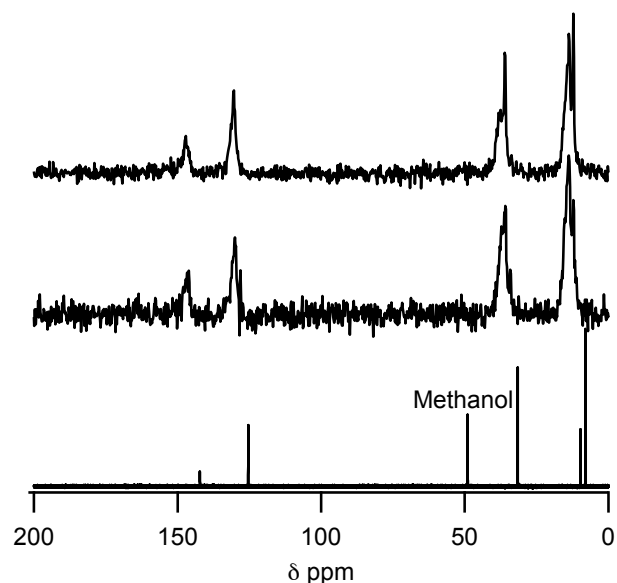


Figure 3. ^{13}C NMR of pentamethylimidazolium in D_2O with methanol standard (lower), ^{13}C CP-MAS NMR of as-made RTH prepared in hydroxide media (middle, sample H4) and ^{13}C CP-MAS NMR of as-made RTH prepared in fluoride media (upper, sample F4).

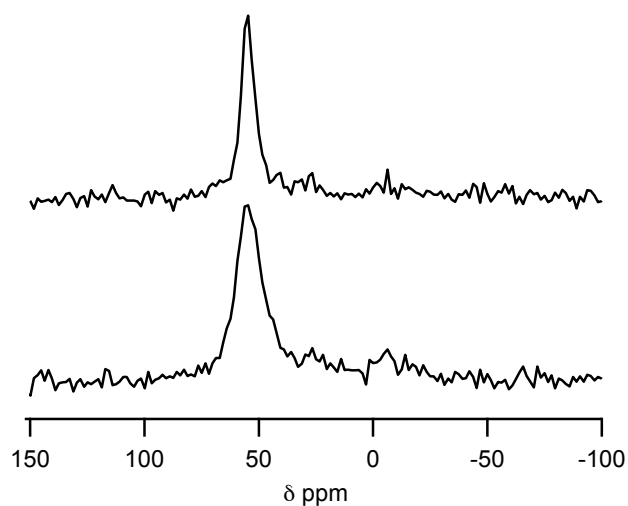


Figure 4. ^{27}Al MAS NMR of low silica RTH synthesized in hydroxide media (lower, sample H1) and prepared in fluoride media (upper, sample F2). The single resonance is at 54 ppm.

3.2 Hydroxide-Mediated Reactions

The success of using pentamethylimidazolium in fluoride-mediated reactions to produce aluminosilicate RTH led us to work in hydroxide-mediated reactions as well, with seeds of RTH added to promote its formation. The results of the syntheses are shown in Table 2. In general, these syntheses were found to be sensitive to reaction time and temperature, and required careful monitoring to avoid the formation of dense phases. Seeds of RTH were added to all reactions to promote the formation of RTH, but the exact influence of the seeds was not extensively investigated. A representative PXRD of the calcined material produced in hydroxide media is shown in the

lower diffraction pattern in Figure 1. The crystal sizes of the products were generally much smaller in hydroxide syntheses than in the fluoride syntheses, as is shown in Figure 2. The smaller crystal sizes observed under these conditions are consistent with what is generally reported in hydroxide syntheses. It is interesting to note that the aggregation appeared to be different in reactions where no sodium was present compared to those with sodium present (Figure 2). ^{13}C CP-MAS NMR showed that pentamethylimidazolium was also occluded intact in the material prepared in hydroxide media (Figure 3). ^{27}Al MAS NMR was used to characterize the sample containing the largest amount of aluminum (sample H1), as was done in the fluoride-mediated case, and is shown in Figure 4. There is a single resonance at 54 ppm corresponding to tetrahedrally coordinated aluminum and no evidence of any significant amount of octahedral aluminum. An argon adsorption isotherm for sample H4 is shown in Figure 5, and the micropore volume was calculated to be $0.16\text{ cm}^3/\text{g}$ (t-plot method). The EDS analyses of the materials synthesized in hydroxide media are given in Table 2, and the results show that RTH can be crystallized across a wide range of compositions from Si/Al of 6 to 59 in the calcined product (a large expansion over previously reported results). Of significant interest are the low-silica syntheses (the lowest product found was Si/Al=6, sample H1), much lower than any other reported compositions.

Table 2. Synthesis results in hydroxide media

Gel Si/Al	Product Si/Al ^a	Gel Na/Si	Gel ROH /Si	Gel H ₂ O/S _i	Time (days)	Sample
5 ^b	6	0.16	0.16	30	10	H1
10 ^b	9	0.16	0.16	30	10	H2
15 ^c	9				9	H3
15 ^b	14	0.16	0.16	30	10	H4
15 ^d	15		0.32	30	15	H5
15 ^e	17				10	H6
20 ^b	20	0.16	0.16	30	12	H7
30 ^f	29				13	H8
50 ^b	45	0.10	0.20	30	9	H9
75 ^b	59	0.10	0.20	30	9	H10

^aReported Si/Al is of calcined material.
^bMade with Ludox AS-40 and sodium aluminate
^cMade with $\text{NH}_4\text{-Y}$ and sodium silicate
^dMade using Cabosil M-5 and Reheiss F-2000
^eMade using CBV 720 as only source of Si and Al
^fMade using CBV 760 as only source of Si and Al

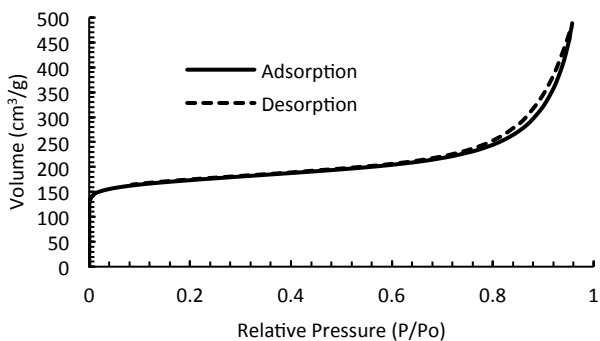


Figure 5. Argon isotherm for aluminosilicate RTH prepared in hydroxide media with product Si/Al=14 (sample H4).

3.3 Comparisons between Materials Prepared from Fluoride and Hydroxide Media

Pentamethylimidazolium was successful in preparing aluminosilicate RTH in both fluoride and hydroxide mediated syntheses. The size and morphology of the RTH crystals are very different between the two synthetic methods, and this could lead to differences in catalyst activity and lifetime. The product composition ranges produced using pentamethylimidazolium are much wider than the previously reported results. The ability to vary the composition of the material will likely be important for specific applications. NO_x reduction generally requires lower Si/Al ratios than MTO reactions, so the ability of pentamethylimidazolium to produce RTH across such a wide composition space is important. Using the OSDA-free methods, the lowest Si/Al ratio reported is 37, and in the results reported by Zones and co-workers, the synthesis using the largest amount of aluminum resulted in ANA as a phase impurity, so the current method is a significant improvement over the known methods.

3.4 Reaction Testing

The catalytic activity of RTH for the MTO reaction was evaluated using three different samples of RTH prepared in hydroxide media at different Si/Al ratios, and the results were compared to samples of SSZ-13 and SAPO-34. The samples of RTH tested were prepared using the CBV 720, CBV 760 and the sodium aluminate and Ludox synthesis routes, with product Si/Al values of 17, 29 and 59, respectively (samples H6, H8, H10). The sample of SSZ-13 had a product Si/Al of 19. The MTO reaction data for the RTH materials is given in Figure 6, the data for SSZ-13 and SAPO-34 are given in Figures S1 and S2, respectively.

The propylene to ethylene ratio is much higher for RTH than SSZ-13 or SAPO-34. In sample H6 with Si/Al=17, the maximum propylene to ethylene selectivity ratio observed was 3.6 at 96 minutes on stream. For sample H8 with Si/Al=29, the maximum propylene to ethylene selectivity ratio observed was 3.9 at 96 minutes on stream. For sample H10 with Si/Al=59, the maximum propylene to ethylene selectivity ratio observed was 3.6 between 25 and 41 minutes on stream. These selectivity ratios are much higher than those observed with SSZ-13 or SAPO-34, where the maximum propylene to ethylene ratios are 1.7 at 96 minutes on stream and 1.3 across several time points, respectively (Figure S1 and Figure S2). This result

shows that RTH would be a superior catalyst in applications where a higher propylene to ethylene ratio is desired.

The selectivity towards butene is also higher for RTH than for SSZ-13 or SAPO-34. The maximum selectivities to butene for the RTH samples were 0.22, 0.27 and 0.25 for the samples with Si/Al=17, 29 and 59, respectively (H6, H8, H10). The highest selectivity observed for SSZ-13 was 0.15 and for SAPO-34 was 0.17 (Figure S1 and S2).

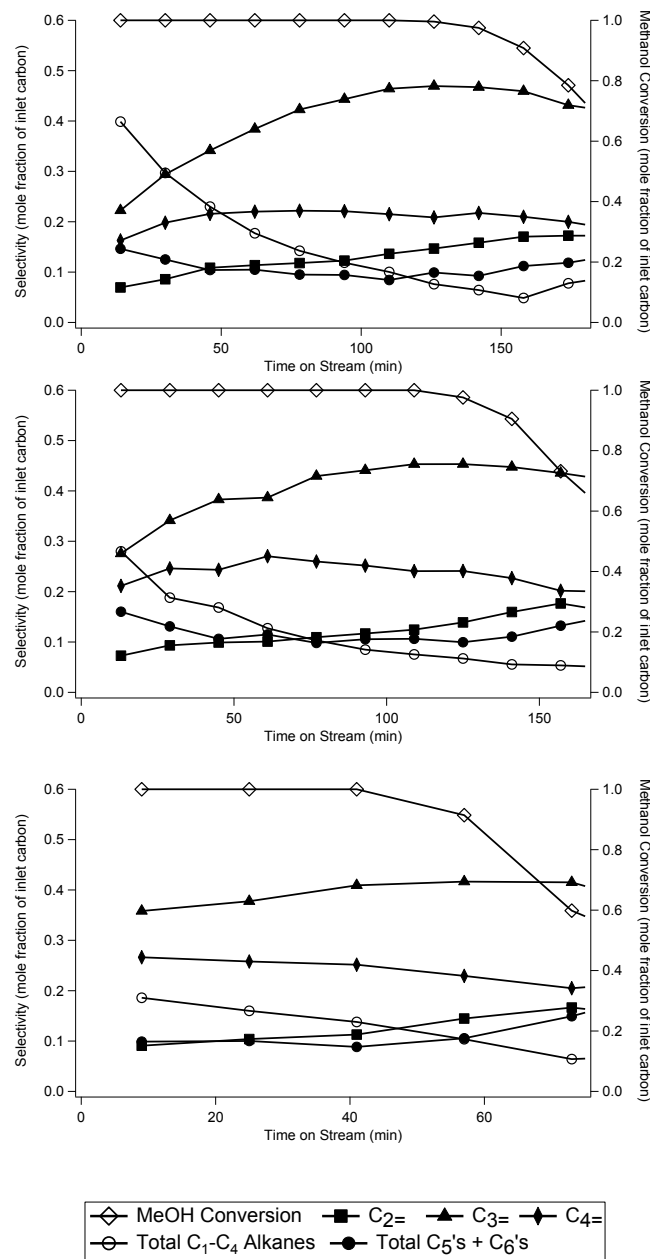


Figure 6. MTO reactivity data for (from top to bottom): RTH with Si/Al=17 (sample H6), RTH with Si/Al=29 (sample H8), RTH with Si/Al=59 (sample H10).

With the RTH samples, one of the main differences between the samples was the selectivity to C_1 - C_4 saturates (mainly propane). The maximum selectivity for each sample occurred at the first time point, and the values were 0.39, 0.28 and 0.19 for the samples with Si/Al=17, 29 and 59, respectively (samples

H6, H8, H10). It was also observed that time on stream with complete methanol conversion decreased with increasing Si/Al ratios. We are currently investigating the origins of these phenomena.

When comparing RTH to SSZ-13 or SAPO-34, one of the main differences observed is the time on stream until the catalyst deactivates. In all the RTH samples, this was significantly less than it was for either SSZ-13 (Figure S1) or SAPO-34 (Figure S2). However, an industrial scale MTO reaction will likely be run in a fluidized-bed reactor, which allows continuous regeneration of the catalyst.⁴⁴ This will allow a system to be operated at any time point along a fixed bed reactor profile, assuming the catalyst can be regenerated. To this end, the ability of RTH to be regenerated was tested by running the Si/Al=17 material (sample H6) for three consecutive MTO reaction runs with regeneration between each run, and the results are given in the supporting information, Figures S3 through S5. There are some small differences between the fresh catalyst (Figure S3) and first regeneration of the catalyst (Figure S4), but the MTO reaction behavior is similar between the first regeneration (Figure S4) and second regeneration (Figure S5) of the material. The regeneration experiment demonstrates that RTH would be suitable for use in fluidized bed systems as it can maintain its activity across multiple regeneration cycles.

4. Conclusions

Pentamethylimidazolium can be easily synthesized from commercially available 1,2,4,5-tetramethylimidazole, and is used to form aluminosilicate RTH in both fluoride and hydroxide-containing syntheses across a wide range of compositions. The flexibility of product composition and relative ease of preparing the OSDA may open new opportunities for evaluating the potential of RTH in applications such as MTO, NO_x reduction and other catalytic uses. When tested for the MTO reaction, RTH shows a higher propylene to ethylene ratio, as well as a higher selectivity towards butene compared to SSZ-13.

ASSOCIATED CONTENT

AUTHOR INFORMATION

Corresponding Author

* Email: mdavis@cheme.caltech.edu

Author Contributions

The manuscript was written through contributions of all authors.

Funding Sources

The authors would like to thank Chevron Energy and Technology Company for providing funding for this work. J.E.S. would like to thank the NDSEG for their support through a fellowship.

Supporting Information Available

Plots of the MTO reaction data for the SSZ-13, SAPO-34 and regeneration of the RTH catalyst are available in the supporting information. This information is available free of charge via the Internet at <http://pubs.acs.org/>.

ACKNOWLEDGMENT

The authors would like to thank Stacey Zones for insightful discussions regarding the synthesis of RTH.

ABBREVIATIONS

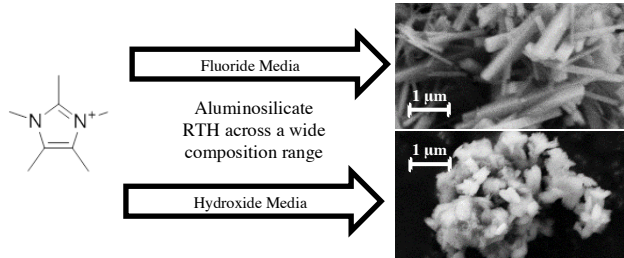
OSDA, organic structure directing agent; PXRD, powder x-ray diffraction

REFERENCES

- (1) Davis, M. E. *Nature* **2002**, *417*, 813.
- (2) Vermeiren, W.; Gilson, J.-P. *Top. Catal.* **2009**, *52*, 1131.
- (3) Cundy, C. S.; Cox, P. A. *Chem. Rev.* **2003**, *103*, 663.
- (4) Pophale, R.; Daeyaert, F.; Deem, M. W. *J. Mater. Chem. A* **2013**, *1*, 6750.
- (5) Verheyen, E.; Joos, L.; Van Havenbergh, K.; Breyneart, E.; Kasian, N.; Gobechiya, E.; Houthoofd, K.; Martineau, C.; Hinterstein, M.; Taulelle, F.; Van Speybroeck, V.; Waroquier, M.; Bals, S.; Van Tendeloo, G.; Kirschhock, C. E. A.; Martens, J. A. *Nat. Mater.* **2012**, *11*, 1059.
- (6) Moliner, M.; Rey, F.; Corma, A. *Angew. Chem. Int. Ed. Engl.* **2013**, *52*, 13880.
- (7) Barrer, R. M.; Denny, P. J. *J. Chem. Soc.* **1961**, 971.
- (8) Burton, A.; Zones, S. *Stud. Surf. Sci. Catal.* **2007**, *168*, 137.
- (9) Zones, S. I.; Burton, A. W.; Lee, G. S.; Olmstead, M. M. *J. Am. Chem. Soc.* **2007**, *129*, 9066.
- (10) Jones, W.; Rao, C. In *Supramolecular organization and materials design*; Cambridge University Press: Cambridge, UK, 2002; pp. 83–102.
- (11) Zones, S. I.; Hwang, S. *Microporous Mesoporous Mater.* **2011**, *146*, 48.
- (12) Moini, A.; Schmitt, K.; Valyocsik, E.; Polomski, R. *Zeolites* **1994**, *14*, 504.
- (13) Ren, L.; Wu, Q.; Yang, C.; Zhu, L.; Li, C.; Zhang, P.; Zhang, H.; Meng, X.; Xiao, F.-S. *J. Am. Chem. Soc.* **2012**, *134*, 15173.
- (14) Cambor, M.; Villaescusa, L.; Diaz-Cabanas, M. *Top. Catal.* **1999**, *9*, 59.
- (15) Zones, S. I.; Hwang, S.-J.; Elomari, S.; Ogino, I.; Davis, M. E.; Burton, A. W. *Comptes Rendus Chim.* **2005**, *8*, 267.
- (16) Cambor, M. A.; Barrett, P. A.; Diaz-Cabanas, M.-J.; Villaescusa, L. A.; Puche, M.; Boix, T.; Pérez, E.; Koller, H. *Microporous Mesoporous Mater.* **2001**, *48*, 11.
- (17) Jiang, J.; Yu, J.; Corma, A. *Angew. Chem. Int. Ed. Engl.* **2010**, *49*, 3120.
- (18) Takewaki, T.; Beck, L. W.; Davis, M. E. *Microporous Mesoporous Mater.* **1999**, *33*, 197.
- (19) Olsbye, U.; Svelle, S.; Bjorgen, M.; Beato, P.; Janssens, T. V. W.; Joensen, F.; Bordiga, S.; Lillerud, K. P. *Angew. Chem. Int. Ed. Engl.* **2012**, *51*, 5810.
- (20) Zhu, Q.; Kondo, J. N.; Ohnuma, R.; Kubota, Y.; Yamaguchi, M.; Tatsumi, T. *Microporous Mesoporous Mater.* **2008**, *112*, 153.
- (21) Zones, S. I. *Microporous Mesoporous Mater.* **2011**, *144*, 1.
- (22) Martínez, C.; Corma, A. *Coord. Chem. Rev.* **2011**, *255*, 1558.
- (23) Fickel, D. W.; Lobo, R. F. *J. Phys. Chem. C* **2010**, *114*, 1633.
- (24) Kwak, J. H.; Tonkyn, R. G.; Kim, D. H.; Szanyi, J.; Peden, C. H. F. *J. Catal.* **2010**, *275*, 187.
- (25) Martínez-Franco, R.; Moliner, M.; Franch, C.; Kustov, A.; Corma, A. *Appl. Catal. B Environ.* **2012**, *127*, 273.
- (26) Moliner, M.; Franch, C.; Palomares, E.; Grill, M.; Corma, A. *Chem. Commun. (Camb)*. **2012**, *48*, 8264.
- (27) Vortmann, S.; Marler, B.; Gies, H.; Daniels, P. *Microporous Mater.* **1995**, *4*, 111.
- (28) Lee, G. S.; Zones, S. I. *J. Solid State Chem.* **2002**, *167*, 289.
- (29) Yokoi, T.; Yoshioka, M.; Imai, H.; Tatsumi, T. *Angew. Chem. Int. Ed. Engl.* **2009**, *48*, 9884.
- (30) Liu, M.; Yokoi, T.; Yoshioka, M.; Imai, H.; Kondo, J. N.; Tatsumi, T. *Phys. Chem. Chem. Phys.* **2014**, *16*, 4155.
- (31) Baerlocher, C.; McCusker, L. B. Database of Zeolite Structures, <<http://www.iza-structure.org/databases/>>.
- (32) Gies, H.; Vortmann, S.; Marler, B.; Muller, U.; Dingerdissen, U. Crystalline solids having the RUB-13 structure. US 5,614,166, March 25, 1997.
- (33) Lee, Greg S.; Zones, Stacey I. Zeolite SSZ-50. US 6,605,267 B1, August 12, 2003.
- (34) Kim, C.; Hwang, S.-J.; Burton, A. W.; Zones, S. I. *Microporous Mesoporous Mater.* **2008**, *116*, 227.
- (35) Yoshioka, M.; Yokoi, T.; Liu, M.; Imai, H.; Inagaki, S.; Tatsumi, T. *Microporous Mesoporous Mater.* **2012**, *153*, 70.

- (36) Meng, X.; Xiao, F.-S. *Chem. Rev.* **2014**, *114*, 1521.
- (37) Corma, A.; Rey, F.; Rius, J.; Sabater, M. J.; Valencia, S. *Nature* **2004**, *431*, 287.
- (38) Cambor, M. a.; Corma, A.; Valencia, S. *J. Mater. Chem.* **1998**, *8*, 2137.
- (39) Díaz-Cabañas, M. J.; Cambor, M. A.; Liu, Z.; Ohsuna, T.; Terasaki, O. *J. Mater. Chem.* **2002**, *12*, 249.
- (40) Schmidt, J. E.; Deem, M. W.; Davis, M. E. *Angew. Chem. Int. Ed. Engl.* **2014**, *53*, 8372.
- (41) Wagner, P.; Nakagawa, Y.; Lee, G. S.; Davis, M. E.; Elomari, S.; Medrud, R. C.; Zones, S. I. *J. Am. Chem. Soc.* **2000**, *122*, 263.
- (42) Robson, H. *Verified synthesis of zeolitic materials*; 2001.
- (43) Hathaway, P. E.; Davis, M. E. *Catal. Letters* **1990**, *5*, 333.
- (44) Moliner, M.; Martínez, C.; Corma, A. *Chem. Mater.* **2014**, *26*, 246.
-

Insert Table of Contents artwork here



The Facile Preparation of Aluminosilicate RTH Across a Wide Composition Range Using a New Organic Structure Directing Agent

Joel E. Schmidt, Mark A. Deimund and Mark E. Davis*

Chemical Engineering, California Institute of Technology, Pasadena, CA 91125

Supporting Information

Methanol to Olefins Reactivity Data

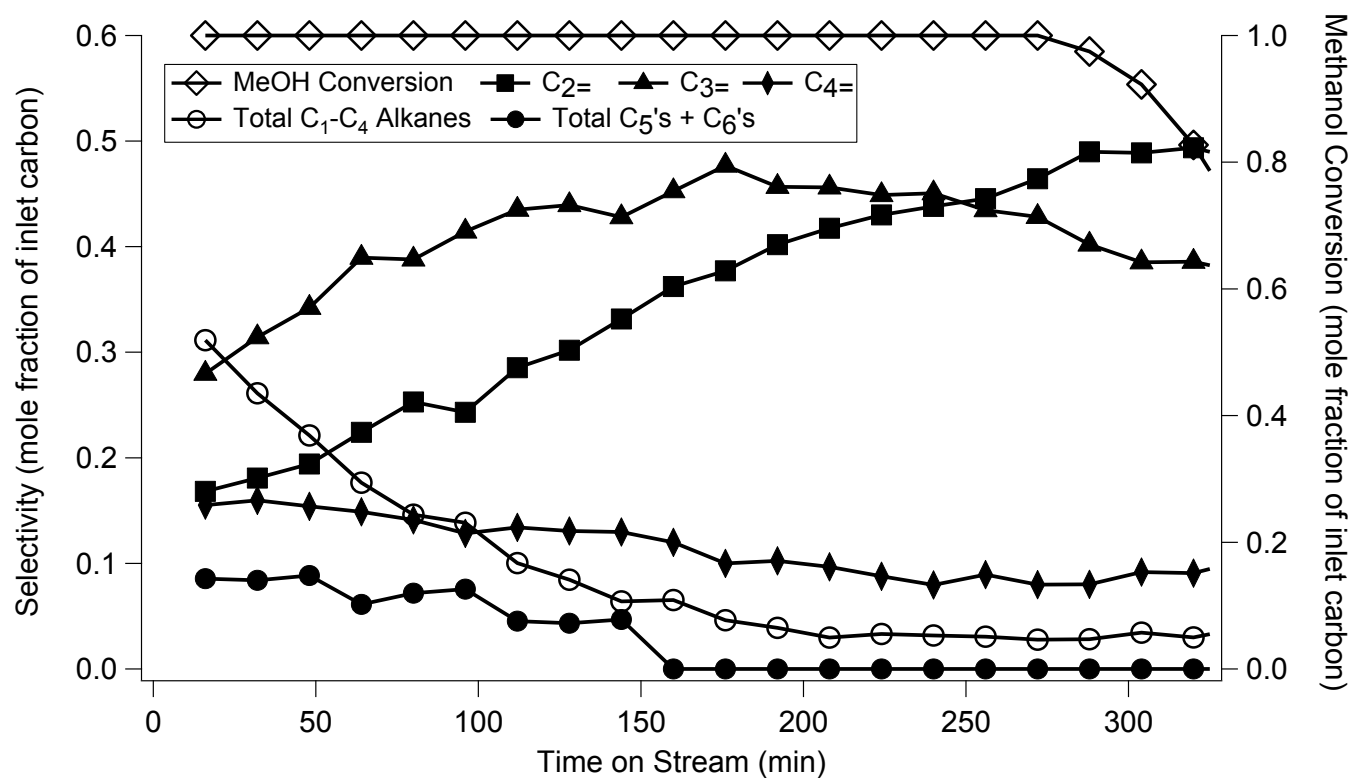


Figure S1. SSZ-13 with Si/Al=19

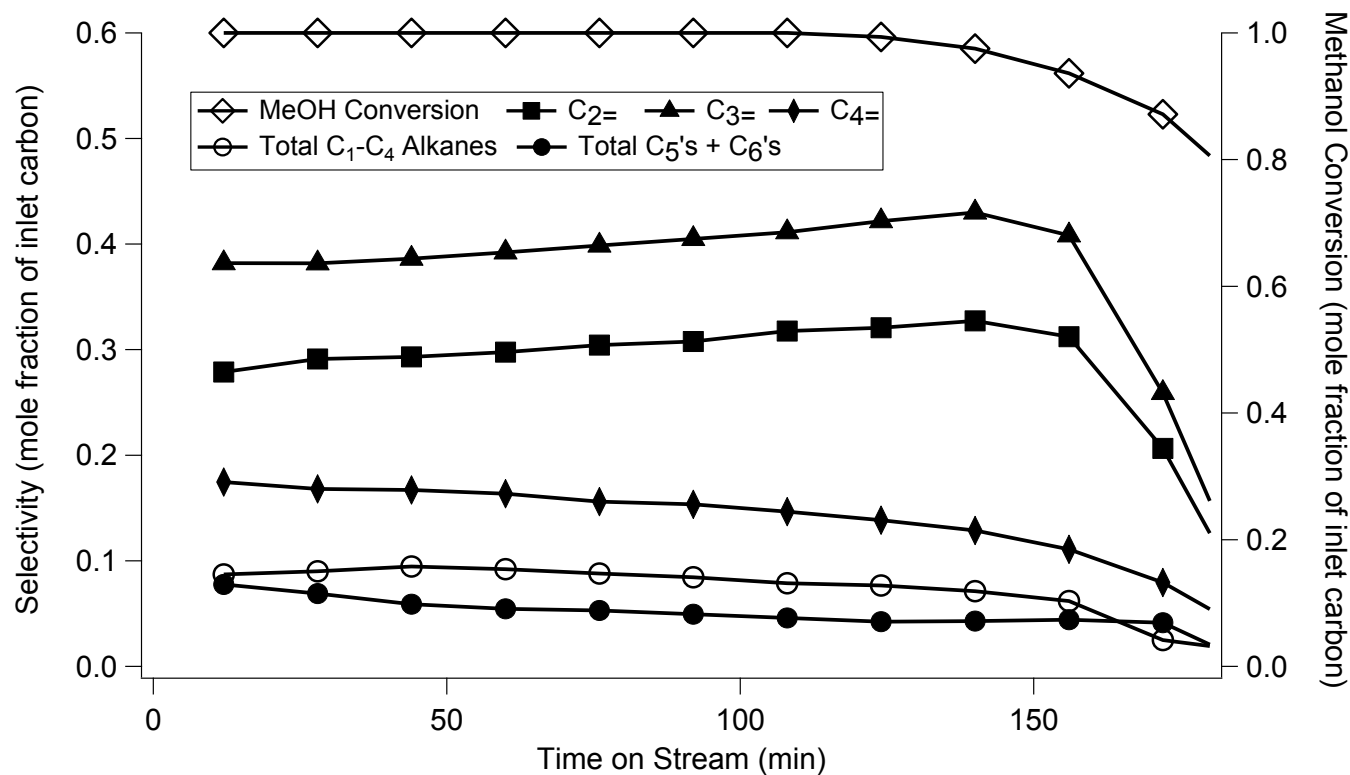


Figure S2. SAPO-34

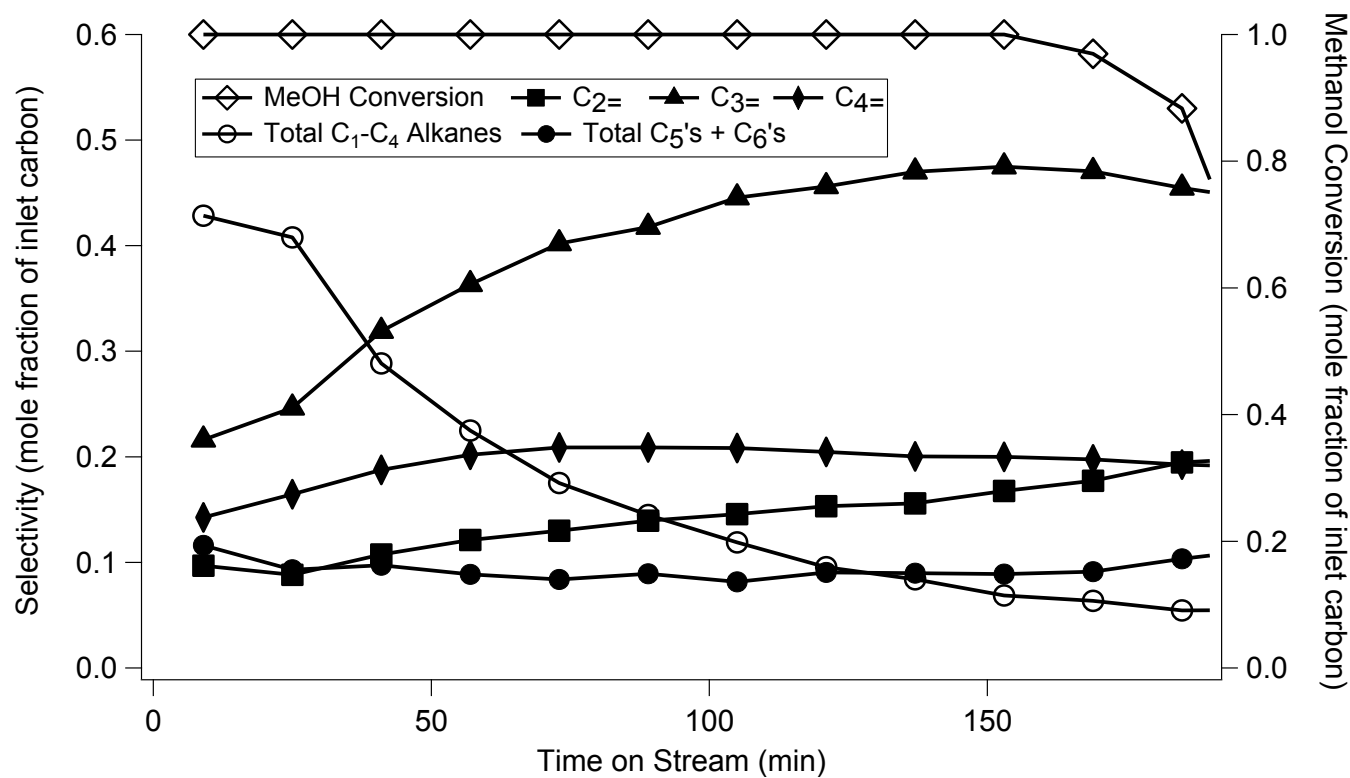


Figure S3. Fresh Si/Al=17 RTH (sample H6)

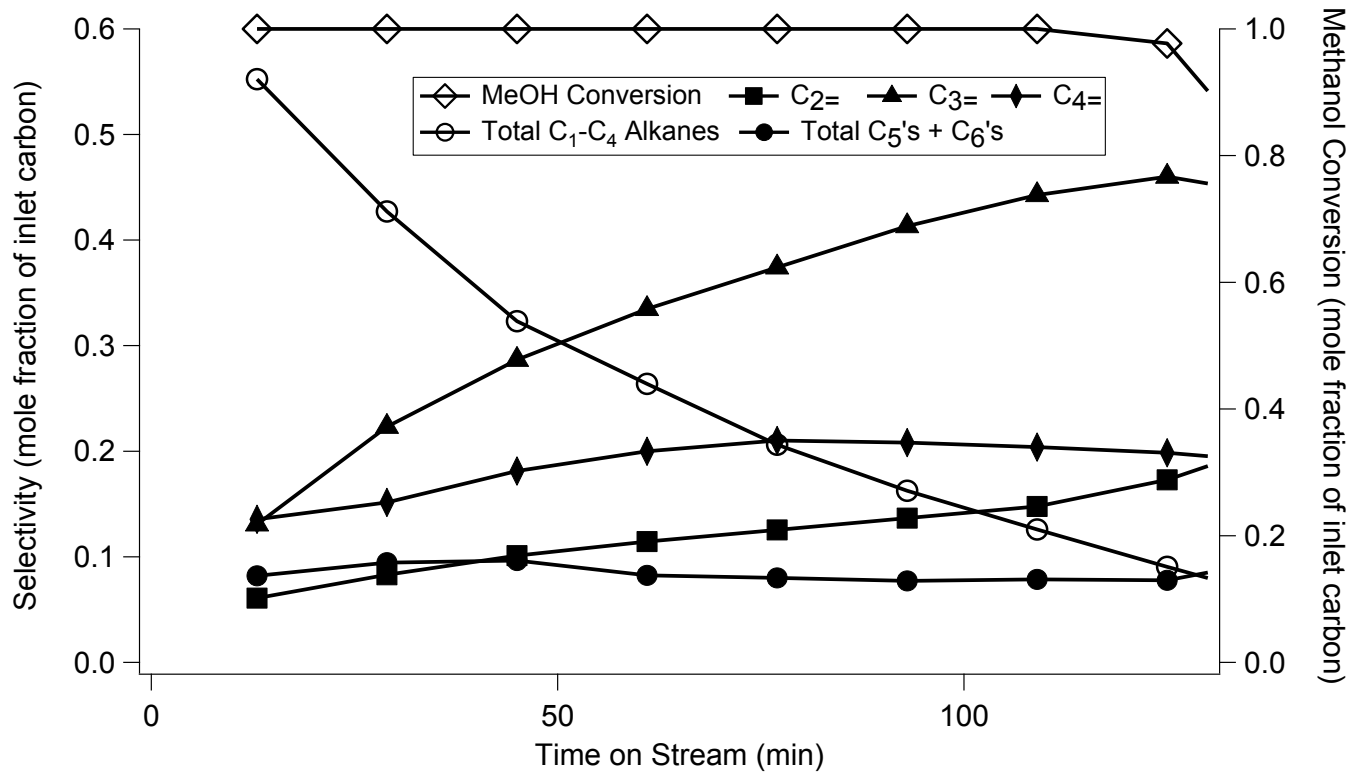


Figure S4. Si/Al=17 RTH regenerated one time (sample H6)

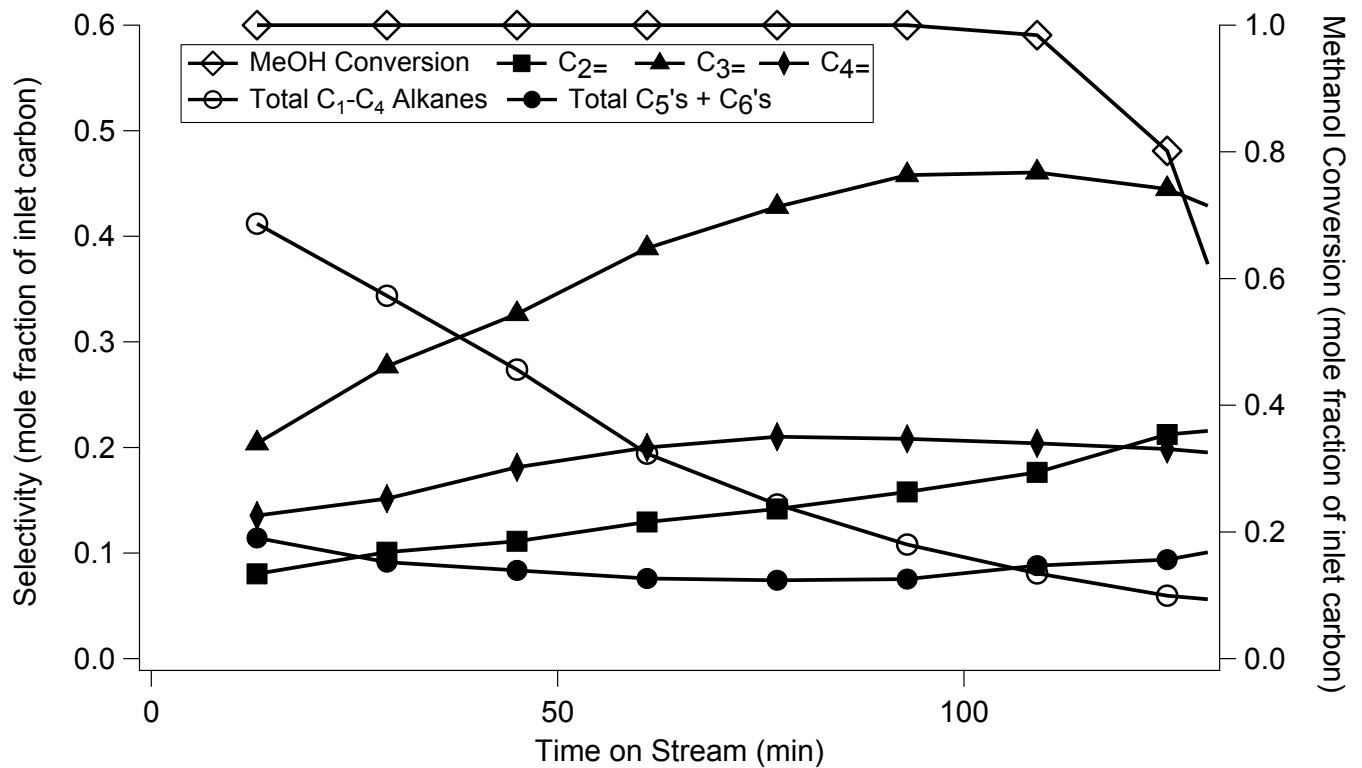


Figure S5. Si/Al=17 RTH regenerated two times (sample H6)

Synthesis of RTH-type Zeolites Using a Diverse Library of Imidazolium Cations

Joel E. Schmidt¹, Mark A. Deimund¹, Dan Xie² and Mark E. Davis^{1*}

¹Chemical Engineering, California Institute of Technology, Pasadena, CA 91125

²Chevron Energy Technology Company, Richmond, CA 94802, USA

RTH-type zeolites are promising catalytic materials for applications that include the important methanol-to-olefins (MTO) and NO_x reduction reactions. Here, **RTH**-type zeolites are prepared using a wide-range of imidazolium-based, cationic organic structure directing agents (OSDAs), that greatly expand the methodologies and compositions that can be used to synthesize these materials. The abilities of the OSDAs to produce **RTH**-type zeolites agree well with results from molecular modeling studies of predicted stabilization energies of the OSDAs in the **RTH** framework. The **RTH**-type zeolites are stable to steaming up to 900°C, and are shown to be active MTO catalysts.

1. Introduction

It is estimated that over 90% of chemical processes use a catalyst, with 80% being a heterogeneous catalyst, amounting to a global demand of \$15 to \$20 billion per year.¹ Microporous materials (pores less than 2 nm) are an important type of heterogeneous catalyst, as they offer shape and size selective environments for catalysis to occur. Additionally, they often exhibit robust hydrothermal stability that allows them to be used under demanding process conditions, such as fluidized catalytic cracking or NO_x reduction in exhaust streams. Synthetic zeolites are produced on a scale 1.7-2 million metric tons per year, and their use as catalysts comprises 27% of the world market for zeolites.² As the cost of the catalyst is estimated to be only 0.1% of the cost of the final product, the demand to innovate in this area remains high.¹

There currently exist over 200 known microporous material frameworks, but of these, less than 20 have been commercialized, and the market is dominated by only five major frameworks.^{2,3} The motivation to develop new materials is strong as there normally is only a single structure and composition for satisfactory performance in a given application.⁴ Much of the discovery of new frameworks and compositions in recent years has resulted from the use of organic structure directing agents (OSDAs), that are normally alkylammonium cations. While OSDAs have led to many new materials, their cost contributes a significant portion of the material cost, that often cannot be recovered as they are generally removed using combustion.^{3,5,6} In some systems, it is possible to partially replace high cost OSDAs with cheaper organics, such as with SSZ-13, where it has been shown that over 80% of the expensive trimethyl-N-1-Adamantammonium hydroxide OSDA can be replaced with the much cheaper benzyltrimethylammonium hydroxide.³ Alternatively, methods to synthesize the materials in the absence of OSDAs are being explored. However, this route can often lead to limited product compositions, and does not eliminate processing steps such as ion exchange and calcination.⁷ Therefore, an attractive route to lower OSDA costs is to find simpler OSDAs to synthesize desired materials.

We have recently reported on a method to synthesize aluminosilicate **RTH**⁸ (SSZ-50) across a wide compositional range using a simple OSDA, pentamethylimidazolium.⁹ Prior to this discovery, SSZ-50 was prepared using a difficult to

produce OSDA (Figure 1) requiring an elaborate, multi-step synthesis or by OSDA free methods that only reported the material over a very limited compositional range.¹⁰⁻¹³ **RTH** has a 2-dimensional system of 8-membered ring (8MR) pores, leading to larger cages. It shows good activity for the methanol-to-olefins reaction (MTO) and has also been proposed as a material for catalytic NO_x reduction.⁹

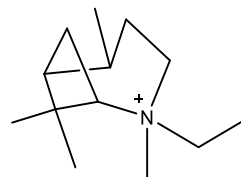


Figure 1. Original OSDA reported to synthesize aluminosilicate **RTH** (SSZ-50).

Here, we show that **RTH**-type zeolites can be produced by a wide range of substituted imidazolium OSDAs. The general structure directing ability of these OSDAs agrees well with the molecular modelling predictions. This study was prompted by our recent work in which we screened a number of imidazoliums to make pure-silica **STW**.¹⁴ We found with many of these OSDAs, that the addition of aluminum to fluoride-mediated systems caused **RTH** to form instead of **STW**. These results are not trivial, as in the original work to produce SSZ-50, modifying the OSDA by a single carbon atom led to a change in product.¹⁰ Additionally, the hydrothermal stability of the **RTH** materials is evaluated and the zeolites are found to be stable under severe hydrothermal conditions and maintain good catalytic activity (MTO).

2. Experimental Section

2.1 OSDA Synthesis

Two different types of reactions were used to produce the imidazolium OSDAs in this work. Specific details including reaction types and product characterizations for each OSDA can be found in

Table 1.

Reaction type 1: The parent imidazole was dissolved in methanol and then cooled in a dry ice/acetone bath. Then a three-

fold molar excess of methyl iodide was slowly added. (Caution: These reactions can be highly exothermic, use appropriate

precautions.) The mixture was then allowed to slowly warm to room

204

Table 1. Characterization of imidazolium cations.

Organic	Parent Imidazole	Supplier	Reaction Type	¹³ C NMR δ (ppm)
1	N-methylimidazole	Aldrich	1	36.32, 123.76, 136.86
2	1,2-Dimethylimidazole	Aldrich	1	8.52, 34.48, 121.64, 144.63
3	4-methylimidazole	Aldrich	2	8.52, 33.37, 35.87, 120.37, 132.33, 135.86
4	2-ethylimidazole	Aldrich	2	9.92, 16.59, 34.71, 122.07, 148.16
5	2,4-dimethylimidazole	Synquest	2	8.62, 9.38, 31.46, 34.36, 118.64, 130.14, 143.89
6	2-ethyl-4-methylimidazole	Aldrich	2	8.80, 10.17, 16.93, 31.52, 34.36, 118.83, 120.23, 130.23, 147.32
7	2-isopropylimidazole	TCI	2	17.55, 24.79, 35.68, 122.65, 149.69
8	1,2,4,5-tetramethylimidazole	TCI	1	7.99, 9.76, 31.58, 125.42, 142.21

temperature and finally refluxed overnight. After cooling, the solvent and excess methyl iodide were removed using rotary evaporation (Caution: Highly toxic vapors present, use appropriate precautions), and the product was recrystallized from acetone and washed with ether.

Reaction type 2: The parent imidazole was dissolved in chloroform and then a two-fold molar excess of potassium carbonate was added. The mixture was cooled in a dry ice/acetone bath and then a two-fold molar excess of methyl iodide was slowly added. (Caution: These reactions can be highly exothermic, use appropriate precautions.) The mixture was then allowed to slowly warm to room temperature and finally refluxed overnight. After cooling to room temperature the potassium carbonate was filtered, and the solids were rinsed with extra chloroform to recover all the product. Then the solvent and excess methyl iodide were removed using rotary evaporation (Caution: Highly toxic vapors present, use appropriate precautions), and the product was recrystallized from acetone and washed with ether.

In both types of reactions the structure was verified using ¹³C NMR in D₂O with methanol added as an internal standard. The products were then converted from iodide to hydroxide form using hydroxide exchange resin (Dowex Marathon A, hydroxide form) in water, and the product was titrated using a Mettler-Toledo DL22 autotitrator using 0.01 M HCl as the titrant.

2.2 Microporous Materials Synthesis

2.2.1 Characterization

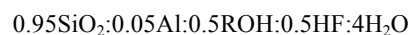
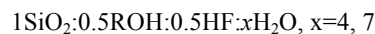
A general synthesis procedure for the microporous materials can be found below. In all situations the samples were spun at 43 rpm in a rotating oven. The ²⁷Al MAS NMR were recorded using a Bruker AM 300 MHz spectrometer with a 4 mm rotor at a spinning rate of 8 kHz, and were conducted in a 7.0 T magnetic field corresponding to a Larmor frequency of 78.172 MHz. The ²⁷Al spectra are referenced to 1.1 M Al(NO₃)₃ as an external standard. Prior to ²⁷Al NMR analysis, the samples were hydrated by placing them in a desiccator containing a saturated aqueous salt solution. All powder X-ray diffraction (PXRD) characterization was conducted on a Rigaku MiniFlex II with Cu K α radiation. Nitrogen adsorption isotherms were

performed on a Quantachrome Autosorb iQ at 77 K. Micropore volume was determined using the t-plot method. Scanning electron microscope (SEM) images were acquired on a ZEISS 1550 VP FESEM, equipped with in-lens SE. EDS spectra were acquired with an Oxford X-Max SDD X-ray Energy Dispersive Spectrometer system.

For all microporous material syntheses, aliquots of the material were taken periodically (generally every 3-4 days) by first quenching the reactor in water and then removing enough material for PXRD. Syntheses were considered to be finished when a crystalline product was observed via PXRD and the broad peak indicative of amorphous material, between 20 and 30° 2 θ , had disappeared. If incomplete crystallization or no crystalline product was observed in PXRD, the syntheses were replaced in the oven. For all syntheses that produced **RTH**, representative synthesis times are included in Table 2. As some variation in synthesis times is generally observed in zeolite synthesis, all samples were evaluated using PXRD to determine completion.

2.2.2 Fluoride-mediated reactions

Tetraethylorthosilicate (TEOS) and aluminum isopropoxide (if necessary) were added to the OSDA in its hydroxide form in a Teflon Parr Reactor. The container was closed and stirred overnight to allow for complete hydrolysis. The lid was then removed, and the ethanol and appropriate amount of water were allowed to evaporate under a stream of air. Once the appropriate mass was reached, aqueous HF was added and the mixture was stirred by hand until a homogenous gel was obtained. In the cases of H₂O/SiO₂=4 a second evaporation step was normally used. The final gel molar ratios were:



The autoclave was sealed and placed in a rotating oven at 175°C. Aliquots of the material were taken periodically by first quenching the reactor in water and then removing enough material for XRD.

2.2.3 Si/Al=15 (NH₄-Y and Sodium Silicate)

Following the method of Wagner et al.¹⁵ 2 mmol of OSDA was mixed with 0.20 g of 1 M NaOH, and water was added to give a total mass of 6 g. Then 2.5 grams of sodium silicate (PQ Corporation, 28.6wt% SiO₂ and 8.9wt% Na₂O) was added to the mixture and finally 0.25 g of NH₄-Y (Zeolyst CBV 500, Si/Al=2.55) was added. The solution was heated at 140°C in a rotating oven.

2.2.4 Si/Al=15 (CBV 720)

3 mmol of OSDA was mixed with 1 g of 1 M NaOH and water was added to bring the total mass to 7 g. Then 1 g of CBV 720 (Zeolyst, Si/Al=15) was added. The solution was heated at 160°C in a rotating oven.

2.2.5 Si/Al=30 (CBV 760)

3 mmol of OSDA was mixed with 1 g of 1 M NaOH and water was added to bring the total mass to 7 g. Then 1 g of CBV 760 (Zeolyst, Si/Al=30) was added. The solution was heated at 175°C in a rotating oven.

2.2.6 Si/Al=50 (Ludox AS-40 and sodium aluminate)

4 mmol of OSDA was mixed with 1.56 g of 1 M NaOH and the total mass was brought to 9.66 g with the addition of water. Then 0.038 g of sodium aluminate (Pfaltz & Bauer) was added and stirred until dissolved. Finally 3 g of Ludox AS-40 was added and stirred until a homogeneous gel was obtained. Seeds were added and then the gel was heated at 160°C in a rotating oven.

2.3 Calcination and Ammonium Exchange

All products were calcined in breathing grade air. The material was heated to 150°C at 1°C/min, held for three hours, then heated to 580°C at 1°C/min and held for six hours to assure complete combustion of the organic. After calcination they were exchanged to ammonium form using 1 M NH₄NO₃ (100 mL of solution per gram of catalyst) at 95°C with stirring for three hours, this was done a total of three times per sample. After ammonium exchange the materials were washed with water and dried and then calcined to proton form using the standard method.

2.4 Material Steaming

Steaming was performed at atmospheric pressure in an MTI OTF-1200X horizontal tube furnace fitted with a 3 in. ID mul-lite tube. Proton form **RTH** samples (approximately 0.5 g in a typical experiment) were loaded into ceramic calcination boats and placed in the center of the tube furnace. The furnace was then ramped at 1°C/min to the desired steaming temperature (700°C-1000°C) and held at this temperature for 8 h before cooling to room temperature. Flowing steam (present for the entire procedure) was created by bubbling zero-grade air at 50 cc/min through a heated water saturator (bubbler) upstream of the furnace. Proton form **RTH** samples were steamed at temperatures of 700°C, 800°C, 900°C and 1000°C, with the bubbler held at 80°C for each sample (corresponding to a steam partial pressure of 47.3 kPa).

2.5 MTO Reaction Testing

The calcined materials were then pelletized, crushed, and sieved. Particles between 0.6 mm and 0.18 mm were support-

ed between glass wool beds in an Auto-clave Engineers BTRS, Jr. SS-316 tubular, continuous flow reactor.

All catalysts were dried at 150°C in situ in a 30 cm³/min flow of 5% Ar/95% He for 4 h prior to the reaction. The reactions were conducted at 400°C in a 10% methanol/inert flow. Methanol was introduced via a liquid syringe pump at 5.4 μL/min, into a gas stream of the inert blend at 30 cm³/min. The reactant flow had a weight hourly space velocity of 1.3 h⁻¹. In a typical run, 200 mg of dry catalyst was loaded. Effluent gases were evaluated using an on-stream GC/MS (Agilent GC 6890/MSD5793N) with a Plot-Q capillary column installed. Conversions and selectivities were computed on a carbon mole basis.

2.6 Molecular Modelling

The location and the van der Waals (vdW) interaction energy of the OSDA within the **RTH** framework were studied by molecular mechanics simulations using the Materials Studio 6 software.¹⁶ The CVFF forcefield¹⁷ was selected for the calculation, and the most stable locations for the OSDA molecules were obtained by simulated annealing. The zeolite framework was assumed to be pure silicate, because the distribution of the Al atoms in the framework is not clear. We limited the modeling strictly to vdW interaction energies between the OSDAs and the framework, and did not include inorganic cations and water molecules to the calculation. The unit cell and the framework atoms were fixed during the calculation, and in this case, there is no need to generate a supercell. The geometry of the OSDA molecule was first optimized using the CVFF forcefield, and then allowed to change after it was docked to the zeolite framework. Initially, two OSDA molecules were docked per unit cell (as there are two cages per unit cell), and then the number was increased. The results indicated that the most stable situation was when there were four imidazolium OSDA molecules per unit cell, or in the case of the OSDA in Figure 1, two OSDAs per unit cell.

3. Results and Discussions

3.1 Synthesis of aluminosilicate **RTH**

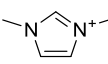
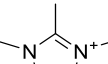
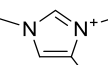
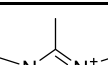
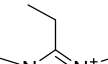
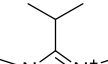
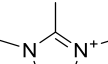
Results of the imidazolium screening reactions are given in Table 2. It was found that nearly all of the imidazolium cations screened in this study led to the formation of **RTH**-type materials. The simplest imidazolium OSDA, **1**, did not produce **RTH** and was found to decompose under many of the conditions tested in this study. However, **1** led to framework materials in fluoride-mediated reactions, and these results are consistent with previous reports.^{18,19} Additionally, OSDA **7** was also unstable under many of the conditions tested in these screening reactions, and was not found to lead to **RTH** under any conditions tested.

Other than OSDAs **1** and **7**, all of the other OSDAs tested were able to produce aluminosilicate **RTH** under a majority of the inorganic conditions employed in this study. The formation of aluminosilicate **RTH** using pentamethylimidazolium was first observed in fluoride-mediated, aluminosilicate conditions, and OSDAs **2-6, 8** were all able to produce **RTH** under this condition, without the use of seeds. Under more conventional, hydroxide-mediated conditions, they also formed **RTH** across a wide range of compositions. In some cases, such as with OSDAs **2-4**, the use of seeds was found to be necessary to cause the formation of **RTH**. It is likely that

these organics were less directing to **RTH**, but are still able to form the material when nucleation to **RTH** is induced through seeding (discussed further in section 3.2). The OSDAs found to be the most strongly directing to **RTH** are **2**, **5** and **8**. (We have previously reported OSDA **8** to produce aluminosilicate **RTH**.)⁹ The ability to obtain **RTH** using a variety of imidazo-

lium cations may open possibilities for OSDA availability. Industrially, imidazoles are produced using the Radziszewski reaction or by dehydrogenation of imidazolines, and are available in high purity; quaternary imidazoliums can then be prepared by standard alkylation methods.²⁰

Table 2. Results from synthesis experiments and molecular modelling calculations. All syntheses that produced RTH-type materials are shaded.

Organic	Number	ure-silica fluoride H ₂ O/SiO ₂ =4	ure-silica fluoride H ₂ O/SiO ₂ =7	Si/Al=20 fluoride	Si/Al=15 Seeds	Si/Al=15 no seeds	CBV 720, seeds	CBV 720, no seeds	CBV 760, seeds	CBV 760, no seeds	Si/Al=50, seeds	interaction energy (4 OSDAs/cell)
	1	TON 4 days		FER 11 days	X		X	X	TON 12 days	TON 12 days		-15.94
	2	ITW 5 days	ITW 5 days	RTH Si/Al=9 12 days (S1)	RTH 3 days	RTH Si/Al=9 6 days (S2)		RTH Si/Al=14 5 days (S3)	RTH Si/Al=18 28 days (S4)	X	RTH + dense 30 days	-18.29
	3	ITW 5 days	ITW 12 days	RTH Si/Al=10 7 days (S5)	RTH Si/Al=9 3 days (S6)	MOR 20 days	X	X	TON 12 days	X	TON 31 days	-17.40
	4	CIT-7, ITW, STW, STF, MTW >4 days	ITW 29 days	RTH Si/Al=12 20 days (S7)	RTH Si/Al=8 7 days (S8)	RTH Si/Al=9 8 days (S9)	RTH Si/Al=14 14 days (S10)	X	X	X	MTW 11 days	-17.90
	5	STW 4 days	STW 4 days	RTH Si/Al=10 5 days (S11)	RTH 10 days	RTH + MOR 12 days	RTH Si/Al=13 5 days (S12)	RTH 5 days	RTH Si/Al=27 12 days (S13)	RTH 12 days		-18.62
	6	STW 16 days	HPM-2 20 days	RTH Si/Al=13 20 days (S14)	RTH Si/Al=9 15 days (S15)	MOR + RTH 16 days	X	X	X	X	MTW 13 days	-15.00
	7	STF 9 days	Unknown 21 days	Unknown 45 days	MOR 16 days	MOR 16 days	X	X	X			-16.45
	8	STW 5 days	STW 7 days	RTH Si/Al=18 10 days (S16)	RTH Si/Al= 9 4 days (S17)	RTH Si/Al=14 10 days	RTH Si/Al=17 10 days	RTH Si/Al=15 20 days (S18)	RTH Si/Al=29 13 days	RTH Si/Al=22 20 days (S19)	RTH Si/Al=45 9 days	-20.02

X=Organic Decomposed

Interaction Energy (kJ/mol per T-atom) = vdW energy values shown in the Table were averaged from 3 repeated runs.

Synthesis times are reported in days.

Material Si/Al ratios were determined using EDS.

Samples with numbers in parentheses refer to SEM images that can be found in the Supporting Information.

The morphology and composition of the samples that that produced **RTH** were studied using SEM and EDS. The SEM images can be found in the Supplementary Information for samples in Table 2. In general fluoride-mediated reactions led to larger crystals than the hydroxide-mediated syntheses. However, there was a large amount of variability found between OSDAs using the same inorganic conditions.

3.2 Molecular Modelling

To gain deeper insight into the ability of the imidazolium cations used in this study to structure direct **RTH**-type materials, molecular modelling calculations were performed and the results are shown in Table 2. In these calculations, 4 OSDAs were populated per unit cell based on energy optimizations for the framework space filling. The results of the predicted interaction energies agree well with the observed experimental results. The OSDAs with the most favorable interaction energies, **5** and **8**, were found to produce **RTH** under many inorganic conditions, with and without seeds. However, OSDAs with less favorable interaction energies compared to **8** did not lead to the formation of **RTH** as readily and generally required seeds to favor the formation of **RTH**. These results were then compared to the stabilization energy for the original **RTH** OSDA (Figure 1), that was found to be -11.10 kJ/mol (for 2 OSDAs per unit cell, the optimal packing). It was surprising that this interaction energy is much less favorable than any of the imidazoliums in this study. One possible explanation for the large energy difference is that the imidazoliums all required two OSDAs per cage while the OSDA in Figure 1 only has a single molecule per cage, requiring less ordering between OSDAs. The positions of the OSDAs within the cages are shown in Figure 2, as determined by molecular modelling.

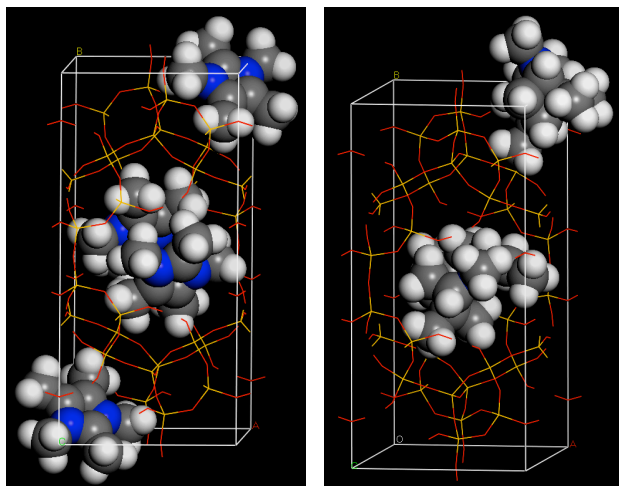


Figure 2. Positions of OSDAs within the **RTH** framework for pentamethylimidazolium (left) and the original SSZ-50 OSDA (right).

3.3 Hydrothermal Stability

The hydrothermal stability of **RTH**-type zeolites prepared from CBV 720 was assessed by steaming the proton form of the material to various temperatures, and then characterizing the solids thus obtained by PXRD, ^{27}Al MAS NMR, nitrogen adsorption isotherms and the MTO reaction to test for catalytic activity. The material was steamed to temperatures ranging from 700 to 1000°C, and details of the steaming procedure can

be found in the experimental section. The PXRDs of the steamed materials (Figure 3) show that the framework structure is intact until at least 900°C, but that the structure essentially collapses by 1000°C. The ^{27}Al MAS NMRs of the proton form and steamed materials are shown in Figure 6, and the distribution of aluminum coordination environments for the various samples is given in Table 3. As the results from the ^{27}Al quantification show, higher temperature steam treatment decreases the amount of tetrahedral (framework) aluminum in the samples, consistent with framework damage. Nitrogen adsorption isotherms of the proton form sample as well as the material after steaming to 900°C (the highest steaming temperature with the structure intact) are shown in Figure 4. The proton form of the material has a micropore volume of 0.24 cc/g while the steamed material has a micropore volume of 0.19 cc/g. The reduced micropore volume of the steamed material indicates that some framework destruction has occurred.

Table 3. Distribution of aluminum coordination in steamed samples from ^{27}Al MAS NMR

	Tetrahedral	Pentacoordinated	Octahedral
Proton Form	100%	--	--
Steamed 700°C	55%	8%	38%
Steamed 800°C	15%	15%	70%
Steamed 900°C	14%	21%	64%

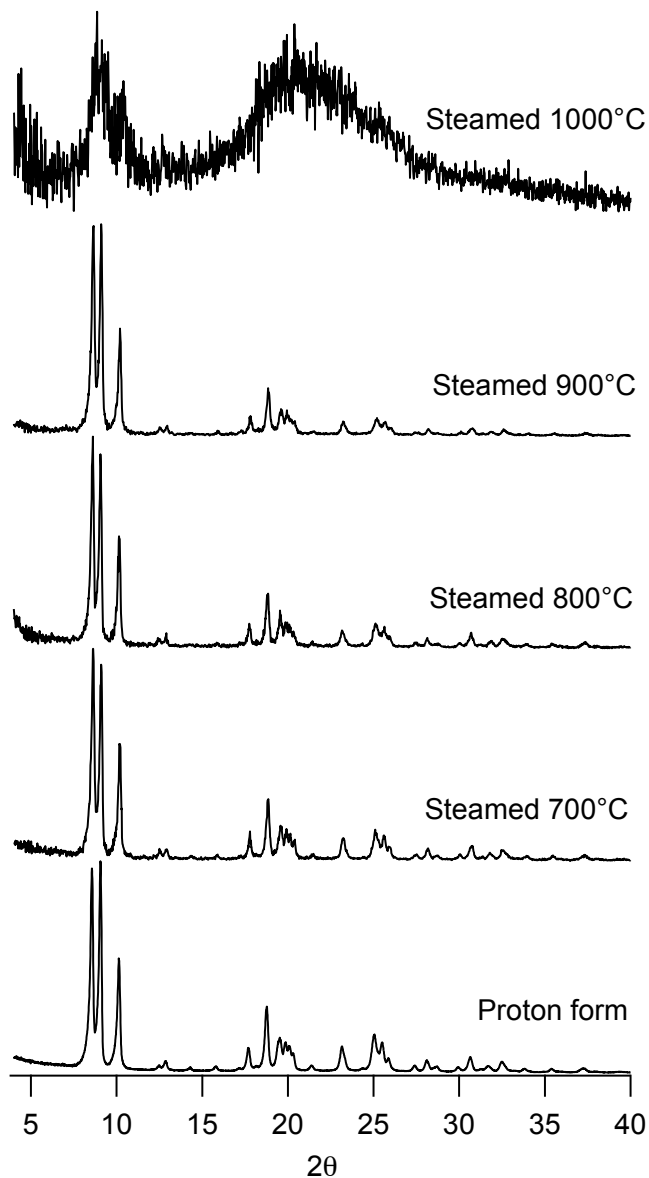


Figure 3. XRDs of steamed and proton form RTH

208

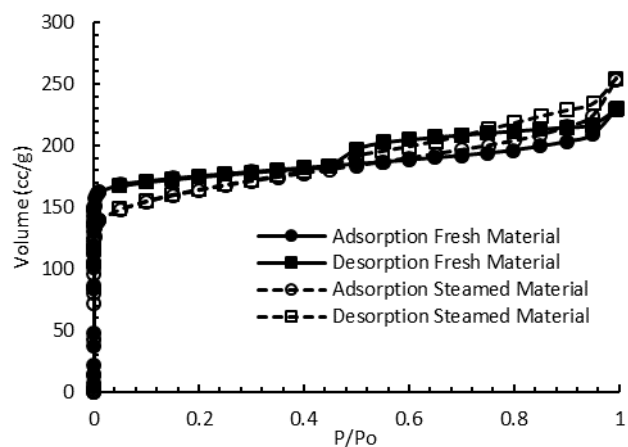


Figure 4. Nitrogen isotherms of fresh and steamed RTH

The steamed materials were also studied as catalysts using the MTO reaction, and the results are shown in Figure 5. The fresh RTH sample has a significantly longer lifetime than the steamed samples. However, the purpose of this test was to assess the effects of hydrothermal treatment on MTO reactivity, and the MTO results show that these materials are catalytically active after severe steam treatments. The sample steamed to 1000°C was also tested for MTO reactivity, and showed no catalytic activity, consistent with the severe degradation evident from XRD. The steaming studies demonstrate that the RTH-type materials are highly resistant to degradation, even under severe hydrothermal conditions.

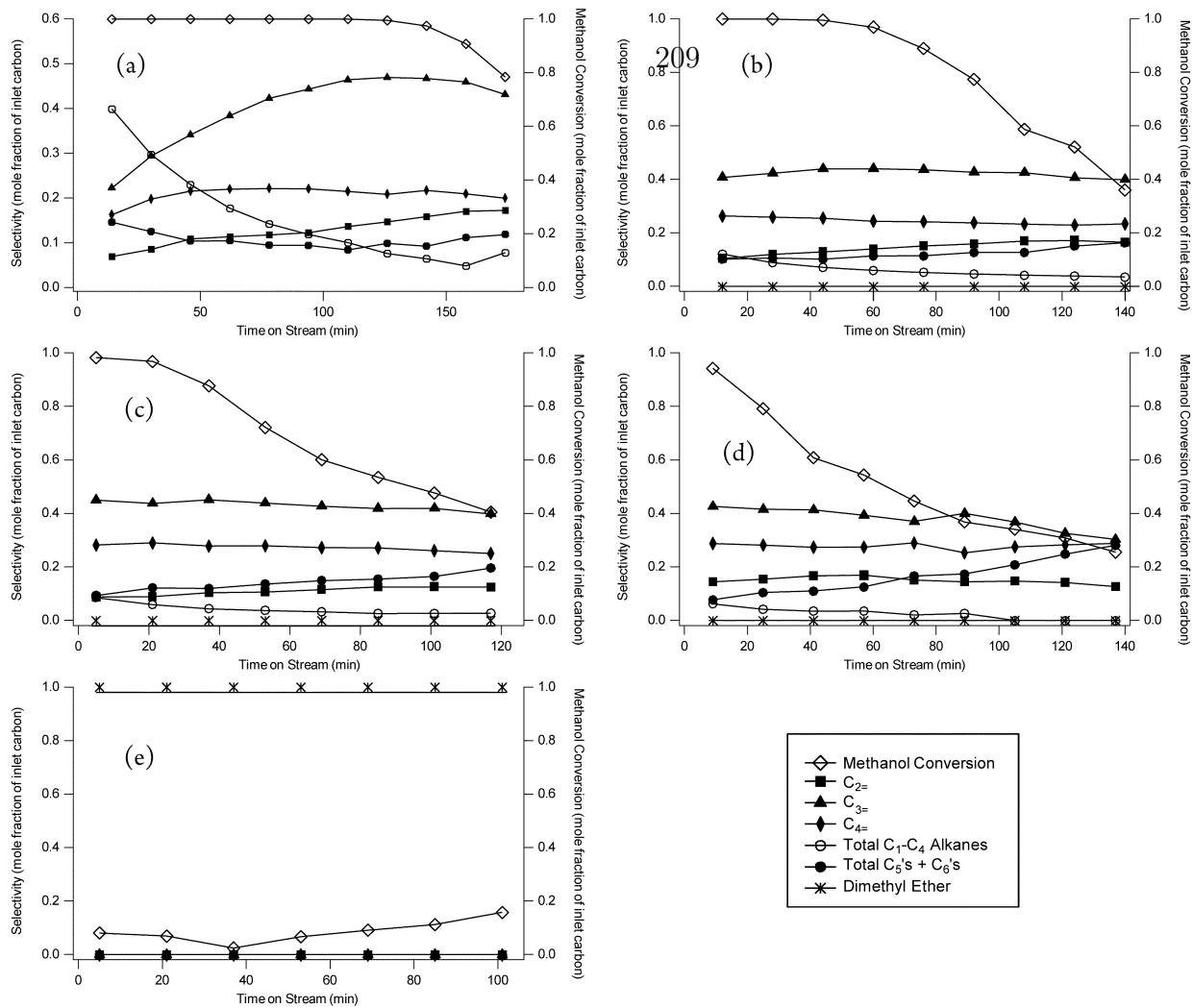


Figure 5. MTO reaction data for (a) fresh **RTH** catalyst, (b) steamed to 700°C, (c) steamed to 800°C, (d) steamed to 900°C and (e) steamed to 1000°C

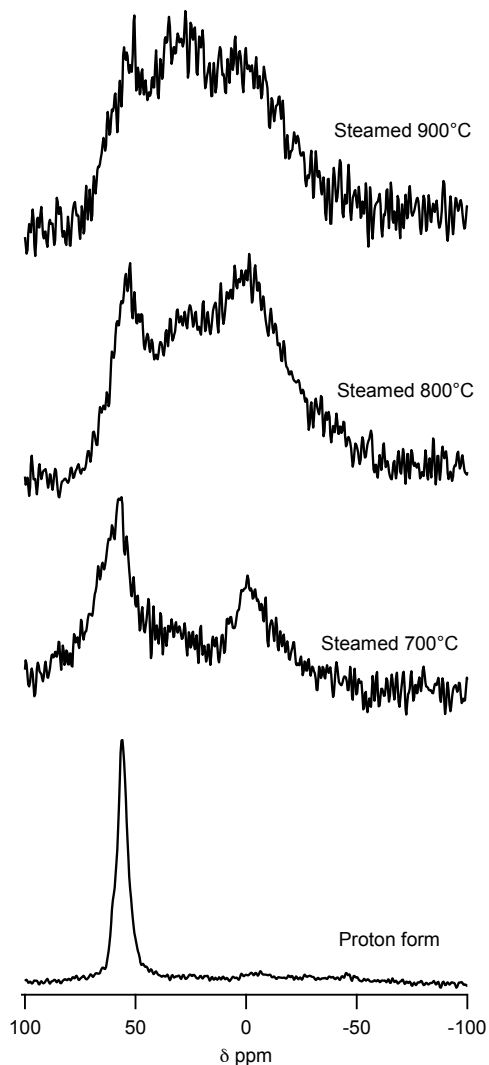


Figure 6. ^{27}Al MAS NMRs of proton form and steamed **RTH**

4. Conclusions

RTH-type zeolites can be produced by a wide-range of imidazolium cations, diversifying the methods for its synthesis. The structure directing ability of the OSDAs used here agrees well with the results predicted by molecular modelling for the stabilization energies of the organics in the **RTH** framework. Additionally, the **RTH** framework is found to be stable to steaming to 900°C, demonstrating potential for utility under demanding process conditions.

ASSOCIATED CONTENT

Supporting Information

SEM images of selected samples from Table 2 can be found in the Supporting Information. This material is available free of charge via the Internet at <http://pubs.acs.org>.

AUTHOR INFORMATION

Corresponding Author

* Email: mdavis@cheme.caltech.edu

Author Contributions

The manuscript was written through contributions of all authors.

Funding Sources

The authors would like to thank Chevron Energy and Technology Company for providing funding for this work. J.E.S. would like to thank the NDSEG for their support through a fellowship.

ACKNOWLEDGMENT

The authors would like to thank Stacey Zones for insightful discussions regarding the synthesis of **RTH**.

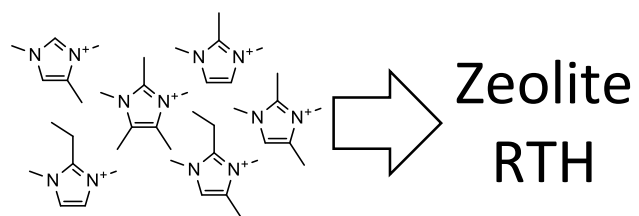
ABBREVIATIONS

OSDA, organic structure directing agent; PXRD, powder x-ray diffraction; SEM, scanning electron microscope; vdW, van der Waals interaction energy

REFERENCES

- Bravo-suárez, J. J.; Chaudhari, R. V.; Subramaniam, B. In *Novel Materials for Catalysis and Fuels Processing*; Bravo-Suárez, J. J.; Kidder, M. K.; Schwartz, V., Eds.; ACS Symposium Series; American Chemical Society: Washington, DC, 2013; Vol. 1132, pp. 3–68.
- Yilmaz, B.; Müller, U. *Top. Catal.* **2009**, *52*, 888.
- Zones, S. I. *Microporous Mesoporous Mater.* **2011**, *144*, 1.
- Pophale, R.; Daeyaert, F.; Deem, M. W. *J. Mater. Chem. A* **2013**, *1*, 6750.
- Zones, S. I.; Hwang, S.-J. *Chem. Mater.* **2002**, *14*, 313.
- Zones, S. I.; Lee, H.; Davis, M. E.; Casci, J.; Burton, A. W. *Stud. Surf. Sci. Catal.* **2005**, *158*, 1.
- Iyoki, K.; Itabashi, K.; Okubo, T. *Microporous Mesoporous Mater.* **2013**, *8*, 1419.
- Three-letter framework type codes (boldface capital letters) for all zeolites mentioned in the text are given in parentheses.
- Schmidt, J. E.; Deimund, M. A.; Davis, M. E. *Chem. Mater.* **2014**, *26*, 7099.
- Lee, G. S.; Zones, S. I. *J. Solid State Chem.* **2002**, *167*, 289.
- Kim, C.; Hwang, S.-J.; Burton, A. W.; Zones, S. I. *Microporous Mesoporous Mater.* **2008**, *116*, 227.
- Yokoi, T.; Yoshioka, M.; Imai, H.; Tatsumi, T. *Angew. Chem. Int. Ed. Engl.* **2009**, *48*, 9884.
- Yoshioka, M.; Yokoi, T.; Liu, M.; Imai, H.; Inagaki, S.; Tatsumi, T. *Microporous Mesoporous Mater.* **2012**, *153*, 70.
- Schmidt, J. E.; Deem, M. W.; Davis, M. E. *Angew. Chem. Int. Ed. Engl.* **2014**, *53*, 8372.
- Wagner, P.; Nakagawa, Y.; Lee, G. S.; Davis, M. E.; Elomari, S.; Medrud, R. C.; Zones, S. I. *J. Am. Chem. Soc.* **2000**, *122*, 263.
- Materials Studio 6.0, Accelrys, Inc.: San Diego, CA, 2012.
- Dauber-Osguthorpe, P.; Roberts, V. A.; Osguthorpe, D. J.; Wolff, J.; Genest, M.; Hagler, A. T. *Proteins* **1988**, *4*, 31.
- Rojas, A.; Martínez-Morales, E.; Zicovich-Wilson, C. M.; Cambor, M. A. *J. Am. Chem. Soc.* **2012**, *134*, 2255.
- Archer, R. H.; Zones, S. I.; Davis, M. E. *Microporous Mesoporous Mater.* **2010**, *130*, 255.
- Ebel, K.; Koehler, H.; Gamer, A.; Jackh, R. In *Ullmann's Encyclopedia of Industrial Chemistry*; Wiley-VCH Verlag GmbH & Co. KGaA: Weinheim, Germany, 2000; pp. 637–645.

Insert Table of Contents artwork here



Synthesis of RTH-type Zeolites Using a Diverse Library of Imidazolium Cations

Joel E. Schmidt¹, Mark A. Deimund¹, Dan Xie² and Mark E. Davis^{1*}

¹Chemical Engineering, California Institute of Technology, Pasadena, CA 91125

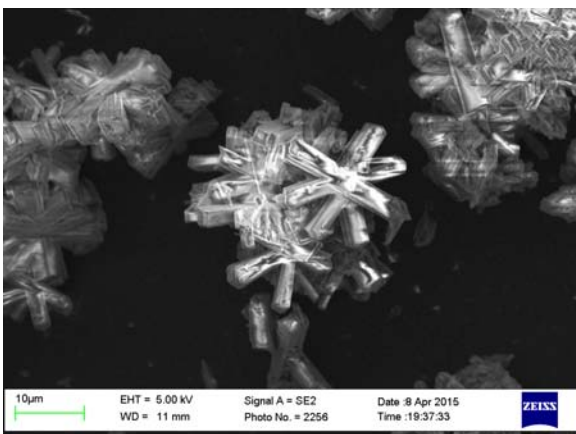
²Chevron Energy Technology Company, Richmond, CA 94802, USA

Supporting Information

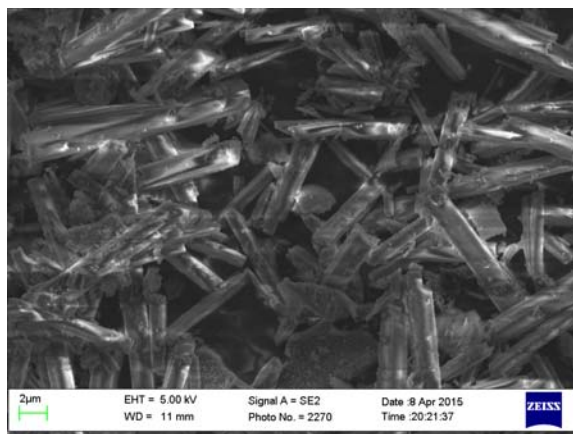
Representative SEM images of selected samples. References to specific SDAs and synthesis conditions can be found in Table 2.

Si/Al=20, fluoride media

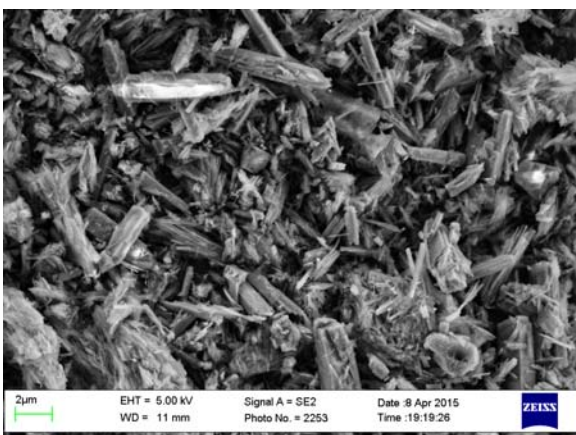
S1



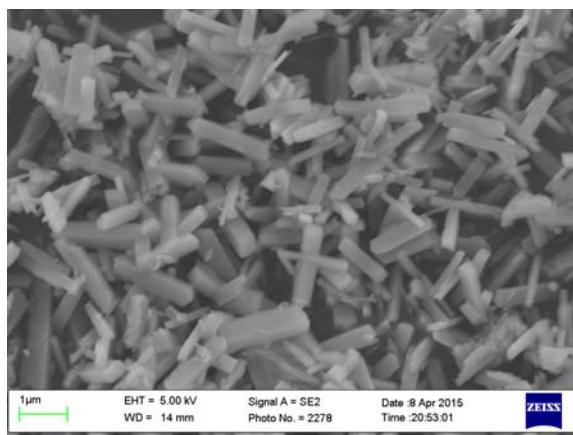
S5



S7

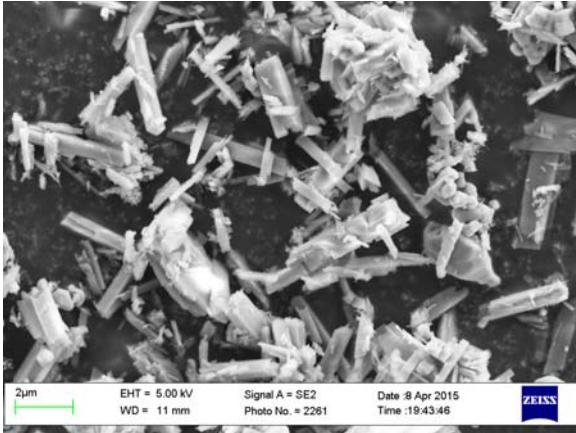


S11

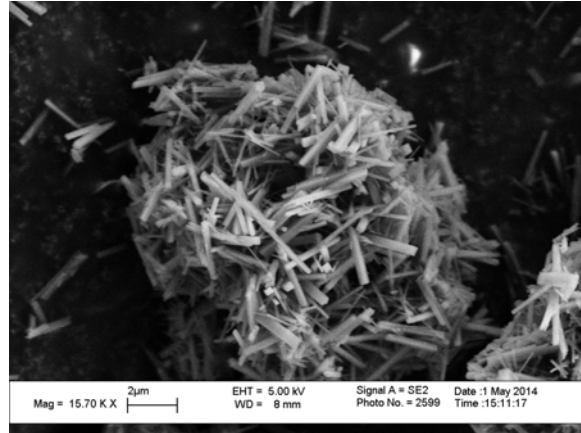


213

S14

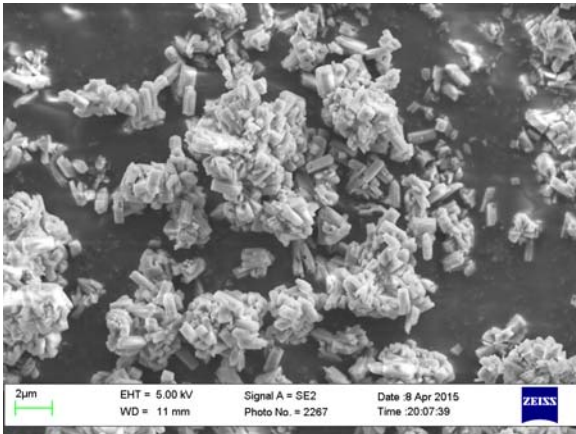


S16

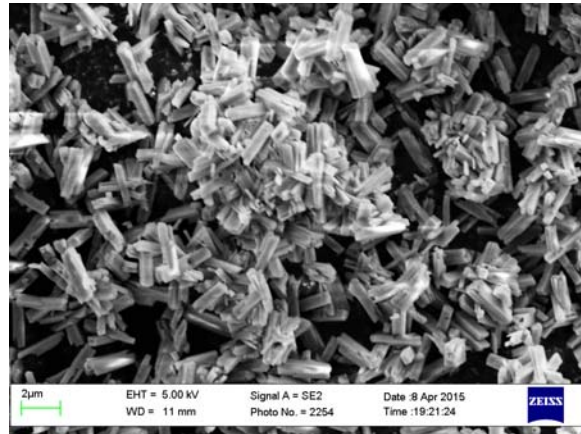


Si/Al=15, seeds

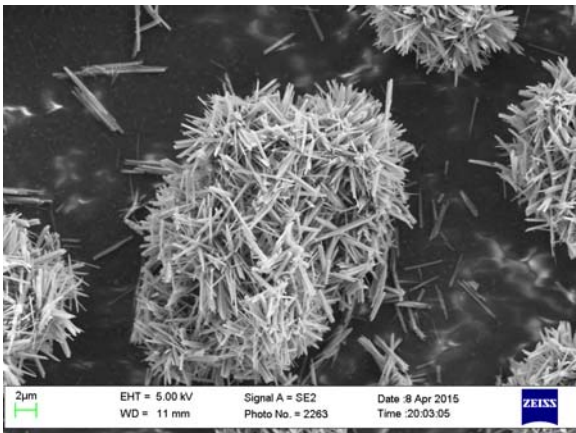
S6



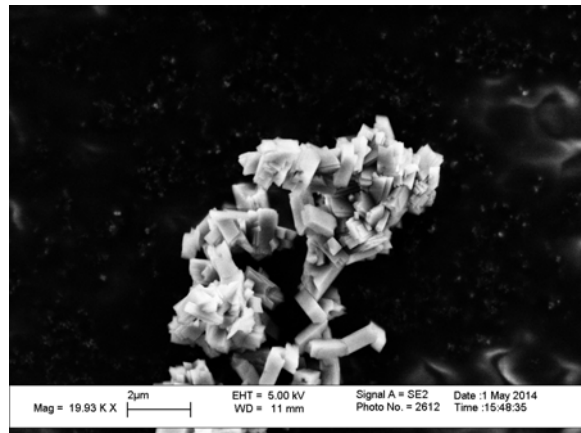
S8



S15

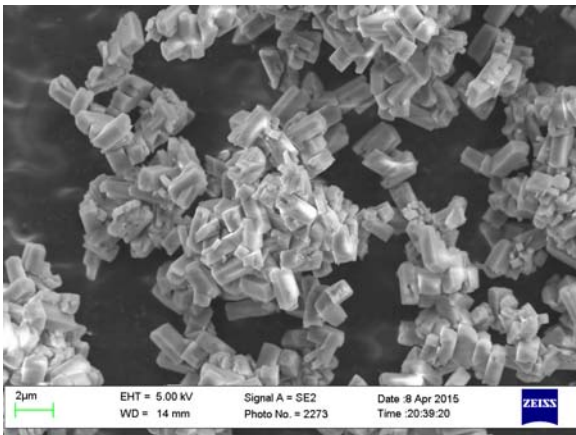


S17

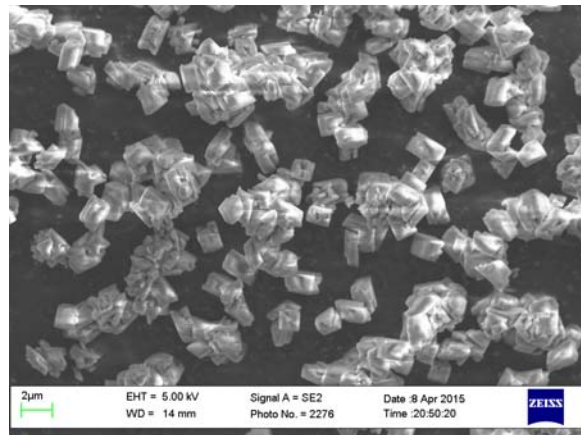


Si/Al=15, no seeds

S2

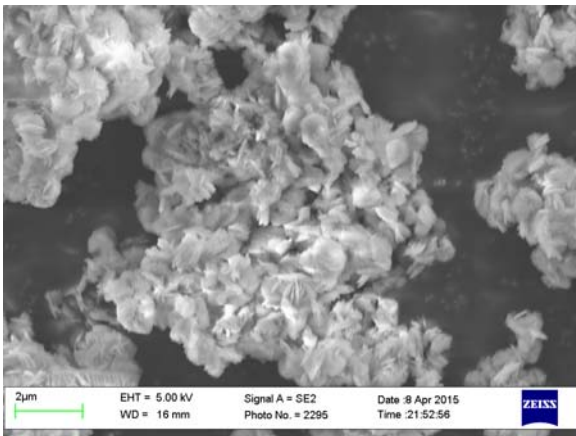


S9

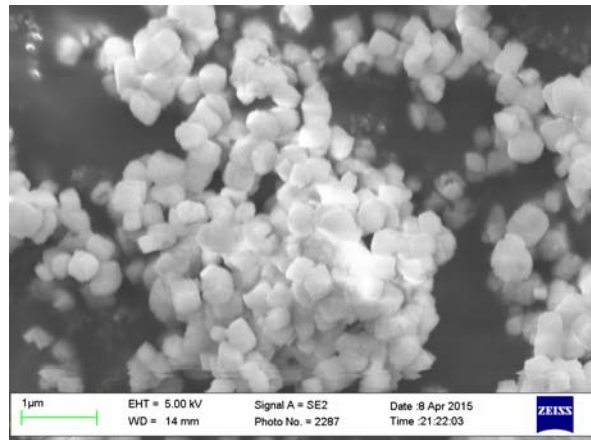


CBV720, seeds

S10

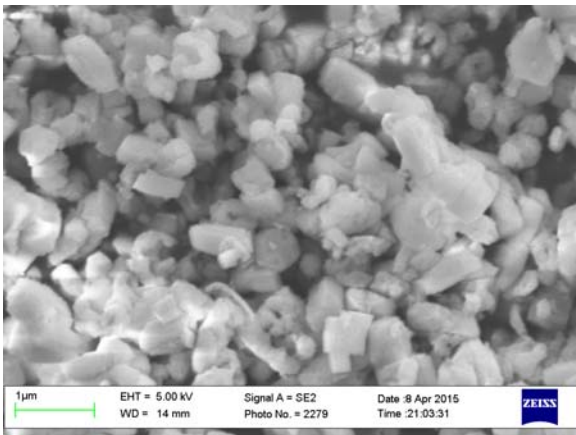


S12

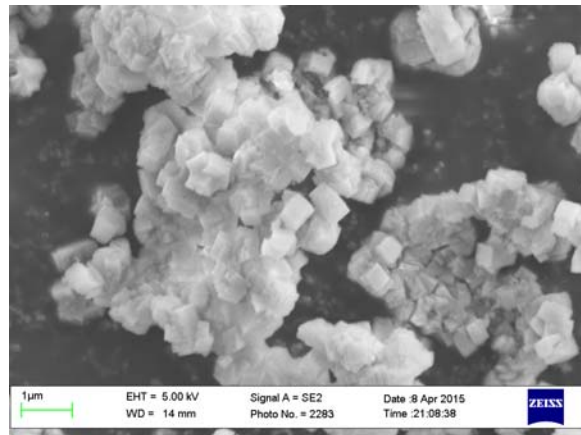


CBV720, no seeds

S3

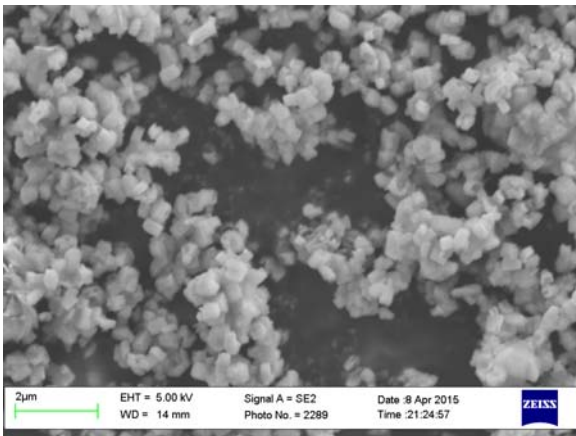


S18

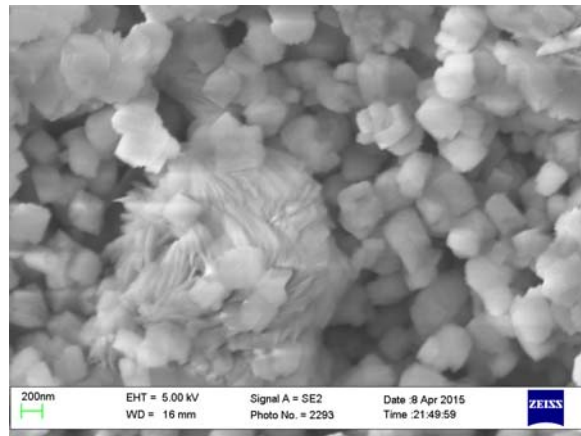


CBV760, seeds

S4

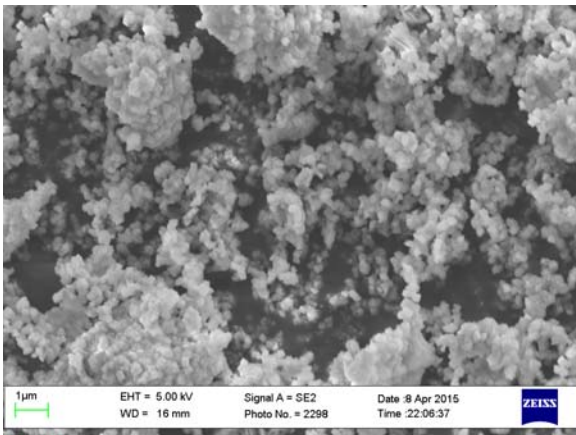


S13



CBV760, no seeds

S19



Effect of Pore and Cage Size on the Formation of Aromatic Intermediates During the Methanol-to-Olefins Reaction

Mark A. Deimund, Joel E. Schmidt and Mark E. Davis*

Chemical Engineering, California Institute of Technology, Pasadena, CA 91125, United States

KEYWORDS: Methanol-to-olefins, zeolites, silicoaluminophosphates, hydrocarbon pool, CHA

ABSTRACT: Six eight-membered-ring (8MR), microporous materials are synthesized and evaluated as catalysts for the methanol-to-olefins (MTO) reaction. The molecular sieves SSZ-13, SAPO-34, SAPO-39, MCM-35, ERS-7 and RUB-37 are investigated since they have 8MR access to the crystal interior but have differences in pore structure and cage size. The polymethylbenzene species that are the proposed reaction intermediates of the MTO reaction should only be able to form in materials with intra-molecular sieve void spaces of sufficient size to accommodate them. Thus, it is hypothesized that 8MR materials without adequately large pores or cages will be inactive for the MTO reaction. SSZ-13 and SAPO-34 (both with CHA framework topology) have interconnected 3-dimensional pore-and-cage systems sufficiently large for formation of the proposed reaction intermediates, while the other 8MR materials have intra-molecular sieve void spaces that are too small to allow formation of these species. The molecular sieves are tested as MTO catalysts at 400°C, and only the molecular sieves with the CHA topology show MTO activity. Post-reaction analysis of the organic content of each solid material is accomplished by HF acid digestion with subsequent ¹H NMR analysis of the extracted hydrocarbon products to confirm the presence of aromatics in the 8MR materials with sufficiently large cages (those with CHA topology), and absence with materials that have smaller void spaces. These data provide further support for the necessity of polymethylbenzene species in the hydrocarbon pool for MTO activity.

1. INTRODUCTION

Solid acid catalysts such as aluminosilicates (zeolites)¹ and silicoaluminophosphates (SAPOs),^{2,3} particularly those with eight-membered ring pores (8MRs) and a cage structure, are capable of converting methanol to light olefins, such as ethylene and propylene. The methanol-to-olefins (MTO) reaction is an industrially viable route for making light olefins from nonpetroleum feedstocks, e.g., natural gas, coal and biomass,⁴ and is of economic value in times of high petroleum feedstock prices.⁵

In the proposed mechanism for the MTO reaction, substituted aromatic molecules⁶ create a “hydrocarbon pool”⁷ that is instrumental in forming light olefins from methanol via side chain reactions.⁸ These reactive aromatic intermediates (polymethylbenzenes) have kinetic diameters ranging from 6.2 Å for *o*-xylene to 7.5 Å for hexamethylbenzene; hence, it is believed that pores or cages of sufficient size and shape to allow formation of these intermediates are critical to the hydrocarbon pool mechanism.⁹ Microporous materials with ten-membered-ring (10MR) or twelve-membered-ring (12MR) pores (such as MFI or *BEA, respectively) may additionally involve the olefin methylation/cracking cycle to form hydrocarbon products from methanol.⁵ The pores of these 10MR and 12MR systems typically cannot retain the aromatic intermediates of the hydrocarbon pool mechanism, and thus they form significant heavier and/or aromatic products in addition to light olefins.

Small-pore materials (8MRs) with cages, conversely, are more effective in retaining these reactive polymethylbenzene

intermediates, and as such, show increased selectivity to light olefins and other nonaromatic products.¹⁰ For example, the chabazite (CHA) topology consists of relatively large cavities (8.35 Å x 8.35 Å x 8.23 Å) that are accessible through 8MR pore openings (3.8 x 3.8 Å).¹¹ Small linear molecules (alcohols and linear alkenes) may diffuse through these 8MR pores; however, the larger branched and aromatic compounds, including the methylated benzene intermediates,^{12,13} can only form in these cages where they remain trapped. While remaining in the cages, these aromatics react with methanol to form light olefins as part of the reaction cycle.

SAPO-34 is one such 8MR SAPO molecular sieve with CHA framework topology that is preferred for the MTO reaction.^{14,15} Commercial MTO plants in China currently employ this catalyst, that can exhibit combined ethylene and propylene selectivities as high as 85-90%, depending on reaction conditions.¹⁶ A similar MTO catalyst, SSZ-13,¹⁷ is the synthetic aluminosilicate analog of SAPO-34. While SSZ-13 also has the CHA topology, it deactivates more rapidly than SAPO-34, in addition to initially producing a significant amount of C₂-C₄ alkanes.^{18,19} Aside from these CHA materials, several other 8MR framework topologies such as LEV, AFX and RTH have been shown to exhibit MTO activity.^{20,21}

Here, we focus on how the molecular sieve pore structure and cage dimensions impact the ability of an 8MR material to form and retain the necessary polymethylbenzene intermediates for the hydrocarbon pool mechanism of the MTO reaction, and thus, to selectively produce light olefins. To study the effects of pore systems and cage sizes, six microporous, 8MR materials were synthesized and tested as

catalysts for the MTO reaction. In addition to the previously mentioned MTO catalysts (SAPO-34 and SSZ-13), three 8MR zeolites with 1-dimensional pore structures (SAPO-39, MCM-35 and ERS-7), as well as one 8MR with a 2-dimensional pore system (RUB-37), were synthesized to observe the impact of pore structure and cage size on MTO activity. Each of these

four materials has a cage size smaller than the minimum kinetic diameter of the smallest polymethylbenzenes, and thus should exhibit no MTO activity due to the hydrocarbon pool mechanism. Table 1 summarizes the pore structures and other pertinent dimensions for each material.

Table 1. Material Pore Structure and Dimensions

Framework	Material	Channel System	8MR Opening (Å)	D_M (Å) ^a	D_a (Å) ^b	D_b (Å) ^b	D_c (Å) ^b
CHA	SSZ-13	3D	3.8 x 3.8	7.37	3.72	3.72	3.72
CHA	SAPO-34	3D	3.8 x 3.8	7.37	3.72	3.72	3.72
ATN	SAPO-39	1D	4.0 x 4.0	5.91	1.94	1.94	4.11
MTF	MCM-35	1D	3.6 x 3.9	6.25	1.58	1.49	4.03
ESV	ERS-7	1D	3.5 x 4.7	6.22	1.78	3.66	1.78
CDO	RUB-37	2D	3.1 x 4.7 2.5 x 4.2	5.78	3.44	1.52	3.35

^a D_M is the maximum included sphere diameter within cages of the material.

^b D_a , D_b and D_c are the maximum free sphere diameters that can diffuse along the a-, b- and c-axis, respectively.

All data obtained from the IZA website.²²

Once synthesized, these materials were calcined, ammonium exchanged (if necessary) and activated via calcination in air to place them in their acidic forms. NH_3 temperature-programmed desorption (TPD) was used to quantify the Brønsted acid sites present in each material. Materials were then reaction tested for MTO activity. Upon completion of each reaction test, the spent material was digested with HF, and any hydrocarbons remaining on the samples were extracted with chloroform. NMR spectroscopy was then used to evaluate the occluded organics from each material for the presence or absence of aromatic compounds, associated with the hydrocarbon pool mechanism. Correlation between the presence of aromatics on each spent catalyst and significant MTO activity was sought. Thermogravimetric analysis (TGA) was additionally used to measure the amount of organic deposited on each material upon completion of the reaction test.

2. MATERIALS AND METHODS

2.1. Synthesis of Microporous Materials

2.1.1 SSZ-13 (CHA)

SSZ-13 was synthesized using a standard method.²³ In a typical preparation, 3.33 g of 1 M NaOH was mixed with 2.81 g of N,N,N -trimethyl-1-adamantammonium hydroxide (Sachem, 1.18 mmol OH/g) and 6.62 g of water. Then 0.077 g of Reheiss F-2000 (55wt% Al_2O_3) was added and stirred until the solution cleared. Finally, 1.00 g of Cabosil M-5 was added and stirred until a homogeneous solution was obtained. The solution was heated at 160°C in a Teflon-lined Parr reactor in a rotating oven for approximately 6 days.

2.1.2 SAPO-34 (CHA)

SAPO-34 was prepared from the following gel composition: 0.5(TEA)₂O:1.5Pr₂NH:0.6SiO₂:1Al₂O₃:1P₂O₅:70H₂O. In a typical preparation, 11.5 g of 85wt% phosphoric acid were dissolved in 4.35 g of water and stirred for 5 minutes. Then 6.875 g of Catapal B alumina were added to 20 g of water and stirred for 10 minutes. The mixtures were then slowly

combined and stirred for 1 h at room temperature. Next, 4.48 g of Ludox HS-40 was added and stirred by hand until a homogenous gel was obtained. Then 20.8 g of 35wt% TEOH and 7.61 g of dipropylamine were added, and the gel was homogenized by manual stirring. The gel was stirred at room temperature for 2 h before being added to a Teflon-lined Parr reactor and heated at 200°C without stirring for 24 hours.

2.1.3 SAPO-39 (ATN)

The SAPO-39 material was supplied by S.I. Zones (Chevron Energy and Technology Company) as prepared in U.S. Patent 6,281,404.²⁴

2.1.4 MCM-35 (MTF)

MCM-35 was prepared according to the method reported in Example 1 of US Patent 4,981,663.²⁵ In a typical synthesis 0.6 g of $Al_2(SO_4)_3 \cdot 18H_2O$ was dissolved in a solution of 1.14 g of 45wt% KOH and 24.7 g of water. Then 4.25 g of Cabosil M-5 was added to the solution and thoroughly mixed. Finally 2.1 g of hexamethyleneimine was added, and the gel was put in a Teflon-lined Parr reactor and heated at 175°C in a rotating oven for 12 days.

2.1.5 ERS-7 (ESV)

ERS-7 was prepared using a modified version of the reported method.²⁶ N,N -dimethylpiperidinium hydroxide was prepared by reacting N -methylpiperidine with an excess of iodomethane (Caution: use appropriate precautions when using iodomethane. An exotherm is possible on addition of iodomethane to a solution of N -methylpiperidine, so cooling may be needed) at reflux in methanol. After cooling to room temperature, the solvent was then removed using rotary evaporation, and the product was washed with ether. The product was converted to the hydroxide form using hydroxide exchange resin (Dowex Marathon A, hydroxide form) in water, and the product was titrated using a Mettler-Toledo DL22 autotitrator with 0.01 M HCl as the titrant. ERS-7 was prepared from a gel composition of 1SiO₂:0.04Al₂O₃:0.3Na₂O:0.2ROH:40H₂O. In a typical

preparation, 6.46 grams of dimethylpiperidinium hydroxide (1.01 mmol OH/g) was added to 13.6 g of water. Then 0.87 g of $\text{Al}_2(\text{SO}_4)_3 \cdot 18\text{H}_2\text{O}$ was dissolved in the solution. Finally 7.00 g of sodium silicate (PQ Corporation, 28.6wt% SiO_2 and 8.9wt% Na_2O) was added and stirred until a homogeneous gel was obtained. The gel was put in a Teflon-lined Parr reactor and heated at 175°C in a rotating oven for 5 days.

2.1.6 RUB-37 (CDO)

Aluminosilicate RUB-37 was prepared using a previously reported method.²⁷ Seeds of pure silica RUB-36 were prepared by mixing diethyldimethylammonium hydroxide (20wt% solution in water, provided by Sachem Inc.) with Cabosil M-5. The mixture was stirred until the gel became homogenous, and then some water was evaporated under a stream of air with stirring at room temperature until a final gel molar ratio of $1\text{SiO}_2:0.5\text{ROH}:10\text{H}_2\text{O}$ was obtained. The mixture was then added to a Teflon-lined Parr reactor and heated at 150°C without stirring for 17 days. Aluminosilicate RUB-36 was prepared using the same method used for pure silica RUB-36, but Reheiss F-2000 was used as a source of aluminum. The gel composition used was $1\text{SiO}_2:0.01\text{Al}_2\text{O}_3:0.5\text{ROH}:10\text{H}_2\text{O}$. Seeds of pure-silica RUB-36 were added and stirred into the gel prior to the addition to a Teflon-lined Parr reactor. The mixture was heated in the reactor at 150°C without stirring for 10 days. Subsequent calcination of the as-made aluminosilicate RUB-36 material formed the desired RUB-37.

2.1.7 Product Recovery

Aliquots of the materials were taken periodically by first quenching the Parr reactors in water and then removing enough material for powder X-ray diffraction (PXRD). All materials were recovered by centrifugation. Once the syntheses were complete, the materials were subjected to at least three cycles of water washing and recovery by centrifugation, as well as a final wash using acetone. Each material was then dried in air at 100°C.

2.2. Ammonium Exchange and Calcination

All materials were calcined in flowing breathing-grade air. Materials were initially heated to 150°C at a heating rate of 1°C/min and held for 3 h before being heated to 580°C at a heating rate of 1°C/min and held for 6 h to assure complete organic combustion.

The materials containing inorganic cations were exchanged to the ammonium form by ion exchanging them three times with 1 M aqueous ammonium nitrate solution at 90°C for 3 h at a ratio of 100 mL of liquid per gram of solid to obtain the NH_4^+ form. The solid product from each exchange was again recovered by centrifugation, washed with water and acetone, and dried overnight at 100°C. These materials were then calcined using the standard method to convert them to proton form.

2.3. Characterization

PXRD patterns were obtained with a Rigaku MiniFlex II instrument using Cu K_α radiation ($\lambda=1.54184 \text{ \AA}$) to determine structure type and purity. Morphology and elemental composition were determined via scanning electron microscopy/energy dispersive spectroscopy (SEM/EDS) on a ZEISS 1550VP instrument equipped with an Oxford X-Max SDD energy dispersive X-ray spectrometer.

To quantify the number of Brønsted acid sites present in each catalyst, NH_3 temperature-programmed desorption (TPD)

was performed on each ammonium-exchanged, calcined material. The materials were pelletized, crushed and sieved. Particles between 0.6 mm and 0.18 mm were supported between quartz wool beds in a continuous flow quartz-tube reactor (part of an Altamira AMI-200 reactor system).

Once loaded, samples were heated to 150°C for 1 h at 10°C/min, followed by heating to 550°C for 1 h at 10°C/min in flowing argon (50 sccm) to remove any adsorbed species. Samples were then cooled to 160°C, and NH_3 was dosed onto each sample at a flow rate of 5 sccm in 50 sccm argon until no further NH_3 uptake was observed via the mass spectrometer. After a 8 h purge in flowing argon (50 sccm) to remove any physisorbed NH_3 , the sample was heated to 550°C at rate of 10°C/min in 30 sccm argon while the mass spectrometer monitored desorbing products, namely $m/z = 17$ fragments corresponding to NH_3 . The sample was held at 550°C for 2 h to ensure all species had fully desorbed.

2.4. MTO Reaction Testing

The samples in proton form were pelletized, crushed and sieved to retain particles between 0.6 mm and 0.18 mm. Approximately 200 mg of each calcined material was then supported between two glass wool beds in an Autoclave Engineers BTRS, Jr. 316SS tubular, continuous flow reactor.

Prior to reaction, all samples were again dried in-situ under a flow of breathing-grade air (30 sccm), during which the temperature was ramped at 1°C/min to 150°C and held for 3 h before being ramped at 1°C/min to 400°C (reaction temperature). The reaction was conducted at 400°C in a feed of 10% methanol in an inert gas blend (95mol% He, 5mol% Ar) at a weight-hourly space velocity (WHSV) of 1.3 h^{-1} and atmospheric pressure. A syringe pump introduced methanol at 5.4 $\mu\text{L}/\text{min}$ into a stream of the inert gas blend (flowing at 30 sccm). Reactor effluent gases were analyzed using an online GC/MS (Agilent GC MSD5793N) with a Plot-Q capillary column installed. Conversions and selectivities were computed on a carbon mole basis.

2.5. Post-Reaction Catalyst Characterization

After the MTO reaction, each catalyst was digested using 48wt% HF. Each spent catalyst was suspended in water, and the digestion vessel was cooled in an ice bath during the addition of HF. Solutions were neutralized using potassium hydroxide (1 M and finally 45wt%, exotherm on addition), and hydrocarbon products were extracted with deuterated chloroform. The extract solution was then dried using magnesium sulfate and filtered to remove any remaining solids. Tetramethylsilane was used as an internal ^1H NMR standard.

To test for the presence or absence of aromatics in each extracted solution, ^1H NMR was performed on a 500 MHz NMR. Peaks from approximately 7-9 ppm were attributed to aromatic compounds, and peaks from approximately 2-3 ppm were attributed to the hydrocarbon (methyl, ethyl, etc.) groups attached to these aromatic rings, consistent with the polymethylbenzene species formed in the hydrocarbon pool mechanism.

Thermogravimetric analyses (TGAs) were performed to quantify the organic remaining on each catalyst after the MTO reaction was completed using a PerkinElmer STA 600. In a typical TGA experiment, approximately 10 mg of spent catalyst was loaded into a pan and heated to 900°C at a heating

rate of 10°C/min in zero-grade air. Mass loss above 300°C was attributed to combustion of coke on each sample.

3. RESULTS AND DISCUSSION

3.1. Characterization

The PXRD patterns of the as-synthesized samples are shown in Figure 1. Additionally, the elemental compositions of each material (by EDS) and the acid site counts (by NH₃ TPD) are shown in Table 2.

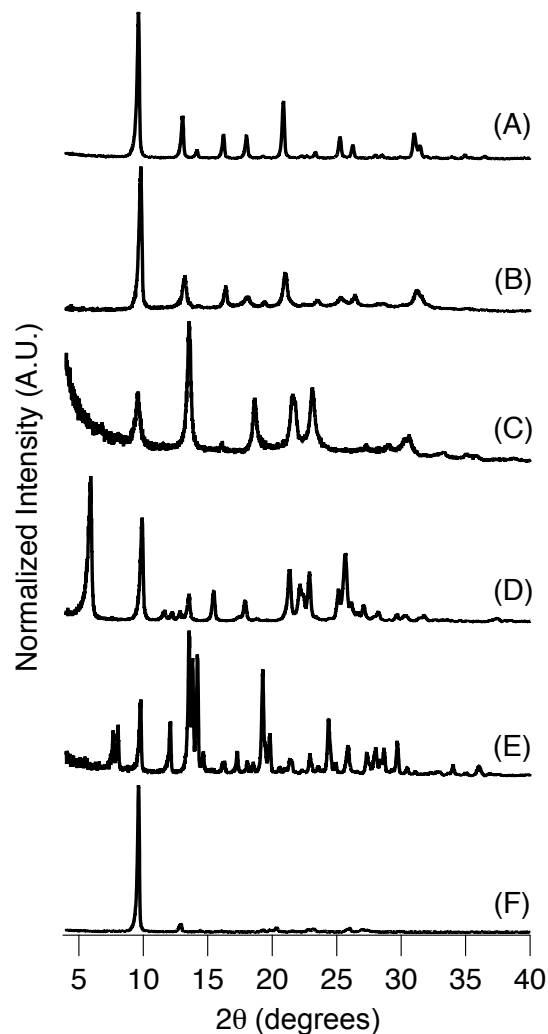


Figure 1. Powder XRD patterns of the proton-form of: (A) SSZ-13, (B) SAPO-34, (C) SAPO-39, (D) MCM-35, (E) ERS-7 and (F) RUB-37.

Table 2. Elemental Compositions for Materials

Material	Si/Al	Acid Site Count [mmol/g]
SSZ-13	17.4 ± 0.6	0.90
SAPO-34	-	0.94
SAPO-39	-	0.31
MCM-35	31.7 ± 2.1	0.59
ERS-7	8.1 ± 0.04	1.41
RUB-37	204 ± 44	0.20

3.2. MTO Reaction Testing

Figure 2 illustrates representative time-on-stream reaction data obtained at 400°C for the samples with CHA topology (SSZ-13 and SAPO-34). Each of the catalysts with CHA topology is active initially in producing C₂-C₄ olefins when methanol conversion is at or near 100%. As time on stream increases, methanol conversion eventually decreases, accompanied by a decrease in olefin selectivities and a simultaneous increase in dimethyl ether (DME) production.

Light alkanes, mainly propane and butane, are also observed among the products at the start of the reaction for the SSZ-13, with selectivities decreasing with time-on-stream.

In addition to the samples with CHA topology, the materials with 1D 8MR structures (SAPO-39, MCM-35 and ERS-7) also underwent MTO reaction testing. For each reaction test, no light olefins were observed at any sample points: the sole product was dimethyl ether (DME) in each case. The final material, RUB-37, which has a 2D 8MR pore system, was also MTO reaction tested. In this case, the primary product was DME, just as with the 1D 8MR materials; however, traces of other hydrocarbon products were also observed initially. Figure 3 shows the reaction profiles for these 8MR materials.

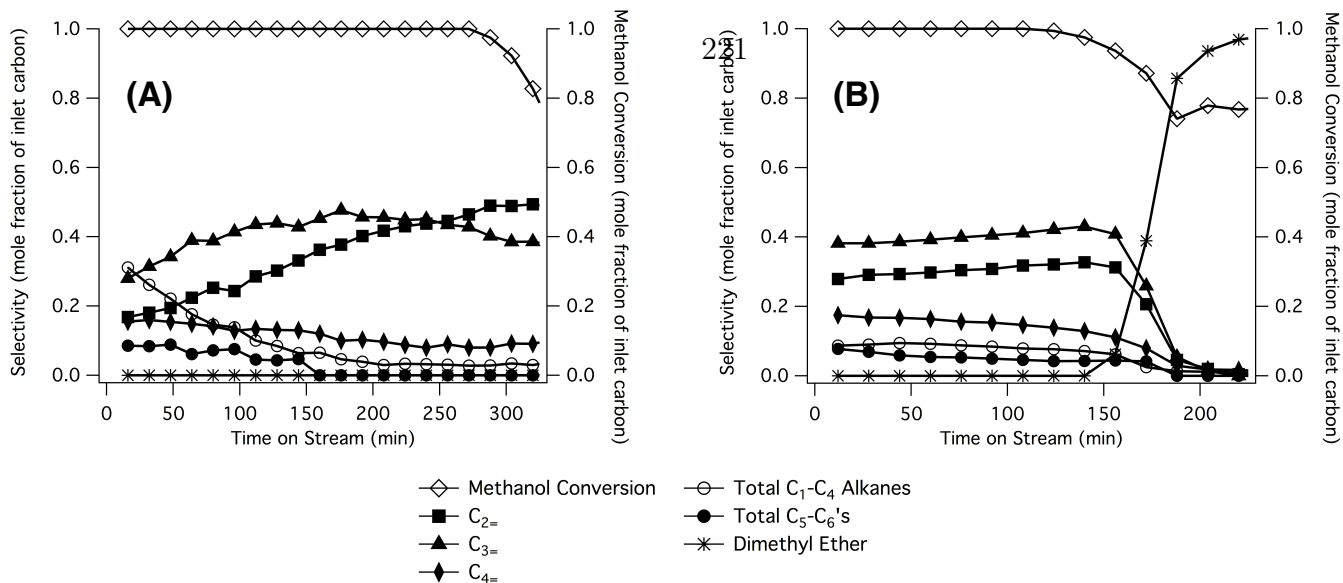


Figure 2. Representative MTO reaction data obtained at 400°C for the proton-form of: (A) SSZ-13 and (B) SAPO-34.

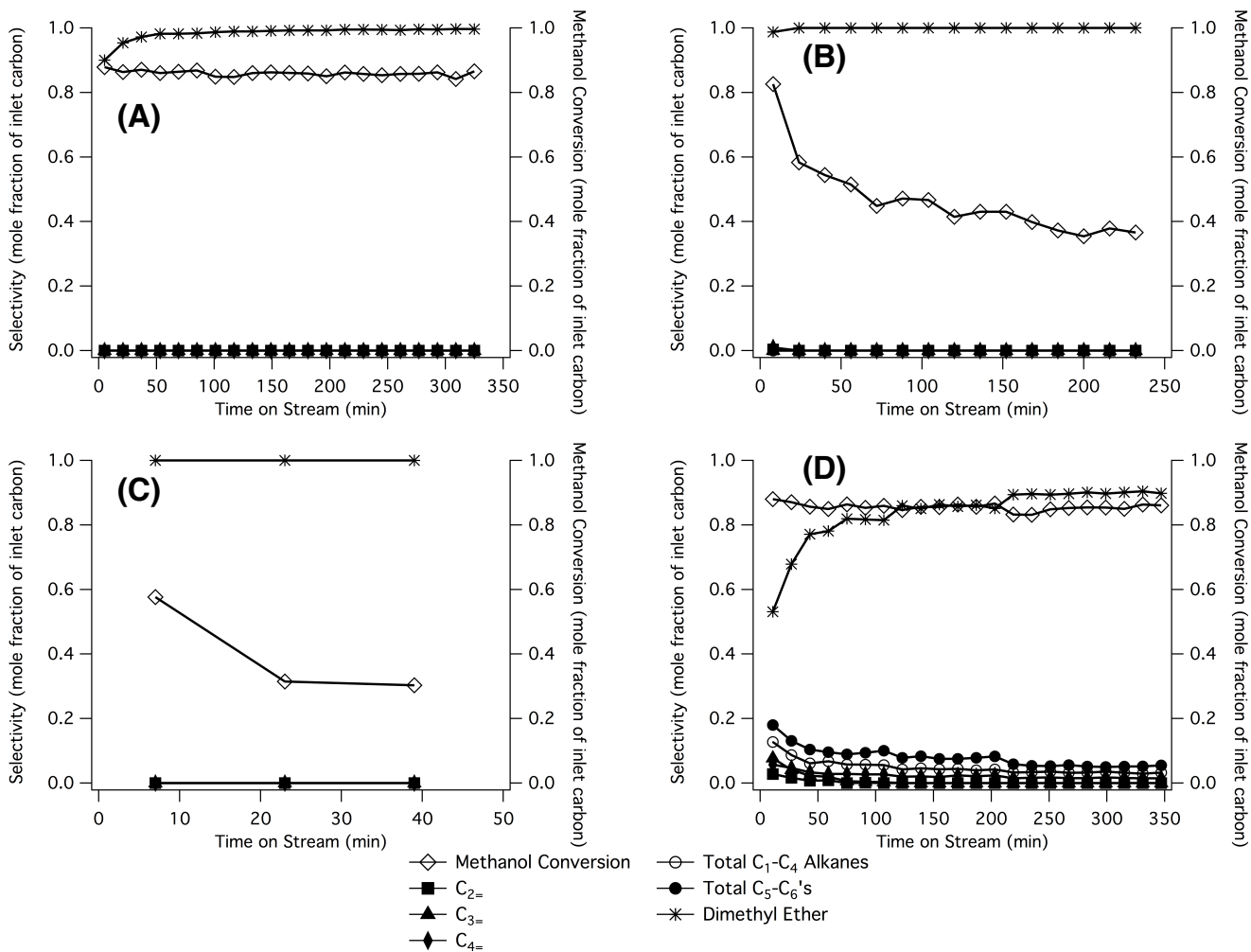


Figure 3. Representative MTO reaction data obtained at 400°C for the proton-form of: (A) SAPO-39, (B) MCM-35, (C) ERS-7 and (D) RUB-37.

From these reaction results, it is clear that the materials with CHA topology (and thus sufficient cage space to form polymethylbenzenes) are active for MTO, while the materials with 1D and 2D 8MR structures and smaller cages do not exhibit MTO activity. RUB-37 forms some alkanes, but the total selectivity to light olefins (ethylene, propylene and butylene) is less than 5% at nearly all points on stream.

3.3. ^1H NMR Results

Upon completion of the MTO reaction test, the catalysts were acid digested, and ^1H NMR spectra were obtained for the organics extracted from these spent materials. Figure 4 shows the ^1H NMR spectra gathered. The chloroform peak is at 7.26 ppm, with associated spinning sidebands. Peaks from

approximately 7-9 ppm are attributed to aromatic species extracted from the cages of the microporous materials. The two CHA materials exhibit these peaks, while the remaining four materials with smaller pores and cages do not. The lack of aromatic species for the 1D and 2D materials correlates with the absence of MTO activity, suggesting that the smaller cages prevent formation of the required aromatic intermediates for the “hydrocarbon pool”.

Peaks approximately in the 2-3 ppm range are attributed to protons associated with methyl, ethyl or propyl groups on the aromatic rings. These peaks are strongly present in the four materials with MTO activity, further confirming the presence of polymethylbenzene species in the microporous materials.

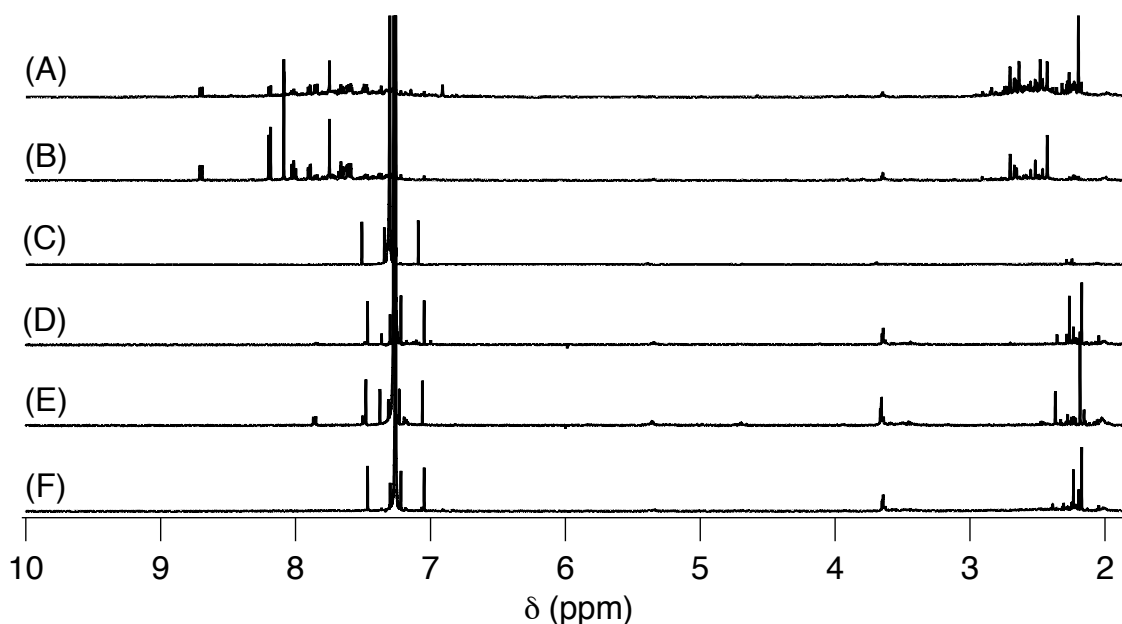


Figure 4. ^1H NMR spectra gathered for (A) SSZ-13, (B) SAPO-34, (C) SAPO-39, (D) MCM-35, (E) ERS-7 and (F) RUB-37 after MTO reaction and acid digestion.

3.4. Thermogravimetric Analysis

Table 3 shows the mass losses for each sample above 300°C, attributed to deposits of organic species. Mass losses for materials with the CHA topology (SSZ-13 and SAPO-34) are higher than for the materials with the other framework topologies. These greater mass losses are consistent with formation of reaction intermediate organic species on the MTO-active CHA samples as part of the hydrocarbon pool mechanism, while the samples inactive for the MTO reaction typically have much smaller mass losses.

Table 3. Organic Mass Losses for Materials by TGA

Material	Mass Loss from 300°C to 900°C (wt%)
SSZ-13	20.8
SAPO-34	12.3
SAPO-39	4.9

MCM-35	1.9
ERS-7	1.8
RUB-37	3.1

CONCLUSION

Several 8MR aluminosilicate and silicoaluminophosphate materials are tested for their ability to catalyze the MTO reaction, and the presence or absence of polymethylbenzenes (a key part of the proposed MTO “hydrocarbon pool” mechanism) measured in order to correlate MTO activity and presence of polymethylaromatics with molecular sieve pore and cage sizes.

Both materials with the CHA topology (3D 8MR pore system with sufficiently large cages) exhibited MTO activity to form light olefins and demonstrated evidence of aromatic compounds in the extracted solutions of acid-digested, spent catalysts via ^1H NMR spectroscopy. Materials that did not have MTO activity (SAPO-39, MCM-35, ERS-7 and RUB-37) did not form polymethylbenzene reaction intermediates (no

evidence of aromatic species in these ¹H NMR spectra). Further, TGA of each sample post-MTO reaction revealed higher mass losses for MTO-active CHA materials, suggesting that a hydrocarbon pool was indeed forming on these samples. Significantly lower mass losses for the 1D and 2D materials suggest a lack of organic buildup in the catalyst, correlating with the lack of MTO activity.

AUTHOR INFORMATION

Corresponding Author

*Email: mdavis@cheme.caltech.edu

Notes

The authors declare no competing financial interest.

ACKNOWLEDGMENT

The authors would like to thank Chevron Energy and Technology Company and the Dow Chemical Company for each providing partial support for this work. J.E.S. would like to thank the NDSEG for their support through a fellowship. We thank Stacey Zones of Chevron Energy and Technology Company for suggesting that we investigate the suite of materials presented here and for supplying the SAPO-39 material.

REFERENCES

- (1) Froment, G. F.; Dehertog, W. J. H.; Marchi, A. J., In *Catalysis: Volume 9*, Spivey, J. J., Ed. The Royal Society of Chemistry: 1992; Vol. 9, pp 1-64.
- (2) Dai, W.; Wang, X.; Wu, G.; Guan, N.; Hunger, M.; Li, L. *ACS Catal.* **2011**, *1*, 292-299.
- (3) Kaiser, S. W., Using silicoaluminophosphate molecular sieve catalyst; U.S. Patent 4,499,327. 1985.
- (4) Vora, B.; Chen, J. Q.; Bozzano, A.; Glover, B.; Barger, P. *Catal. Today.* **2009**, *141*, 77-83.
- (5) Olsbye, U.; Svelle, S.; Bjørgen, M.; Beato, P.; Janssens, T. V. W.; Joensen, F.; Bordiga, S.; Lillerud, K. P. *Angew. Chem. Int. Ed. Engl.* **2012**, *51*, 5810-5831.
- (6) Hereijgers, B. P.; Bleken, F.; Nilsen, M. H.; Svelle, S.; Lillerud, K.-P.; Bjørgen, M.; Weckhuysen, B. M.; Olsbye, U. *J. Catal.* **2009**, *264*, 77-87.
- (7) Dahl, I. M.; Kolboe, S. *Catal. Lett.* **1993**, *20*, 329-336.
- (8) Bjørgen, M.; Svelle, S.; Joensen, F.; Nerlov, J.; Kolboe, S.; Bonino, F.; Palumbo, L.; Bordiga, S.; Olsbye, U. *J. Catal.* **2007**, *223*, 195-207.
- (9) Zhu, Q.; Kondo, J. N.; Tatsumi, T.; Inagaki, S.; Ohnuma, R.; Kubota, Y.; Shimodaira, Y.; Kobayashi, H.; Domen, K. *J. Phys. Chem. C.* **2007**, *111*, 5409-5415.
- (10) Chen, D.; Moljord, K.; Fuglerud, T.; Holmen, A. *Microporous Mesoporous Mater.* **1999**, *29*, 191-203.
- (11) Baerlocher, C.; McCusker, L. B.; Olson, D. H., *Atlas of Zeolite Framework Types*. 6th revised ed.; Elsevier: London, 2007.
- (12) Haw, J. F.; Marcus, D. M. *Top. Catal.* **2005**, *34*, 41-48.
- (13) Arstad, B.; Nicholas, J. B.; Haw, J. F. *J. Am. Chem. Soc.* **2004**, *126*, 2991-3001.
- (14) Liang, J.; Li, H.; Zhao, S.; Guo, W.; Wang, R.; Ying, M. *Appl. Catal.* **1990**, *64*, 31-40.
- (15) Vora, B. V.; Marker, T. L.; Barger, P. T.; Nilsen, H. R.; Kvisle, S.; Fuglerud, T. *Stud. Surf. Sci. Catal.* **1997**, *107*, 87-98.
- (16) Chen, J. Q.; Bozzano, A.; Glover, B.; Fuglerud, T.; Kvisle, S. *Catal. Today.* **2005**, *106*, 103-107.
- (17) Zones, S. I., Zeolite SSZ-13 and its method of preparation; US Patent 4,544,538. 1985.
- (18) Yuen, L.-T.; Zones, S. I.; Harris, T. V.; Gallegos, E. J.; Auroux, A. *Microporous Mater.* **1994**, *2*, 105-117.
- (19) Zhu, Q. J.; Kondo, J. N.; Ohnuma, R.; Kubota, Y.; Yamaguchi, M.; Tatsumi, T. *Microporous Mesoporous Mater.* **2008**, *112*, 153-161.
- (20) Bhawe, Y.; Moliner-Marin, M.; Lunn, J. D.; Liu, Y.; Malek, A.; Davis, M. E. *ACS Catal.* **2012**, *2*, 2490-2495.
- (21) Schmidt, J. E.; Deimund, M. A.; Davis, M. E. *Chem. Mater.* **2014**, *26*, 7099-7105.
- (22) Baerlocher, C.; McCusker, L. B. Database of Zeolite Structures, <<http://www.iza-structure.org/databases/>>. Accessed 3 December 2014.
- (23) Robson, H. *Verified Synthesis of Zeolitic Materials*; 2001.
- (24) Miller, S. J., Process for olefin isomerization; US Patent 6,281,404.
- (25) Rubin, M. K., Synthetic crystal MCM-35; US Patent 4,981,663. 1991.
- (26) Campbell, B. J.; Cheetham, A. K.; Bellussi, G.; Carluccio, L.; Perego, G.; Millini, R.; Cox, D. E. *Chem. Commun.* **1998**, *008*, 1725-1726.
- (27) Yilmaz, B.; Müller, U.; Feyen, M.; Zhang, H.; Xiao, F.-S.; De Baerdemaeker, T.; Tijsebaert, B.; Jacobs, P.; De Vos, D.; Zhang, W.; et al. *Chem. Commun. (Camb)*. **2012**, *48*, 11549-11551.

Jay A. Labinger*, David C. Leitch, John E. Bercaw, Mark A. Deimund and Mark E. Davis

Upgrading Light Hydrocarbons: A Tandem Catalytic System for Alkane/Alkene Coupling

Division of Chemistry and Chemical Engineering, California Institute of Technology, Pasadena, CA 91125

*Jay Labinger, jal@its.caltech.edu, tel: 1-626-395-6520; fax: 1-626-449-4159

Abstract

Light hydrocarbons, with relatively low fuel value, are abundant from several sources, including mixed alkane/alkene refinery byproduct streams. A tandem system consisting of a compatible combination of a homogeneous alkane dehydrogenation catalyst (known to be kinetically efficient but thermodynamically disfavored at low temperatures) with an olefin dimerization catalyst could effect the coupling of an alkane and alkene to produce a heavier, more valuable fuel molecule ($C_nH_{2n+2} + C_nH_{2n} = C_{2n}H_{4n+2}$), a reaction that is thermodynamically favorable below 250 °C. We have demonstrated that coupling with a tandem homogeneous catalyst, consisting of a pincer-ligated iridium alkane dehydrogenation catalyst and an organometallic tantalum alkene dimerization catalyst; the combination couples 1-hexene/*n*-heptane to C₁₃/C₁₄ products at temperatures ranging from 100-150°C, operating with up to 90% cooperativity. This particular combination generates alkene products rather than the desired alkanes, however, because the regioselectivity of the dimerization catalyst preferentially yields highly substituted alkenes that are not reactive towards hydrogen transfer. A complete cycle should be attainable by combining the dehydrogenation catalyst with an alternate dimerization catalyst that gives mostly linear and monosubstituted alkenes; we have synthesized a novel class of nickel-exchanged zirconosilicates that exhibit the desired dimerization catalytic behavior.

Introduction (Part I): Mark Davis and Me¹

In 1991, Mark moved from VPI to Caltech, where I had been since 1986. My research work at Caltech was almost entirely focused on organometallic chemistry and homogeneous catalysis. I had formed strong interests in heterogeneous catalysis, and especially on making productive connections between the two (often disjunct) fields, during my preceding position at ARCO, but there was little or no heterogeneous catalysis going on in either chemistry or chemical engineering (Henry Weinberg left Caltech just around the time I arrived). Mark's remarkable program on zeolitic and other catalytic materials, with its strong emphasis on understanding structure and reactivity as close to the molecular level as possible, looked to offer an great opportunity for reviving those interests! And so it proved to be: continuously since his arrival, Mark and I have interacted and collaborated on many projects. Not only in research, but also teaching: we introduced and jointly taught a new Caltech course "Catalysis" that covered a wide range of topics in heterogeneous and homogeneous catalysis, and the relations between them.

Our² first idea for a joint project — generation of novel forms of zeolite-supported transition metal catalysts using metal complexes as structure-directing agents — never quite worked out. (There have been a few such syntheses reported subsequently [1], but no especially interesting catalysts have resulted.) Our first *productive* joint project was an investigation of the mechanism of alkane oxidation by TS-1 [2], a problem for which my work on homogeneous catalytic oxidation mechanism [3,4] and Mark's expertise in zeolite chemistry nicely dovetailed.

Soon afterwards we were approached by BP, who were interested in new methodology for the selective oxidation of light alkanes, especially propane and butane. Mark and I (with a couple of additional collaborators) put together a proposal centered around constructing selective oxidation catalysts by stabilizing small metal oxide clusters inside microporous solids. It was accepted, and that initial program resulted in promising catalysts, some directly based on the initial premise [5], and others following new leads suggested thereby [6]. Even more importantly, that initial interaction with BP soon underwent inflationary expansion. First our colleague John Bercaw joined the program, with the addition of homogeneous catalysis, for not only alkane oxidation but also other projects that took us in important new directions, such as selective alkene trimerization [7].

Out of that enlarged program grew the even bigger "MC²" (Methane Conversion Cooperative) program, a joint venture between BP, Caltech, UC Berkeley and several other labs, that is ongoing (with some modification of title and aims) right up to the present. Within this program, John, Mark and I have looked at several ways to combine the advantages of homogeneous and heterogeneous catalysis — of which the material that makes up the bulk of this paper is a prime example. And I have continued my

¹ JAL

² Actually it was mostly mine, and reflected more than a little naïvete on my part. Mark was (correctly) dubious about its prospects, but graciously agreed to give it a chance.

interactions with Mark's catalysis group, always learning more from Mark's encyclopedic knowledge and amazing intuition, and (hopefully) contributing a little from my own areas of expertise now and then [8]. Unquestionably my experience and career at Caltech would have been seriously impoverished had Mark not decided to join us. I appreciate this opportunity to congratulate him on the well-deserved award that this symposium recognizes, and to thank him for everything we've done together.

Introduction (Part II): Upgrading Light Hydrocarbons via Tandem Catalysis

Effective utilization of light hydrocarbons represents a significant challenge in the current energy landscape. This is by no means a new problem: a long-forgotten document found in the Caltech archives (Fig. 1) shows that an academic-industrial collaboration in this area was contemplated fully 70 years ago, although there is no surviving evidence that it actually came to pass, nor what approach was to have been followed. Now increased natural gas production and burgeoning interest in Fischer-Tropsch are adding new light alkane sources to the ongoing abundance of off-streams from refinery processes such as catalytic cracking, making the question of what to do with relatively low value "light ends" such as C_{2-5} alkanes and C_{4-5} alkenes more pressing. Upgrading to fuels — say, highly branched C_{6-10} alkanes for gasoline, unbranched or lightly branched C_{10-16} alkanes for diesel and jet fuel (the latter appears a more attractive target under current market projections) would be a highly attractive approach. Light alkenes can be oligomerized — although to date there is no really good technology for the sort of highly selective (including regioselectivity) dimer- and trimerization catalysis that would be needed — but it is far from clear what to do with light alkanes.

At its meeting on July 7, 1945, in 27 Gates, the Division of Chemistry and Chemical Engineering adopted by a unanimous vote the following resolution. Those present, in addition to the Chairman (Pauling), were Badger, Bates, Buchman, Koepfli, Lacey, Lucas, Niemann, Sage, Swift, and Zechmeister, all of whom voted. The resolution as adopted was amended somewhat in wording from that recommended by a special committee of the Division.

There has been under discussion for some time a proposed contract between the California Institute of Technology and the Texaco Development Corporation for work to be done on the properties of hydrocarbons (the development of a method of converting hydrocarbons of low molecular weight into hydrocarbons of higher molecular weight) in the Chemical Engineering Laboratory of the California Institute. If the contract were executed, this work would probably be continued for ten or fifteen years, and, after the initial period, its magnitude would be such as to involve an annual budget probably about \$100,000.00.

Fig. 1 Excerpt from a document found in the Caltech archives

The potential for homogeneous catalysis in such large-scale processes has long been intriguing. It has been known for over 25 years that organometallic complexes are able to activate C-H bonds, even in alkanes, under remarkably mild conditions [9], suggesting the tantalizing possibility of carrying out low-temperature chemistry that would be more amenable to product control and selectivities generally unattainable with more traditional,

high-temperature heterogeneous catalysts. Most of the promising advances here, though, have involved oxidative functionalization of C-H bonds; transformations involving only hydrocarbons are constrained by thermodynamics, often unfavorable at lower temperatures.

Thus, for example, dehydrogenation of light alkanes to alkenes can be readily achieved with a number of organometallic catalysts, most notably an array of iridium complexes with “pincer” ligands (see below), at temperatures typically below 200 °C [10]. However, at such low temperatures the reaction (Eq 1) is uphill; the reaction must be driven by providing a sacrificial H₂ acceptor — obviously impractical for the industrial-scale processes considered here — or, in special cases, with higher-boiling hydrocarbons (again, not applicable to the present goals), by shifting the unfavorable equilibrium by purging liberated H₂. The same considerations would apply to the (as yet hypothetical) dehydrogenative coupling of alkanes (Eq 2).

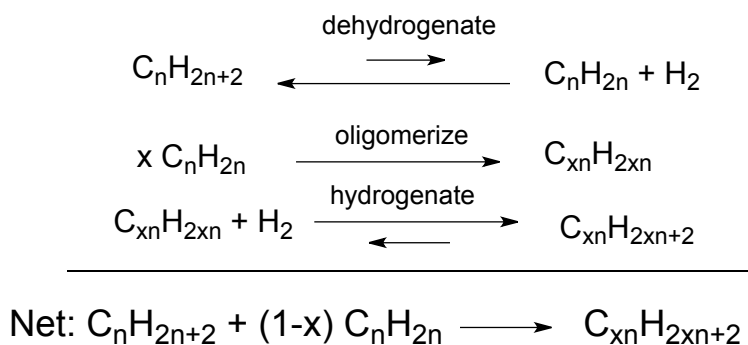
One interesting approach to alkane coupling involves so-called alkane metathesis (Eq 3), whereby alkanes are in effect cut up and redistributed, analogously to the far-better-known alkene metathesis reaction. Alkane metathesis over a single catalyst, derived from surface-supported organometallic complexes, was first reported in 1997 [11]; only low activities were obtained. Although there was no mechanistic explanation at the time, subsequent studies implicated a sequence of dehydrogenation via C-H activation and alkene metathesis. That in turn suggested the possibility of improving performance by means of tandem catalysis — two catalysts, one to carry out each of those steps — allowing in principle for their separate optimization. Indeed, such an experiment had been reported earlier, using two well-known heterogeneous catalysts, platinum on alumina for dehydrogenation and tungsten oxide on silica for alkene metathesis; it gave moderate conversion at relatively high temperature (400 °C) [12].



More recently, recognizing the possibility of combining the remarkable alkene metathesis activity of homogeneous catalysts with the pincer-iridium dehydrogenation catalysts mentioned above, Goldman, Brookhart and coworkers devised an all-homogeneous tandem catalytic system and applied it to a prime target, conversion of *n*-hexane to *n*-decane (Eq 3) as a test reaction at a much lower temperature, 125 °C [13]. Note that there should be little or no thermodynamic constraints: converting two alkanes to two other alkanes will have very little enthalpic or entropic consequences. And indeed it works — but there are limitations. The reaction showed low to moderate activity (TOF ~ 10⁻³ sec⁻¹), stability (1-2 days), and especially selectivity, with maximum C₁₀ yields

around 5% (19% selectivity at 24% conversion). Constraints on selectivity are inherent in this approach, as the reactivity of products and reactants are (necessarily) virtually the same. Also Eq 3 depends on metathesis involving exclusively terminal alkenes, which are indeed selectively produced by these dehydrogenation catalysts; but there is competing isomerization, and metathesis of the resulting internal alkenes will eventually generate a wide distribution of products. Finally, for any C_n reactant, $1/n$ of the feed must be wasted (or, at least, converted to a less valuable product) in the form of ethane. So although this approach is highly interesting, and might offer some practical possibilities, it appears worthwhile to seek potentially more selective alternatives.

One such is alkane-alkene coupling, represented schematically in Scheme 1, which could be applied to mixed light alkane-alkene streams that are common byproducts of refinery processes. Here, as in alkane metathesis, the fed alkane undergoes a small equilibrium degree of dehydrogenation at one catalyst; the resulting alkene is coupled to the fed alkene by the second catalyst, giving a higher alkene which is hydrogenated by the first catalyst. The thermodynamic considerations are a bit more complex here: in contrast to straightforward alkane dehydrogenation, the overall reaction is enthalpically favored but entropically disfavored, imposing a maximum rather than a minimum temperature, estimated to be around 250 °C [14]; but that should be compatible with the temperature range expected to be compatible with a tandem system containing (at least) one homogeneous catalyst. Accordingly we set out to assess the feasibility of this approach, and here report our preliminary, but quite encouraging, results.



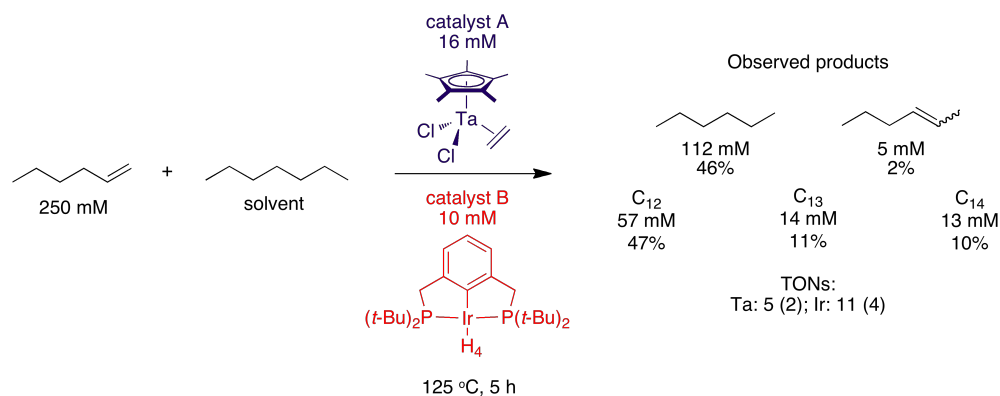
Scheme 1

Alkane-Alkene Coupling via Tandem Catalysis: Proof of Concept

For our initial studies, the pincer-Ir complexes were an obvious choice for transfer hydrogenation, but what should the dimerization catalyst be? The most important criteria at this stage had to be compatibility. The vast majority of known dimerization/oligomerization catalysts exhibit (one or both) of the following undesirable (for this purpose) properties. First, they may not be operable within the temperature window required by the Ir catalyst, typically 100-200 °C: too low for good activity with many heterogeneous catalysts; too high for thermal stability with most homogeneous catalysts. Second, many catalysts (both homogeneous and heterogeneous) require a potent activator, often acid or a strong reductant such as an alkylaluminum reagent; while

the Ir complexes are remarkably *thermally* robust, they are *chemically* quite the opposite and would not survive such conditions. Hence, to demonstrate the viability of our approach, we selected a homogeneous catalyst developed by Schrock *et al.* in the 1970s, Cp*TaCl₂(C₂H₄) [15], which offers the major advantages of 1) high thermal stability; 2) requiring no activator; and 3) good specificity (for terminal alkenes) and regioselectivity (Eq. 4), although as we will see the particular alkene isomers it generates are actually not desirable for completing the target transformation.

As a test, we examined the reaction of 1-hexene in *n*-heptane in the presence of the two catalysts, and after some initial adjustment of reaction parameters (by trial and error), obtained the results shown in Scheme 2. The formation of *n*-hexane (along with heptenes, presumably, but they were hard to detect in the presence of the large excess of heptane) shows that transfer hydrogenation has taken place, while the formation of (large amounts of) C₁₂ alkenes shows that dimerization is operating as well, so at least the two catalysts do not interfere with one another. More importantly, the appearance of C₁₃ and C₁₄ products demonstrates tandem catalysis: the heptene produced by transfer hydrogenation has been successfully coupled with the hexene (as well as with itself)! How well did it work? We can define two measures of efficacy. Tandem *yield* is the number of moles of monomeric alkene incorporated into C_{13/14} products divided by the number of moles of hexene initially present; tandem *cooperativity* is the fraction of heptenes produced by transfer hydrogenation (measure by the amount of hexane formed) that end up in the C_{13/14} products. For this initial demonstration, those are 21% and 35% respectively [14].



Scheme 2

Tandem Catalysis: Optimization via Mechanism

Improving catalytic performance by adjusting the nature of the catalyst and/or the reaction parameters, in a rational as opposed to Edisonian, trial-and-error manner, is facilitated by thorough mechanistic study. (At least, academic chemists like to believe that!) This issue is particularly crucial to the case of tandem catalysis, for which we need to understand not only how each catalyst operates on its own, but also whether and, if so, how the presence of one may modify the behavior of the other [16]. For the present Ir/Ta tandem system, we first addressed the latter question: do transfer hydrogenation and

dimerization function independently in a common solution? Fig. 2 shows that in fact they do: each catalyst performs exactly the same, within experimental precision, with or without the other present.

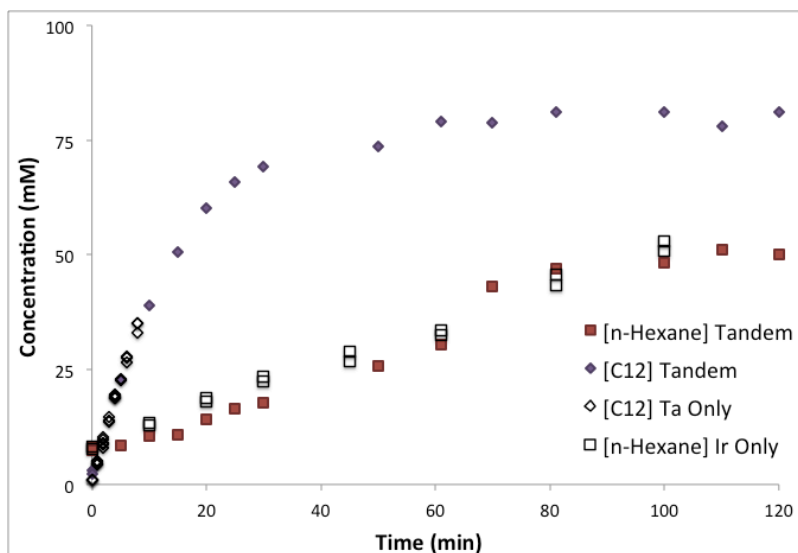
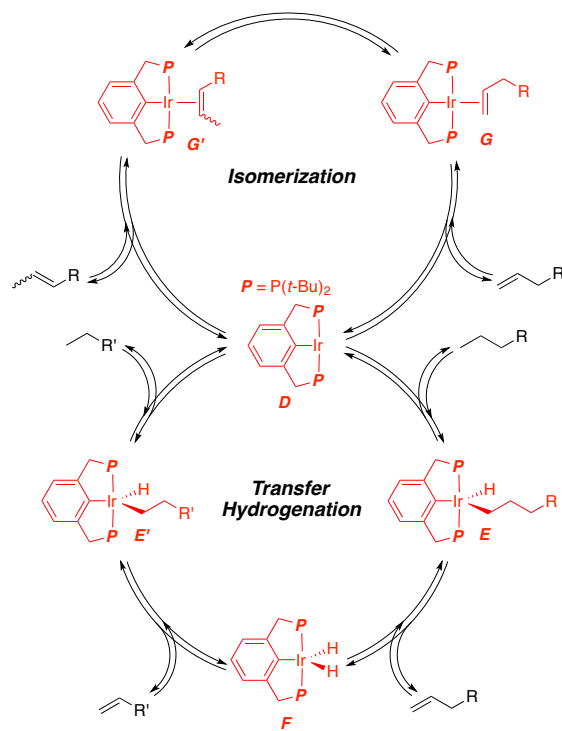
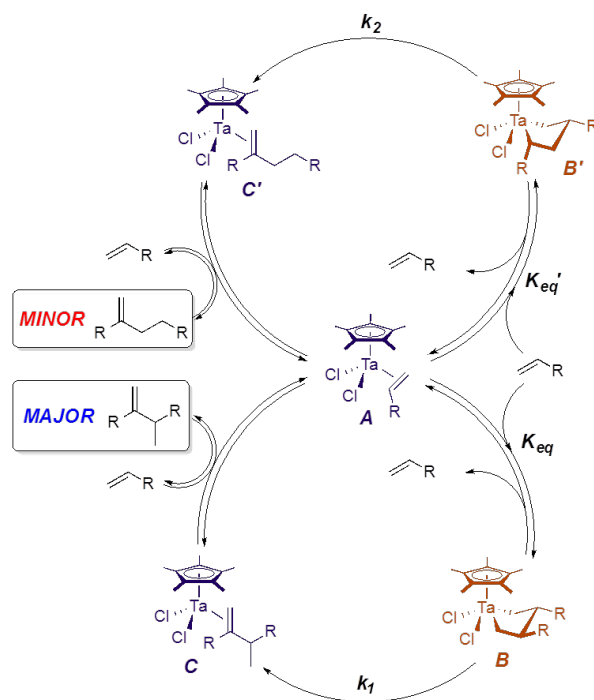


Fig 2 Time evolution of products from the reaction of Scheme 2: *n*-hexane (squares) and C₁₂ (diamonds) obtained with Ir and Ta catalysts respectively, by themselves (open shapes) and in the presence of the other (filled shapes)

Next we examined the detailed mechanisms for each of the two components. The basic sequences had already been established for both the Ta-catalyzed dimerization [17] and the Ir-catalyzed transfer hydrogenation [10], as shown in Schemes 3 and 4 respectively, and our findings confirm them, with some additional details specifically relevant to the conditions where the tandem process may operate. Most importantly, the two processes exhibit very different dependencies on both alkene concentration and temperature. Ir-catalyzed transfer hydrogenation is *inversely* dependent on [alkene], while the competing isomerization of 1-alkene to internal alkenes (which are not dimerized at all by the Ta catalyst) is approximately first-order in [alkene] (Fig. 3). In contrast, Ta-catalyzed dimerization is directly related to [alkene]; more precisely, it exhibits saturation kinetics: first-order at low [alkene] turning to zero-order at higher levels (Fig. 4). Furthermore, transfer hydrogenation rates increase strongly (both absolutely and relative to competing isomerization), whereas dimerization rates decrease modestly, with increasing temperature; these behaviors are entirely consistent with the mechanisms of Schemes 3 and 4 [16].



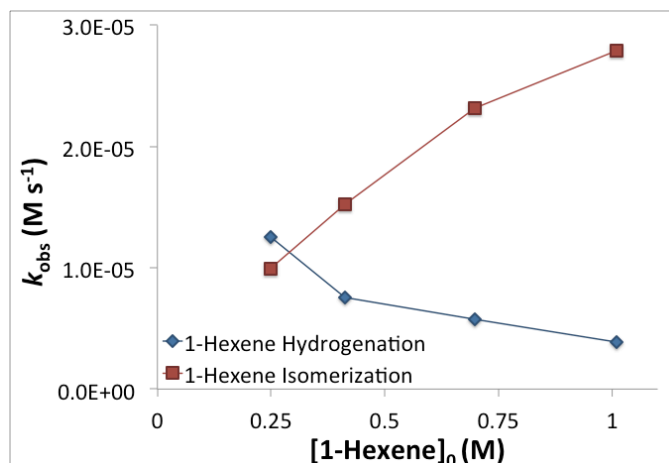


Fig 3 Rate constants for Ir-catalyzed transfer hydrogenation (diamonds) and isomerization (squares) of 1-hexene as a function of concentration

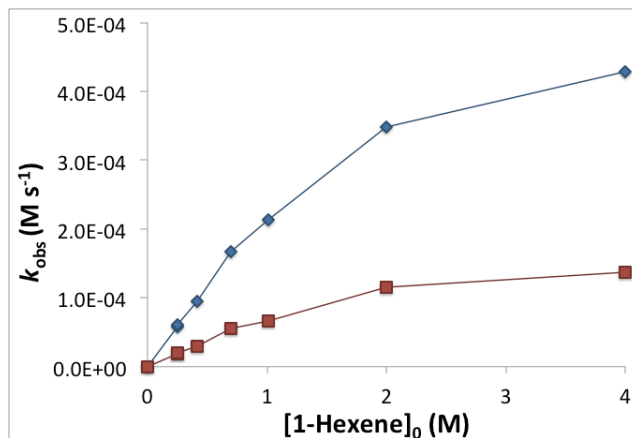


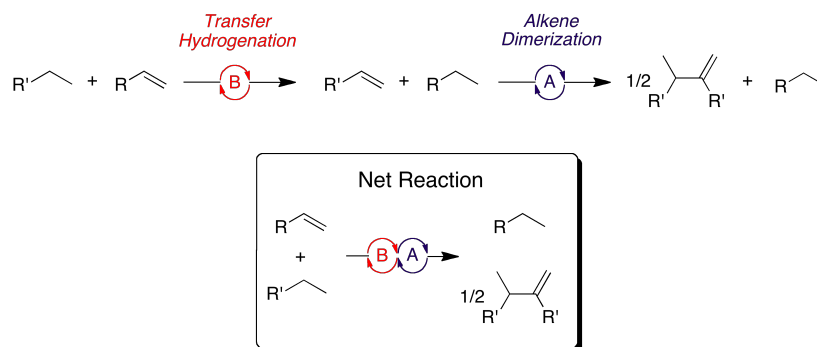
Fig 4 Rate constants for Ta-catalyzed dimerization of 1-hexene to major (diamonds) and minor (squares) isomers as a function of concentration

This mismatch in optimal conditions for the individual reactions imposes constraints on the tandem process: at high [alkene], dimerization will far outpace transfer hydrogenation, resulting in very inefficient alkane utilization; while at low [alkene] only a limited overall conversion can be achieved. The solution to this dilemma is gradual addition of alkene to the reaction mixture. Table 1 shows the striking improvement achieved by slow addition of the 1-hexene by syringe pump, such that the concentration at any given time is kept quite low. Compared to the initial results of Scheme 2, the overall yield of tandem product is doubled; and cooperativity is now over 90%, showing that the two catalytic processes are working together with excellent efficiency [14].

Table 1 Effect of slow addition of alkene on tandem catalytic performance

[1-Hexene] added (mM)	C ₁₂ mM (%)	C ₁₃ + C ₁₄ mM (%)	TON for Ta	TON for Ir	Yield %	Cooperativity %
1200 (~50 mM h ⁻¹)	293 (49)	240 (40)	67 (30)	66 (60)	40	91
1000 (one shot)	432 (86)	29 (6)	58 (4)	17 (8)	13	45

Unfortunately this demonstration system does *not* carry out the entire target cycle: the dimeric hydrocarbons are alkenes, not alkanes; the net reaction is that of Scheme 5, not Scheme 1, with the alkene feedstock acting as sacrificial hydrogen acceptor as well as substrate. The reason for this shortcoming is clear: the highly-branched dimeric alkene isomers preferentially produced by the Ta catalyst are too sterically encumbered to undergo transfer hydrogenation at Ir. To complete the cycle, we need to find a dimerization catalyst that can produce less-branched alkene isomers, and/or a transfer hydrogenation catalyst that can operate on highly substituted ones. Both approaches are being pursued; here we will present some preliminary findings on the former.

**Scheme 5**

Ni-Exchanged Zincosilicates: Advantages of Charge Matching

As noted earlier, there is a large array of known alkene dimerization/oligomerization catalysts, both homogeneous and heterogeneous, but not so many that seem likely to be compatible with the Ir transfer hydrogenation catalysts and thus be viable tandem catalysis candidates. The most common issue of concern is the need for activation by “harsh” reagents such as alkylaluminum compounds. One potentially interesting class of catalyst that does not (always) require such activation is nickel-exchanged zeolitic materials, such as zeolites with FAU or MFI topology as well as mesoporous aluminosilicates; these convert light alkenes such as propene to dimers and higher oligomers, with moderate selectivity and activity at temperatures generally in the range of 100-300°C [18]. It occurred to us that one cause of less-than-optimal performance might be charge mismatch: nickel is incorporated in the form of Ni²⁺, whereas the substitution of Al for Si in the framework results in but a single negative charge, requiring *two* such sites for each Ni. In contrast, *zincosilicates* have a double negative charge at each

heteroatom site (Fig. 5). One might thus expect that, for a given heteroatom (Al or Zn) content, the probability of finding a suitable exchange site would be considerably higher for Zn, permitting higher Ni loadings. More importantly, *unpaired* Al sites where exchange does not occur will remain in the H^+ form and generate fairly strong Brønsted acid sites, which under reaction conditions are likely to catalyze unselective side reactions such as cracking and isomerization. Hence Ni-exchanged zincosilicates might well afford improved catalytic performance for alkene oligomerization.

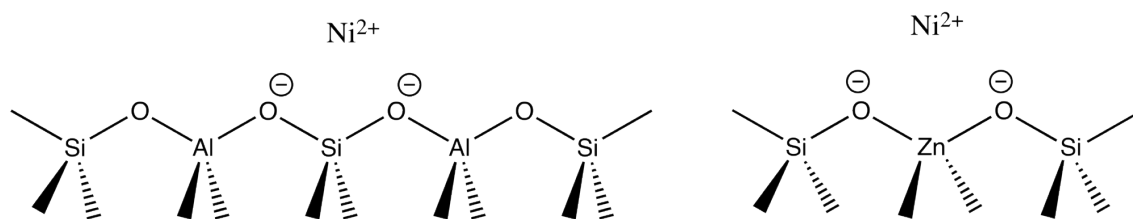


Fig 5 Interaction of Ni^{2+} ion with dinegative sites in aluminosilicate (left) vs. zincosilicate (right) frameworks

Two zincosilicates synthesized in the Davis lab, CIT-6 (a zeolite with *BEA topology) [19] and Zn-MCM-41 [20], were exchanged with $Ni(NO_3)_2$ and tested as propene oligomerization catalysts at 180 and 250 °C, with high-aluminum zeolite beta (HiAl-BEA) and ultra-stable zeolite Y (USY) as reference materials; loadings were chosen so as to maintain approximately comparable numbers of Ni^{2+} exchange sites in each. Typical results are shown in Fig. 4; while there are no obvious trends in activity or stability, the zincosilicate-based catalysts show clear superiority in selectivity. For Ni-CIT-6, selectivity to oligomers ($C_6 + C_9$) is on the order of 95%, with the majority consisting of the linear (2-hexene) and monobranched (2-methyl-2-pentene + 4-methyl-2-pentene) C_6 isomers, along with smaller amounts of C_9 and other C_6 isomers. Ni-Zn-MCM-41 is even more selective for oligomers: less than 1% of non- C_{3n} products are produced. With both of these Ni-zincosilicates, the linear:branched ratio of isomers is (desirably) high, around 1 for Ni-CIT-6 and 1.3 for Ni-Zn-MCM-41. In contrast, the Ni-aluminosilicate catalysts show much lower C_{3n} selectivity, with concomitantly higher levels of products resulting from cracking, isomerization, and recombination (C_4, C_5, C_7, C_8). The linear/branched ratios are also much lower, on the order of 0.25-0.3 [21].

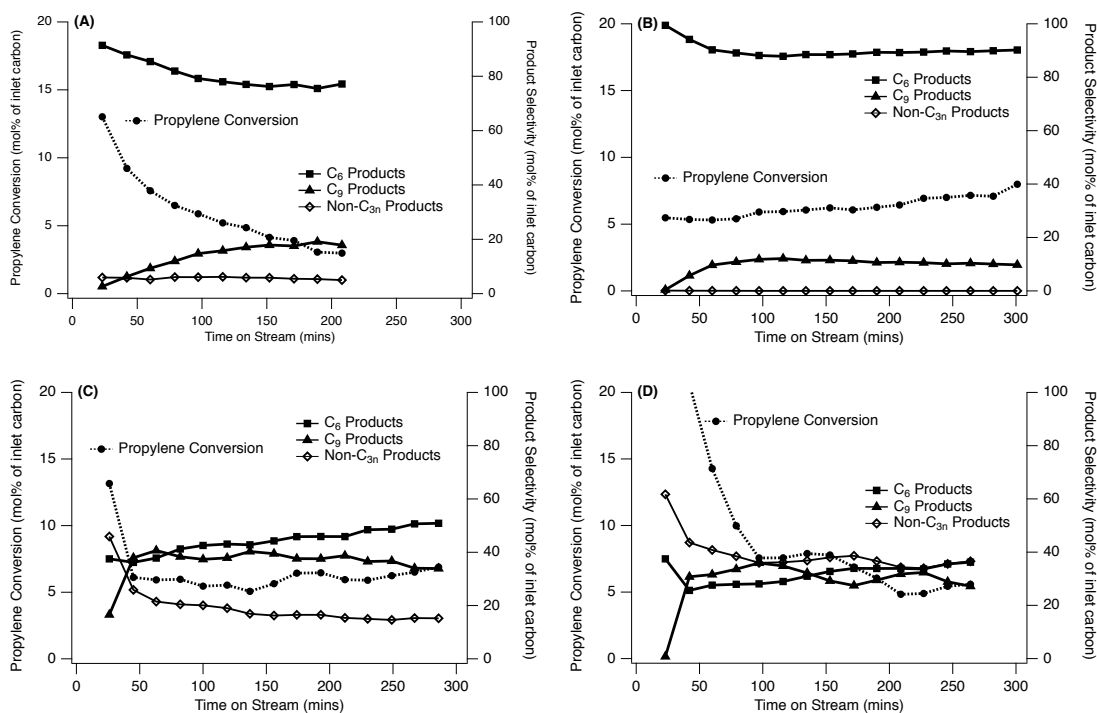


Fig 2 Representative time-on-stream profiles of conversion, C₆ and C₉ selectivity for Ni-CIT-6 (A), Ni-Zn-MCM-41 (B), Ni-HiAl BEA (C), and Ni-USY (D) at 180 °C [21]

We interpret these findings as a consequence of the presence of strong Brønsted sites, which are (at least) comparably active to the Ni sites but not nearly so selective for alkene oligomerization, validating the hypothesis that matching the negative charge created by the framework heteroatom to the positive charge of the exchanged ion should lead to a more effective catalyst.

Conclusions and Prospects

We have shown above that the concept of combining two catalysts — one to activate alkanes by transfer hydrogenation and the other to oligomerize alkenes — can be a viable route for incorporating light alkanes and alkenes into higher hydrocarbon products. By means of mechanistic analysis, we have shown how performance of a tandem catalytic system may be optimized, and also understood the failure of our initial model to achieve the complete targeted process as a consequence of a mismatch between the preferred isomeric substrates and products, respectively, of the two individual catalysts. Lastly, we have generated a new class of oligomerization catalyst that exhibits improved behavior in several key aspects; in particular, it produces isomers that should be compatible with the specificity of the Ir-based transfer hydrogenation catalyst, and allow the complete cycle to operate.

It now remains to be shown that we can in fact combine these two catalysts and demonstrate the full cycle. Chemical compatibility does not appear to be an insurmountable issue: we have found that the Ir catalysts operate normally in a solution

containing suspended Ni-CIT-6. Also there are several known methods for supporting Ir catalysts on silica or alumina, so operating in a flow reactor with a physical mixture of catalysts (or even supporting the Ir catalyst directly on the Ni-zincosilicate) should be a viable option. Work along these lines is being actively pursued.

Acknowledgments

We thank BP for supporting this work through the XC² program. DCL thanks the National Science and Engineering Research Council of Canada for a postdoctoral fellowship.

References

- 1 See for example: Balkus KJ, Shepelev S (1993) *Microporous Materials* 1: 383-391; Garcia R, Coombs TD, Shannon IJ, Wright PA, Cox PA (2003) *Top. Catal.* 24: 115-124.
- 2 Khouw CB, Dartt CB, Li HX, Davis ME, Labinger JA (1994) *J. Catal.* 149: 195-205.
- 3 Labinger JA, Herring AM, Lyon DK, Luinstra GA, Bercaw JE, Horváth I, Eller K (1993) *Organometallics* 12: 895-905.
- 4 Labinger JA (1994) *Catal. Lett.* 26: 95-99.
- 5 Okamoto M, Luo L, Labinger JA, Davis ME (2000) *J. Catal.* 192: 128-136.
- 6 Davis ME, Dillon CJ, Holles JH, Labinger JA (2002) *Angew. Chem. Int. Ed. Engl.* 41: 858-860.
- 7 Agapie T, Schofer SJ, Labinger JA, Bercaw JE (2004) *J. Am. Chem. Soc.* 126: 1304-1305.
- 8 Román-Leshkov Y, Moliner M, Labinger JA, Davis ME (2010) *Angew. Chem. Int. Ed. Engl.* 49: 8954-8957.
- 9 Labinger JA, Bercaw JE (2002) *Nature* 417: 507-514.
- 10 Choi J, MacArthur AHR, Brookhart M, Goldman AS (2011) *Chem. Rev.* 111: 1761-1779.
- 11 Vidal V, Theolier A, Thivolle-Cazat J, Basset J-M (1997) *Science* 276: 99-102.
- 12 Burnett RL, Hughes TR (1973) *J. Catal.* 31: 55-64.
- 13 Goldman AS, Roy AH, Huang Z, Ahuja R, Schinski W, Brookhart M (2006) *Science* 257-261.
- 14 Leitch DC, Lam YC, Labinger JA, Bercaw JE (2013) *J. Am. Chem. Soc.* 135: 10302-10305.
- 15 McLain SJ, Schrock RR (1978) *J. Am. Chem. Soc.* 100: 1315-1317.
- 16 Leitch DC, Labinger JA, Bercaw JE (2014) *Organometallics* 33: 3353-3365.
- 17 McLain SJ, Sancho J, Schrock RR (1980) *J. Am. Chem. Soc.* 102, 5610-5618.
- 18 See for example: Mlinar AN, Baur BG, Bong GG, Getsoian A, Bell AT (2012) *J. Catal.* 296: 156-164; Mlinar AN, Shylesh S, Ho OC, Bell AT (2014) *ACS Catal.* 4: 337-343; and references cited therein.
- 19 Takewaki T, Beck LW, Davis ME (1999) *Top. Catal.* 9: 35-42.
- 20 Takewaki T, Hwang S-J, Yamashita H., Davis ME (1999) *Microporous Mesoporous Mater.* 32: 265-278.
- 21 Deimund ME, Labinger JA, Davis ME (2014) *ACS Catal.*, submitted for publication.